UNIVERSITY OF CALIFORNIA,
IRVINE

Exploring and controlling the supramolecular assembly of amyloid-forming peptides and proteins with chemical model systems.

DISSERTATION

submitted in partial satisfaction of the requirements
for the degree of

DOCTOR OF PHILOSOPHY

in Chemistry

by

Patrick J. Salveson

Dissertation Committee:
Professor James S. Nowick, Chair
Professor Gregory A. Weiss
Professor David L. Van Vranken

2018

DEDICATION

To my parents.

TABLE OF CONTENTS

LIST OF FIGURES

LIST OF TABLES

LIST OF CHARTS

Page

LIST OF SCHEMES

Page

ACKNOWLEDGMENTS

I would like to thank my advisor, Professor James S. Nowick. The best piece of advice I have received prior to embarking on my Ph.D. was given to me by my community college chemistry professor. She told me "your advisor will make or break your time in graduate school". James with out a doubt has made the past 5 years a phenomenal experience. He has provided guidance to me as I have shaped my interests as a scientist. He has allowed me to explore avenues that excite me and to develop my own voice within his laboratory. James has also greatly shaped my ability to communicate my science. His tutelage has had dramatic impact of my ability to write effectively and informatively. I am deeply fortunate to have had James as my advisor.

I would like to thank the members of my thesis committee, Professor Gregory Weiss and Professor David Van Vranken. Both Greg and Dave have been incredible sources for support and inspiration. I deeply admire both Dave and Greg's ability to communicate science, both as lectures and as researchers. I strive to emulate their enthusiasm and their style in my own presentations.

I would like to thank past and current members of the Nowick Laboratory. I am especially grateful for the training I received under the guidance of Dr. Ryan Spencer. My skills in X-ray crystallography are due solely to his training. I am also grateful for the training I received under the guidance of Dr. Adam Kreutzer. His knowledge and training allowed me to learn tissue culture skills. I am also grateful for the career advice that Dr. Pin-Nan Cheng has provided me throughout my time in the Nowick Laboratory. The other members of the Nowick Laboratory have also provided unparalleled feedback into my projects over the years. Both in formal group meetings, and in just day to day interactions. This feedback has greatly elevated my science. Beyond the feedback that members of the Nowick Laboratory have provided me, you are all an incredibly fun group of people to work alongside. The lab is an incredibly fun place to be. I will miss our bi-weekly trips to Cafe Rio.

I would like to thank two undergraduate students whom I have had the privilege to mentor. Both Alexander Thuy-Boun and Sepehr Haerianardakani have been phenomenally motivated students whose work ethic often puts mine to shame. Both Alex and Sepehr have contributed to the work presented in chapters 4 and 5. Their synthetic efforts have served to greatly enrich both of those projects.

I would like to that the facilities I have used over the course of my time at UCI. I would like to that the UCI Laser Facility, and Dr. Dmitry A. Fishman, for assistance with circular dichroism and fluorescence measurements. Dmitiry has also been incredibly supportive of my attempts to learn new spectroscopic techniques. I would also like to thank the UCI Mass Spectrometry facility and its director, Dr. Felix Grun, for assistance with mass spectrometry. I would also like to thank the UCI NMR facility and its director, Dr. Philip R. Dennison, for assistance with NMR measurements.

I would like to thank the UCI Chemistry department as a whole. The faculty in this department have built an incredible training environment for graduate students. Additionally, the support staff are all phenomenal and have facilitated me successfully navigating the administrative requirements of my Ph.D.

I would like to thank the numerous educators who have shaped and guided my interests as a chemist. I am deeply indebted to faculty at Riverside Community College. Specifically Dr. Ellen Kime-Hunt, who was my general chemistry professor. Her guidance and support initially set me on the track to pursue a Ph.D in chemistry.

I would like to thank the many sources of funding that have supported myself and my graduate education. I have been supported by the UCI Training Program in Chemical and Structural Biology in the form of training grant support (T32 GM108561). I am also deeply indebted and grateful to the ARCS Foundation Orange County for additional support. The work presented in chapter 2 was supported by the National Science Foundation (NSF CHE-1507840). The Berkeley Center for Structural Biology is supported in part by the National Institutes of Health, National Institute of General Medical Sciences, and the Howard Hughes Medical Institute. The Advanced Light Source is supported by the Director, Office of Science, Office of Basic Energy Sciences, of the U.S. Department of Energy under Contract No. DEAC02-05CH11231. The work presented in chapter 3 was supported by the National Institutes of Health (Grant No. GM097562). The work presented in chapter 4 was supported by the National Institutes of Health (GM097562). The work presented in chapter 5 was supported by the National Institutes of Health (GM097562). Calculations were performed on the UltraScan LIMS cluster at the Bioinformatics Core Facility at the University of Texas Health Science Center at San Antonio and multiple High Performance Computing clusters supported by NSF XSEDE Grant MCB070038 (to Borries Demeler).

I would like to thank the American Chemical Society for permission in reproducing several chapters of this thesis. Chapter 2 is reproduced with permission from Salveson, P. J.; Spencer, R. K.; Nowick, J. S. *J. Am. Chem. Soc.* **2016**, *138*, 4458–4467. Copyright 2016 American Chemical Society. Chapter 3 is reproduced with permission from Salveson, P. J.; Spencer, R. K.; Kreutzer, A. G.; Nowick, J. S. *Org. Lett.* **2017**, *19*, 3462–3465. Copyright 2017 American Chemical Society. Chapter 4 is reproduced with permission from Salveson, P. J.; Haerianardakani, S.; Thuy-Boun, A.; Kreutzer, A. G.; Nowick, J. S. *J. Am. Chem. Soc.* **2018**, *140*, 5842–5852. Copyright 2018 American Chemical Society.

I would like to thank my close friends, Chris Shirran and John Roberts, for providing me an outlet to decompress over the years. I would also like to thank the many friends I have made in graduate school. You have all made this an incredibly fun time: Adam Kreutzer, Yilin Wang, Nari Ryu, Luke Hanna, Lucas Erickson, and Mikhail Konev.

I would like to thank my extended family for their love and support. I am incredibly fortunate to be surrounded by many aunts, uncles and cousins who care for me deeply and who are all incredibly supportive of me.

I would like to thank my parents for their eternal love and support. You have provided me with the foundation on which others have only added to. I am deeply grateful for your support and your patience as I have grown from a petulant child into the person I am today.

I would like to thank my fiancée, Kathryn "katamaran" Samarin. You have supported me in ways I am not sure how I can repay. You have pushed me to better myself. I am incredibly excited for our life together.

CURRICULUM VITAE

Patrick J. Salveson

EDUCATION

Doctor of Philosophy in Chemistry **2018**
University of California, Irvine

Bachelor of Science in Chemical Biology **2013**
University of California, Berkeley

RESEARCH EXPERIENCE

Graduate Research Assistant **2013–2018**
University of California, Irvine

Undergraduate Research Assistant **2012–2013**
University of California, Berkeley

NSF REU Research Assistant **2011**
University of California, Riverside

AWARDS

ARCS Foundation Scholar **2016–2018**
Chemical and Structural Biology Training Fellow **2015–2017**
Chancellor's Fellow **2013–2015**
Melvin J. Heger-Horst Undergraduate Fellowship **2012–2013**
Rose Hills Foundation Science and Engineering Scholar **2012–2013**
Undergraduate Research Apprenticeship Program Internship **2012–2013**
National Science Foundation Research Experience for Undergraduates **2011**
President's Honor List **2009–2011**

PUBLICATIONS

1. Spencer, R. K.; Kreutzer, A. G.; Salveson, P. J.; Li, H.; Nowick, J. S. X-ray crystallographic structure of oligomers of peptides derived from β2-microglobulin. *J. Am. Chem. Soc.* **2015**, *137*, 6304–6311

2. Salveson, P. J.; Spencer, R. K.; Nowick, J. S. X-ray crystallographic structure of oligomers formed by a toxic β-hairpin derived from α-synuclein: trimers and higher-order oligomers. *J. Am. Chem. Soc.* **2016**, *138*, 4458–4467

3. Salveson, P. J.; Spencer, R. K.; Kreutzer, A. G.; Nowick, J. S. X-ray crystallographic structure of a compact dodecamer from a peptide derived from $A\beta_{16–36}$. *Org. Lett.* **2017**, *19*, 3462–3465

4. Kreutzer, A. G.; Spencer, R. K.; McKnelly, K. J.; Yoo, S.; Hamza, I.; Salveson, P. J.; Nowick, J. S. A hexamer of a peptide derived from $A\beta_{16–36}$. *Biochemistry* **2017**, *56*, 6061–6067

5. Salveson, P. J.; Haerianardakani, S.; Thuy-Boun, A.; Kreutzer, A. G.; Nowick, J. S. Controlling the oligomerizaiton state of Aβ-derived peptides with light. *J. Am. Chem. Soc.*, **2018**, *140*, 5842–5852

6. Salveson, P. J.; Haerianardakani, S.; Thuy-Boun, A.; Yoo, S.; Kreutzer, A. G.; Demeler, B.; Nowick, J. S. Repurposing triphenylmethane dyes to bind to trimers derived from Aβ. *Submitted 6-22-2018*

PATENTS

1. Nowick, J. S.; Kreutzer, A. G.; Spencer, R. K.; Salveson, P. J. Synthetic β-amyloid capable of forming stable antigenic oligomers. Patent Application 15/794,776 filed October 26, **2017**

PRESENTATIONS

1. Salveson, P. J.; Nowick, J. S. Seeing the unseeable in Parkinson's disease: An atomic resolution structure of a neurotoxic oligomer of α-synuclein. Presented at the Associated Graduate Student Symposium at the University of California Irvine, Irvine, CA. April 22, **2015**

2. Salveson, P. J.; Nowick, J. S. X-ray crystallographic structure of oligomers formed by a toxic β-hairpin derived from α-synuclein: Trimers and higher-order oligomers. Presented at the 45th Western Regional Meeting of the American Chemical Society, San Marcos, Ca. November 6–8, **2015**

3. Salveson, P. J.; Nowick, J. S. X-ray crystallographic structure of oligomers formed by a toxic β-hairpin derived from α-synuclein: Trimers and higher-order oligomers. Presented at the 251st National Meeting of the American Chemical Society, San Diego, CA. March 13–17, **2016**; paper ORGN 5

4. Salveson, P. J.; Nowick, J. S. X-ray crystallographic structure of oligomers formed by a toxic β-hairpin derived from α-synuclein: Trimers and higher-order oligomers. Recorded for ACS LiveSlides presentation

5. Salveson, P. J.; Thuy-Boun, A.; Kreutzer, A. G.; Yoo, S.; Nowick, J. S. Triphenylmethane dyes that recognize oligomers of Aβ derived peptides. Presented at the 253rd National Meeting of the American Chemical Society, San Fransisco, CA. April 2–7, **2017**; paper ORGN 695

6. Salveson, P. J.; Haerianardakani, S.; Thuy-Boun, A.; Kreutzer, A. G.; Nowick, J. S. Switching the oligomerizaiton state of Aβ-derived peptides with light. Presented at the Chemistry and Biology of Peptides Gordon Research Seminar, Ventura, CA. February 10–11, **2018**

POSTERS

1. Salveson, P. J.; Barding, G. A.; Larive, C. K. Evaluation of metabolite extraction methods of Arabidopsis and maize tissue on 1H-NMR. Presented at the CEPCEB REU Poster Session at the University of California Riverside, Riverside CA. August, **2011**

2. Hu, K.; Wang, S. B.; Lu, E.; Salveson, P. J.; Gao, Y.; Gronert, K. Dietary DHA abrogate intrinsic sex-specific differences in lacrimal gland lipid mediator circuits during dry eye. Presented at the annual Association for Research in Vision and Ophthalmology, Seattle, WA. May 5–9, **2013**

3. Salveson, P. J.; Spencer, R. K.; Kreutzer, A. G.; Nowick, J. S. A compact dodecamer from a peptide derived from $A\beta_{16–36}$. Presented at the 17th Annual Orange County ARCS Scholar Awards Dinner, Irvine, CA. March 16th, **2017**

4. Yoo, S.; Salveson, P. J.; Kreutzer, A. G.; Nowick, J. S. Detecting amyloid oligomer assembly in a chemical model system. Presented at the 253rd National Meeting of the American Chemical Society, San Fransisco, CA. April 2–7, **2017**; paper ORGN 605

5. Hart, C. H.; Yoo, S.; Salveson, P. J.; Truex, N. T.; Nowick, J. S. Detecting amyloid oligomer assembly using triarylmethane dyes. Presented at the 2017 UCI Undergraduate Research Symposium, Irvine, CA. May 20, **2017**

6. Salveson, P. J.; Haerianardakani, S.; Thuy-Boun, A.; Kreutzer, A. G.; Nowick, J. S. Switching the oligomerizaiton state of Aβ-derived peptides with light. Presented at the Chemistry and Biology of Peptides Gordon Research Seminar, Ventura, CA. February 10–11, **2018**

7. Salveson, P. J.; Haerianardakani, S.; Thuy-Boun, A.; Kreutzer, A. G.; Nowick, J. S. Switching the oligomerizaiton state of Aβ-derived peptides with light. Presented at the Chemistry and Biology of Peptides Gordon Research Conference, Ventura, CA. February 12–16, **2018**

SOFTWARE

Peptide Ion Calculator	iOS and Android
NMR Peak Splittings	iOS
Isotope Pattern Simulator	iOS

TEACHING EXPERIENCE

Organic Chemistry Lab Teaching Assistant **2013–2014**
University of California, Irvine

PROFESSIONAL MEMBERSHIPS

American Chemical Society	**2016–**
Apple Developer Program	**2016–**

ABSTRACT OF THE DISSERTATION

Exploring and controlling the supramolecular assembly of amyloid-forming peptides and proteins with chemical model systems.

By

Patrick J. Salveson

Doctor of Philosophy in Chemistry

University of California, Irvine, 2018

Professor James S. Nowick, Chair

Chapter 1 overviews the phenomenon of the self-assembly of small peptides and proteins in several neurodegenerative diseases, including Alzheimer's disease and Parkinson's disease. This chapter provides context for the rest of the dissertation. The aberrant assembly of peptides and proteins into large structures defines a class of human pathologies, which are collectively known as amyloid diseases. In these diseases, native peptides and proteins misfold and proceed to assemble into structures that mediate the disease. The characterization of these assemblies is particularly challenging due to their heterogeneity and metastability. Within this cornucopia of assemblies, a subset known as soluble oligomers have emerged as likely neurotoxic species responsible for the progression of neurodegenerative diseases. The structures of these oligomers remain unknown. This dissertation describes my efforts to explore and control the structures of these oligomers with chemical model systems.

Chapter 2 presents the X-ray crystallographic structure and biological characterization of oligomers formed by a macrocyclic β-hairpin peptide derived from α-synuclein. The peptide adopts a β-hairpin structure, which assembles in a hierarchical fashion. Three β-hairpins assemble to form a triangular trimer. Three copies of the triangular trimer assemble to form a basket-shaped nonamer. Two nonamers pack to form an octadecamer. Molecular modeling

suggests that full-length α-synuclein may also be able to assemble in this fashion. Circular dichroism spectroscopy demonstrates that the peptide interacts with anionic lipid bilayer membranes, like oligomers of full-length α-synuclein. LDH and MTT assays demonstrate that the peptide is toxic toward SH-SY5Y cells. Comparison of the peptide to homologues suggests that this toxicity results from nonspecific interactions with the cell membrane. The oligomers reported are fundamentally different than the proposed models of the fibrils formed by α-synuclein and suggest that α-$Syn_{36–55}$, rather than the NAC, may nucleate oligomer formation.

Chapter 3 explores the effect of shifting the residue pairing of Aβ-derived β-hairpins on the structures of the oligomers that form through X-ray crystallography. Three residue pairings were investigated using constrained macrocyclic β-hairpins in which $Aβ_{30–36}$ is juxtaposed with $Aβ_{17–23}$, $Aβ_{16–22}$, and $Aβ_{15–21}$. X-ray crystallography reveals that the $Aβ_{16–22}$–$Aβ_{30–36}$ pairing forms a compact ball-shaped dodecamer composed of fused triangular trimers, the $Aβ_{17–23}$–$Aβ_{30–36}$ forms a spherical dodecamer composed of triangular trimers, and that the $Aβ_{15–21}$–$Aβ_{30–36}$ pairing forms a fibril-like assembly. Both the compact dodecamer and the spherical dodecamer may help explain the structures of the trimers and dodecamers formed by full-length Aβ.

Chapter 4 describes the design, synthesis, and characterization of macrocyclic β-hairpins that contain the *N*-2-nitrobenzyl photolabile protecting group. Each peptide contains two heptapeptide segments from $Aβ_{16–22}$ or $Aβ_{17–23}$ constrained into β-hairpins. The *N*-2-nitrobenzyl group is appended to the amide backbone of Gly_{33} to disrupt the oligomerization of the peptides by disrupting intermolecular hydrogen bonds. X-ray crystallography reveals that *N*-2-nitrobenzyl groups can either block assembly into discrete oligomers or permit formation of trimers, hexamers, and dodecamers. Photolysis of the *N*-2-nitrobenzyl groups with long-wave UV light unmasks the amide backbone and alters the assembly and the biological properties of the macrocyclic β-hairpin peptides. SDS–PAGE studies show that removing

the N-2-nitrobenzyl groups alters the assembly of the peptides. MTT conversion and LDH release assays show that decaging the peptides induces cytotoxicity. Circular dichroism studies and dye leakage assays with liposomes reveal that decaging modulates interactions of the peptides with lipid bilayers. Collectively, these studies demonstrate that incorporating *N*-2-nitrobenzyl groups into macrocyclic β-hairpin peptides provides a new strategy to probe the structures and the biological properties of amyloid oligomers.

Chapter 5 presents the discovery that crystal violet and other $C3$ symmetric triphenylmethane dyes bind to triangular trimers derived from Aβ. Although many small molecules bind to these assemblies, the details of how these molecules interact with Aβ oligomers remain unknown. This chapter reports that crystal violet, and other $C3$ symmetric triphenylmethane dyes, bind to $C3$ symmetric trimers derived from Aβ. Binding changes the color of the dyes from purple to blue, and causes them to fluoresce red when irradiated with green light. Job plot and analytical ultracentrifugation experiments reveal that two trimers complex with one dye molecule. Studies with several triphenylmethane dyes reveal that three *N*,*N*-dialkylamino substituents are required for complexation. Several mutant trimers, in which Phe_{19}, Phe_{20}, and Ile_{31} were mutated to cyclohexylalanine, valine, and cyclohexylglycine, were prepared to probe the triphenylmethane dye binding site. Size exclusion chromatography, SDS-PAGE, and X-ray crystallographic studies demonstrate that these mutations do not impact the structure or assembly of the triangular trimer. Fluorescence spectroscopy and analytical ultracentrifugation experiments reveal that the dye packs against an aromatic surface formed by the three Phe_{20} side chains and is clasped by the side chains of Ile_{31}. Docking and molecular modeling provide a working model of the complex in which the triphenylmethane dye is sandwiched between two triangular trimers. Collectively, these findings demonstrate that the X-ray crystallographic structures of triangular trimers derived from Aβ can be used to guide the discovery of ligands that bind to soluble oligomers derived from Aβ.

Chapter 1

Supramolecular assemblies in amyloid diseases

1.1 Introduction

Alzheimer's disease is a fatal neurodegenerative disorder for which there is no known cure.[1] Tremendous progress has been made in understanding the molecular basis of this disease. These studies have uncovered the importance that supramolecular assemblies play in the progression of Alzheimer's disease. This chapter describes the discovery and characterization of the supramolecular assemblies that can form in Alzheimer's disease and other amyloid diseases. A focus is placed on the unifying themes of self-assembly that have been uncovered by high resolution structures of the assemblies.

Alzheimer's disease belongs to a much larger class of human diseases known as amyloid diseases (Table 1.1).[2,3] Many amyloid diseases are neurodegenerative disorders. These include Alzheimer's disease, Parkinson's disease, and many others. Amyloid diseases are not limited to neurodegenerative disorders and can instead affect other organs; medullary thyroid

Table 1.1: Several amyloid diseases and the proteins that mediate them

Disease	aggregating peptide/protein
Alzheimer's disease	β-amyloid (Aβ), tau
Parkinson's disease	α-synuclein
Huntington's disease	huntingtin
Creutzfeldt-Jakob disease	prion protein (PrP)
amyotrophic lateral sclerosis (ALS)	superoxide dismutase (SOD1)
light-chain amyloidosis	immunoglobulin light chains
type-2 diabetes	islet amyloid polypeptide (IAPP)
dialysis-related amyloidosis	β_2-microglobulin (β_2M)
familial amyloid cardiomyopathy	transthyretin (TTR)
rheumatoid arthritis	serum amyloid A
medullary thyroid cancer	calcitonin

cancer affects the thyroid, familial amyloid cardiomyopathy affects the heart. Many amyloid diseases can instead be systemic diseases that affect several organs simultaneously. These include dialysis-related amyloidosis, rheumatoid arthritis, and amyloid light-chain amyloidosis, type-2 diabetes, and many others.

All amyloid diseases share an common molecular phenomenon that unifies them. In these diseases, small peptides or proteins aggregate into large structures.[2,3] These supramolecular assemblies proceed to damage the surrounding tissue. These assemblies are heterogenous, polymorphic, and metastable. They can vary in size, in shape, and in solubility. These assemblies can be segregated into two classes: large insoluble assemblies known as fibrils, and smaller soluble assemblies known as oligomers. Studies of these assemblies have revealed a complex process of self-assembly and supramolecular chemistry. Within this complexity lies unifying themes of supramolecular chemistry that unite the disparate diseases.

1.2 Amyloid Fibrils

The first report of supramolecular assemblies forming in an amyloid disease was described by Alois Alzheimer in his 1906 lecture titled "A characteristic serious disease of the cerebral cortex".[4] In this lecture, Dr. Alzheimer described the appearance of thread-like structures in dissected brains from individuals who presented with dementia. These structures have since become known as fibrils and tangles. The deposition of fibrils, sometimes referred to as plaques, is a hallmark of all amyloid diseases.[5] The fibrils in Alzhiemer's disease are formed by the β-amyloid peptide, Aβ.[6] The tangles are formed by the microtubule-associated protein tau.[7] Numerous studies have been conducted to understand the molecular structures of these fibril since their initial description.

Aβ fibrils are characterized by a "cross-β" structure. This type of assembly was first described from the X-ray diffraction of fibrils in 1968.[8,9] The molecular details of these assemblies have since been characterized by solid-state NMR (ssNMR) and cryoelectron microscopy (cryo-EM).[10–19] The details of these structures have been described in depth elsewhere, however, a brief comparison of these structures is warranted as they highlight a key feature of the supramolecular assemblies formed in amyloid diseases.[20]

The high-resolution structures of Aβ fibrils determined by ssNMR and cryo-EM demonstrate that a single amyloidogenic peptide can assemble in numerous fashions (Figure 1.1). The structures of Aβ fibrils all differ in the precise details of their assemblies, yet they share common themes. They are all composed of many copies Aβ, either $A\beta_{40}$ or $A\beta_{42}$, arranged into a one dimensional lattice. The individual Aβ molecules that comprise the fibrils fold into compact structures that are rich in β-strands. This folding buries large patches of hydrophobic residues within the core of the assembly. Even though the precise fold of Aβ differs amongst these structures, they are primarily governed by the central ($A\beta_{15–23}$) and the *C*-terminal ($A\beta_{30–36}$) hydrophobic regions of the peptide.

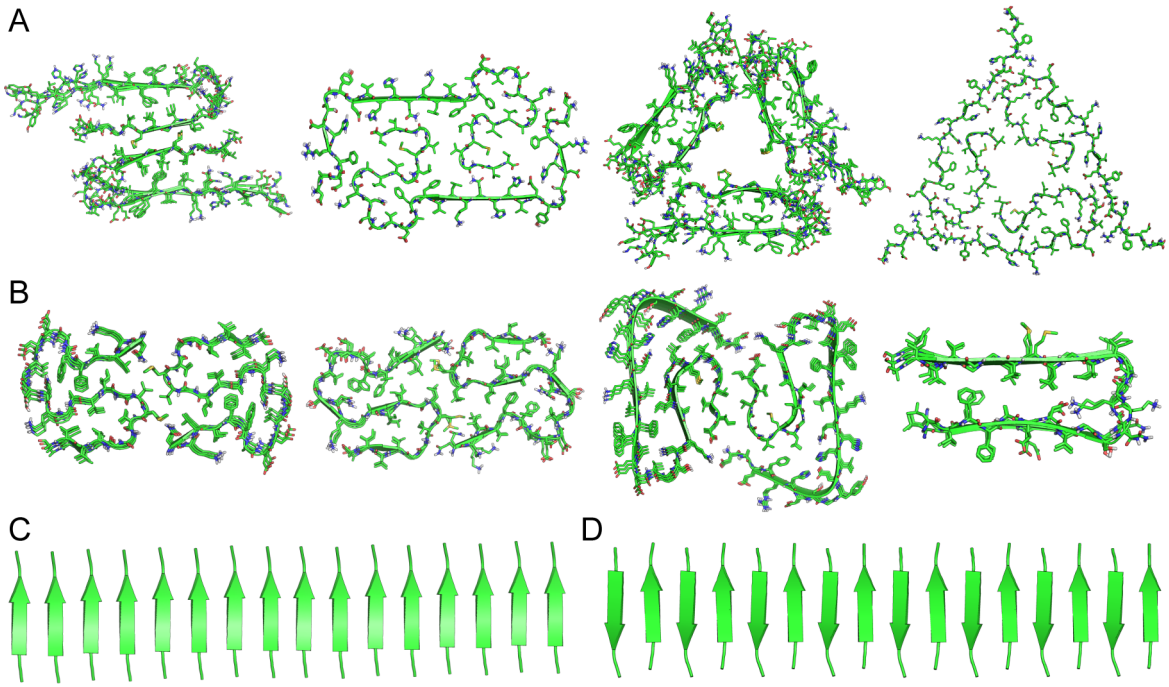

Figure 1.1: Representative high-resolution structures of Aβ fibrils. (A) solid-state NMR structures of $A\beta_{40}$ fibrils (PDB from left to right: 2LMN, 2MVX, 2LMP, 2M4J). (B) solid-state NMR and cryo-EM structures of $A\beta_{42}$ fibrils (PDB from left to right: 2NAO, 5KK3, 5OQV, 2BEG). (C) X-ray crystallographic structure of an $A\beta_{30–35}$ fibril, comprising parallel β-sheets (PDB 2Y3J). (D) X-ray crystallographic structure of an $A\beta_{16–21}$ fibril, comprising anti-parallel β-sheets (PDB 3OW9).

Each Aβ molecule interacts with other Aβ molecules along the fibril axis through the formation of parallel or anti-parallel β-sheets (Figure 1.1C and D). These β-sheets are oriented orthogonal to the fibril axis. Nearly all fibril structures reported thus far comprise Aβ arranged into parallel β-sheets. The fibril structure of the Iowa familial mutant is one counter example of this trend.[12] The β-sheets that comprise the Aβ fibrils are not twisted like those that comprise proteins, but instead are flat.[21]

These structures provide a framework, or a set of rules, that describes how Aβ can assemble into a fibril: $A\beta_{15–23}$ and $A\beta_{30–36}$ fold into β-strands that pack together to form a network of flat parallel or anti-parallel β-sheets. Further, these structures highlight the polymorphic nature of the structures that amyloid-forming peptides and proteins can adopt. This structural

heterogeneity is a central theme to the supramolecular assembly of this class of peptides and proteins.

These fibril assembly rules are not specific to Aβ but instead extend to other amyloidogenic peptides and proteins that mediate other amyloid diseases (Figure 1.2). Thus far, the application of ssNMR and cryo-EM to determine the structures of other amyloid fibrils has been limited to α-synuclein and tau fibrils.[22,23] These structures reveal that the amyloidogenic proteins that comprise the fibrils are folded into compact β-strand-rich structures, much like Aβ. The individual amyloidogenic proteins within the fibrils interact with neighboring proteins in the fibril through the formation of parallel β-sheets, like in the fibrils formed by Aβ. These β-sheets are oriented orthogonal to the fibril axis. The two tau fibrils depicted in Figure 1.2B also demonstrate that a single amyloid-forming protein can assemble in different fashions. As more high resolution fibril structures of other amyloid-forming peptides and proteins are determined, they will likely continue to highlight these common themes of supramolecular assembly.

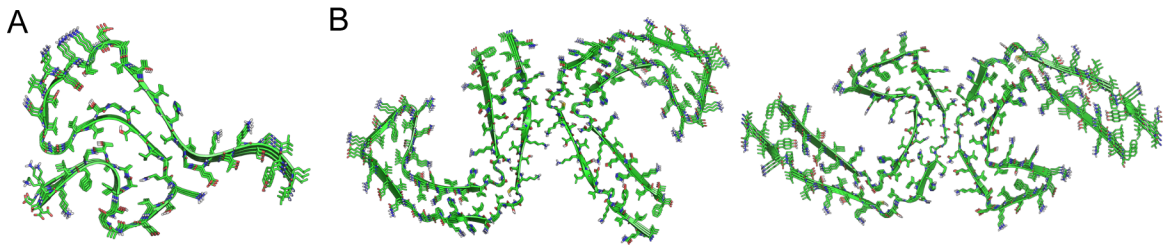

Figure 1.2: High resolution structures of α-synuclein and tau fibrils. (A) solid-state NMR structure of an α-synuclein fibril (PDB 2N0A). (B) Cryo-EM structures of tau fibrils (PDB from left to right: 5O3O, 5O3T).

X-ray crystallographic and micro-electron diffraction (microED) studies of peptide fragments derived from full-length amyloid-forming peptides and proteins have expanded our understanding of the structures of other amyloid fibrils.[24–34] These structures provide further insights into amyloid fibrils when fibril structures of the full-length peptide or protein are unavailable. The nuances of these structures have recently been described thoroughly

elsewhere,[35,36] however, they again demonstrate that the peptide-fragment fibrils share the common themes of assembly described above for fibrils formed by full-length proteins. The peptide fragments fold into β-strands. The peptides interact with neighboring peptides in the fibril to form parallel or anti-parallel β-sheets (Figure 1.3). These β-sheets are oriented orthogonal to the fibril axis. Layers of these fibrils stack together through the formation of "steric zippers". These hydrophobic cores are characterized by the inter-digitation of the amino acid side chains. There appear to be few exceptions to these rules for fibril assembly.[37] These rules likely extend to the vast majority of amyloid-forming peptides and proteins that mediate amyloid diseases.

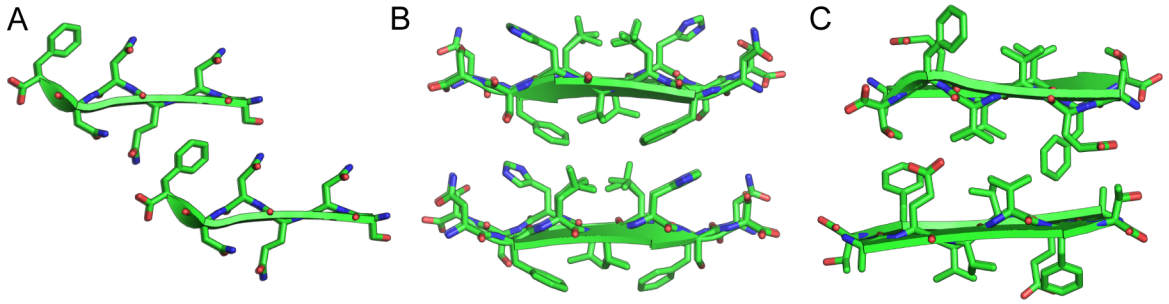

Figure 1.3: Representative high-resolution structures of amyloid-derived peptide fibrils. (A) X-ray crystallographic structure of an $hPrP_{120–125}$ fibril (PDB 2OL9). (B) X-ray crystallographic structure of an $IAPP_{14–20}$ fibril (PDB 3FTH). (C) X-ray crystallographic structure of a $TTR_{111–116}$ fibril (PDB 4XFN).

The high resolution structures of fibrils have not only expanded our understanding of how these assemblies form in amyloid diseases, but have also served as inspiration for the design of functional materials.[38,39] These rules have been used to design peptides that can dynamically form fibril-like assemblies.[40,41] The high resolution structure of these peptide assemblies are similar to the fibrils formed by amyloid-forming peptide and proteins described above.[42] These design rules have also been used to design fibrils with catalytic activity.[43–47]

1.3 Amyloid Oligomers

The deposition of fibrils in diseased tissue initially lead to the hypothesis that their formation mediates Alzheimer's disease.[48] In recent years this view has changed. Instead, the smaller soluble assemblies of Aβ, known as oligomers, are now thought to be important to the development of the disease.[49,50] Similar shifts have occurred in our understanding of other amyloid diseases.

In contrast to the large fibrils described in the preceding section, the structures of amyloid oligomers remain unknown. There are no high resolution structures of a full-length amyloid-forming peptide or protein assembled into an oligomer. A number of low resolution structural studies have shown that the oligomers are polymorphic, heterogenous and metastable.[51] The oligomers appear to share common themes in their self-assembly, analogous to the common features in the fibrils structures discussed above. The oligomers do not resemble fibrils, but instead are constructed though rules unique to these assemblies. For example, oligomers appear to be constructed through the formation of primarily anti-parallel β-sheets, instead of the parallel β-sheets that dominate the fibril structures.

The high resolution structures of peptide fragments have shaped much of our understanding of amyloid oligomer structures (Figure 1.4). These peptide fragments provide insights into the structures of amyloid oligomers while no oligomer structures of the full-length peptide or protein are available. The first glimpse of an amyloid oligomer was described in 2012.[52] The X-ray crystallographic structure of αB-crystalin$_{90–100}$ revealed a cylindrin motif (Figure 1.4A and B). In this motif, six peptides pack to form a cylindrical assembly. The individual peptides fold into β-strands. These β-strands interact to form an antiparallel β-sheet that wraps around the cylinder. The cylindrin motif has also been proposed to be adopted by *C*-terminal fragments of Aβ.[53] A similar cylindrical assembly was subsequently observed in the X-ray crystallographic structure of fragments of the human prion protein hPrP (Figure

1.4C and D).[54] In this structure six copies of the disulfide-linked fragments of hPrP pack to form a hexameric β-barrel-like assembly. Both the cylindrin and β-barrel-like assembly are composed of twisted β-sheets, in contrast to the flat β-sheets that dominate the fibril structures.

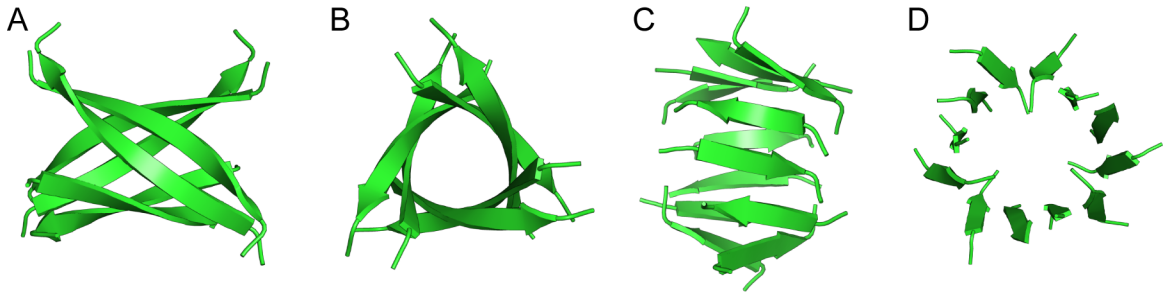

Figure 1.4: X-ray crystallographic structures of α-B crystallin-derived and hPrP-derived peptide oligomers. (A and B) The α-B crystalin$_{90–100}$ cylindrin (PDB 3SGO). The image in B is rotated 90° relative to the image in A. (C and D) The hPrP$_{177–182}$–hPrP$_{211–216}$ hexamer (PDB 4E1I). The image in D is rotated 90° relative to the image in C.

These structures suggest that amyloid oligomers formed by different amyloid-forming peptides and proteins may share similar themes in their assembly. As more structures of peptide fragments become available, these rules will likely be refined. This understanding may allowing the relationship between oligomer structure and biological activity to be characterized. Such information could lead to the development of therapeutics for Alzheimer's disease and other amyloid diseases. Alternatively, these rules may lead to the design of functional materials, in the same way that the structures of the fibrils have guided the design of functional materials.

1.4 Chemical Model Systems

The structures of peptide fragments described by Eisenberg and coworkers and Surewicz and coworkers represent the first tantalizing insights into the supramolecular assemblies of amyloid oligomers.[52,54] In tandem to these groups, the Nowick lab has pioneered the use

of macrocyclic β-hairpins as a tool to study the structures of amyloid oligomers at high resolution.[55] These chemical model systems contain two heptapeptide fragments derived from an amyloid-forming peptide or protein. These two fragments are constrained into a β-hairpin through the macrocyclization with two δ-linked ornithine turn units ($^{\delta}$Orn). These two unnatural amino acids act as β-turn mimics. The macrocyclic β-hairpin peptides are prone to aggregation due to the hydrophobic, amyloidogenic sequences they contain. To limit uncontrolled aggregation, these peptides bear a single *N*-methyl group appended to the backbone. This *N*-methyl group disrupts continuous networks of β-sheets, like those that form in the fibril and fibril-like assemblies depicted in Figures 1.1, 1.2, and 1.3. This disruption serves to trap the macrocyclic β-hairpin peptides, and the amyloidogenic sequences that they contain, in oligomeric assemblies. Fortuitously, the resulting assemblies are often characterizable at high-resolution by X-ray crystallography.

This approach to studying amyloid oligomers was developed by Dr. Ryan K. Spencer, a previous graduate student in the Nowick Laboratory.[56–58] Dr. Spencer designed and synthesized macrocyclic β-hairpins **1.1** and **1.2** (Chart 1.1). Peptide **1.1** is derived from the amyloidogenic protein β_2-microglobulin (β_2M). In this peptide, $\beta_2M_{63–69}$ is juxtaposed by a designed heptapeptide sequence. Dr. Spencer designed peptide **1.1** and several homologues to study the impact that a single point mutation can have on the structures of amyloid oligomers. In contrast, peptide **1.2** contains two heptapeptide derived from $A\beta_{17–36}$. Dr. Spencer designed this peptide to mimic a β-hairpin adopted by Aβ.[59]

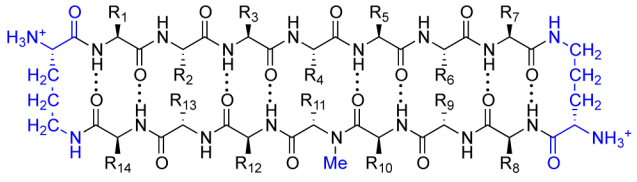

macrocyclic β-hairpin peptide

peptide **1.1** cyclo(YLLF^{l}YTG $^{\delta}$O KVAA_{Me}AVK $^{\delta}$O)
peptide **1.2** cyclo(LVFF AED $^{\delta}$O A I I G_{Me}LOV $^{\delta}$O)

Chart 1.1

The X-ray crystallographic structures of peptides **1.1**, its homologues, and **1.2** differ in the precise details of their assemblies, yet share similar themes in supramolecular assembly (Figure 1.5). In these structures, the individual β-hairpin peptides pack to form triangular trimers and hydrogen-bonded dimers. The individual β-hairpins that comprise these trimers and dimers are highly twisted. These trimer and dimer subunits serve as building blocks for higher-order oligomers such as hexamers, octadecamers, and dodecamers. These common features are reminiscent to the similarities present in fibril structures discussed in the preceding subsections. These structures suggest that amyloid oligomers formed by different amyloid-forming peptides or proteins might comprise similar structural motifs. Those motifs might be triangular trimers like the ones depicted in Figure 1.5. These structures have led the Nowick laboratory to suggest a model for amyloid oligomer formation wherein the amyloid-forming peptide or protein folds into a β-hairpin, the β-hairpin assembles into triangular trimers, and the triangular trimers assemble into related higher-order oligomers (Figure 1.5C).

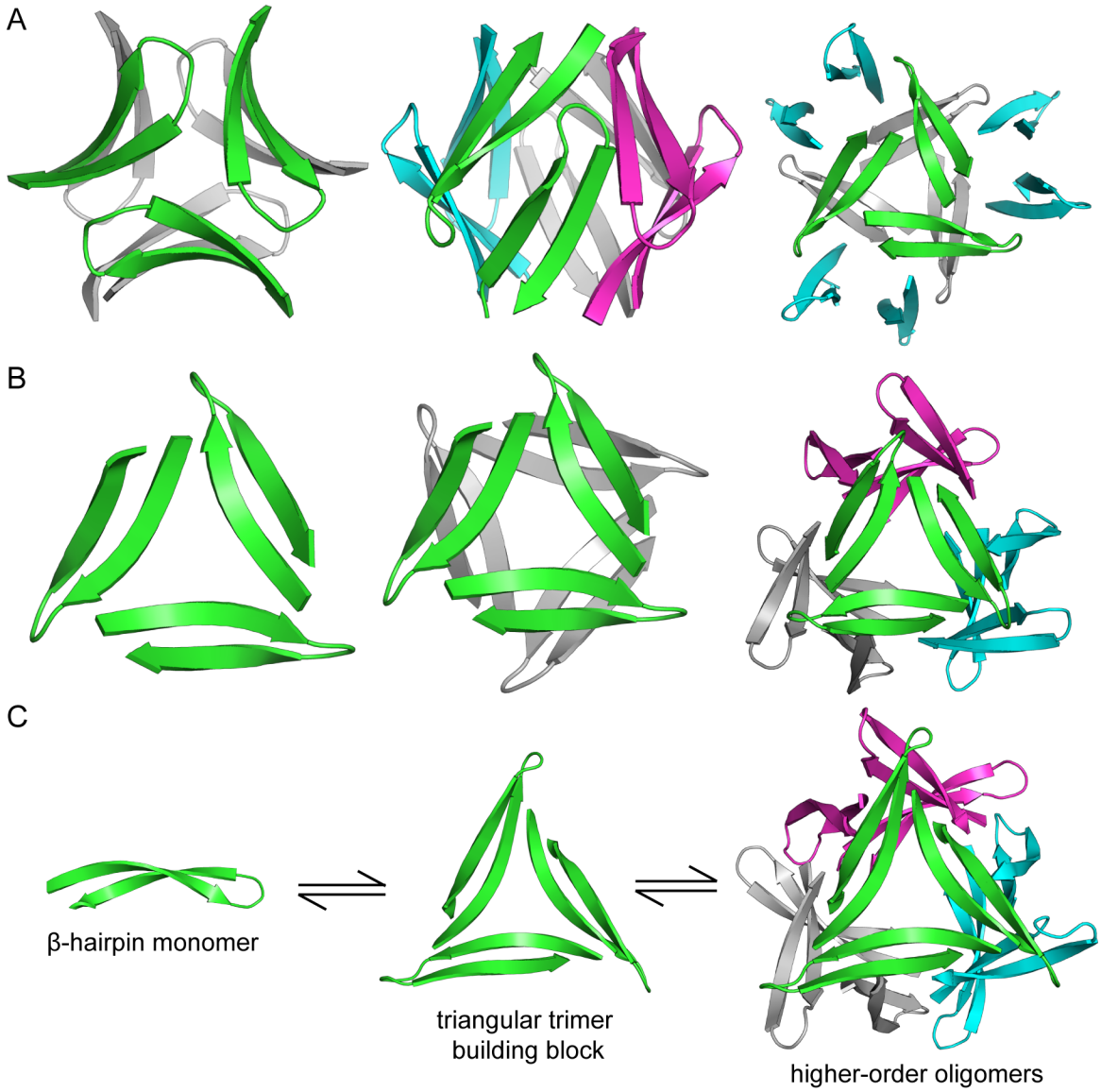

Figure 1.5: X-ray crystallographic structures of oligomers formed by macrocyclic β-hairpin peptides **1.1** and **1.2**. (A) X-ray crystallographic structures of peptide **1.1** and its homologues (PDB from left to right: 4P4V, 4P4Z, 4P4W). (B) X-ray crystallographic structure of a triangular trimer, sandwich-like hexamer, and spherical dodecamer formed by peptide **1.2** (PDB 4NTR). (C) Model for the hierarchical assembly of β-hairpins into triangular trimers and related higher-order oligomers.[60]

The structures depicted in Figure 1.5A and B represented the Nowick Laboratory's understanding of amyloid oligomers when I joined the laboratory in 2013. Since then, the Nowick laboratory has refined the model depicted in Figure 1.5C through the design and charac-

terization of macrocyclic β-hairpin peptides like peptides **1.1** and **1.2**. Work by Dr. Adam Kreutzer has expanded upon this model in context of Aβ-derived peptides.[60–62]

This dissertation describes my contributions to this model. In Chapter 2, I explore the supramolecular assembly of α-synuclein derived peptides. I find that α-synuclein may assemble into triangular trimers and related higher-order oligomers like those depicted in Figure 1.5.[63] In Chapter 3, I explore the self-assembly of homologues of peptide **1.2**. I find that a simple perturbation of the β-hairpin can alter the resulting oligomer structure.[64] In Chapter 4, I develop a new tool that allows the oligomer's assembly to be dynamically controlled with light. I find that oligomerization is required to induce cell-death.[65] In Chapter 5, I describe the discovery that triphenylmethane dyes bind to triangular trimers derived from Aβ. I find that the three-fold symmetric triangular trimers bind to three-fold symmetric small molecules. Collectively, my contributions have expanded the model depicted in Figure 1.5C to additional amyloid forming peptides, and have provided new tools with which the supramolecular assemblies of amyloid-derived peptides can be controlled and interrogated.

Chapter 2

X-ray crystallographic structure of oligomers formed by a toxic β-hairpin derived from α-synuclein: trimers and higher-order oligomers

2.1 Introduction

Parkinson's disease is one of several amyloid disorders, collectively referred to as synucleinopathies, whose pathology is characterized by the aggregation of the presynaptic protein α-synuclein (α-Syn) into Lewy bodies.[66–68] Despite the appearance of these Lewy bodies in diseased brains, soluble oligomers of α-Syn seem to be the toxic agent in Parkinson's disease.[69] The characterization of α-Syn oligomers is an outstanding biophysical challenge due to their heterogeneity and propensity to aggregate. These properties have precluded α-Syn oligomers from high-resolution structural characterization by X-ray crystallography and have

limited their characterization to a range of low-resolution techniques, including size-exclusion chromatography, SDS-PAGE, dynamic light scattering, analytical ultracentrifugation, and cryo-TEM.[70] The same properties have precluded oligomers formed by many amyloidogenic proteins from structural characterization at high resolution.

Small peptides derived from amyloidogenic proteins have afforded high-resolution structures that provide insights into the structures of amyloid oligomers formed by full-length proteins.[52,54,57,58,71–73] Studying the assembly of small peptides derived from α-Syn may provide insights into oligomeric assemblies of the protein. Several structural studies of α-Syn oligomers have suggested that two β-strands loosely defined by residues 36–43 and 49–58 form the core of the toxic oligomers associated with Parkinson's disease.[74–76] Most notably, Hoyer et al. recently observed a β-hairpin defined by residues 36–55 in monomeric α-Syn by NMR spectroscopy (Figure 2.1A).[77] The authors found that sequestering this β-hairpin in an engineered binding protein markedly reduces the toxicity of aged α-Syn and inhibits its fibrillization. The β-hairpin has also been observed in solution by others.[78,79]

Five of the six known disease-causing point mutations of Parkinson's disease are located within this β-hairpin, further emphasizing the importance that this region plays in the pathology of Parkinson's disease.[80–85] Recently, Schulten et al. have found through molecular dynamics simulations that residues 36–55 adopt a β-hairpin similar to that observed by Hoyer et al.[86] The authors also found that disease-causing point mutations stabilize the β-hairpin. They further suggest that β-hairpin formation precedes aggregation of α-Syn in the pathway to pathology. The concurrence of genetic and structural evidence motivated us to design a macrocyclic β-sheet that mimics this β-hairpin, with the goal of creating a high-resolution structural model of α-Syn oligomers (Figure 2.1).

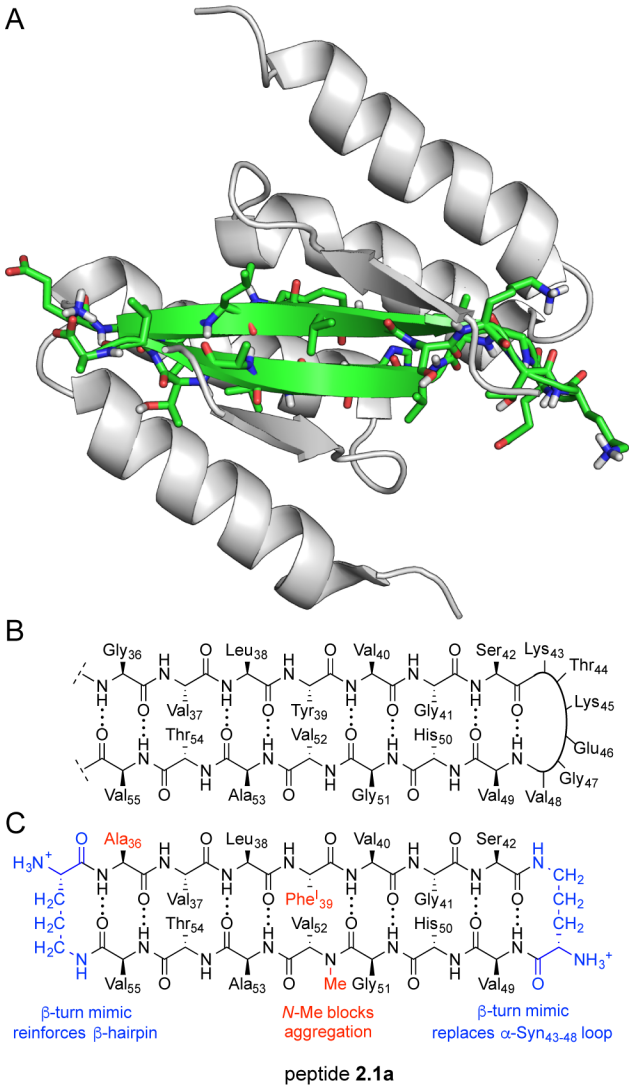

Figure 2.1: Design of peptide **2.1a**. (A) NMR structure of the β-hairpin formed by residues 36–55 in full-length α-Syn (green) bound by an engineered affibody (white) (PDB 4BXL).[77] (B) Chemical structure of the β-hairpin formed by α-Syn$_{36–55}$. (C) Chemical structure of peptide **2.1a**.

We designed macrocyclic β-sheet peptide **2.1a** to mimic the β-hairpin formed by α-Syn$_{36–55}$ (Figure 2.1B and C): We incorporated the heptapeptides α-Syn$_{36–42}$ (GVLYVGS) and α-Syn$_{49–55}$ (VHGVATV) into the top and bottom strands of the macrocycle to maintain the same alignment and hydrogen-bonding patterns observed in the NMR structure. We replaced the residues that form the loop of the β-hairpin (43–48) with a δ-linked ornithine turn unit, which serves as a β-turn mimic and enforces a β-sheet conformation.[87] We connected residues

36 and 55 with a second δ-linked ornithine turn to further enforce a β-sheet conformation. We mutated Gly_{36} to Ala to enhance the folding of peptide **2.1a**. We incorporated a single *N*-methyl group on Val_{52} to limit the uncontrolled aggregation of peptide **2.1a**.[56] We mutated Tyr_{39} to 4-iodophenylalanine (Phe^{I}) to allow X-ray crystallographic phase determination using single wavelength anomalous dispersion (SAD) phasing.

This approach has allowed us to determine the X-ray crystallographic structure of oligomers formed by this β-hairpin derived from α-$Syn_{36–55}$.[88] In this structure, we observe a hierarchical assembly of β-hairpins: three β-hairpins assemble to form a trimer, three trimers assemble to form a nonamer, and two nonamers pack to form an octadecamer. This structure is the first reported X-ray crystallographic structure of oligomeric assemblies of peptides derived from α-Syn. These oligomers suggest a model for α-Syn oligomerization in which self-assembly of α-Syn is centered around α-$Syn_{36–55}$.

2.2 Results

X-ray crystallographic structure of a peptide derived from α-$Syn_{36–55}$. Peptide **2.1a** and its derivatives were synthesized using Fmoc-based solid-phase peptide synthesis (Scheme 2.1).[56,57] Screening peptide **2.1a** in 288 conditions yielded a single condition in which crystals grew: 0.1 M HEPES buffer at pH 8.0, 0.5 M $(NH_4)_2SO_4$, and 34% 2-methyl-2,4-pentanediol (MPD). Diffraction data were collected to 1.97 Å at the Advanced Light Source at Lawrence Berkeley National Laboratory with a synchrotron source at 0.976 Å. Data were scaled and merged with XDS.[89] The locations of the anomalous scattering atoms were determined using the program HySS (hybrid structure search).[90] The structure of peptide **2.1a** was solved and refined in space group $P2_13$. Coordinates for hydrogen atoms were added during refinement in phenix.refine.[90] Table 2.1 summarize the crystallographic properties,

crystallization conditions, data collection, and model refinement statistics for peptides **2.1a** and *ent*-**2.1a**.

The asymmetric unit contains six distinct copies of peptide **2.1a**, each of which is folded into an antiparallel β-hairpin with minor differences in the conformations of Thr_{54}, Val_{55}, and the δ-linked ornithine turn unit that joins Ala_{36} to Val_{55} (Figures 2.2 and 2.3). The residues of the β-hairpin are displayed on the front or back surfaces of the β-sheet: Ala_{36}, Leu_{38}, Val_{40}, Ser_{42}, Val_{49}, Gly_{51}, Ala_{53}, and Val_{55} are displayed on the front surface; Val_{37}, Phe^{I}_{39}, Gly_{41}, His_{50}, *N*-Me Val_{52}, and Thr_{54} are displayed on the back surface.[21] The β-hairpin monomers have a right-handed twist ranging from approximately 15–30° per residue along the β-strand axis, thus mimicking the highly twisted β-hairpin observed by Hoyer et al. (Figure 2.3B).

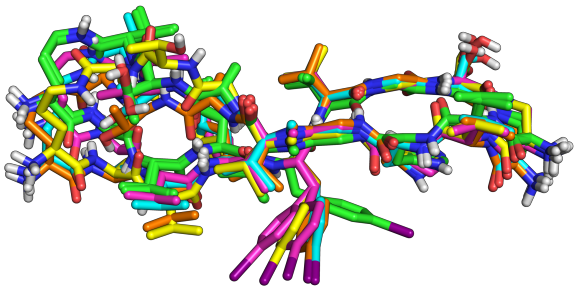

Figure 2.2: Overlay of the six molecules of peptide **2.1a** from the asymmetric unit (PDB 5F1T). The average RMSD overlay is 0.83 Å.

Table 2.1: Crystallographic properties, crystallization conditions, and data collection and model refinement statistics for peptides **2.1a** and *ent*-**2.1a**

peptide	**2.1a**	*ent*-**2.1a**
PDB ID	5F1T	5F1W
space group	$P2_13$	$P2_13$
a, *b*. *c* (Å)	77.518, 77.518, 77.518	77.91, 77.91, 77.91
α, β, γ (^{o})	90, 90, 90	90, 90, 90
peptides in asymmetric unit	6	6
crystallization conditions	0.1 M HEPES, pH 8.0, 0.5 M NH_4SO_4, 34% racemic 2-methyl-2,4-pentanediol	
	Data Collection[a]	
wavelength (Å)	0.976	0.997
resolution (Å)	38.76–1.971 (2.041–1.971)	31.81–2.162 (2.239–2.162)
total reflections	65593 (6546)	17323 (1682)
unique reflections	11211 (1122)	8669 (841)
multiplicity	5.9 (5.8)	2.0 (2.0)
completeness (%)	99.85 (100.00)	100 (100)
mean I/σ	12.38 (2.49)	5.84 (2.27)
Wilson B-factor	21.66	34.71
R_{merge}	0.1117 (0.6654)	0.06961 (0.4373)
$R_{measure}$	0.1229	0.09844
$CC_{1/2}$	0.997 (0.735)	0.989 (0.454)
CC*	0.999 (0.92)	0.997 (0.79)
	Refinement	
R_{work}	18.28	22.29
R_{free}	22.09	28.29
non-hydrogen atoms	821	754
RMS_{bonds}	0.012	0.026
RMS_{angles}	1.51	0.80
Ramachandran favored (%)	100	21.82[b]
outliers (%)	0	78.18[b]
clashscore	2.21	2.70
average B-factor	29.50	46.89

[a]Values for the highest resolution shell are show in parentheses. [b]Ramachandran-favored values for peptide *ent*-**2.1a** should be ignored, as it is composed of all D-amino acids

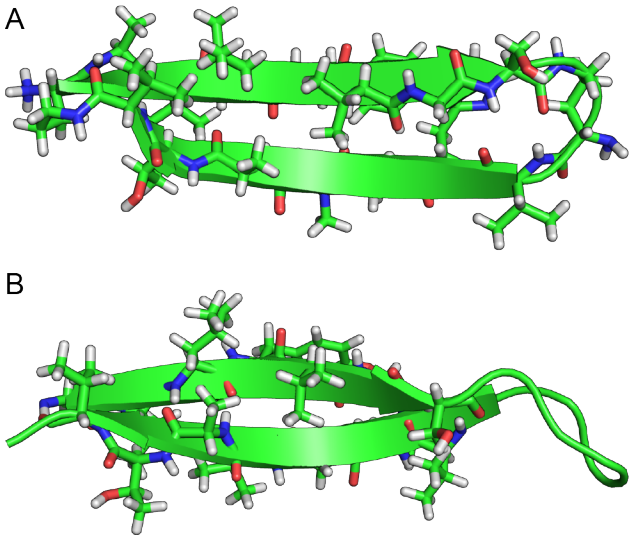

Figure 2.3: Peptide **2.1a** mimics the structure of α-Syn$_{36–55}$. (A) Representative β-hairpin monomer from the crystal lattice of peptide **2.1a** (PDB 5F1T). (B) β-Hairpin monomer formed by α-Syn$_{36–55}$ (PDB 4BXL, affibody omitted).[77]

The differences in conformations of Thr$_{54}$ appear to be responsible for the slight differences among the β-hairpin monomers (Figure 2.4). Four of the six monomers in the asymmetric unit form an ideal β-hairpin. In the fifth monomer, the hydroxy group of Thr$_{54}$ is positioned such that it disrupts the interchain hydrogen bond between the amide proton of Val$_{55}$ and the carbonyl oxygen of Ala$_{36}$ (Figure 2.4B). In the sixth monomer, Thr$_{54}$ participates in a γ-turn between Ala$_{53}$ and Val$_{55}$ (Figure 2.4C). Both of these conformations abrogate the intramolecular hydrogen bonding between Ala$_{36}$ and Val$_{55}$ and distort the conformation of the δ-linked ornithine turn that connects them.

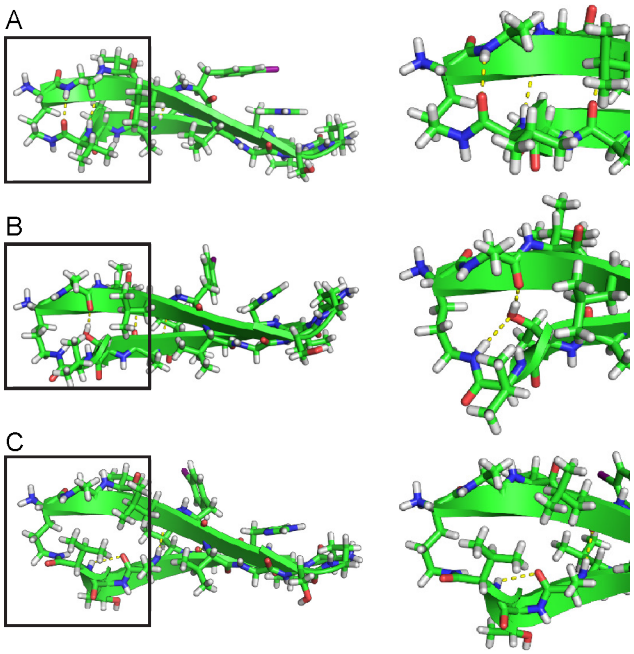

Figure 2.4: β-Hairpin monomers from the asymmetric unit of peptide **2.1a**. (A) β-Hairpin monomer of peptide **2.1a** in which the β-strands are completely hydrogen bonded, with a magnified view of the hydrogen bonding between Ala_{36} and Val_{55}. (B) β-Hairpin monomer in which the hydroxy group of Thr_{54} hydrogen bonds with the carbonyl of Ala_{36} and the δNH of ornithine, with a magnified view of the disrupted hydrogen bonding between Ala_{36} and Val_{55} by Thr_{54}. (C) β-Hairpin monomer in which Ala_{53}, Thr_{54}, and Val_{55} form a γ-turn, with a magnified view of the disrupted hydrogen bonding between Ala_{36} and Val_{55} by the γ-turn.

The six β-hairpin monomers of the asymmetric unit further assemble into two triangular trimers in which three monomers occupy the edges of the triangle (Figure 2.4A). The two trimers differ little in structure. Each trimer is composed of two monomers in one orientation and one monomer in a different orientation. The relative orientations of the *N*-methyl groups within the trimer highlight the lack of internal symmetry; two of the methyl groups point into the center of the trimer, whereas the third points outward (Figure 2.4B).

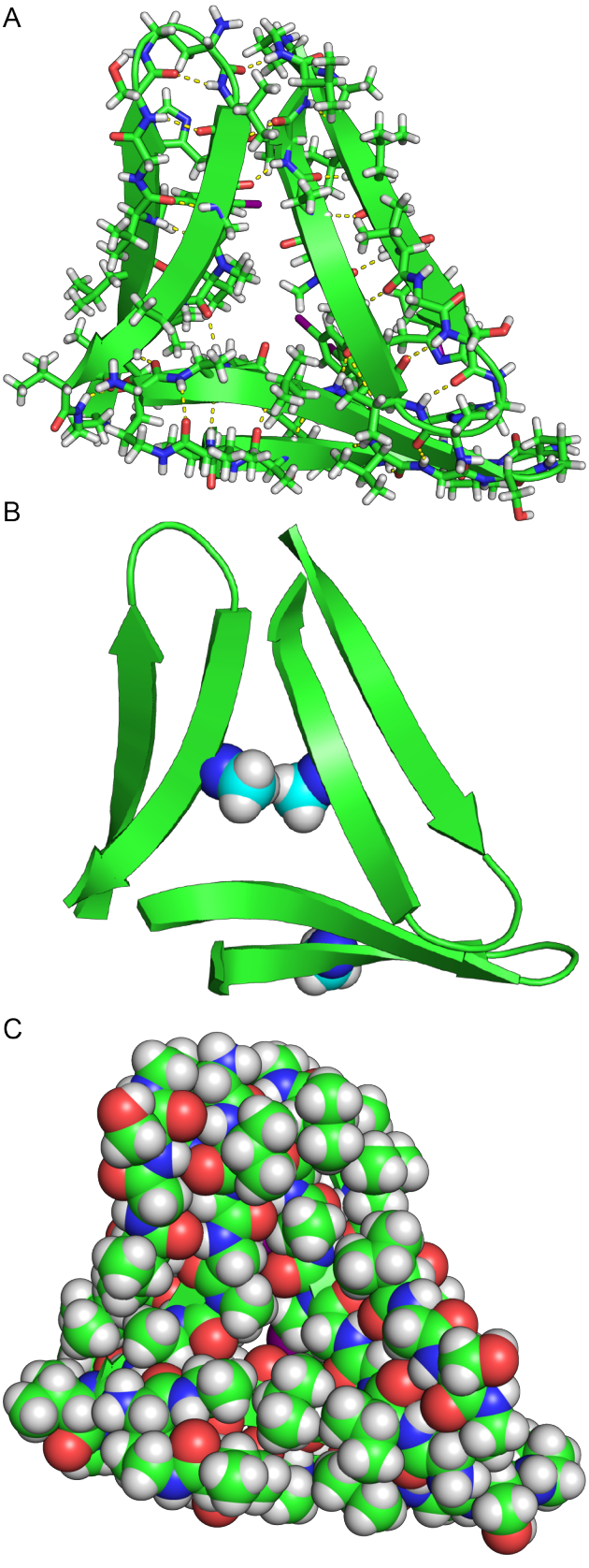
A
B
C

Figure 2.4: Triangular trimer of peptide **2.1a**. (A) Cartoon and stick representation depicting the intramolecular and intermolecular hydrogen bonding within the trimer (front surface view). (B) Cartoon representation depicting the location of the *N*-methyl groups in the trimer (front surface view). (C) Sphere representation depicting the hydrophobic packing of residues in the trimer (front surface view).

The packing of the monomers in this fashion buries *ca.* 1300 Å^2 of surface area per trimer, averaging 450 Å^2 of buried surface area per β-hairpin monomer (Figure 2.4C). This area corresponds to more than one fourth of the total surface area of the monomers. The two surfaces of each trimer display different residues: the front surface of each trimer displays the residues on the front surface of the β-hairpin monomers; the back surface of each trimer displays the residues on the back surface β-hairpin monomers. Intermolecular hydrogen bonds at the apexes of the trimer further stabilize this assembly.

The two crystallographically distinct trimers further assemble to form two distinct basket-shaped nonamers, each of which is a trimer of the triangular trimers. (Figure 2.4A). The two nonamers differ little in structure. Unlike the trimer subunit, each nonamer contains internal $C3$ symmetry, resulting in uniform packing of the trimer subunits against one another. Hydrogen bonding between the trimer subunits stabilizes the basket-shaped nonamer (Figure 2.4B). The vertices of the trimer subunits within the nonamers form extensive networks of hydrogen bonds. At the juncture of each of the trimers, four β-hairpins come together to form an eight-stranded β-barrel (Figure 2.5). Each nonamer contains three such β-barrels. The top of the basket-shaped nonamer comprises a hydrogen-bonded triangular interface (Figure 4B). In this interface, each triangular trimer subunit contributes one β-hairpin and each of these β-hairpins forms six intermolecular hydrogen bonds.

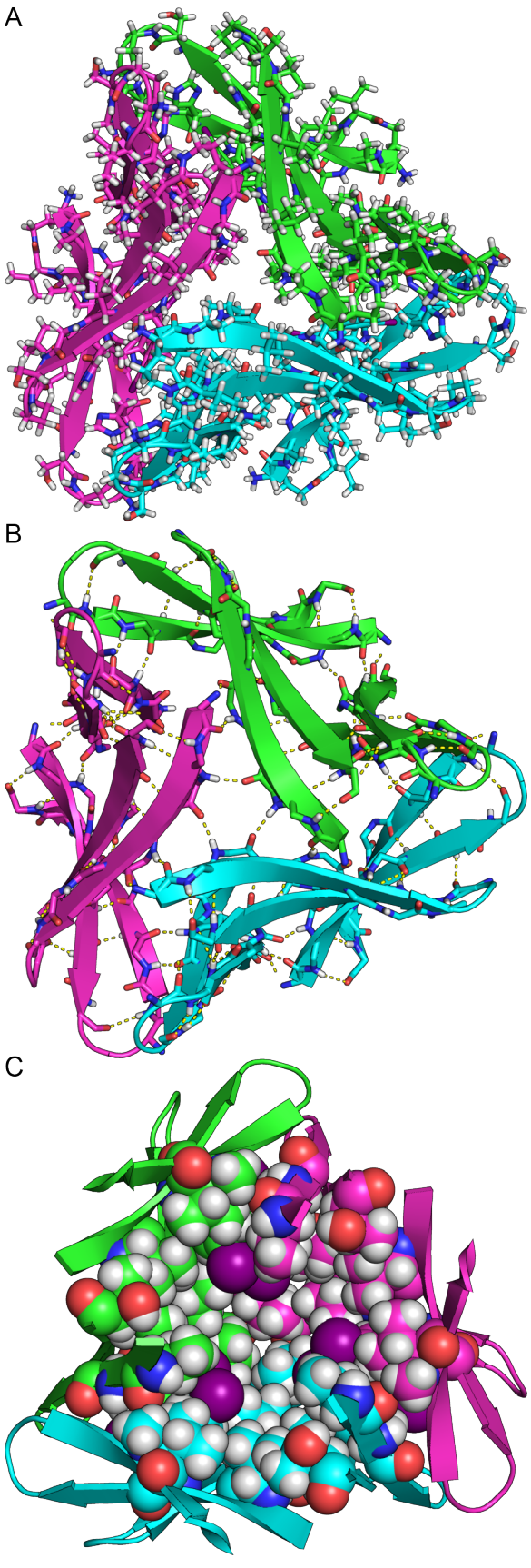
A
B
C

Figure 2.4: Basket-shaped nonamer formed by peptide **2.1a**. (A) Cartoon and stick representation (outer surface view). (B) Cartoon and stick representation depicting the main-chain hydrogen-bonding networks (outer surface view). (C) Hydrophobic packing in the core of the nonamer (inner surface view, image is rotated 180° with respect to A and B about the vertical axis).

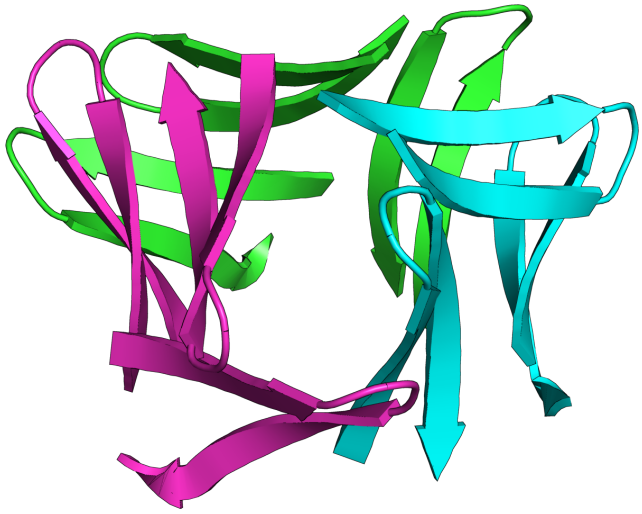

Figure 2.5: Cartoon representation of the basket-shaped nonamer, oriented to look down one of the three identical eight-stranded β-barrels within the assembly.

Hydrophobic contacts between the triangular trimers also stabilize each nonamer (Figure 2.4C). The trimer subunits pack against each other along their back surfaces to form a densely packed hydrophobic core consisting of residues Val_{37}, Phe^{I}_{39}, His_{50}, Val_{52}, and Thr_{54}. The front surfaces of the trimer subunits are largely exposed to solvent. The packing of the trimers against one another buries *ca.* 3000 Å^2 of surface area in the nonamer assembly: nearly 1000 Å^2 per trimer subunit. This area corresponds to roughly one third of the total surface area of the trimer.

The two nonamers further dimerize to form an octadecamer (Figure 2.6A). The nonamers pack against one another through hydrophobic contacts between Ala_{36}, Leu_{38}, Val_{40}, Val_{55}, and the δ-linked ornithine turn unit that connects Ala_{36} to Val_{55} (Figure 2.6B). This interface buries *ca.* 1300 Å^2 of surface area, of which each nonamer contributes roughly 650 Å^2. The

octadecamer appears to be the largest oligomer in the crystal lattice. Contacts between octadecamers within the lattice are small, roughly 300 $Å^2$ per octadecamer.

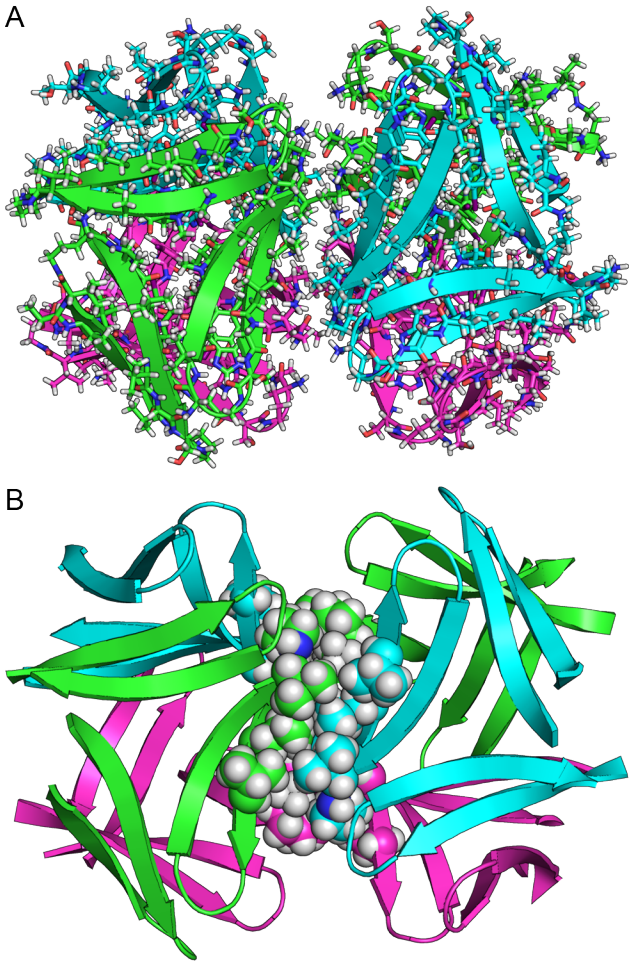

Figure 2.6: Octadecamer formed by peptide **2.1a**. (A) Cartoon and stick representation. (B) Sphere representation depicting the contact surface between the nonamer subunits.

Inspired by the interest in racemic and enantiomeric proteins, we also determined the X-ray crystallographic structure of peptide *ent*-**2.1a**.[91,92] As expected, peptide *ent*-**2.1a** crystalizes from the same conditions as peptide **2.1a** and forms crystals in the same space group with similar unit cell dimensions as those formed by peptide **2.1a**. The asymmetric unit of peptide *ent*-**2.1a** contains six molecules of *ent*-**2.1a**, each of which is folded into a β-hairpin that is the mirror image of that formed by peptide **2.1a** (Figure 2.7). Peptide *ent*-**2.1a** assembles to form oligomers that are mirror images of those formed by peptide **2.1a**. These enantiomeric

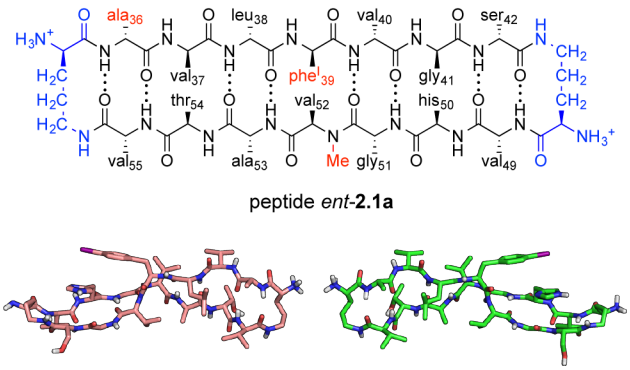

Figure 2.7: Monomers from the crystal lattice of peptide *ent*-**2.1a** (left, PDB 5F1W) and peptide **2.1a** (right, PDB 5F1T). Non-polar hydrogens are omitted for clarity.

oligomers are identical in every fashion — except handedness — to those formed by peptide **2.1a**. Although racemates often crystalize more readily than individual enantiomers, attempts to cocrystalize peptides **2.1a** and *ent*-**2.1a** have failed[93].

Crystallographically based model of an α-Syn$_{33–58}$ nonamer. We envisioned that full-length α-Syn could assemble in the same fashion as the oligomers formed by peptide **2.1a**, but were concerned whether the trimers and nonamers would accommodate the loop and additional *N*- and *C*-terminal residues. To address this question, we modeled Ac-α-Syn$_{33–58}$-NHMe into the crystallographic coordinates of the nonamer[94]. We built residues 43–48 (KTKEGV), 33–35 (TKE), and 56–58 (AEK) into the crystallographic coordinates of peptide **2.1a** and performed replica-exchange molecular dynamics (REMD) to generate realistic conformations of the loops and the *N*- and *C*-terminal fragments of the β-hairpin.[95,96] The REMD simulation shows that the nonamer successfully accommodates the additional residues from the full-length protein without any significant clashes amongst residues (Figure 2.8). The *N*- and *C*-terminal fragments of α-Syn project out of the assembly and do not interfere with nonamer formation. The residues on each of the loops at the apexes of the nonamer pack against one another, suggesting that these additional residues from the full-length protein could stabilize this assembly. Incorporation of the loops as well as the additional *N*- and *C*-terminal residues into the nonamer buries an additional 400 Å^2 of surface area per trimer subunit, providing an additional 1200 Å^2 of buried surface area beyond

the crystallographic nonamer. Table 2.2 summarizes the size of the contact surfaces within the crystallographic oligomers and the model of α-Syn$_{33–58}$. The X-ray crystallographic and REMD structures generated herein may serve as models for the core of the oligomers formed by full-length α-Syn.

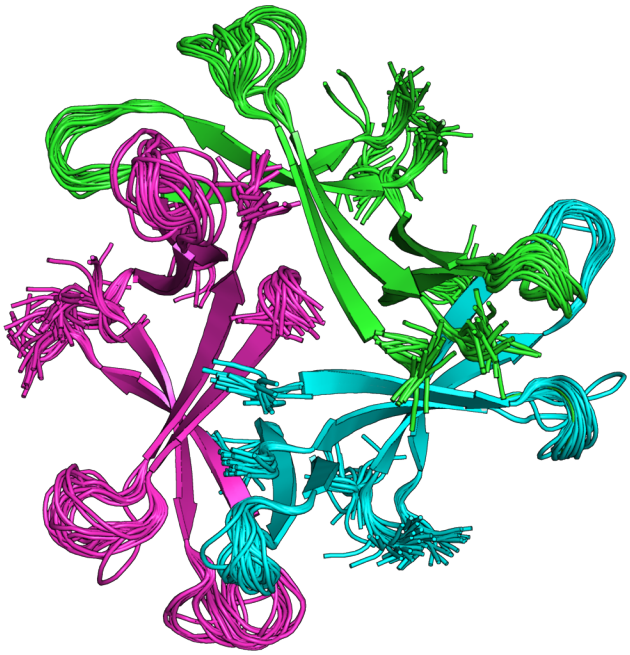

Figure 2.8: Crystallographically based model of the α-Syn$_{33-58}$ nonamer. Superposition of 20 structures of Ac-α-Syn$_{33–58}$-NHMe generated by replica-exchange molecular dynamics.

Table 2.2: Buried surface area within the oligomers formed by peptides **2.1a** and the α-Syn$_{33–58}$ model

assembly	subunit	BSA[a](Å^2)	BSA/subunit[b] (Å^2)
trimer (**2.1a**)	monomer	1300	450
trimer (model)	monomer	1700	550
nonamer (**2.1a**)	trimer	3000	1000
nonamer (model)	trimer	4200	1400

[a]Buried surface area; [b]Average BSA per subunit.

Membrane-induced folding of peptides derived from α-Syn$_{36–55}$. The interaction of α-Syn with the anionic membranes of neurons induces conformational changes and nucleates self-assembly of the protein.[97] To test the effects of membranes on the conformation of peptide **2.1a**, we compared the circular dichroism (CD) spectra of peptide **2.1a** in the presence of anionic or neutral liposomes to that of peptide **2.1a** in aqueous buffer (Figure 4.13).[98–100] The CD spectrum of peptide **2.1a** in aqueous buffer displays negative bands centered at 220 nm and 200 nm[101]. Upon the addition of anionic phosphatidylcholine:phosphatidylserine (PC:PS) large unilamellar vesicles (LUVs), the CD spectrum of peptide **2.1a** changes dramatically: the negative band at 220 nm becomes more intense and a positive band appears below *ca.* 210 nm. This change in CD spectrum upon addition of the liposomes indicates that peptide **2.1a** adopts a β-sheet-rich conformation upon interaction with anionic PC:PS liposomes.

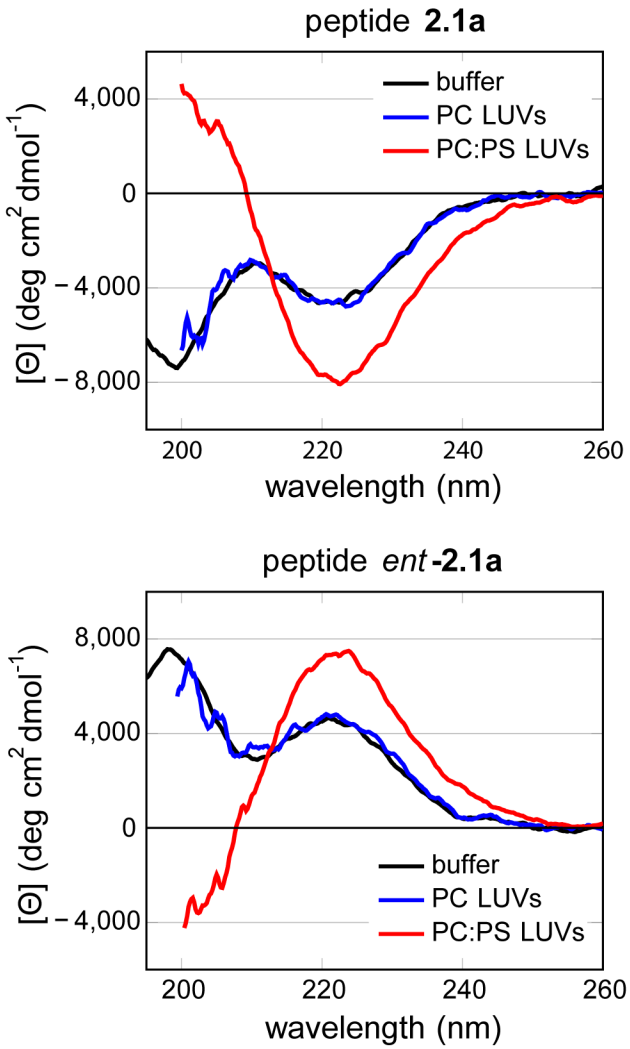

Figure 2.9: Effects of liposomes on the CD spectra of peptide **2.1a** and *ent*-**2.1a**. Spectra of 50 µM peptide in 10 mM sodium phosphate buffer at pH 7.4 were acquired in the presence or absence of 1.0 mM lipids, constituting either phosphatidylcholine (PC) or phosphatidylcholine:phosphatidylserine (PC:PS) liposomes. Data are graphed as mean residue ellipticity. The CD spectra could not be recorded below *ca.* 200 nm in the presence of the liposomes.

In contrast to anionic PC:PS LUVs, neutral phosphatidylcholine (PC) LUVs do not induce changes in the conformation of peptide **2.1a**. The CD spectrum of peptide **2.1a** in the presence of PC LUVs is superimposable with the CD spectrum of peptide **2.1a** in aqueous buffer. The contrasting effects of the PC and PC:PS liposomes indicates that electrostatic interactions between the cationic peptide and the anionic liposomes are essential to the membrane-induced conformational changes observed.

To test the importance of chirality in the interaction of peptide **2.1a** with PC:PS liposomes, we investigated the effect of liposomes on the CD spectra of peptide *ent*-**2.1a**. The CD spectra of peptide *ent*-**2.1a** are identical but opposite in sign to those of peptide **2.1a** in the three sets of conditions studied. In aqueous buffer, the CD spectrum of peptide *ent*-**2.1a** displays positive bands centered at 220 nm and 200 nm. In the presence of PC:PS LUVs, the positive band at 220 nm becomes more intense and a negative band appears below *ca.* 210 nm. No change in the CD spectrum is observed upon the addition of PC LUVs. The equivalent behavior of the enantiomeric peptide suggests that chiral interactions are not important in the interaction with liposomes, even though the individual lipid molecules are chiral. Instead, the interaction appears to reflect the importance of the charged head groups and the hydrophobic lipids.

Cytotoxicity of peptides derived from α-Syn$_{36–55}$. The oligomers formed by full-length α-Syn are thought to induce cell death upon interaction with the cell membrane.[102] To determine whether the propensity of peptide **2.1a** to bind lipid membranes imparts toxicity, we studied the effect of peptide **2.1a** and several control peptides on a neuronally derived cell line. Treatment of SH-SY5Y cells with peptide **2.1a** results in cell death as measured by lactate dehydrogenase release (LDH) and 3-(4,5-dimethylthiazol-2-yl)-2,5-diphenyltetrazolium bromide (MTT) conversion assays (Figure 2.10). A dose-response relationship is observed at concentrations ranging from 5–40 µM, with maximal toxicity occurring at 40 µM. Maximal cell death occurs within 16 hours after treatment with 40 µM peptide **2.1a** (Figure 2.11). These results demonstrate that peptide **2.1a** is cytotoxic but do not establish that the toxicity results from membrane interaction.

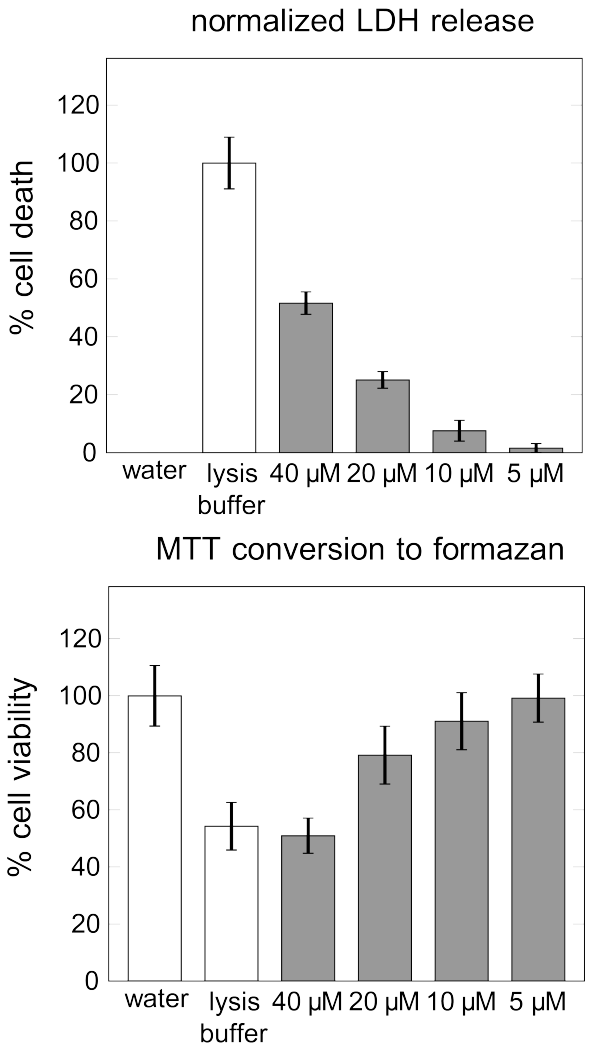

Figure 2.10: LDH and MTT assays of the toxicity of peptide **2.1a** towards SH-SY5Y cells with varying concentrations. Cells were incubated with 5–40 μM of peptide **2.1a** for 24 hours before performing the assays. Cell death and viability were determined spectrophotometrically as previously described.[103,104] Error bars represent standard deviation propagated from five replicate runs.

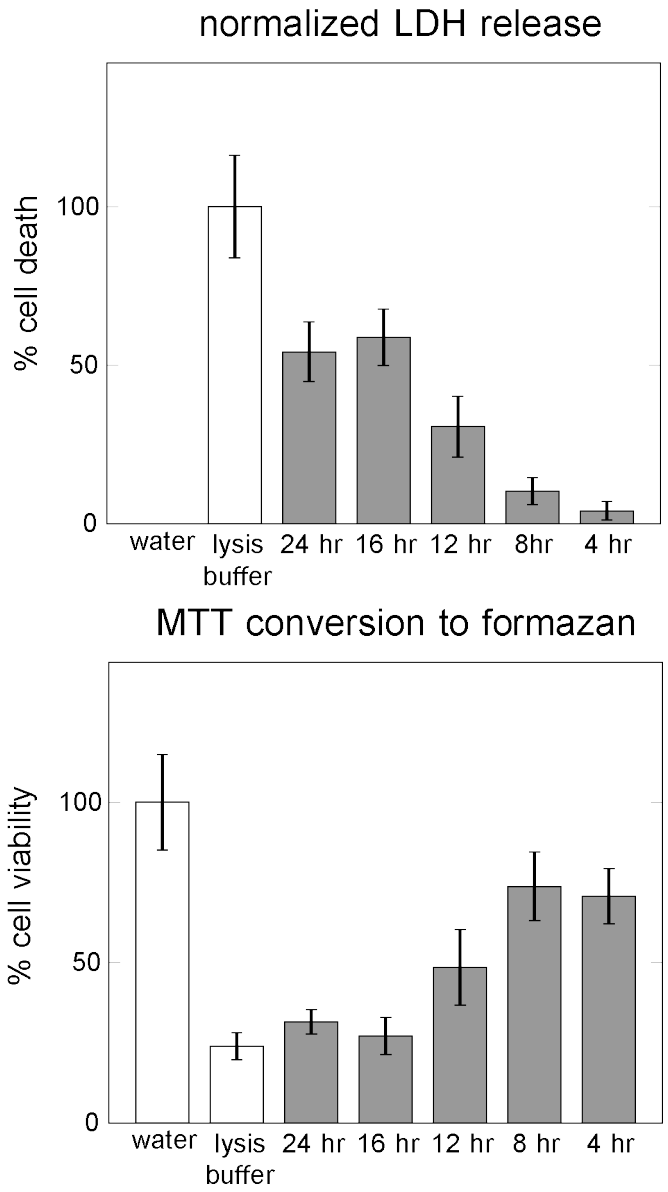

Figure 2.11: LDH and MTT assays of the toxicity of peptide **2.1a** towards SH-SY5Y cells with varying incubation times. Cells were incubated with 40 µM of peptide **2.1a** for 4–24 hours before performing the assays. Cell death and viability were determined spectrophotometrically as previously described.[103,104] Error bars represent standard deviation propagated from five replicate runs.

To establish whether cell death occurs from membrane interaction, we compared peptide **2.1a** to three homologues (*ent*-**2.1a**, $\mathbf{2.1a_{A53E}}$, and **2.1b**) in LDH and MTT assays (Figure 2.12). Treatment of SH-SY5Y cells with either peptide *ent*-**2.1a** or peptide **2.1a** results in nearly equal levels of cell death. The comparable toxicity of peptides *ent*-**2.1a** and **2.1a**

suggest that toxicity results from non-specific interactions with the cells, rather than through specific interaction with a receptor protein.

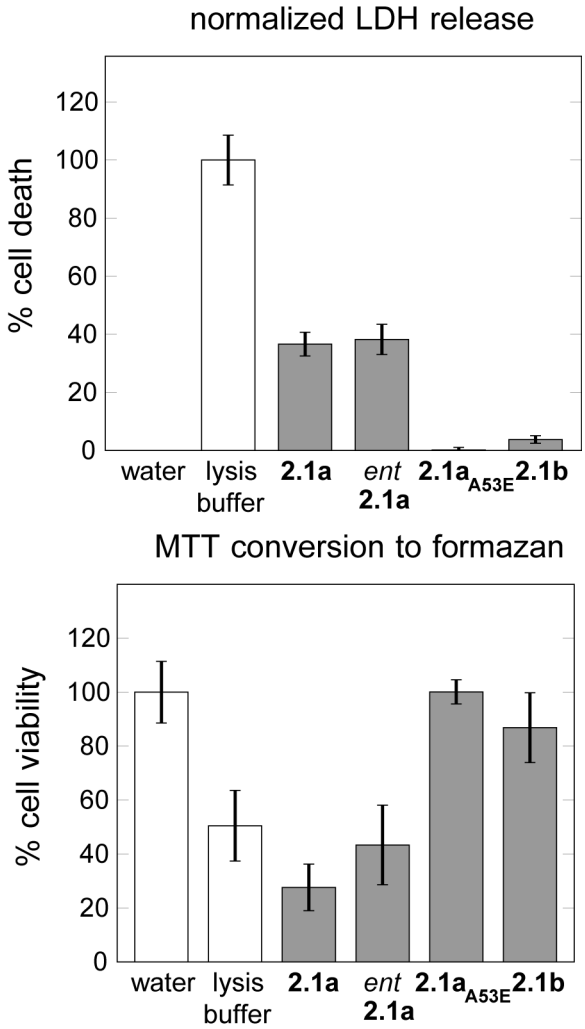

Figure 2.12: LDH and MTT assays of the toxicity of peptide **2.1a** and its homologues towards SH-SY5Y cells. Cells were incubated with 40 µM of peptide **2.1a**, *ent*-**2.1a**, **2.1a$_{a53E}$**, or **2.1b** for 24 hours before performing the assays. Cell death and viability were determined spectrophotometrically as previously described.[103,104] Error bars represent standard deviation propagated from five replicate runs.

Peptide **2.1a$_{A53E}$** is identical to peptide **2.1a** in amino acid sequence with exception of the A53E familial point mutation. This mutation reduces the affinity of full-length α-Syn to anionic lipid membranes and delays its aggregation.[85] CD spectroscopy shows that this mutation blocks interactions between peptide **2.1a$_{A53E}$** and anionic lipid membranes: the

CD spectra of peptide **2.1a$_{\mathbf{A53E}}$** are identical in the presence or absence of PC:PS LUVs (Figure 2.13). Peptide **2.1a$_{\mathbf{A53E}}$** produces no measurable cell death at 40 uM (Figure 2.12). The lack of toxicity of peptide **2.1a$_{\mathbf{A53E}}$** in conjunction with its lack of membrane interactions supports that membrane interaction is central to the toxicity of peptide **2.1a**.

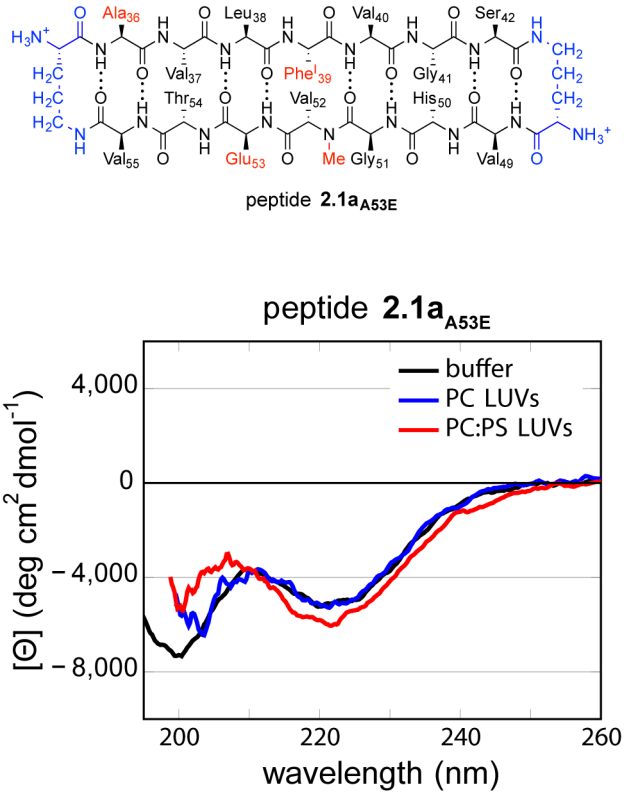

Figure 2.13: Effects of liposomes on the CD spectra of peptide **2.1a$_{\mathbf{A53E}}$**. Spectra of 50 µM peptide in 10 mM sodium phosphate buffer at pH 7.4 were acquired in the presence or absence of 1.0 mM lipids, constituting either phosphatidylcholine (PC) or phosphatidylcholine:phosphatidylserine (PC:PS) liposomes. Data are graphed as mean residue ellipticity. The CD spectra could not be recorded below *ca.* 200 nm in the presence of the liposomes.

Peptide **2.1b** was designed to test the role of the crystallographically observed oligomers in the toxicity elicited by peptide **2.1a**. Peptide **2.1b** is identical to peptide **2.1a** in amino acid sequence, but is *N*-methylated at Gly$_{41}$ instead of Val$_{52}$. We anticipated that *N*-methylation at Gly$_{41}$ would disrupt the formation of the trimer and the basket-shaped nonamer by disrupting the hydrogen-bonding within the oligomers and forcing the subunits apart. Peptide **2.1b** is much less cytotoxic than peptide **2.1a**, as determined by both the LDH and MTT

assays (Figure 2.12). *N*-Methylation at Gly_{41} does not impair the interaction of peptide **2.1b** and lipid bilayer membranes: upon the addition of PC:PS LUVs, the CD spectrum of peptide **2.1b** changes dramatically, in a fashion similar to the changes observed for peptide **2.1a** (Figure 2.14). The marked decrease in toxicity of peptide **2.1b** is consistent with, but does not prove, the involvement of the crystallographically observed oligomers in the cytotoxicity associated with peptide **2.1a**.

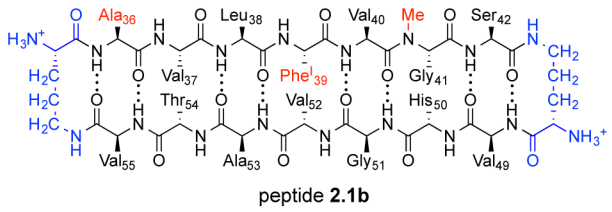

peptide **2.1b**

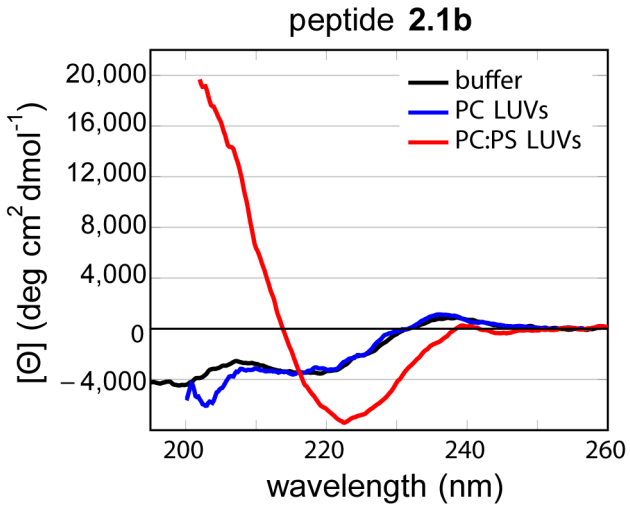

Figure 2.14: Effects of liposomes on the CD spectra of peptide **2.1b**. Spectra of 50 µM peptide in 10 mM sodium phosphate buffer at pH 7.4 were acquired in the presence or absence of 1.0 mM lipids, constituting either phosphatidylcholine (PC) or phosphatidylcholine:phosphatidylserine (PC:PS) liposomes. Data are graphed as mean residue ellipticity. The CD spectra could not be recorded below *ca.* 200 nm in the presence of the liposomes.

2.3 Discussion

The X-ray crystallographic studies of peptide **2.1a** and the molecular modeling studies of the α-Syn$_{33–58}$ nonamer suggest a model for oligomer formation by full-length α-Syn. In this model, residues 36–55 of full-length α-Syn form a β-hairpin, three of these β-hairpins assemble to form triangular trimers, and the trimers assemble to form basket-shaped nonamers or related higher-order oligomers. To our knowledge, the X-ray crystallographic structure of peptide **2.1a** provides the first high-resolution structures of oligomers of peptides derived from α-Syn. There are currently no reported high-resolution structures of oligomers of the full-length protein. The structures described herein should help bridge the gap between the plethora of low-resolution structural information of full-length α-Syn oligomers and a still needed high-resolution structure.

The structures of the oligomers formed by peptide **2.1a** are fundamentally different from the proposed structure of the fibrils formed by α-Syn (Figure 2.15).[105,106] Although there are no high-resolution structures of the fibrils, the current understanding of fibril structures suggests that the monomer units fold onto themselves to form a five-layer β-sandwich. In the fibril, the folded monomers hydrogen bond with neighboring monomers to form a network of parallel β-sheets. Although many of the details of the fibril assembly are still being debated, commonalities such as multilayered parallel β-sheets are widely accepted.[107,108] In contrast to the proposed assembly of the fibril, the oligomers we observe assemble in an entirely separate fashion: through the intermolecular interactions amongst antiparallel β-hairpins. This stark difference suggests that the structures of the oligomers formed by full-length α-Syn may differ wildly from the structures of α-Syn fibrils in both monomer conformation and in themes of higher-order assembly.

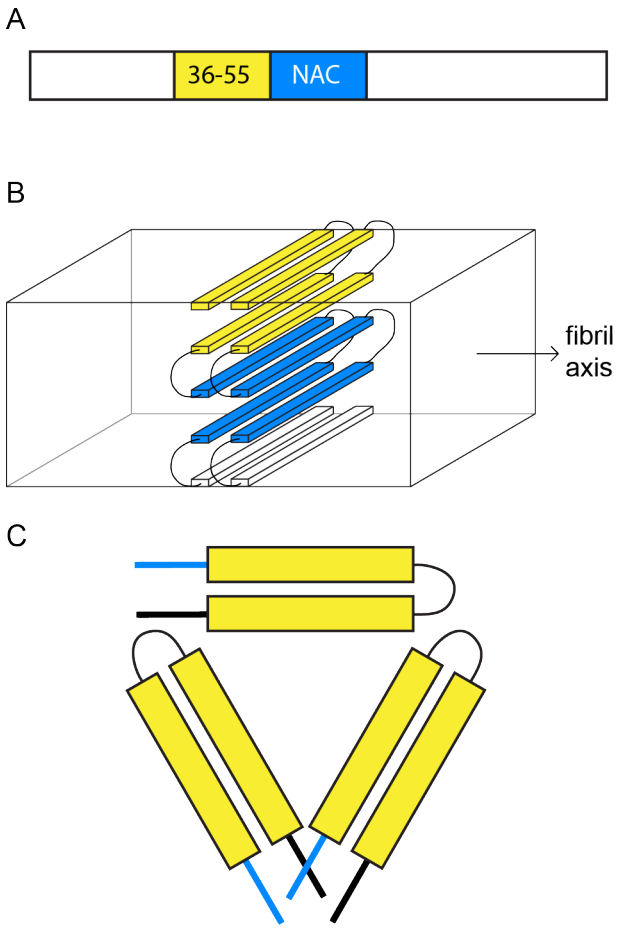

Figure 2.15: Models of an α-Syn fibril and an α-Syn oligomer. (A) Cartoon of α-Syn monomer. Residues 36–55 are colored yellow and the NAC is colored blue. (B) Cartoon of α-Syn fibril, showing two monomer subunits arranged into a five-layered β-sheet.[106] (C) Cartoon of α-Syn trimer subunit of basket-shaped nonamers or related higher-order oligomers, showing three β-hairpins arranged into a trimer.

Our findings suggest that the region of α-Syn that drives fibrillization may differ from that which drives oligomerization (Figure 2.15). Residues 61–95 of α-Syn, termed the NAC[109], are required for fibrillization of α-Syn.[30,110–112] The currently accepted model of the α-Syn fibril places the NAC at the core of the assembly and α-Syn$_{36–55}$ at the periphery.[113] Our model of α-Syn oligomers suggests that the exact opposite may be true for some oligomers, placing α-Syn$_{36–55}$ at the core of the oligomers, while the NAC and remainder of the protein decorates the periphery. Our results do not rule out the possibility of other types of α-Syn oligomers with the NAC at their core. Our results do, however, suggest that the NAC is not

the only driver of oligomer formation. As α-Syn oligomers are known to be polymorphic, there may be multiple families of oligomers in which different regions of α-Syn drive assembly.

The occurrence of five of the six known familial point mutations in α-Syn$_{36–55}$ suggests that this region is important in the pathology of synucleinopathies. With exception of H50Q, all of these point mutations would be displayed on the solvent-exposed surface of the basket-shaped nonamer. These mutations might stabilize the nonamers or component trimers, or might drive the protein into oligomers with different structures. Alternatively, these mutations may merely destabilize native tetramers of α-Syn and thus promote aggregation.[114,115] An X-ray crystallographic structure of a derivative of peptide **2.1a** bearing any of these point mutations would be edifying. Our own attempts to crystalize homologues of peptide **2.1a** with point mutations H50Q, G51D, A53E, or A53T have thus far been unsuccessful.

The oligomers formed by full-length α-Syn may differ from those formed by peptide **2.1a** while still retaining the general features of β-hairpins and trimers. We have, for example, observed that β-hairpins derived from β-amyloid and β_2-microglobulin form symmetrical trimers, rather than the asymmetric trimer observed for peptide **2.1a**.[57,58] These trimers further assemble to form hexamers, octamers, and dodecamers instead of nonamers and octadecamers. Although all of these amyloid-derived peptides differ in sequence and the oligomers differ in precise structure, they share the common theme of β-hairpins assembling into triangular trimers that further assemble into complex and intricate higher-order assemblies.

Trimers may be a unifying motif of toxic amyloid oligomers formed by full-length amyloidogenic proteins. SDS-stable trimeric assemblies of full-length α-Syn have been observed in immunoblots of mouse brain extracts.[69] The appearance of these species strongly correlates with an increased loss of dopaminergic neurons *in vivo*. Similarly, trimeric assemblies of β-amyloid have been shown to disrupt cognitive function in rats.[116] The occurrence of the triangular trimeric motif in crystal structures reported by our group has lead us to be-

lieve that trimers may be unifying substructures of amyloid oligomers that are composed of β-hairpin monomers. The CD studies, in conjunction with the toxicity assays, suggest that the cytotoxicity of peptide **2.1a** may result from interactions of trimers or higher-order oligomers with cell membranes, in the same fashion as the oligomers of full-length α-Syn.[67] At this point, we cannot conclusively say that the crystallographic oligomers are forming under the conditions used in the cell assays;[117] however, the substantial decrease in toxicity of the alternatively *N*-methylated peptide **2.1b** supports the involvement of the trimer and/or nonamers in cell death.

2.4 Conclusion

Here we present the first X-ray crystallographic structure of oligomers formed by a peptide derived from α-Syn. This peptide was designed to mimic a β-hairpin motif thought to be important in α-Syn oligomer formation. This designed peptide mimics key properties of oligomers of full-length α-Syn: affinity for membranes that imparts toxicity. The structure suggests a model for α-Syn oligomer formation centered around α-Syn$_{36–55}$, in which α-Syn$_{36–55}$ folds into a β-hairpin that further assembles into trimers and higher-order oligomers. These structures differ in topology from those of α-Syn fibrils and suggest that regions of α-Syn not important for its fibrillization may play a central role in its oligomerization. The X-ray crystallographic structure of peptide **2.1a** and the model of the α-Syn$_{33–58}$ nonamer may be used as starting points to design small molecules that interact with α-Syn oligomers or to rationalize the modes of interactions between α-Syn oligomers and small molecules that interact with them.

2.5 Materials and Methods

2.5.1 General information

All chemicals were used as received except where otherwise noted. Methylene chloride was passed through alumina under nitrogen prior to use. Anhydrous, amine free dimethylformamide (DMF) was purchased from Alfa Aesar.* All reactions were performed at ambient temperature (*ca.* 20 °C), unless otherwise noted. Peptide synthesis was performed on a Protein Technologies PS3 synthesizer. Analytical reverse-phase HPLC was performed on an Agilent 1200 equipped with a Aeris PEPTIDE 2.6u XB-C18 column (Phenomonex). Preparative reverse-phase HPLC was performed on a Beckman Gold Series P equipped with a ZORBAX SB-C18 column (Agilent). HPLC grade acetonitrile and 18 MΩ deionized water, each containing 0.1% trifluoroacetic acid, were used for analytical and preparative reverse-phase HPLC. All peptides were prepared and used as the trifluoroacetate salts and were assumed to have three molecules of trifluoroacetic acid (TFA) per molecule of peptide.

2.5.2 Representative synthesis of peptide 2.1a

he synthesis of peptides **2.1** were performed using techniques previously described by our group.[56] A representative protocol used to perform the synthesis of peptide **2.1a** is detailed below and diagramed in Scheme 2.1.

*In our hands, lesser quality DMF dramatically impacts yields

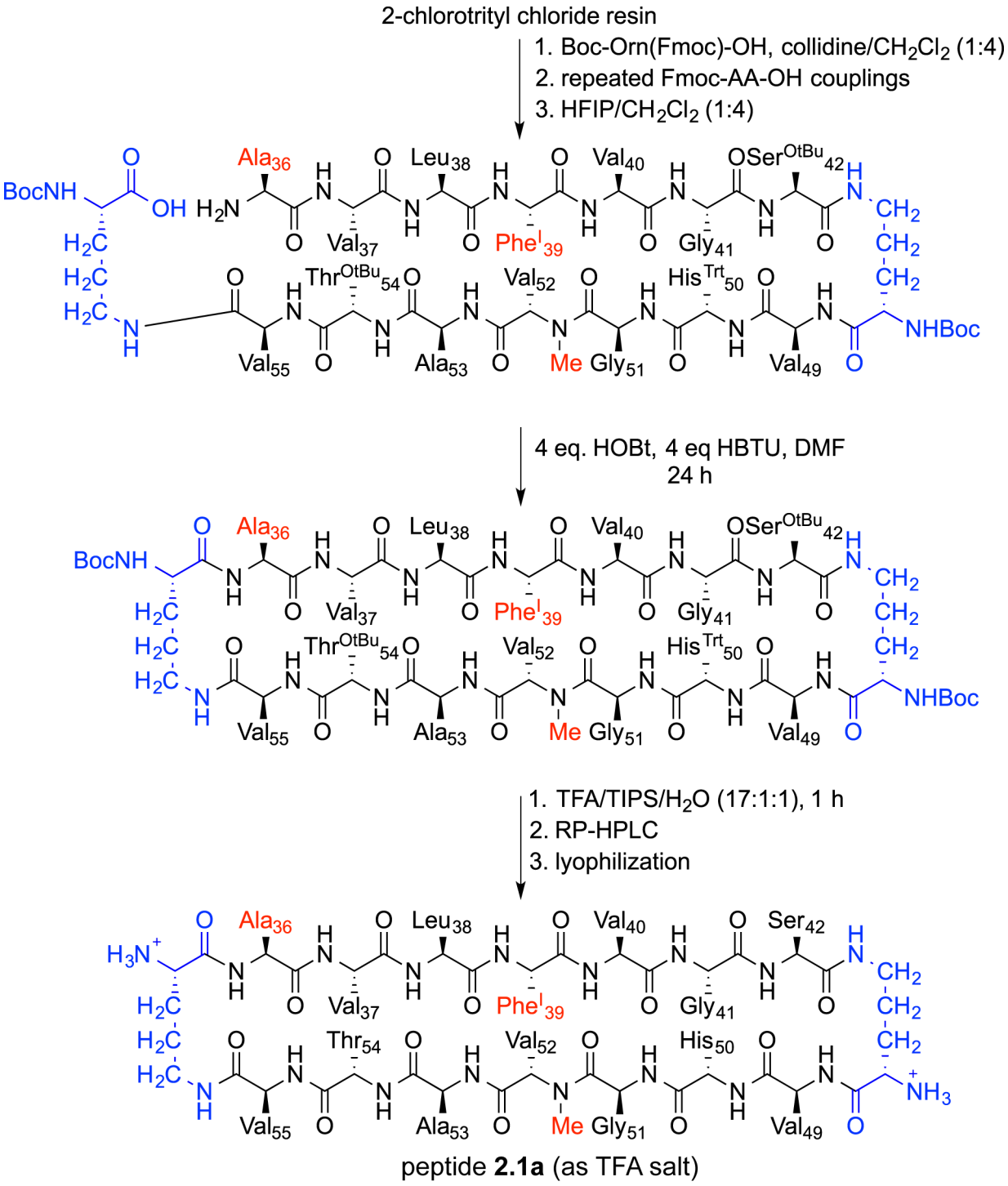

Scheme 2.1

Loading resin: 2-Chlorotrityl chloride resin (300 mg, 1.2 mmol/g capacity) was added to a BioRad Poly-Prep column. Methylene chloride (*ca.* 5 mL) was added to swell the resin.

After 30 min, the methylene chloride was drained with the aid of N_2. Boc-Orn(Fmoc)-OH (0.5 eq., 80 mg, 0.18 mmol) dissolved in 5 mL of a 20% solution of 2,4,6-collidine in methylene chloride was added to the resin. The suspension was agitated overnight on a platform rocker. The solution was then drained from the resin and replaced with a solution of CH_2Cl_2/MeOH/DIPEA (17:2:1, 8 mL) to cap unreacted sites. The suspension was agitated for 1 h, after which the solution was drained and the resin was washed with methylene chloride and dried under a N_2 stream. Resin loading was checked by taking a weighed portion of loaded resin (*ca.* 1 mg) and performing a UV analysis of the Fmoc-deprotection product using 3 mL of a 20% piperidine in DMF solution (301 nm, ε 7800). Typically 0.30–0.40 mmol/g of Boc-Orn(Fmoc)-OH was loaded for all repetitions of this procedure (*ca.* 0.1 mmol scale synthesis).

Peptide coupling: The loaded resin was transferred into a glass peptide synthesizer reaction vessel and submitted to repetitive Fmoc-deprotection and amino acid coupling using Fmoc protected amino acid building blocks. All linear peptides were synthesized from the *C*- to *N*-terminus. Each coupling step consisted of the following: i. Fmoc-deprotection with 3 mL of 20% piperdine in DMF for 10 minutes, ii. washing with 3 mL of DMF (3x), iii. amino acid coupling using 4 eq. of both the Fmoc-AA-OH building block and HCTU in 20% NMM in DMF for 20 mins, iv. washing with 3 mL of DMF (5x). A double coupling was utilized for the amino acid to be coupled onto the *N*-methyl amino acid in order to ensure complete coupling: in place of iii. in the above procedure, two 1 h couplings of the requisite amino acid with 4 eq. of both HOAt and HATU in place of HCTU were used to achieve complete coupling. After coupling the final amino acid, a final Fmoc-deprotection was preformed to remove the terminal Fmoc group, and the resin was transferred to a BioRad Poly-Prep column and washed with methylene chloride.

Cleavage of the linear protected peptide from the resin: The linear protected peptide was cleaved from the resin using a 20% hexafluoro-2-propanol (HFIP) in methylene chloride

solution. A 10 mL portion of this solution was added to the resin and the suspension was agitated for 1 h. (Addition of this solution to the resin often results in the formation of a brilliant red color.) The solution was drained with the aid of N_2 into a 250 mL round bottom flask. The resin was washed with an additional 10 mL of the 20% HFIP/CH_2Cl_2 solution, and the combined filtrates were concentrated under reduced pressure to afford a glassy solid. This solid was further dried under vacuum (*ca.* 0.1 mmHg) for 1 h or more.

Cyclization of the linear protected peptide: The linear protected peptide was dissolved in *ca.* 125 mL of anhydrous DMF (dried and traces of dimethylamine removed by passage through 3A molecular sieves followed by an isocyanate scavenger resin column). HOBt and HBTU (4 equiv each) were added, and the solution was stirred for 30 min under N_2. DIPEA (1 mL, distilled from KOH) was added, and the reaction mixture was stirred for 24 h under N_2. The solvent was removed by rotary evaporation under reduced pressure to afford a yellow/orange solid, which was further dried under vacuum (*ca.* 0.1 mmHg) for 1 h or more.

Global deprotection and purification of the cyclic peptide: A TFA/TIPS/H_2O mixture (17:1:1, 10 mL) was added to the solid from the preceding step, and the suspension was stirred for 1.5 h under N_2. The solvent was removed under reduced pressure to afford a yellow/orange oil. The oil was dissolved in 50 mL of MeOH and heated at reflux for 1 h to cleave TFA esters that formed during deprotection.* The solution was then concentrated by rotary evaporation under reduced pressure to give an oil. The oil was dissolved in 20% acetonitrile in water (*ca.* 8 mL), and the suspension was filtered through a 0.2 µm syringe filter. The resulting clear solution was then purified by RP-HPLC with a gradient of 20–40% acetonitrile in water, each containing 0.1% TFA, over 40 mins. Fractions were collected and then analyzed by analytical RP-HPLC. The pure fractions were combined and lyophilized to afford peptide **2.1a** as a white solid (20 mg). Peptides *ent*-**2.1a**, $\mathbf{2.1a_{A53E}}$, and **2.1b** were prepared in a similar fashion to yield white powders: *ent*-**2.1a**, 16 mg; $\mathbf{2.1a_{A53E}}$, 11 mg; **2.1b**, 10 mg.

*This step was omitted for peptide $\mathbf{2.1a_{A53E}}$ to avoid esterifying the glutamate residue.

2.5.3 X-ray Crystallography

*Crystallization of peptides **2.1**.* The Hampton Research Pre-Crystalization Test (PCT) was used to identify optimal concentrations of peptides for crystal growing. Concentrations of 5, 10, and 20 mg/mL peptide in 18 MΩ deionized water were tested, and 10 mg/mL was selected on the basis of the PCT. Crystallization conditions were screened in 96-well plates using the hanging-drop vapor-diffusion method. Three kits from Hampton Research (Crystal Screen, Index, and PEG/ION) were used to screen each peptide, for a total of 288 separate crystallization experiments (three 96-well plates). Each well in the 96-well plates was loaded with 100 µL of a solution from the kits. The hanging drops were set up using a TTP Labtech Mosquito pipetting robot. Each hanging drop was formed by mixing 150 nL of a 10 mg/mL peptide solution with 150 nL of the well solution.

Conditions from the 96-well plates in which crystals grew were further optimized in a 4x6 matrix using Hampton VDX 24-well plates. In the optimization, the pH and cryoprotectant concentrations were varied across the 4x6 matrix to generate crystals that diffracted well. The hanging drops for these optimizations were prepared on glass slides by combining 1 or 2 µL of peptide solution with 1 or 2 µL of well solution in ratios of 1:1, 2:1, and 1:2. Crystals that formed were checked for diffraction using a Rigaku Micromax-007 HF diffractometer with a Cu rotating anode at 1.54 Å.

All homologues of peptide **2.1a** were screened for crystallization; only peptides **2.1a** and *ent*-**2.1a** grew crystals in any of the screened conditions.

*X-ray diffraction data collection, data processing, and refinement for peptides **2.1a** and ent-**2.1a**.* The structures of peptides **2.1a** and *ent*-**2.1a** were determined using techniques previously outlined by our laboratory.[88,*]

*For a procedural guide to solving X-ray crystallographic structures of small peptides complied by our lab, see: http://www.chem.uci.edu/~jsnowick/groupweb/files/Standard_practices_for_X-ray_crystallographic_structure_determination_in_the_Nowick_Laboratory.pdf

Data collection: Crystals were harvested with nylon loops attached to steel pins and frozen in liquid N_2. Data were collected from crystals of peptides **2.1a** and *ent*-**2.1a** on beamline 8.2.1 at the Advanced Light Source located at the Lawrence Berkeley National Laboratory with 0.5° rotation per image using a wavelength of 0.976 Å for peptide **2.1a** and 0.997 Å for peptide *ent*-**2.1a**.

*Data processing for peptide **2.1a**:* The data were integrated and scaled using XDS, and then merged using aimless.[89,118] Hybrid structure search (HySS) in the Phenix software suite was used to determine the coordinates of the anomalous signal for peptide **2.1a**.[90] The electron density map for **2.1a** was generated using the coordinates of the anomalous signal as initial positions in Autosol.

*Data processing for peptide ent-**2.1a**:* The data were integrated and scaled using Imosfilm and then merged using aimless. Xtriage indicated that no anomalous signal was present in the data set; therefore, we instead turned to molecular replacement in order to generate a starting model. The enantiomeric structure of peptide **2.1a** was used as a search model in Phaser.[119,*] Phaser found one solution containing one copy of the search model with a log-likelihood (LLG) of 1270.263. In order to validate the molecular-replacement solution, we prepared six omit maps in phenix.refine, in which, we omitted one of the six copies of peptide *ent*-**2.1a**. In all cases density returned around the omitted chains.

Refinement and model manipulation: Phenix.refine was used to refine the models of peptide **2.1a** and *ent*-**2.1a**. Coot was used to manipulate the coordinates for both peptides.[120] Table 2.1 summarizes the crystal properties, data collection, and data processing for peptides **2.1a** and *ent*-**2.1a**.

*We generated this model by multiplying the x,y,z position of each atom in 5F1T by -1. We wrote a short script in Python to accomplish this inversion. The script is include below.

2.5.4 Replica-exchange molecular dynamics simulation

A model of the α-$Syn_{33–58}$ nonamer was generated by replica-exchange molecular dynamics as follows: Starting coordinates for α-$Syn_{33–58}$ were generated from the crystallographic coordinates of peptide **2.1a**. Symmetry mates of peptide **2.1a** were displayed in PyMOL. Nine copies of peptide **2.1a** corresponding to the basket-shaped nonamer were selected and saved to a new PDB file. The two δ-linked ornithine residues were deleted from each macrocycle. Ser_{42} and Val_{49} were connected with six alanine residues in PyMOL. Three alanine residues were added to the *N*-terminus of the β-hairpin, and three alanine residues were added to the *C*-terminus. These added residues were minimized in PyMOL using the clean function, ensuring that the crystallographic coordinates of α-$Syn_{36–42}$ and α-$Syn_{49–55}$ were not perturbed. After this minimization, each added alanine was mutated to the wild-type residue from α-Syn. The mutated residues were again minimized in PyMOL using the clean function. Each Phe^{I}_{39} was replaced with the wild-type Tyr_{39}, and each *N*-Me-Val_{52} was replaced with the wild-type Val_{52}.

The autopsf plugin in VMD was used to prepare the required files for simulation. Both the *N*-terminal patch ACE (acetylated amide) and *C*-terminal patch CT3 (methyl amide) were applied to the model. The coordinates for α-$Syn_{36–42}$ and α-$Syn_{49–55}$ were fixed throughout the simulation using the python script included below.

REMD simulations were run in NAMD with the CHARMM22 force field and generalized Born implicit solvent (GBIS) on 32 replicas. The temperatures for these replicas varied between 300 and 800K. The simulation was performed for 10 ns. Representative coordinates were selected uniformly from the last 9 ns of the simulation.

2.5.5 Surface area calculations

The surface areas of the monomer, trimer, nonamer, and octadecamer were calculated using the internet-based program PDBePISA (http://www.ebi.ac.uk/pdbe/pisa/).[121] PDB files of the oligomers were generated from the crystallographic structure of peptide **2.1a** as well as the model of the α-$Syn_{33–58}$ nonamer from REMD. The buried surface area (BSA) in an assembly of A and B is calculated given the following formula:[122]

$$BSA_{\mathrm{AB}} = SA_{\mathrm{A}} + SA_{\mathrm{B}} - SA_{\mathrm{AB}}$$

Where BSA_{AB} is the buried surface area in the assembly of A and B, SA_{A} and SA_{B} are the solvent-exposed surface area in A and B* when not assembled into the AB complex, and SA_{AB} is the solvent-exposed surface area of the complex.

In the case of a trimer, the buried surface area is given by:

$$BSA_{\mathrm{ABC}} = SA_{\mathrm{A}} + SA_{\mathrm{B}} + SA_{\mathrm{C}} - SA_{\mathrm{ABC}}$$

In a homodimer, in which two subunits assemble in a symmetrical fashion, the buried surface area per monomer (BSA_{subunit}) is given by:

$$BSA_{\mathrm{subunit}} = BSA_{\mathrm{AB}}/2$$

In the case of a homotrimer, in which three subunits assemble in a symmetrical fashion, the buried surface area per monomer is given by:

$$BSA_{\mathrm{subunit}} = BSA_{\mathrm{ABC}}/3$$

*A and B may, themselves, be assemblies of other objects.

2.5.6 Cytotoxicity assays

Cytotoxicity assays were performed and analyzed as described previously by our group.[58]

Cell Culture. The cytotoxicity of peptides **2.1** were assessed in the human neuroblastoma cell line SH-SY5Y.** Cultures were maintained in 1:1 mixture Dubelcco's modified Eagles medium and Ham's F12 (DMEM/F12) medium supplemented with 10% fetal bovine serum (FBS), 100 U/mL penicillin and 100 µg/mL streptomycin at pH 7.4 and maintained in a humidified 5% CO_2 atmosphere at 37 °C. All experiments were performed using *ca.* 60–70% confluent cultures on passages ranging from 3–12.

MTT and LDH assays. SH-SY5Y cells were plated into 96-well plates at 15,000 cells per well in 100 µL 1:1 DMEM/F12 medium supplemented with 10% FBS, 100 U/mL penicillin and 100 µg/mL streptomycin at pH 7.4 and incubated in a humidified 5% CO_2 atmosphere at 37 °C for 24 h. Prior to treatment, the medium was aspirated and replaced with 90 µL serum-free DMEM/F12 media. The cells were incubated for an additional 24 h in a humidified 5% CO_2 atmosphere at 37 °C. Solutions of peptides **2.1a**, *ent*-**2.1a**, $\mathbf{2.1a_{A53E}}$, and **2.1b** were prepared gravimetrically by dissolving the lyophilized peptide in the appropriate amount of 18 MΩ deionized water to achieve a 5 mM stock. From the 5 mM stock solutions, 10X solutions were made by dilution with 18 MΩ deionized water. 10 µL of the 10X solutions were added to the wells on the 96-well plates, bringing the total volume of each well to 100 µL. Cells were treated and incubated in replicates of five in the presence of each compound for 24 h in a humidified 5% CO_2 atmosphere at 37 °C prior to performing both MTT and LDH assays. Each experiment was repeated three times.

Both MTT (Sigma) and LDH (Thermo Scientific) assays were performed on the each plate. A 50-µL aliquot of supernatant media was transferred to a new 96-well plate and spectrophotometrically analyzed for LDH content according to the manufacturer's instructions. The

**Generously provided by Dr. Kim Green (Dept. of Biological Sciences, UC Irvine)

remainder of the media was aspirated and replaced with 100 µL of serum free, phenol-red free DMEM/F12 medium supplemented with 0.2 mg/mL MTT. The cells were incubated for 4 h in a humidified 5% CO_2 atmosphere at 37 °C in the presence of the MTT containing media. Formazan crystals from the MTT reaction were dissolved in 10% SDS in 10 mM HCl for 4 h in a humidified 5% CO_2 atmosphere at 37 °C. MTT plates were read spectrophotometrically at 570 nm.

MTT data were graphed as a percentage versus the water treatment control, whereas LDH data were analyzed and ploted as previously described.[103]

2.5.7 Circular dichroism spectroscopy

CD spectra were acquired on a Jasco J-810 circular dichroism spectropolarimeter at ambient temperature (*ca.* 20 °C). A 50 µM solution of each peptide was prepared by adding 4 µL of a 5 mM stock solution of peptide in 18 MΩ deionized water to 396 µL of either 10 mM sodium phosphate buffer at pH 7.4 or 10 mM sodium phosphate buffer at pH 7.4 containing 1 mM lipids in a 1 mm quartz cuvette. Data were collected using 0.2 nm intervals from 260 nm to 190 nm and averaged over 5 accumulations.[99] Spectra were smoothed using Savitsky-Golay smoothing with a 21 point window. Data are graphed as mean residue ellipticity, [Θ], which is calculated as follows:[98,99]

$$[\Theta] = \text{millidegrees}/(\text{path length(mm)} \times [\text{peptide}]\ (\text{M}) \times \text{number of residues})$$

Data were omitted below wavelengths at which the voltage in the photomultiplier tube exceeded 600 V.

2.5.8 Liposome preparation

Chicken egg-derived L-α-phosphatidylcholine (PC, product number: 840051C) and porcine brain-derived L-α-phosphatidylserine (PS, product number: 840032) were purchased from Avanti Polar Lipids as 10 mg/mL solutions in chloroform. Liposomes were prepared using 2.6 micromoles of lipids, either solely PC or as a 1:1 molar ratio of PC and PS. A solution of 2.6 micromoles lipid in chloroform was placed into a 12 x 75 mm disposable culture tube. Chloroform was removed under a stream of dry N_2 gas to yield a lipid film. The culture tube was put under vacuum (< 1 mmHg) for *ca.* 12 h to ensure complete removal of chloroform from the lipid film. 2.6 mL of 10 mM sodium phosphate buffer (pH 7.4) was added to the lipid film. The suspension was left to stand for 1 h after which it was vortexed and extruded through a 100 nm polycarbonate filter using a mini extruder from Avanti Polar Lipids. Dynamic light scattering (DLS) was performed on the resulting solution of liposomes in order to confirm that the extrusion had generated liposomes 100 nm in diameter. Briefly, 150 µL of liposomes and 150 µL of buffer were added to a disposable 1 cm cuvette. Size distributions were determined using a Malvern Zetasizer ZS Nano DLS.

2.5.9 Python scripts

Fixing coordinates for REMD simulations

```
#Written by Patrick J. Salveson.
#To run, save this code as a file named fixed.py
#Place fixed.py and the PDB generated by autopsf in same folder
#in a terminal navigate to aforementioned folder and enter:
#python fixed_coord.py NAMEOFPDBFILE.PDB

from sys import argv
script, inputPDB = argv
inputF = open(inputPDB, 'r')

FixedAA = ['36', '37', '38', '39', '40', '41', '42', '49', '50', '51', '52', '53', '54', '55']
fixedAtoms = ['CA', 'C', 'N', 'O']

for i in inputF:
    if len(i) > 50:
        #this statements selects resides that will be fixed
        if residueNumber in FixedAA:
            if atomIdentity in fixedAtoms:
                #this statement selects backbone atoms, writes them as fixed
                writeToNewPDB(i[:7], i[7:11], i[11:17], i[17:22], i[22:26], i[26:56], '1.00
','fixed',i[66:])
            else:
                #this statement selects sidechain atoms, writes them as not fixed
                writeToNewPDB(i[:7], i[7:11], i[11:17], i[17:22], i[22:26], i[26:56], '1.00
','notfixed',i[66:])
        else:
            #writes non fixed residues as not fixed
            writeToNewPDB(i[:7], i[7:11], i[11:17], i[17:22], i[22:26], i[26:56], '1.00
','notfixed',i[66:])
    else:
        f = "fixed_script_output.pdb"
        outputF = open(f, 'a')
        outputF.write(i)
        outputF.close()

def writeToNewPDB(firstPart, atomNum, atomID, resiIDchainID, resiNum, coord, occ, fixedNotFixed, lastPart):
    f = "fixed_script_output.pdb"
    outputF = open(f, 'a')
    if fixedNotFixed == 'fixed':
        outputF.write(firstPart + atomNum + atomID + resiIDchainID + resiNum + coord + '1.00
' + '1.00' + lastPart)
    elif fixedNotFixed == 'notfixed':
        outputF.write(firstPart + atomNum + atomID + resiIDchainID + resiNum + coord + '1.00
' + '0.00' + lastPart)
    else:
        print 'something bad happened'
    outputF.close()

inputF.close()
```

Conversion of PDB file into the enantiomer

```
#Written by Patrick J. Salveson
#To run, save this code as a file named ent.py
#Place ent.py and the PDB to be inverted in same folder
#in a terminal navigate to aforementioned folder and enter:
#python ent.py NAMEOFPDBFILE.PDB

from sys import argv
from decimal import *

script, inputPDB = argv
inputF = open(inputPDB, 'r')

for i in inputF:
    atomIdentity = i[11:17].strip()
    residueNumber = i[22:26].strip()
    atomOrNot = i[:7].strip()

    if len(i) == 81 and (atomOrNot == 'ATOM' or atomOrNot == 'HETATM'):
        x = i[31:38].strip()
        y = i[38:46].strip()
        z = i[46:54].strip()

        newX = Decimal(x)*(-1)
        newY = (-1) * Decimal(y)
        newZ = (-1) * Decimal(z)

        #convert the negative floats to strings

        newXString = str(newX)
        newYString = str(newY)
        newZString = str(newZ)

        # need to check X length
        dX = len(i[31:38]) - len(newXString)
        dY = len(i[38:46]) - len(newYString)
        dZ = len(i[46:54]) - len(newXString)

        finalX = dX*" " + newXString
        finalY = dY*" " + newYString
        finalZ = dZ*" " + newZString
        newCoord = finalX + finalY + finalZ

        writeToNewPDB(i[:7], i[7:11], i[11:17], i[17:22], i[22:26], i[26:31], newCoord, i[54:])

def writeToNewPDB(firstPart, atomNum, atomID, resiIDchainID, resiNum, blank, coord, lastPart):
    f = "occupancy_script_output.pdb"
    outputF = open(f, 'a')
    outputF.write(firstPart + atomNum + atomID + resiIDchainID + resiNum + blank + coord + lastPart)
    outputF.close()

inputF.close()
```

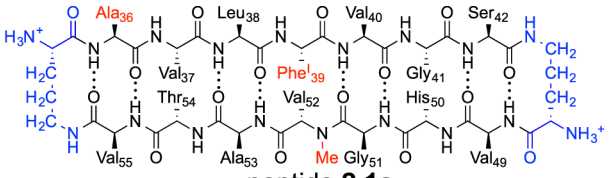

peptide **2.1a**

```
Data File D:\NOWICK HPLC USERS\PATRICK\PJS-I-204_100UM.D
Sample Name: PJS-I-204_100uM

======================================================================
Acq. Operator   : Patrick
Acq. Instrument : Agilent HPLC                    Location : Vial 42
Injection Date  : 11/8/2014 1:26:42 PM
                                                  Inj Volume : 20.0 µl
Acq. Method     : D:\NOWICK HPLC USERS\ZHENGJ\METHODS\RKS 5-100 OVER 20 MIN AT 214 AT 1 ML.M
Last changed    : 11/4/2014 2:58:52 AM by Kevin
Analysis Method : D:\NOWICK HPLC USERS\ZHENGJ\METHODS\KHC-FRACTIONCHECK-25-100.M
Last changed    : 12/9/2015 11:12:03 AM by SY
                  (modified after loading)
```

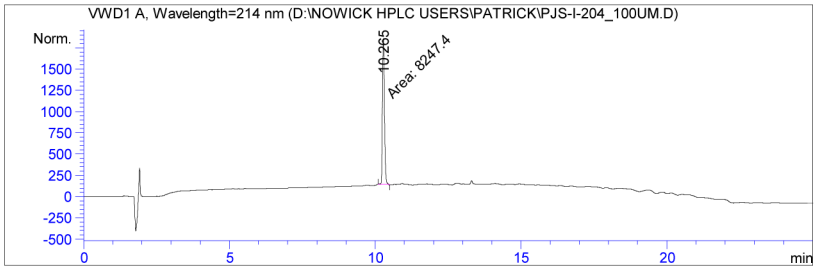

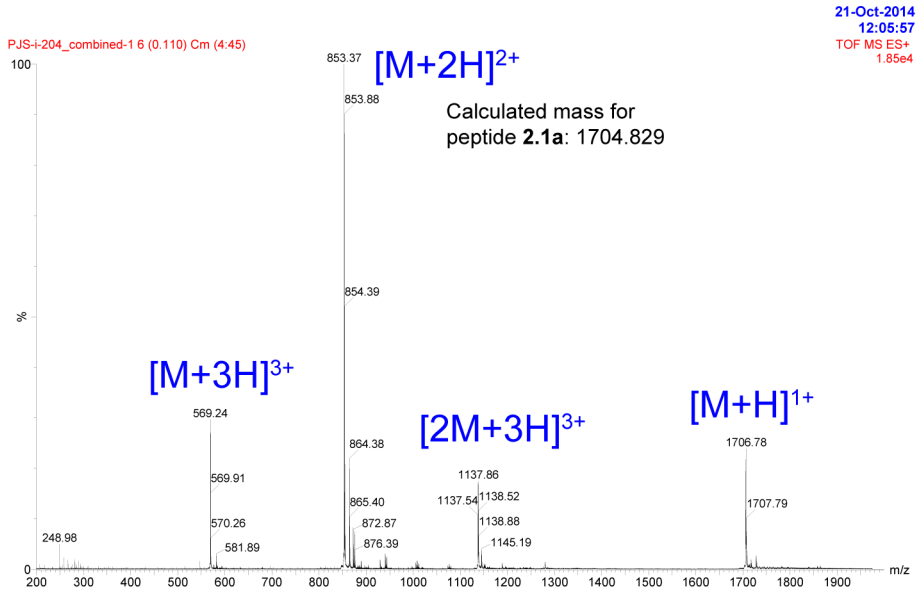

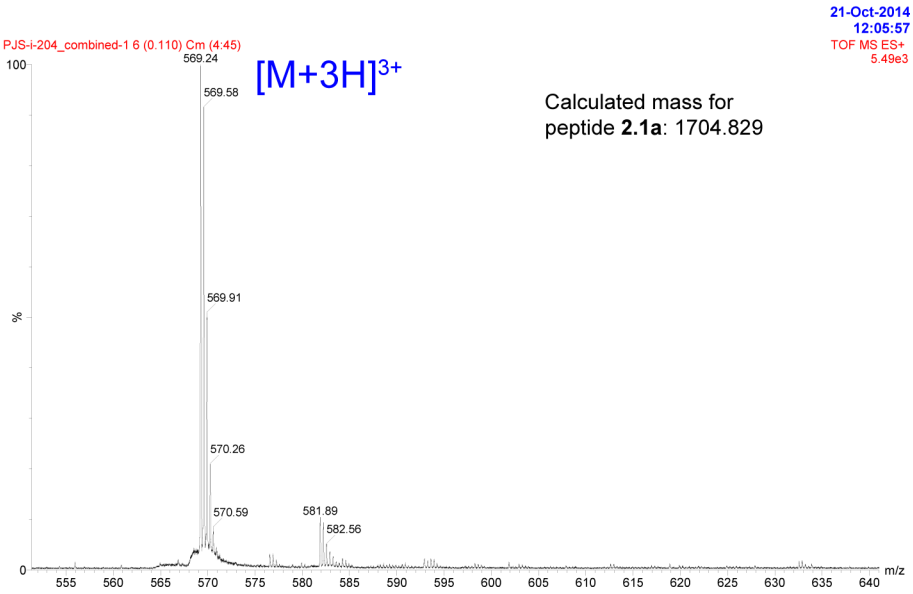
21-Oct-2014
12:05:57
TOF MS ES+
5.49e3
PJS-i-204_combined-1 6 (0.110) Cm (4:45)
[M+3H]3+
Calculated mass for
peptide 2.1a: 1704.829
100
%
0
569.24
569.58
569.91
570.26
570.59
581.89
582.56
555 560 565 570 575 580 585 590 595 600 605 610 615 620 625 630 635 640
m/z

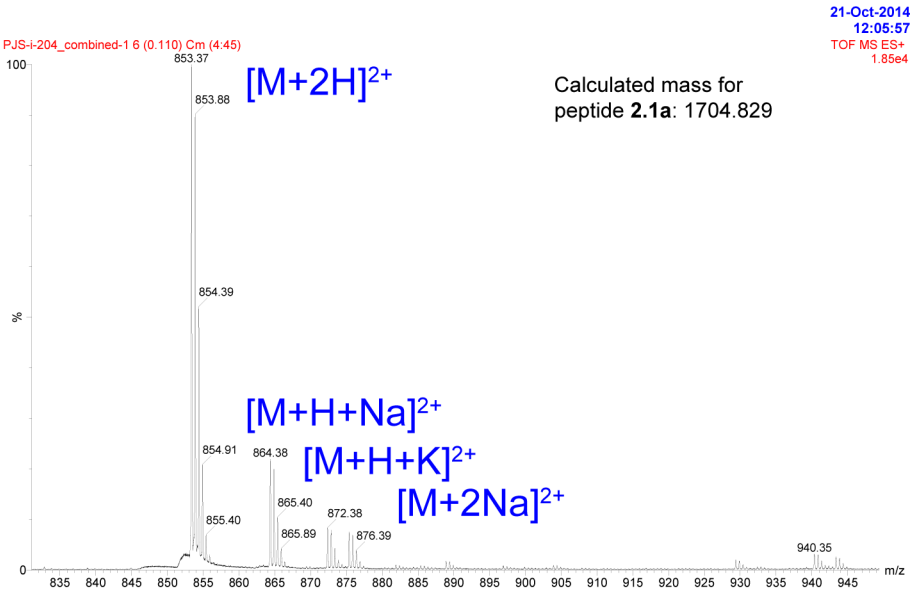
21-Oct-2014
12:05:57
TOF MS ES+
1.85e4
PJS-i-204_combined-1 6 (0.110) Cm (4:45)
[M+2H]2+
Calculated mass for
peptide 2.1a: 1704.829
100
%
0
853.37
853.88
854.39
[M+H+Na]2+
854.91
864.38
[M+H+K]2+
865.40
[M+2Na]2+
855.40
872.38
865.89
876.39
940.35
835 840 845 850 855 860 865 870 875 880 885 890 895 900 905 910 915 920 925 930 935 940 945
m/z

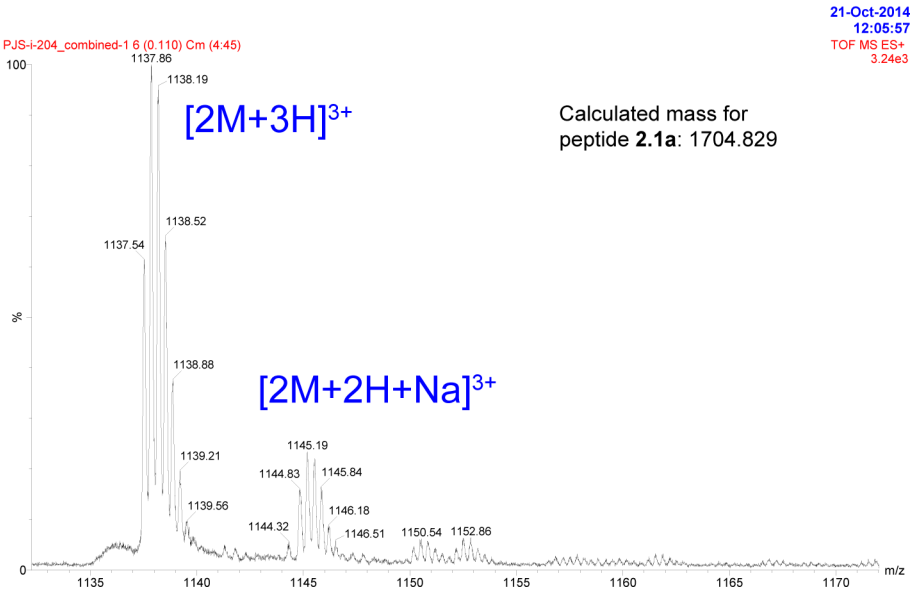
21-Oct-2014
12:05:57
TOF MS ES+
3.24e3
PJS-i-204_combined-1 6 (0.110) Cm (4:45)
100
%
0
1137.86
1138.19
1138.52
1137.54
1138.88
1139.21
1139.56
1144.32
1144.83
1145.19
1145.84
1146.18
1146.51
1150.54
1152.86
[2M+3H]3+
[2M+2H+Na]3+
Calculated mass for
peptide 2.1a: 1704.829
1135
1140
1145
1150
1155
1160
1165
1170
m/z

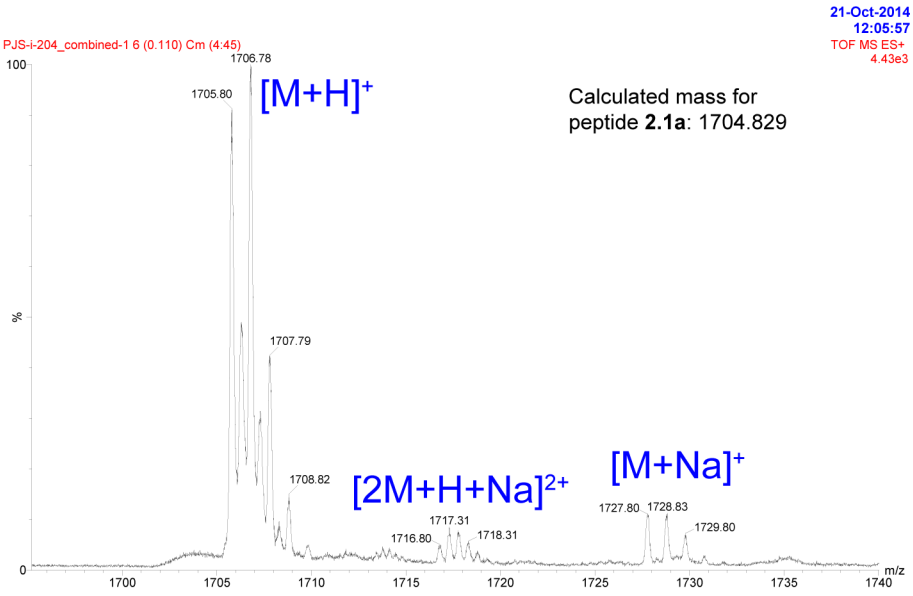
21-Oct-2014
12:05:57
TOF MS ES+
4.43e3
PJS-i-204_combined-1 6 (0.110) Cm (4:45)
100
%
0
1706.78
1705.80
1707.79
1708.82
1716.80
1717.31
1718.31
1727.80
1728.83
1729.80
[M+H]+
[2M+H+Na]2+
[M+Na]+
Calculated mass for
peptide 2.1a: 1704.829
1700
1705
1710
1715
1720
1725
1730
1735
1740
m/z

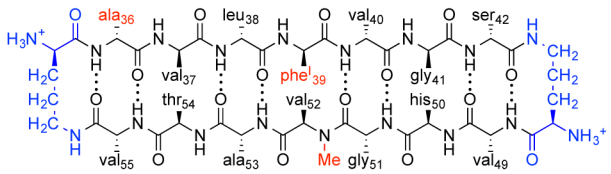

peptide *ent*-**2.1a**

```
Data File D:\NOWICK HPLC USERS\PATRICK\PJS-I-202_COMBINED.D
Sample Name: PJS-I-202_combined

=====================================================================
Acq. Operator   : Patrick
Acq. Instrument : Agilent HPLC                    Location : Vial 51
Injection Date  : 10/14/2014 1:50:52 PM
                                                  Inj Volume : 20.0 µl
Acq. Method     : D:\NOWICK HPLC USERS\ZHENGJ\METHODS\RKS 5-100 OVER 20 MIN AT 214 AT 1 ML.M
Last changed    : 10/13/2014 10:07:34 PM by Adam
Analysis Method : D:\NOWICK HPLC USERS\YANG\YANG POLAR 5-100 40MIN 214NM PUMPCND.M
Last changed    : 4/27/2015 3:22:13 PM by NT
                  (modified after loading)
```

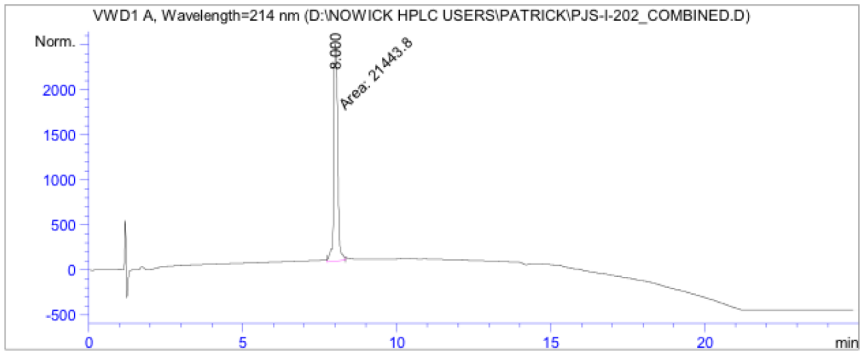

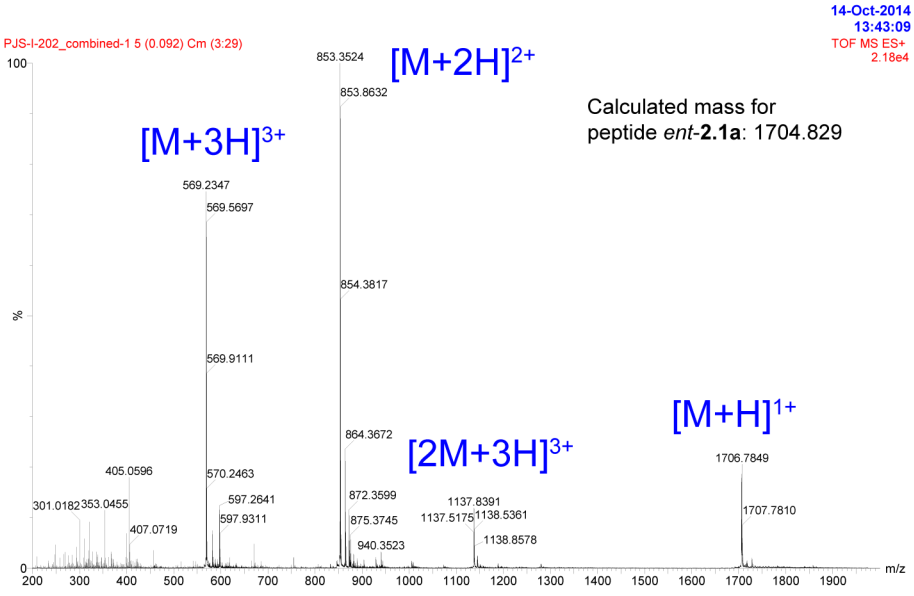

Calculated mass for peptide *ent*-**2.1a**: 1704.829

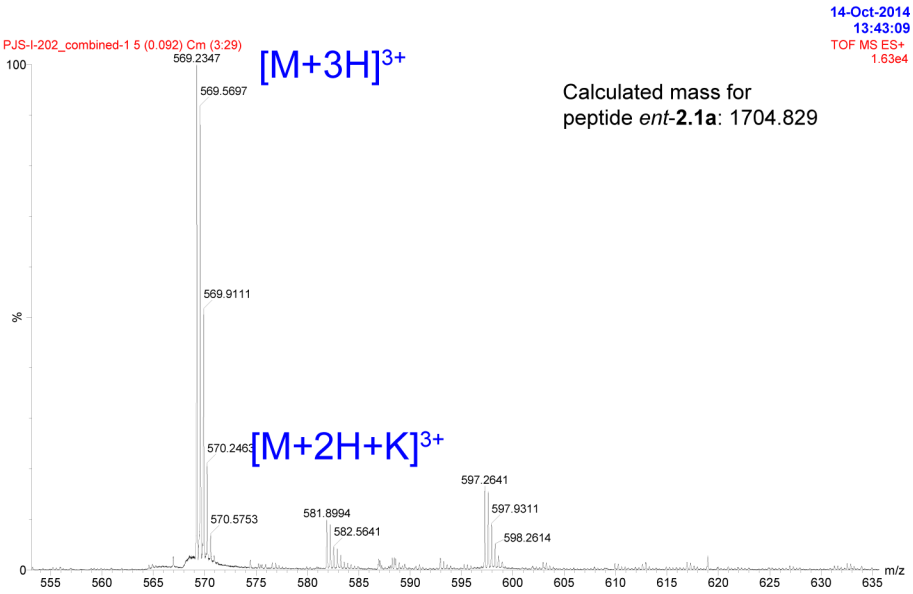
14-Oct-2014
13:43:09
TOF MS ES+
1.63e4
PJS-I-202_combined-1 5 (0.092) Cm (3:29)
[M+3H]3+
Calculated mass for
peptide ent-2.1a: 1704.829
[M+2H+K]3+
m/z

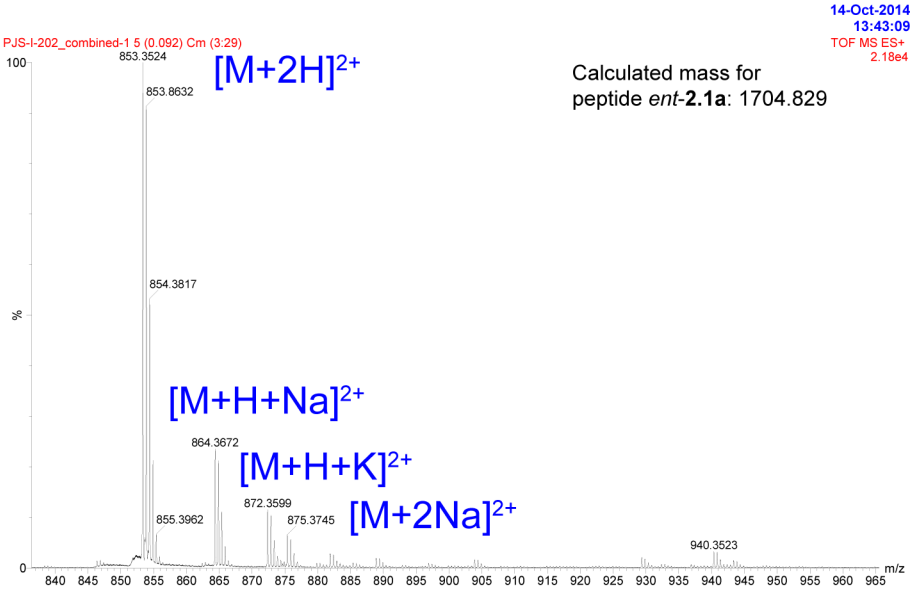
14-Oct-2014
13:43:09
TOF MS ES+
2.18e4
PJS-I-202_combined-1 5 (0.092) Cm (3:29)
[M+2H]2+
Calculated mass for
peptide ent-2.1a: 1704.829
[M+H+Na]2+
[M+H+K]2+
[M+2Na]2+
m/z

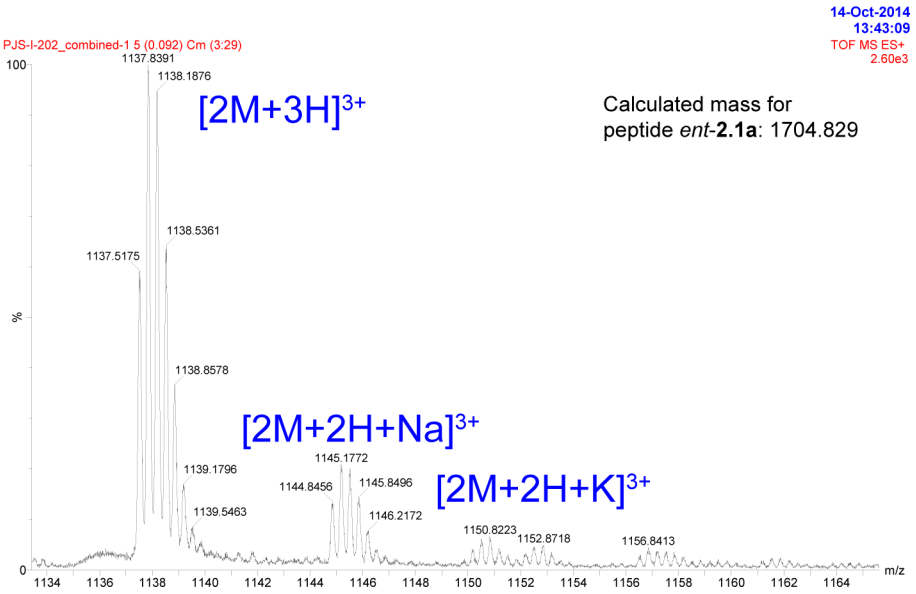
14-Oct-2014
13:43:09
TOF MS ES+
2.60e3
PJS-I-202_combined-1 5 (0.092) Cm (3:29)
[2M+3H]3+
Calculated mass for
peptide ent-2.1a: 1704.829
[2M+2H+Na]3+
[2M+2H+K]3+
1137.8391
1138.1876
1138.5361
1137.5175
1138.8578
1139.1796
1145.1772
1144.8456
1145.8496
1139.5463
1146.2172
1150.8223
1152.8718
1156.8413
%
m/z

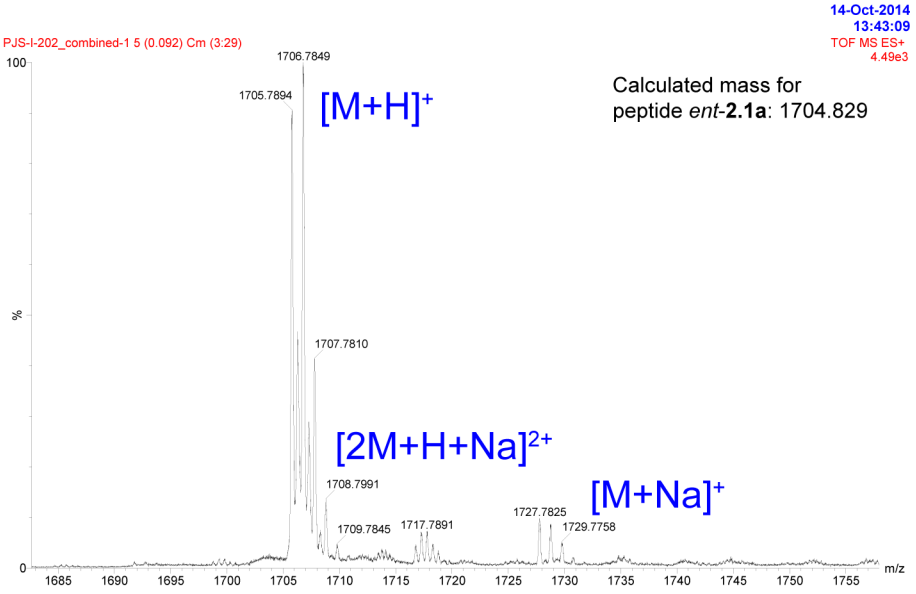
14-Oct-2014
13:43:09
TOF MS ES+
4.49e3
PJS-I-202_combined-1 5 (0.092) Cm (3:29)
[M+H]+
Calculated mass for
peptide ent-2.1a: 1704.829
[2M+H+Na]2+
[M+Na]+
1706.7849
1705.7894
1707.7810
1708.7991
1709.7845
1717.7891
1727.7825
1729.7758
%
m/z

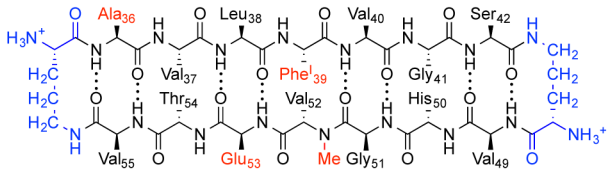

peptide **2.1a**$_{A53E}$

```
Data File D:\NOWICK HPLC USERS\PATRICK\PJS-I-245_COMBINED.D
Sample Name: PJS-I-245_combined

    ======================================================================
    Acq. Operator    : Patrick
    Acq. Instrument : Agilent HPLC                    Location : Vial 41
    Injection Date   : 12/16/2014 2:32:44 PM
                                                    Inj Volume : 20.0 µl
    Acq. Method      : D:\NOWICK HPLC USERS\ZHENGJ\METHODS\RKS 5-100 OVER 20 MIN AT 214 AT 1 ML.M
    Last changed     : 12/4/2014 2:29:03 PM by yilinw
    Analysis Method : D:\NOWICK HPLC USERS\YANG\YANG POLAR 5-100 40MIN 214NM PUMPCND.M
    Last changed     : 4/27/2015 3:22:13 PM by NT
                       (modified after loading)
```

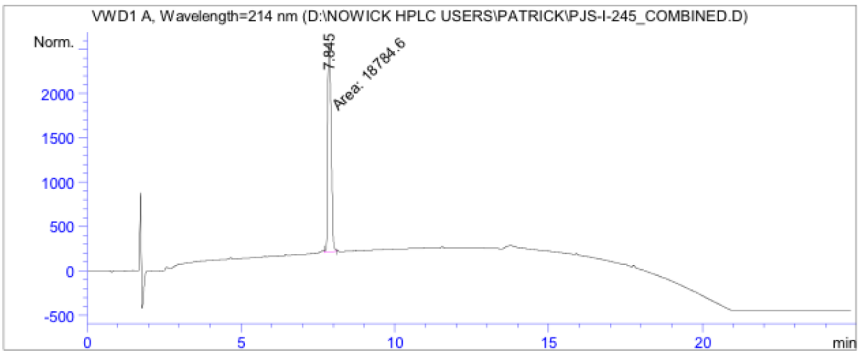

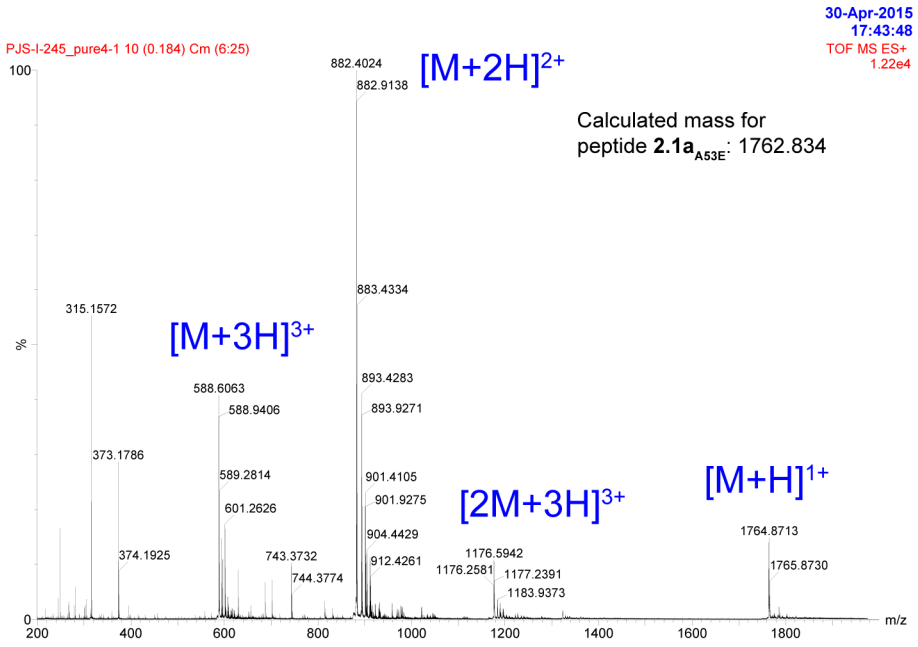

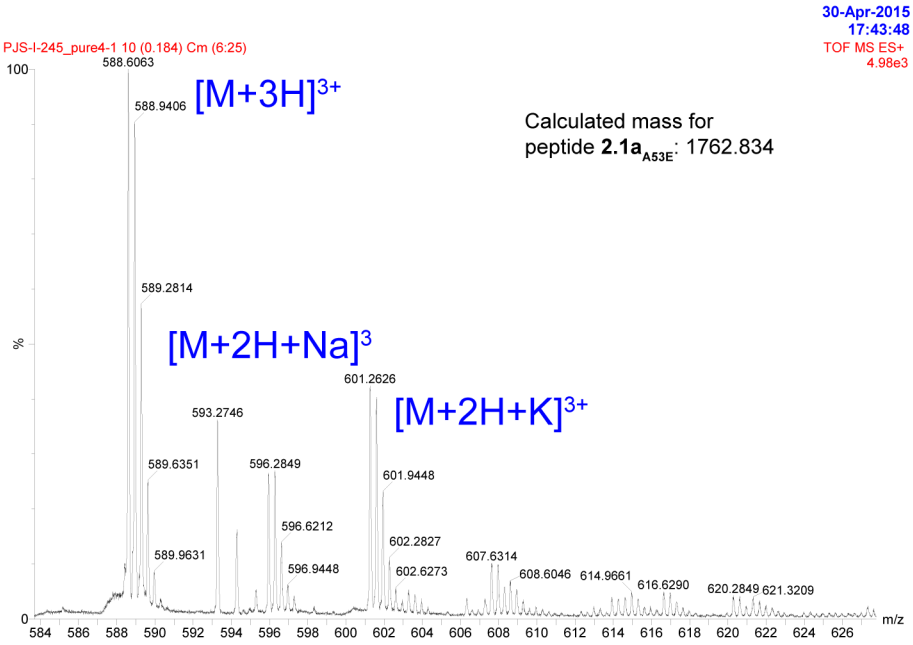
30-Apr-2015
17:43:48
TOF MS ES+
4.98e3
PJS-I-245_pure4-1 10 (0.184) Cm (6:25)
100
%
0
588.6063
588.9406
589.2814
589.6351
589.9631
593.2746
596.2849
596.6212
596.9448
601.2626
601.9448
602.2827
602.6273
607.6314
608.6046
614.9661
616.6290
620.2849
621.3209
[M+3H]3+
[M+2H+Na]3
[M+2H+K]3+
Calculated mass for
peptide 2.1a A53E: 1762.834
584 586 588 590 592 594 596 598 600 602 604 606 608 610 612 614 616 618 620 622 624 626
m/z

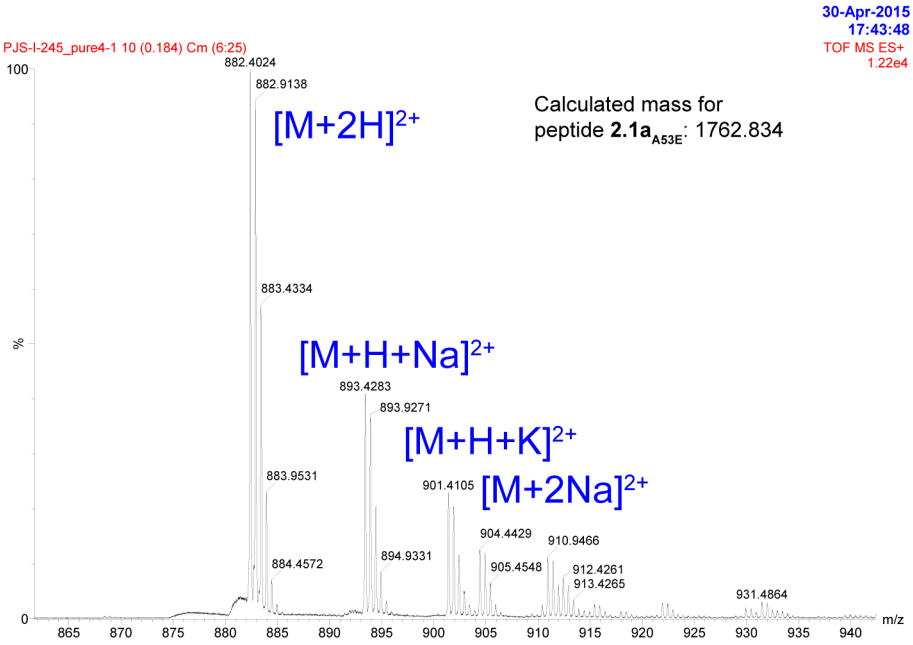
30-Apr-2015
17:43:48
TOF MS ES+
1.22e4
PJS-I-245_pure4-1 10 (0.184) Cm (6:25)
100
%
0
882.4024
882.9138
883.4334
883.9531
884.4572
893.4283
893.9271
894.9331
901.4105
904.4429
905.4548
910.9466
912.4261
913.4265
931.4864
[M+2H]2+
[M+H+Na]2+
[M+H+K]2+
[M+2Na]2+
Calculated mass for
peptide 2.1a A53E: 1762.834
865 870 875 880 885 890 895 900 905 910 915 920 925 930 935 940
m/z

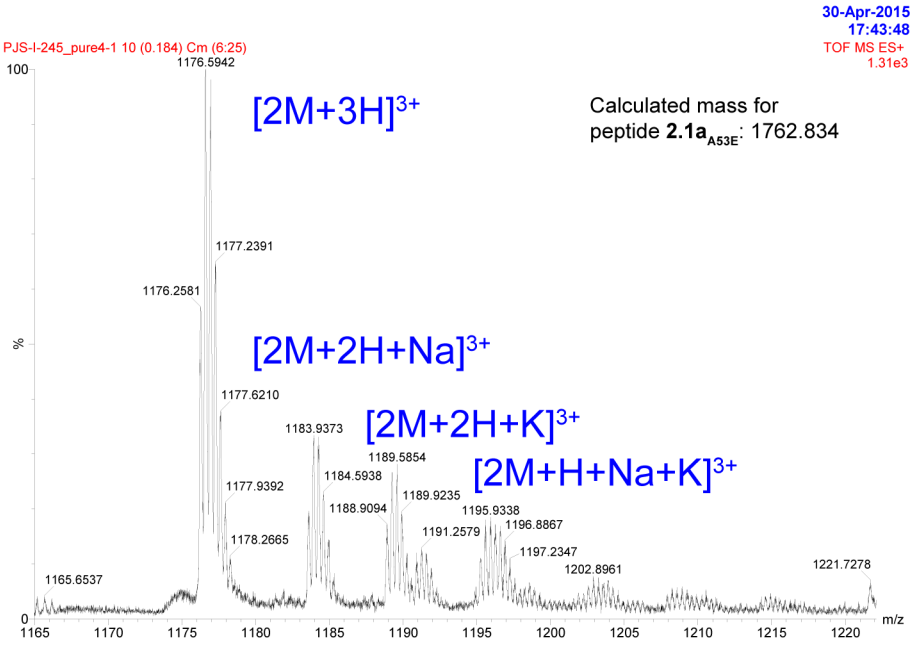
30-Apr-2015
17:43:48
TOF MS ES+
1.31e3
PJS-I-245_pure4-1 10 (0.184) Cm (6:25)
[2M+3H]3+
Calculated mass for
peptide 2.1a A53E: 1762.834
[2M+2H+Na]3+
[2M+2H+K]3+
[2M+H+Na+K]3+
1176.5942
1177.2391
1176.2581
1177.6210
1183.9373
1189.5854
1184.5938
1177.9392
1189.9235
1188.9094
1195.9338
1196.8867
1191.2579
1178.2665
1197.2347
1202.8961
1221.7278
1165.6537
%
m/z

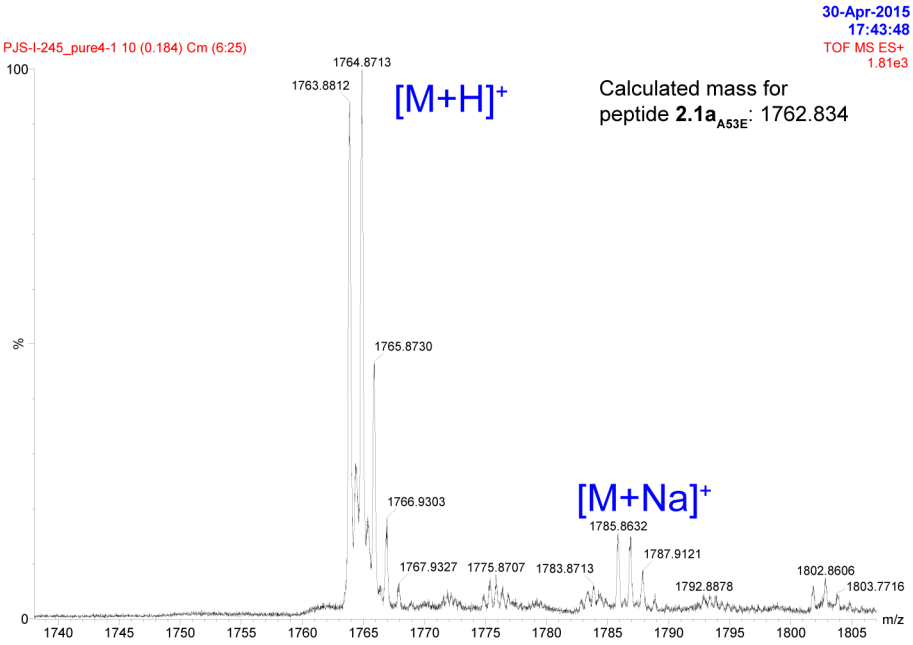
30-Apr-2015
17:43:48
TOF MS ES+
1.81e3
PJS-I-245_pure4-1 10 (0.184) Cm (6:25)
[M+H]+
Calculated mass for
peptide 2.1a A53E: 1762.834
[M+Na]+
1764.8713
1763.8812
1765.8730
1766.9303
1785.8632
1787.9121
1767.9327
1775.8707
1783.8713
1802.8606
1792.8878
1803.7716
%
m/z

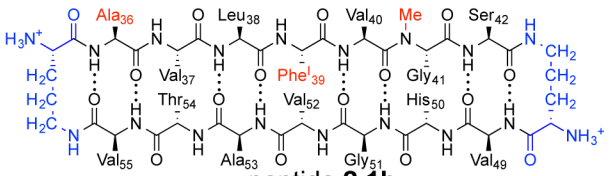

peptide **2.1b**

Data File D:\NOWICK HPLC USERS\PATRICK\PJS_II-36_REPUR_COMBINED.D
Sample Name: PJS_II-36_repur_combined

==========

Acq. Operator : Patrick
Acq. Instrument : Agilent HPLC Location : Vial 81
Injection Date : 3/27/2015 2:32:36 PM
Inj Volume : 20.0 µl
Acq. Method : D:\NOWICK HPLC USERS\NT\5-100 OVER 20MIN AT 214NM [PUMPCND].M
Last changed : 3/18/2015 4:29:49 PM by yilinw
Analysis Method : D:\NOWICK HPLC USERS\ZHENGJ\METHODS\KHC-FRACTIONCHECK-25-100.M
Last changed : 12/9/2015 11:12:03 AM by SY
(modified after loading)

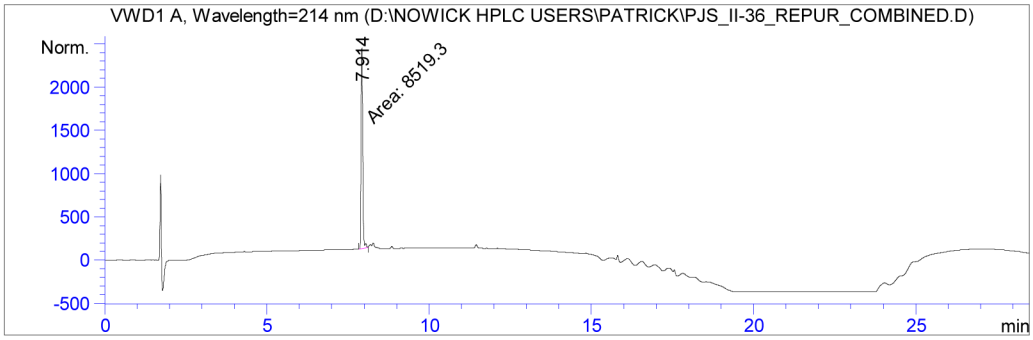

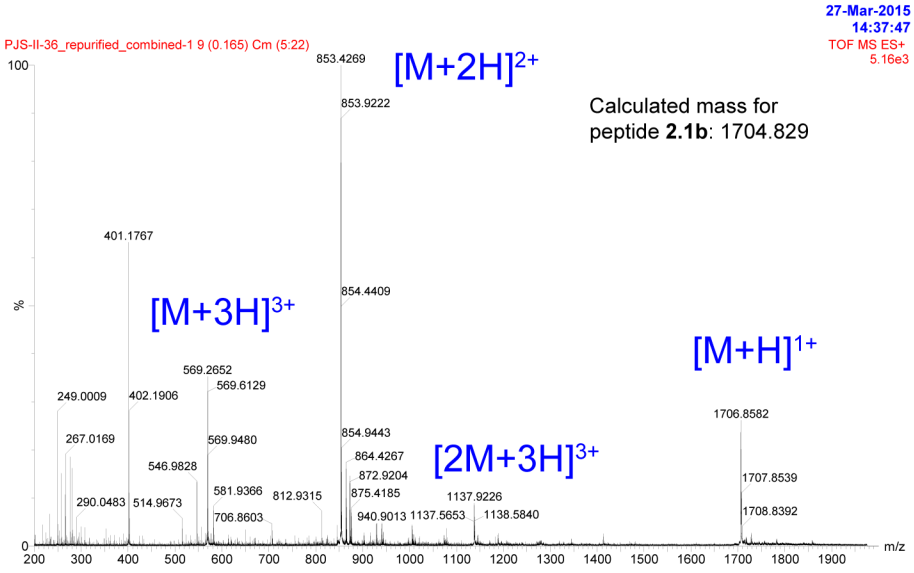

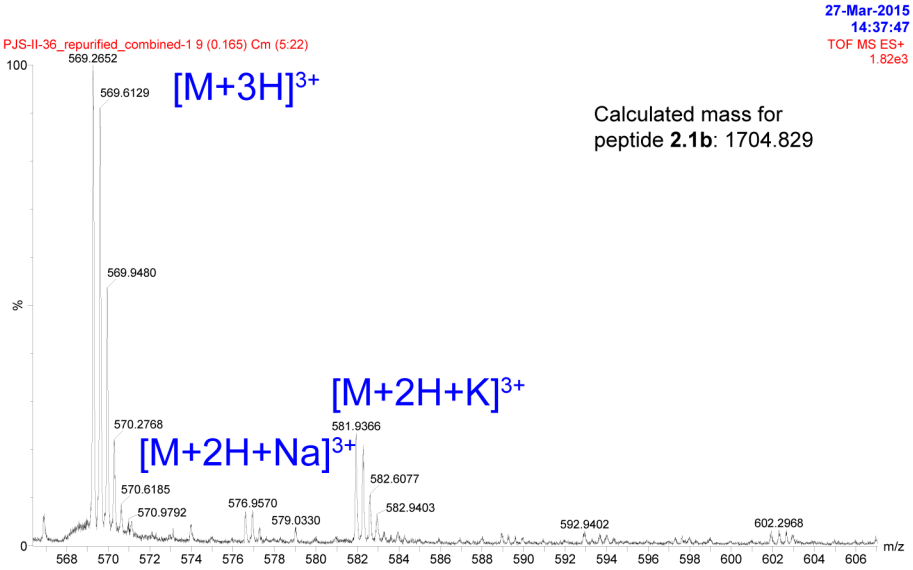
27-Mar-2015
14:37:47
TOF MS ES+
1.82e3
PJS-II-36_repurified_combined-1 9 (0.165) Cm (5:22)
[M+3H]3+
Calculated mass for
peptide 2.1b: 1704.829
[M+2H+K]3+
[M+2H+Na]3+
m/z

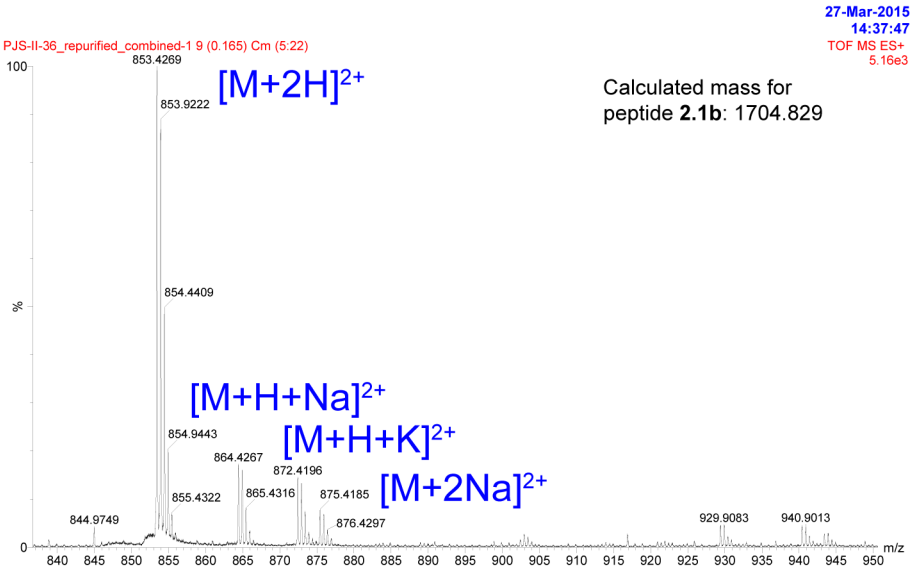
27-Mar-2015
14:37:47
TOF MS ES+
5.16e3
PJS-II-36_repurified_combined-1 9 (0.165) Cm (5:22)
[M+2H]2+
Calculated mass for
peptide 2.1b: 1704.829
[M+H+Na]2+
[M+H+K]2+
[M+2Na]2+
m/z

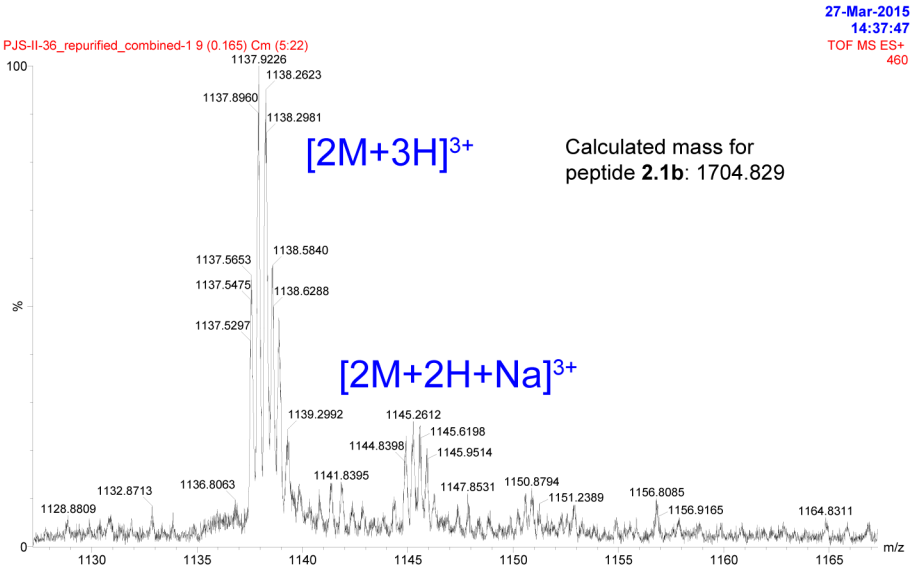
27-Mar-2015
14:37:47
TOF MS ES+
460
PJS-II-36_repurified_combined-1 9 (0.165) Cm (5:22)
[2M+3H]3+
Calculated mass for
peptide 2.1b: 1704.829
[2M+2H+Na]3+
m/z

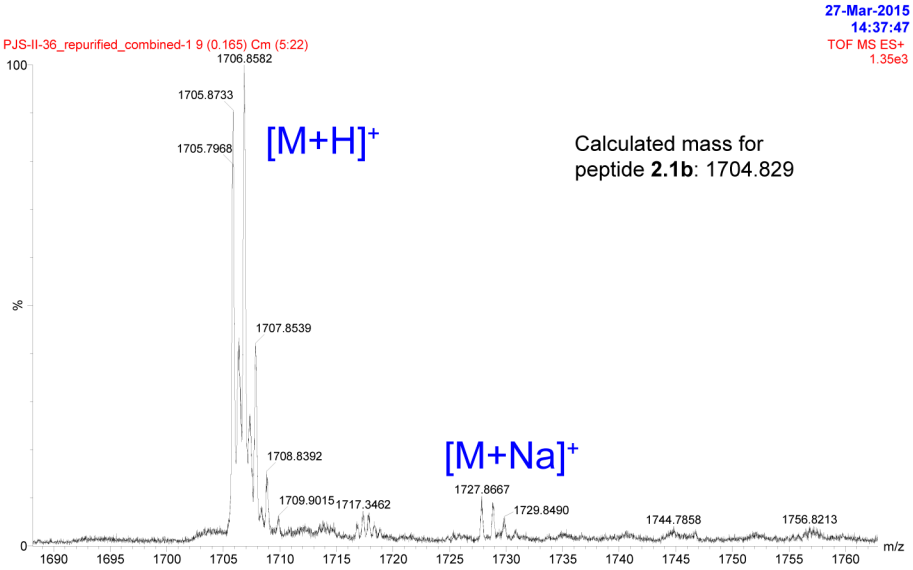
27-Mar-2015
14:37:47
TOF MS ES+
1.35e3
PJS-II-36_repurified_combined-1 9 (0.165) Cm (5:22)
[M+H]+
Calculated mass for
peptide 2.1b: 1704.829
[M+Na]+
m/z

Chapter 3

X-ray crystallographic structure of a compact dodecamer from a peptide derived from $A\beta_{16–36}$

3.1 Introduction

β-Hairpins are emerging as key building blocks of amyloid oligomers.[59,77,86,123–128] The twisted shape, exposed hydrogen-bonding edges, and hydrophobic surfaces of β-hairpins impart a unique propensity to self-assemble. Characterization of the assemblies that form at high-resolution has been challenging, because the resulting amyloid oligomers are heterogenous and polymorphic. The ability of β-hairpins to fold in a variety of ways adds to the potential for heterogeneity and polymorphism. There is a desperate need for high-resolution structural models of the oligomers formed by amyloidogenic peptides and proteins. Here we report the X-ray crystallographic structure of a compact ball-shaped dodecamer derived from the β-amyloid peptide, Aβ, that is composed of fused trimers.

Several research groups have generated models of Aβ oligomers composed of either β-hairpins or β-sheets.[52,53,57,60,129] The Härd group proposed an assembly of six β-hairpins, arranged in a barrel-like structure.[129] Our own laboratory described the X-ray crystallographic structures of trimers, hexamers, and dodecamers formed by macrocyclic β-hairpin peptide **3.1** derived from $A\beta_{17-36}$.[57] Peptide **3.1** contains the heptapeptide β-strands $A\beta_{17-23}$ and $A\beta_{30-36}$ connected by two δ-linked ornithine β-turn mimics ($^{\delta}$Orn) to form a macrocycle.[87] In designing peptide **3.1**, we replaced the native hydrophobic Met_{35} with the polar isostere ornithine (α-linked) to enhance solubility and reduce the propensity of the peptide to aggregate. Peptide **3.1** assembles into triangular trimers that further assemble into spherical dodecamers (PDB 4NTR). The interface between the dodecamers constitutes a hexamer in which two trimers pack together. We subsequently reported that a homologue of peptide **3.1** containing the loop of the β-hairpin assembles in a similar fashion.[60]

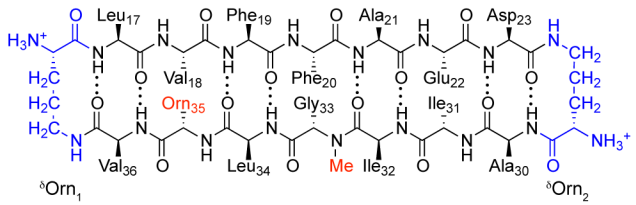

peptide **3.1** (from $A\beta_{17-36}$)

In the current study, we set out to explore how altering the residue pairing of the β-hairpin associated with peptide **3.1** alters the resulting supramolecular assembly. We envisioned a scenario in which $A\beta_{15-23}$ is free to adopt three pairings with $A\beta_{30-36}$: one in which $A\beta_{17-23}$ pairs with $A\beta_{30-36}$, one in which $A\beta_{16-22}$ pairs with $A\beta_{30-36}$, and one in which $A\beta_{15-21}$ pairs with $A\beta_{30-36}$. Figure 3.1 illustrates this concept. These shifts in pairing sequentially pull Lys_{16} and Gln_{15} into the upper β-strand while pushing Asp_{23} and Glu_{22} out of the β-strand and into the loop.

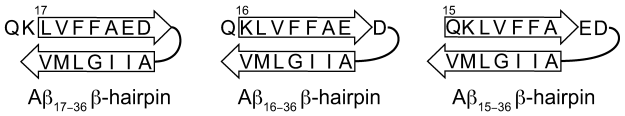

Figure 3.1: Cartoons of three different β-hairpins formed by $A\beta_{15–36}$, with different residue pairings.

3.2 Results and Discussion

We designed macrocyclic β-hairpin peptides **3.2**, **3.3**, and **3.4** to explore the concept embodied in Figure 3.1 and characterized the resulting assemblies by X-ray crystallography. Peptides **3.2**–**3.4** mimic only three of the six potential arrangements of β-strands associated with the $A\beta_{17–36}$, $A\beta_{16–36}$, and $A\beta_{15–36}$ β-hairpins. The other three arrangements of β-strands cannot be achieved with these macrocyclic β-sheets. We incorporated the native Met_{35} into each of these peptides, rather than the α-linked ornithine isostere, to better mimic the native β-hairpins. We replaced Phe_{19} with *para*-iodophenylalanine (Phe^{I}) to facilitate crystallographic phase determination by single wavelength anomalous diffraction phasing.[88] We synthesized, crystalized, and determined the crystallographic structures of peptides **3.2**–**3.4** using procedures that we have previously reported[130]. Table 3.1 summarizes the crystallographic properties, crystallization conditions, data collection, and model refinement statistics for peptides **3.2**, **3.3** and **3.4**.

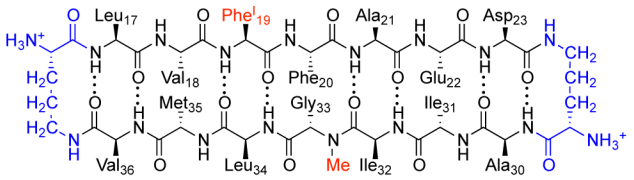

peptide **3.2** (from $A\beta_{17-36}$)

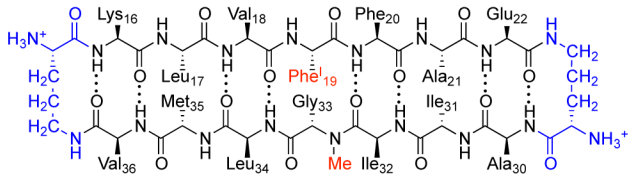

peptide **3.3** (from $A\beta_{16-36}$)

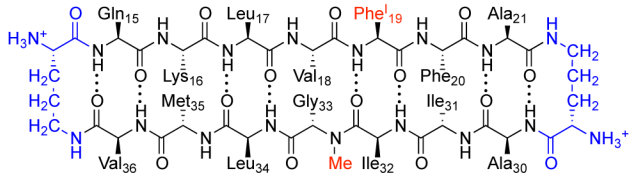

peptide **3.4** (from $A\beta_{15-36}$)

Peptide **3.2** assembles in an identical fashion to peptide **3.1**, forming triangular trimers that further assemble into spherical dodecamers (Figure 3.2). In each trimer, three monomers occupy the edges of an equilateral triangle (Figure 3.2A). The $A\beta_{17-23}$ β-strands of the monomers come together, hydrogen bonding to each other and to three water molecules that sit in the center of each trimer. The $A\beta_{30-36}$ β-strands of the monomers form the outer edges of the trimer. The side chains of Leu_{17}, Phe^{I}_{19}, and Val_{36} of one monomer pack against the side chains of Ala_{21}, Asp_{23}, Ile_{32}, and Leu_{34} from an adjacent monomer at the three vertices of the trimer. Four trimers further assemble in a tetrahedral arrangement into a loosely packed hollow dodecamer (Figure 3.2B). The diameter of the dodecamer spans 4–6 nm, depending on the points of measure, while its central cavity spans *ca.* 1.4 nm. The side chains of Phe^{I}_{19}, Leu_{34}, and Val_{36} line the cavity. The dodecamers further pack to form the lattice, with each interface between two dodecamers constituting a sandwich-like hexamer (Figure 3.2C). The side chains of Phe_{20}, Glu_{22}, and Ile_{31} pack against one another in the interior of the hexamer.

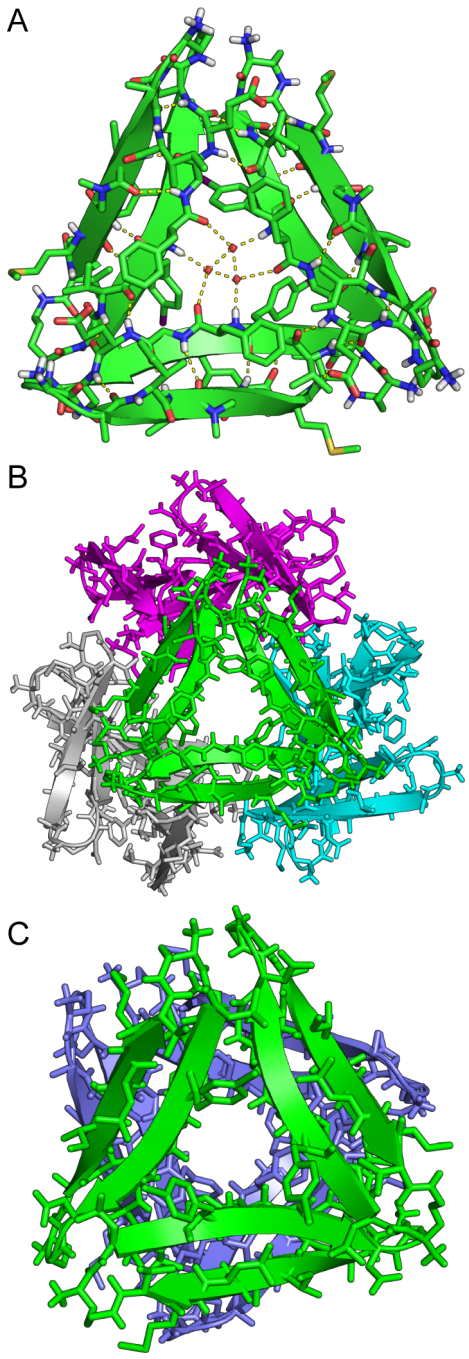

Figure 3.2: Trimer, dodecamer, and hexamer formed by peptide **3.2** (PDB 5V65). (A) Triangular trimer. (B) Dodecamer comprising four triangular trimers, colored green, magenta, cyan, and grey. (C) Sandwich-like hexamer comprising two triangular trimers that constitutes the interface between two dodecamers.

Peptide **3.3** assembles into compact ball-shaped dodecamers that differ from those formed by peptide **3.2** (Figure 3.3). The dodecamer formed by peptide **3.2** comprises discrete

triangular trimers, while the dodecamer formed by peptide **3.3** comprises fused triangular trimers. Each trimer in the dodecamer formed by peptide **3.3** shares three edges with the three adjacent trimers. As a result, the trimers are not discrete entities within the ball-shaped dodecamer, but instead are fused like the benzene rings of naphthalene or graphite (Figure 3.4). Our laboratory has previously observed a similar assembly formed by a cross-linked trimer derived from $A\beta_{17-36}$.[61]

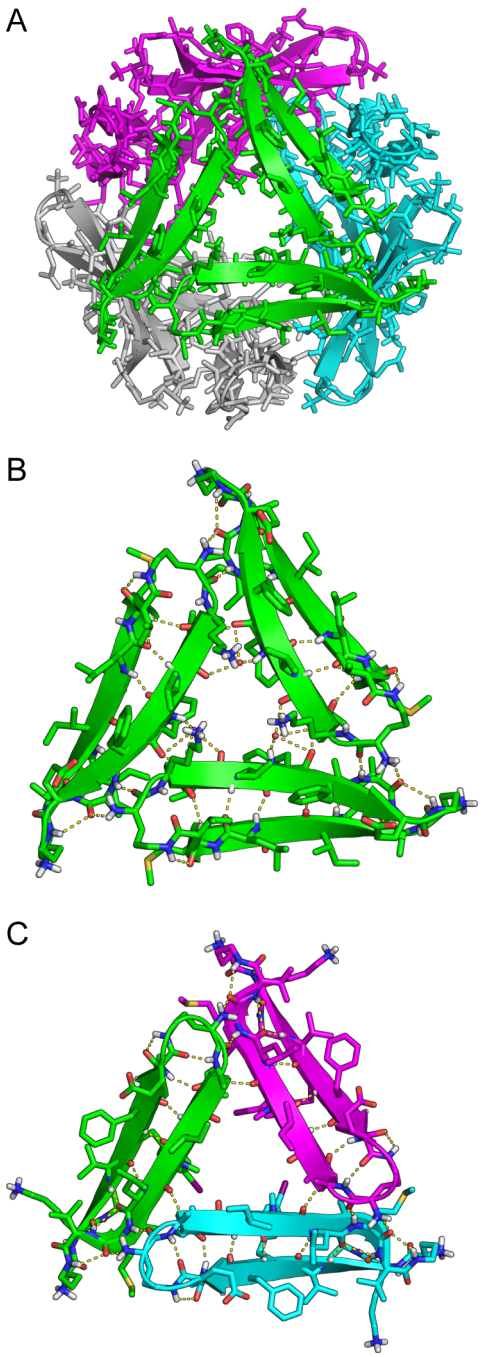

Figure 3.3: Trimers and ball-shaped dodecamer formed by peptide **3.3** (PDB 5V63). (A) Ball-shaped dodecamer. Trimers of one type are colored green, magenta, cyan, and grey; trimers of the other type are composed of monomers of three different colors. (B) One type of triangular trimer within the ball-shaped dodecamer. This trimer centers around the $A\beta_{16–22}$ β-strands. (C) The other type of triangular trimer within the ball-shaped dodecamer. This trimer centers around the $A\beta_{30–36}$ β-strands.

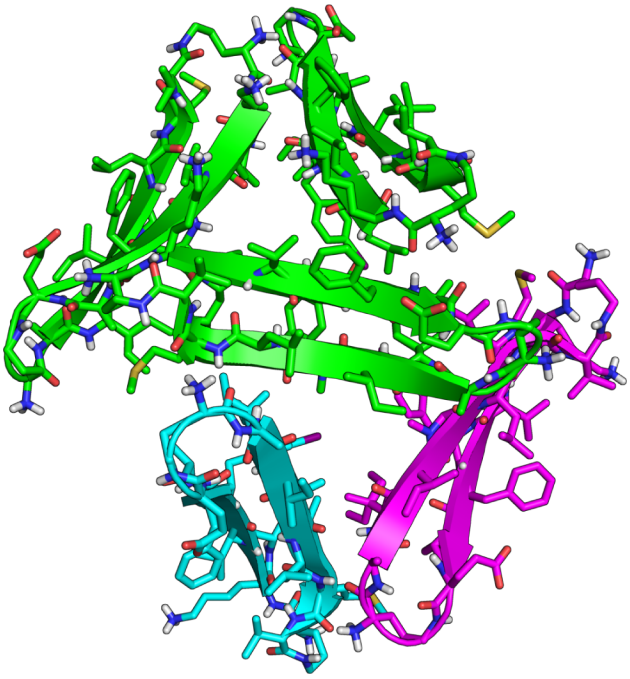

Figure 3.4: Two fused trimer subunits within the ball-shaped dodecamer formed by peptide **3.3**.

Two types of trimers make up the ball-shaped dodecamer formed by peptide **3.3** (Figures 3.3B and C). The two types of trimers differ in the placement of the $A\beta_{16–22}$ and $A\beta_{30–36}$ β-strands. The $A\beta_{16–22}$ β-strands of the monomers hydrogen bond to each other within the trimer depicted in Figure 3.3B, while the $A\beta_{30–36}$ β-strands hydrogen bond to each other within the trimer depicted in Figure 3.3C. The outer edges of the trimer depicted in Figure 3.3B lie within three different trimers, like the one depicted in Figure 3.3C. Conversely, the outer edges of the trimer depicted in Figure 3.3C lie within three different trimers, like the one depicted in Figure 3.3B. Three water molecules occupy the center of the trimer depicted in Figure 3.3B. The three *N*-methyl groups occupy the center of the trimer depicted in Figure 3.3C, in lieu of three water molecules.

The ball-shaped dodecamer formed by peptide **3.3** is hollow, like the dodecamer formed by peptide **3.2**. The diameter of the ball-shaped dodecamer spans 3–4 nm depending on the points of measure, while its central cavity spans *ca.* 1.0 nm. The side chains of Phe^{I}_{19} line

the cavity, while the exterior surface of the dodecamer displays the side chains of Lys_{16}, Val_{18}, Phe_{20}, Glu_{22}, Ala_{30}, Ile_{32}, Leu_{34}, and Val_{36}. Unlike the dodecamers formed by peptide **3.2**, the dodecamers formed by peptide **3.3** do not form sandwich-like hexamers. Instead these dodecamers pack hexagonally and stack like cannonballs.

The dodecamers formed by peptides **3.2** and **3.3** share similar themes in self-assembly, as both are composed of triangular trimer subunits. Mapping the triangular subunits of each dodecamer onto an octahedron highlights these similarities, as well as key differences (Figure 3.5). In the dodecamer formed by peptide **3.2**, the four trimers occupy four of the eight triangular faces of the octahedron. The interfaces between the trimers define the remaining four triangular faces. In the dodecamer formed by peptide **3.3**, each monomer occupies one edge of the octahedron, and each trimer defines one of the eight triangular faces of the octahedron. At each of the six vertices of the octahedron, four monomers of peptide **3.3** form an eight-stranded β-barrel-like opening. An analogous opening is absent in the dodecamer formed by peptide **3.2**. The hydrogen-bonding network that helps stabilize both dodecamers is more extensive in the dodecamer formed by peptide **3.3**, which contains 36 additional intermolecular hydrogen bonds beyond those that compose the hydrogen-bonding network in the dodecamer formed by peptide **3.2**.

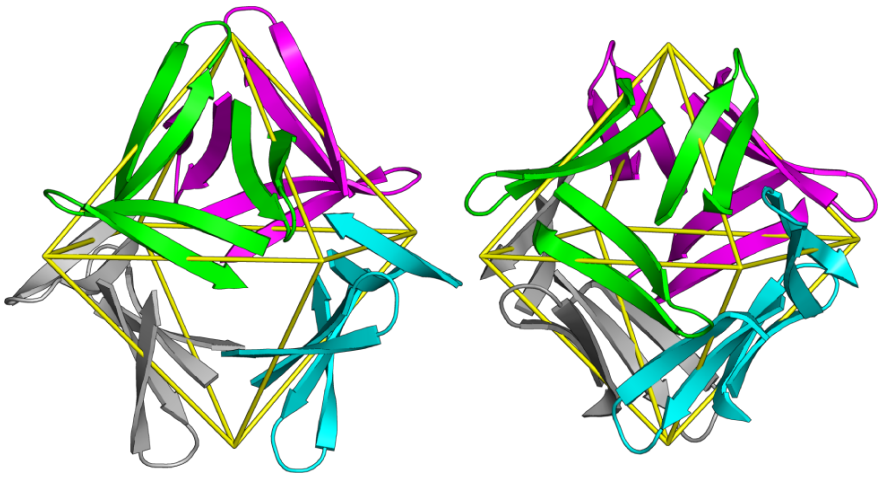

Figure 3.5: Dodecamers formed by peptides **3.2** (left) and **3.3** (right) superimposed on octahedra (yellow). Both dodecamers are depicted on the same scale.

The dodecamer formed by peptide **3.3** is more densely packed than the dodecamer formed by peptide **3.2**. Assembly of peptide **3.3** into a dodecamer buries *ca.* 10,800 Å^2 of surface area, whereas assembly of peptide **3.2** into a dodecamer buries only *ca.* 8,100 Å^2. It is not obvious from their sequences or structures why peptide **3.3** forms a more compact dodecamer that differs from that of peptide **3.2**.

In contrast to the discrete oligomers formed by peptides **3.2** and **3.3**, peptide **3.4** forms a fibril-like assembly (Figure 3.6). Each monomer of peptide **3.4** hydrogen bonds with the two neighboring monomers along the fibril axis. The interface between monomers constitutes a parallel β-sheet with three intermolecular hydrogen bonds in which Leu_{17}, Val_{18}, and Phe^{I}_{19} pair with $^{\delta}Orn_2$, Ala_{30}, and Ile_{31}. The *N*-methyl group on Gly_{33} blocks formation of a fully hydrogen-bonded interface, prying apart the β-sheets and requiring a water molecule to bridge a hydrogen bond between the NH group of Phe_{20} and the carbonyl group of Ile_{31}. Each monomer is flipped upside down with respect to the neighboring monomers in the fibril such that the surfaces of the monomers are displayed in an alternating pattern along the surface of the fibril: one monomer displays its top surface, the next monomer displays its bottom surface, and so on down the fibril (Figure 3.7).

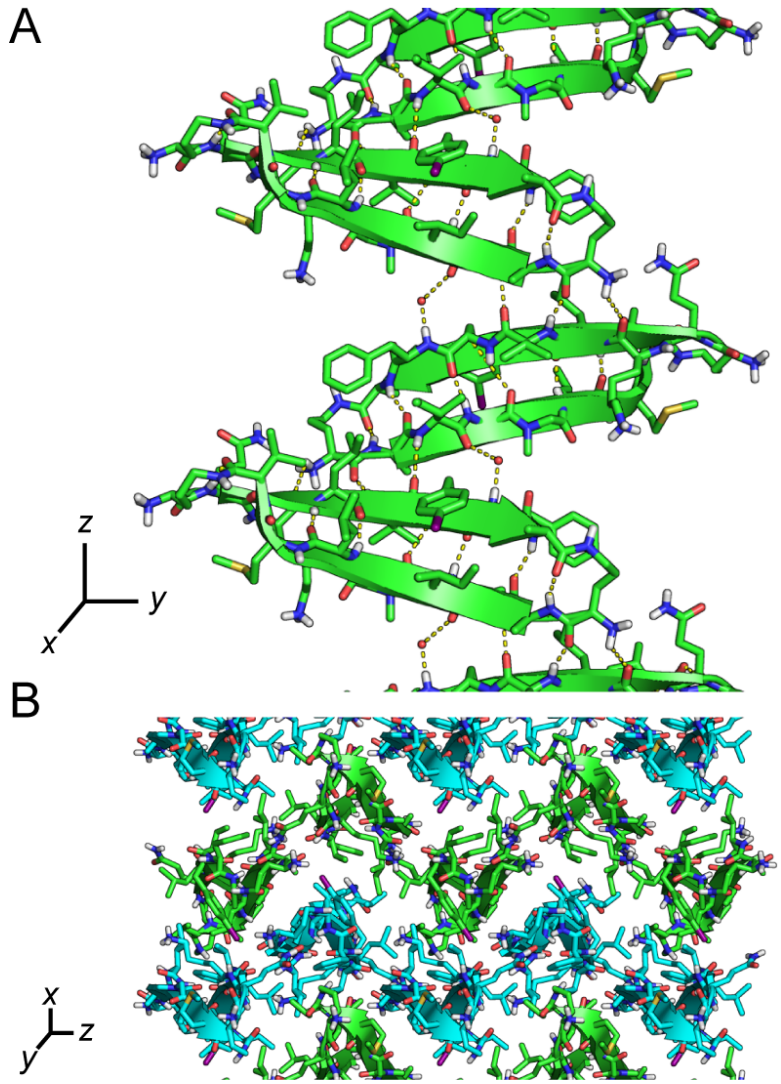

Figure 3.6: Fibril-like assembly formed by peptide **3.4** (PDB 5V64). (A) Top view of the fibril formed by peptide **3.4**. (B) Side view of four layers of fibrils colored to highlight the zig-zag. The image in B is rotated 90° about both the z- and x-axes with respect to the image in A.

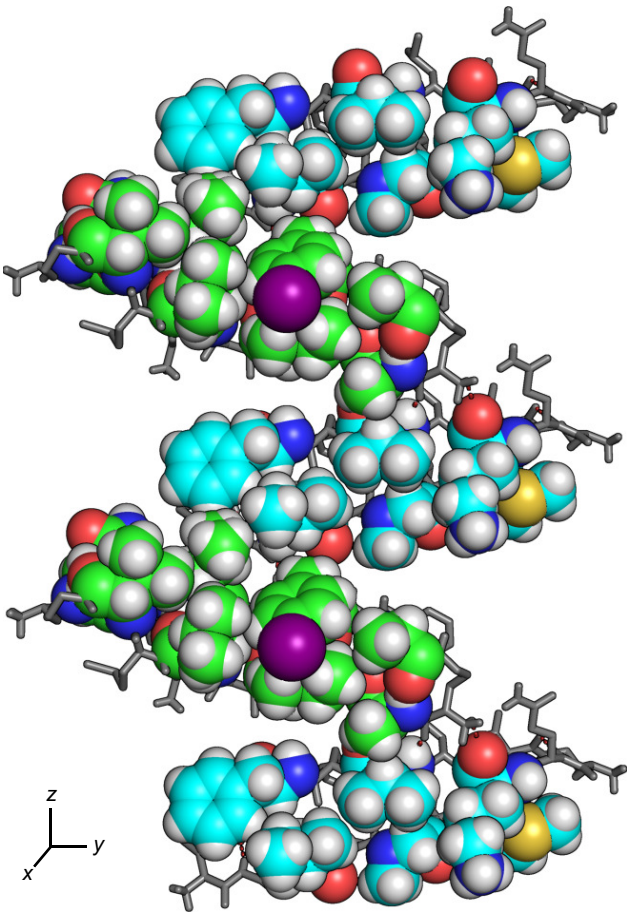

Figure 3.7: Fibril-like assembly formed by peptide **3.4**. Monomer subunits are arranged alternately displaying top (green) and bottom (blue) surfaces of peptide **3.4**.

The fibril-like assemblies formed by peptide **3.4** are not flat; instead they zig-zag in the x-z plane as depicted in Figure 3.6B. The fibrils stack along the x-axis, creating densely packed layers in the x-z plane. The layers run in opposite directions to one another. Within each layer, all of the N-methyl groups point in the same direction. In the green layers in Figures 3.6A and B, the N-methyl groups point in the negative z direction, while in the cyan layers, the N-methyl groups point in the positive z direction (Figure 3.8). The layers pack tightly through hydrophobic interactions, with the top surface of a monomer in one layer packing against the bottom surface of its neighbor in the adjacent layer. This heterofacial packing of residues contrasts the exclusively homofacial packing of residues in the dodecamers formed

by peptides **3.2** and **3.3**. It is not obvious why peptide **3.4** forms fibril-like assemblies in the crystal lattice, instead of the trimers and dodecamers formed by peptides **3.2** and **3.3**.

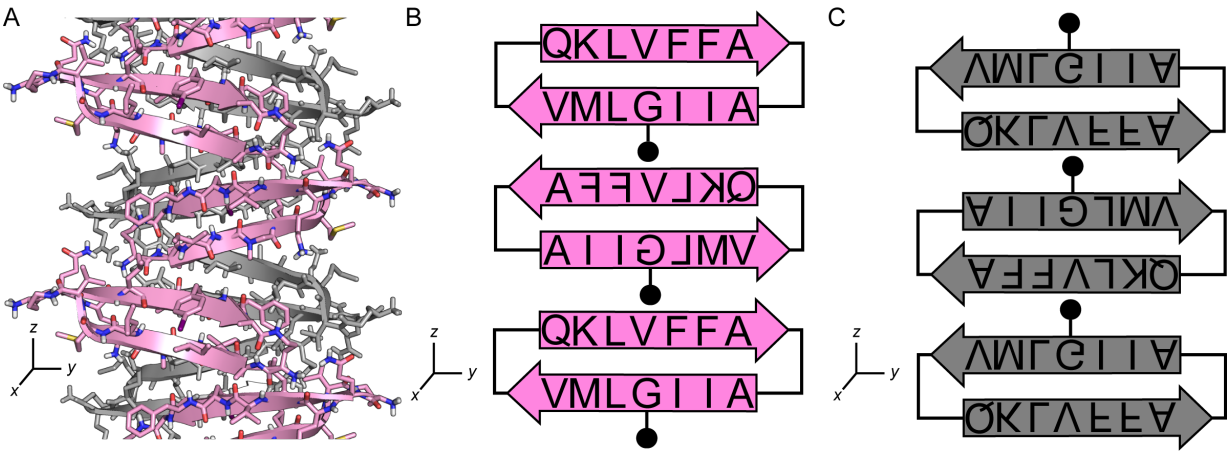

Figure 3.8: Directionality of the fibril-like assembly formed by peptide **4**. (A) Top view of two layers of the fibril-like assembly formed by peptide **4** in the crystal lattice. (B) Cartoon diagram of the pink layer depicted in A. (C) Cartoon diagram of the grey layer depicted in A. The black balls in B and C represent the *N*-methyl groups on Gly_{33}.

The different assemblies of peptides **3.2**–**3.4** reflect the rich and diverse modes of β-hairpin self-assembly and illustrate their propensity to form both fibril-like and oligomeric assemblies. The assembly of β-hairpins into dodecamers comprising triangular trimer subunits offers an alluring high-resolution model for the enigmatic oligomers reported for full-length Aβ. Selkoe et *al.* reported that Aβ trimers inhibit long-term potentiation.[131] Ashe et *al.* reported that putative dodecamers of Aβ, termed Aβ*56, cause memory deficits in a mouse model of Alzheimer's disease.[132] The putative Aβ*56 dodecamers appear to be composed of trimer subunits. The trimers and dodecamers formed by peptides **3.2** and **3.3** provide two models of how Aβ may oligomerize in Alzheimer's disease. The formation of trimeric oligomers is also a common theme of full-length peptides and proteins associated with other amyloid diseases.[69] We have also reported trimeric assemblies and related higher-order oligomers formed by peptides derived from α-synuclein and β_2-microglobulin.[58,63]

3.3 Conclusion

Shifting the residue pairings of the two β-strands within a β-hairpin may dramatically alter the self-assembly. The approach of systematically varying the residue pairings in constrained macrocyclic β-hairpins has revealed a compact ball-shaped dodecamer containing fused trimers and stabilized by an extensive network of hydrogen bonds. The importance of residues 15–36 in the aggregation of full-length Aβ makes peptides **3.2**–**3.4** relevant models for the assembly of full-length Aβ. We envision that full-length Aβ may be able to fold and assemble in a similar fashion. We do not yet understand the relationship between the sequence of a β-hairpin and its mode of assembly. This gap in understanding represents an exciting frontier in supramolecular assembly.

3.4 Materials and Methods

3.4.1 General information

All chemicals were used as received except where otherwise noted. Methylene chloride was passed through alumina under argon prior to use. Anhydrous, amine free dimethylformamide (DMF) was purchased from Alfa Aesar.* All reactions were performed at ambient temperature (*ca.* 20 °C), unless otherwise noted. Peptide synthesis was performed on a Protein Technologies PS3 synthesizer. Analytical reverse-phase HPLC was performed on an Agilent 1200 equipped with a Aeris PEPTIDE 2.6u XB-C18 column (Phenomonex). Preparative reverse-phase HPLC was performed on a Beckman Gold Series P equipped with a ZORBAX SB-C18 column (Agilent). HPLC grade acetonitrile and 18 MΩ deionized water, each containing 0.1% trifluoroacetic acid, were used for analytical and preparative reverse-phase

*In our hands, lesser quality DMF dramatically impacts yields

HPLC. All peptides were prepared and used as the trifluoroacetate salts and were assumed to have a molecule of trifluoroacetic acid (TFA) per ammonium group present in each peptide.

The synthesis of peptides **3.2**–**3.4** were performed using techniques previously described by our laboratory.[56–58,63]

3.4.2 X-ray crystallography

X-ray crystallographic studies of peptide **3.2**–**3.4** were performed using the protocols previously published by our laboratory.[63] We found that sonication of peptide **3.2** in a bath sonicator for 2 h was necessary to solubilize peptide **3.2** prior to crystal growth. Table 3.1 summarizes the crystallization, data collection, data processing and refinement statistics for peptides **3.2**–**3.4**.

Table 3.1: Crystallographic properties, crystallization conditions, and data collection and model refinement statistics for peptides **3.2**, **3.3** and **3.4**

peptide	**3.2**	**3.3**	**3.4**
PDB ID	5V65	5V63	5V64
space group	R3:H	F23	$P2_12_12$
a, *b*. *c* (Å)	67.1, 67.1, 169.6	55.01, 55.01, 55.01	20.35, 22.03, 31.60
α, β, γ (^{o})	90, 90, 120	90, 90, 90	90, 90, 90
peptide per asymmetric unit	16	1	1
crystallization conditions	0.1 M HEPES pH 6 24% jeffamine	0.1 M HEPES pH 7.0 0.2 M $MgCl_2$ 28% isopropanol	0.1 M NaCitrate pH 5.25 24% PEG 4000 23% isopropanol
Data Collection[a]			
wavelength (Å)	1.54	1.54	1.54
resolution (Å)	33.86–2.52 (2.61–2.52)	19.45–2.091 (2.166–2.091)	18.07–2.023 (2.095–2.023)
total reflections	39933(2366)	12665 (1140)	4390 (932)
unique reflections	9726 (1019)	3062 (330)	1049 (272)
multiplicity	4.1 (2.3)	4.1 (3.5)	4.2 (2.3)
completeness (%)	98.8 (92.3)	94.7 (95.1)	98.0 (93.7)
mean I/σ	14.4 (5.4)	13.8 (5.6)	13.7 (8.0)
R_{merge}	0.05 (0.11)	0.03 (0.08)	0.07 (0.15)
$R_{measure}$	0.06	0.04	0.09
$CC_{1/2}$	0.996 (0.960)	0.997 (0.908)	0.994 (0.977)
CC*	0.945 (0.856)	1 (0.993)	0.998 (0.982)
Refinement			
R_{work}	23.4	27.9	17.0
R_{free}	29.8	28.6	24.8
number of non-hydrogen atoms	2070	140	151
number of non-peptide atoms	70	6	24
RMS_{bonds}	0.025	0.005	0.018
RMS_{angles}	1.18	0.77	3.93
Ramachandran favored (%)	100	100	100
outliers (%)	0	0	0
clashscore	1.05	3.75	0
average B-factor	40.53	23.28	20.5

[a]Values for the highest resolution shell are show in parentheses.

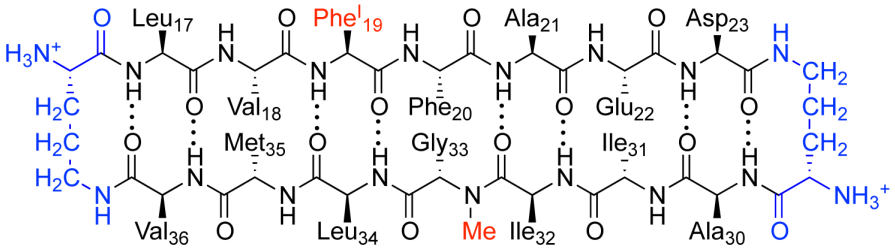

peptide **3.2**

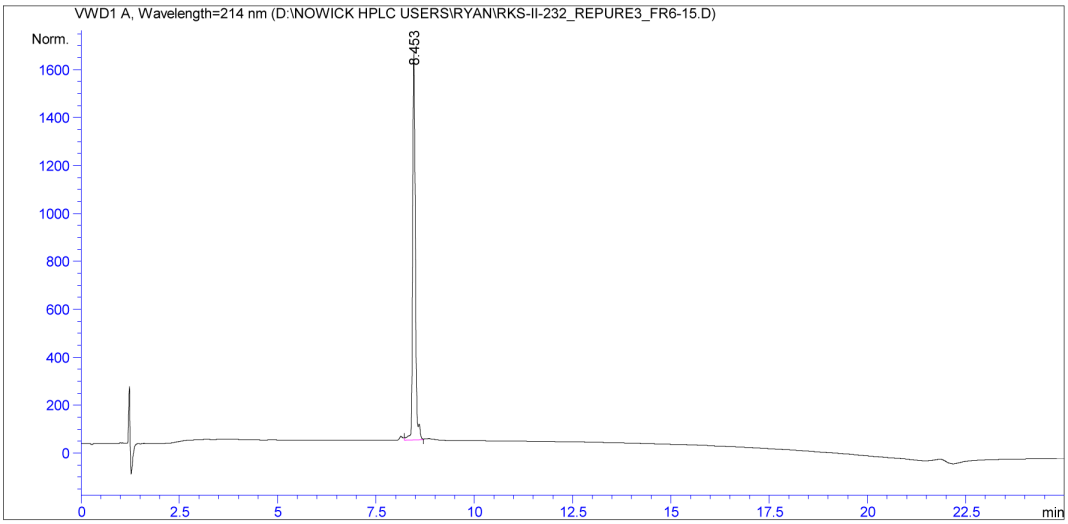

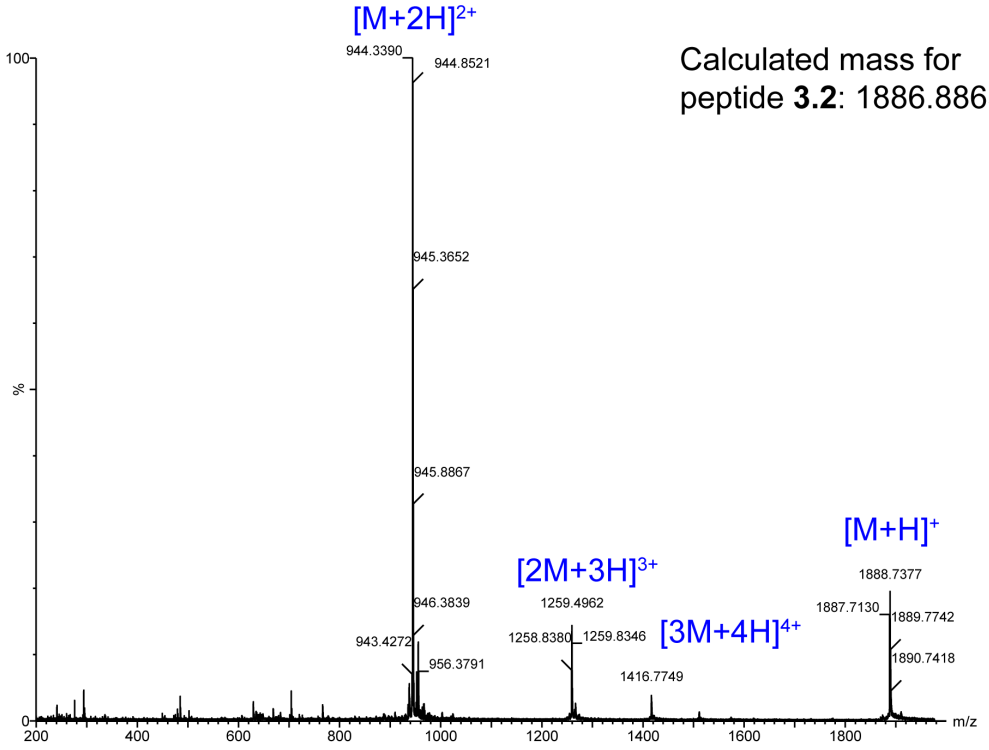

Calculated mass for peptide **3.2**: 1886.8865

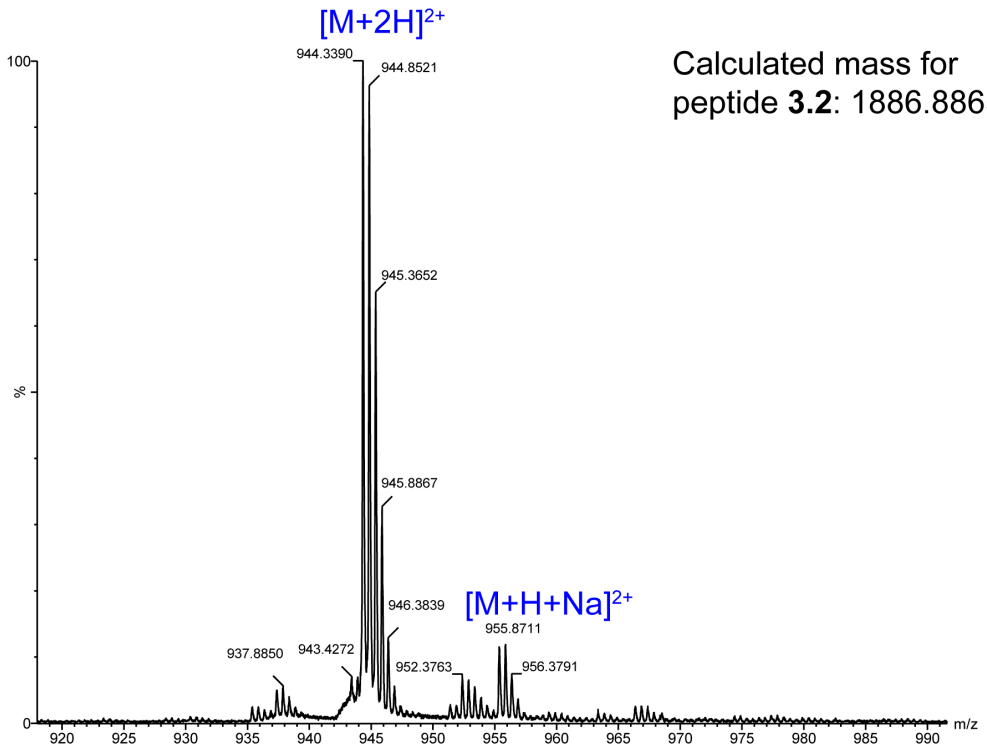

Calculated mass for peptide **3.2**: 1886.8865

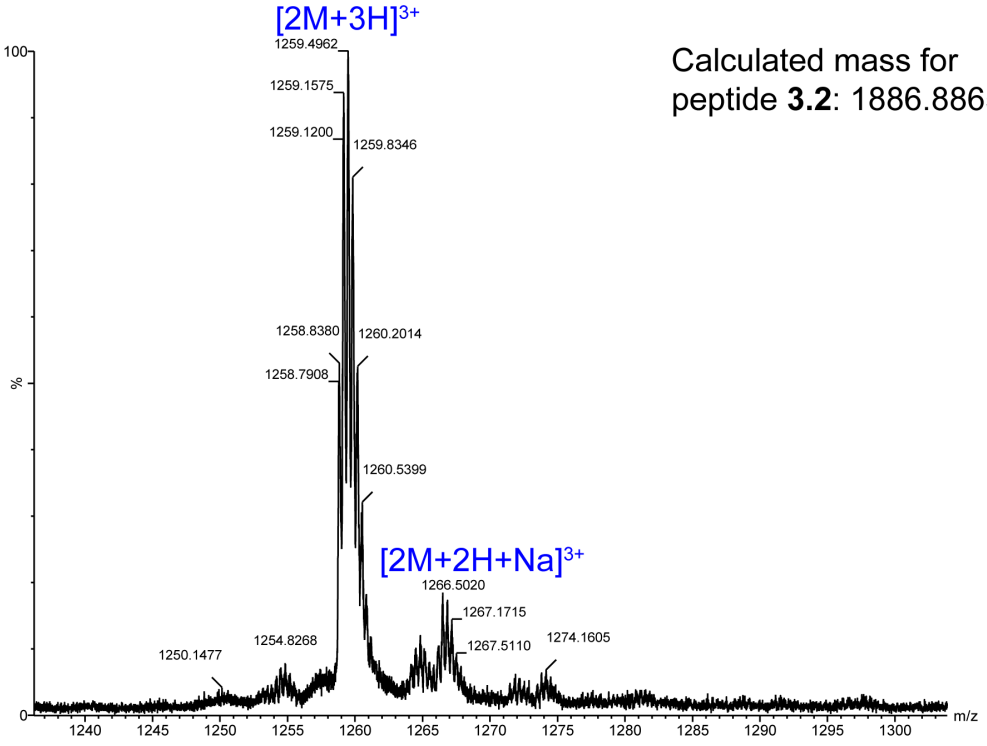

Calculated mass for peptide **3.2**: 1886.8865

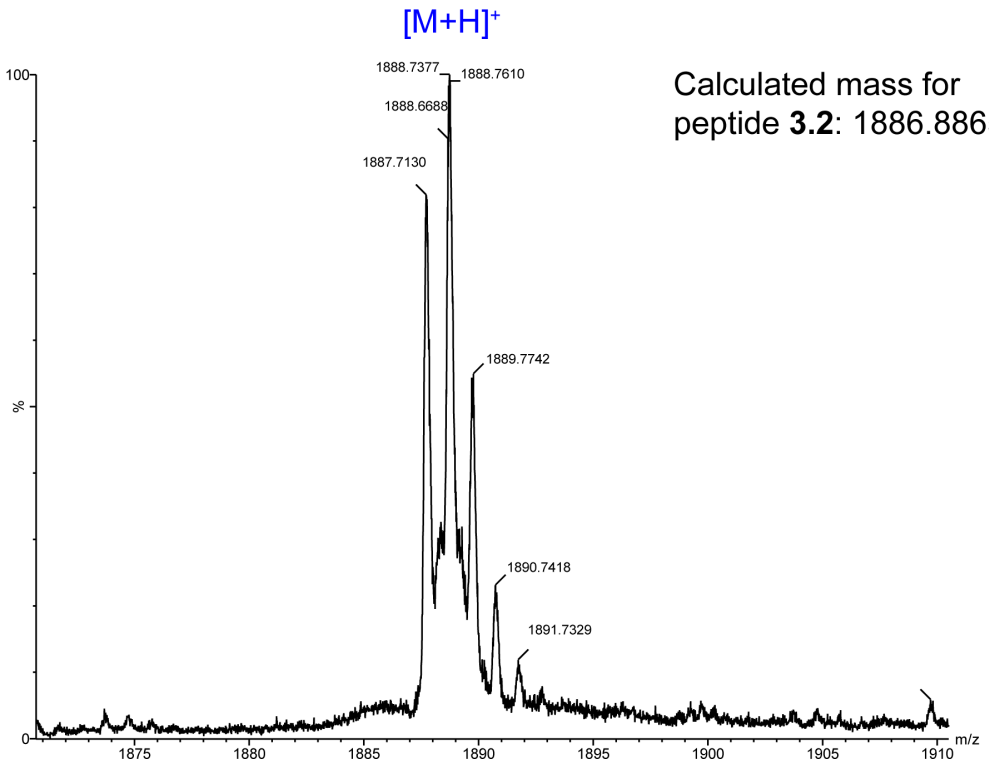

Calculated mass for peptide **3.2**: 1886.8865

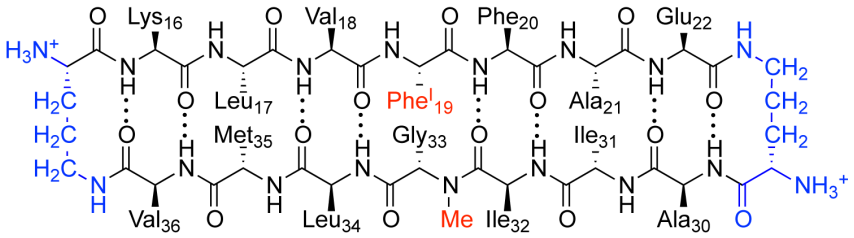

peptide **3.3**

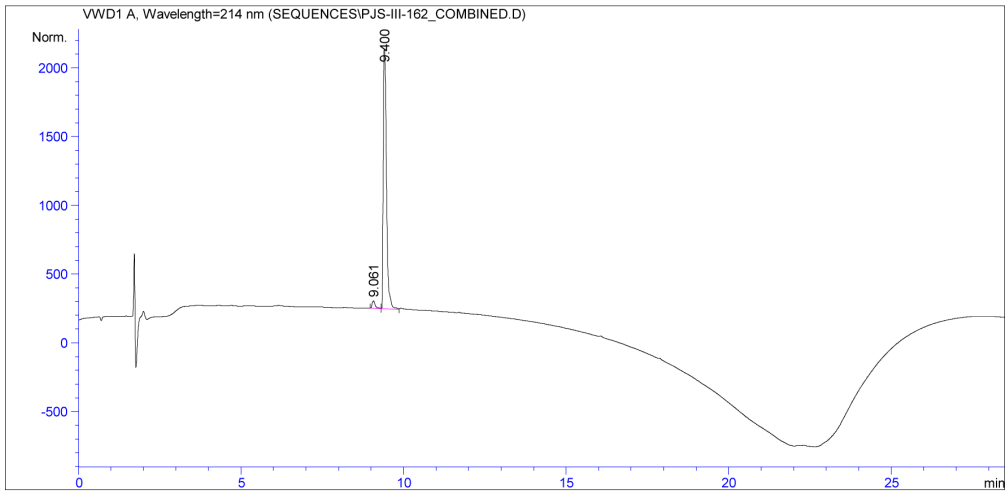

Peak #	RetTime [min]	Type	Width [min]	Area mAU *s	Height [mAU]	Area %
1	9.061	VV	0.1070	378.61429	54.64420	2.8334
2	9.400	VV	0.1062	1.29840e4	1892.65271	97.1666

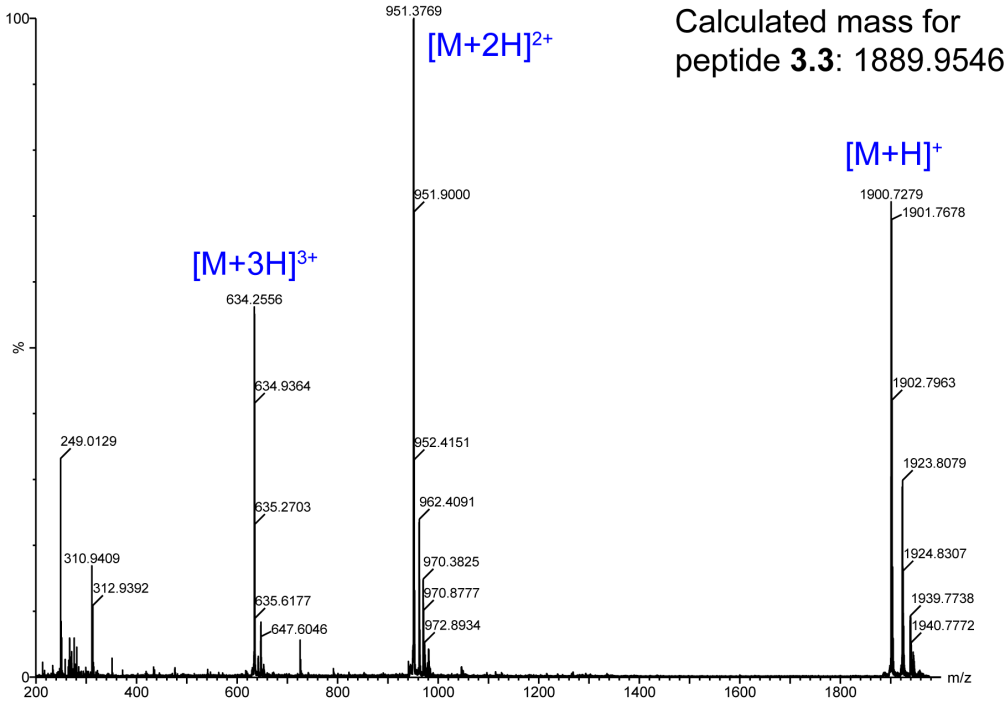

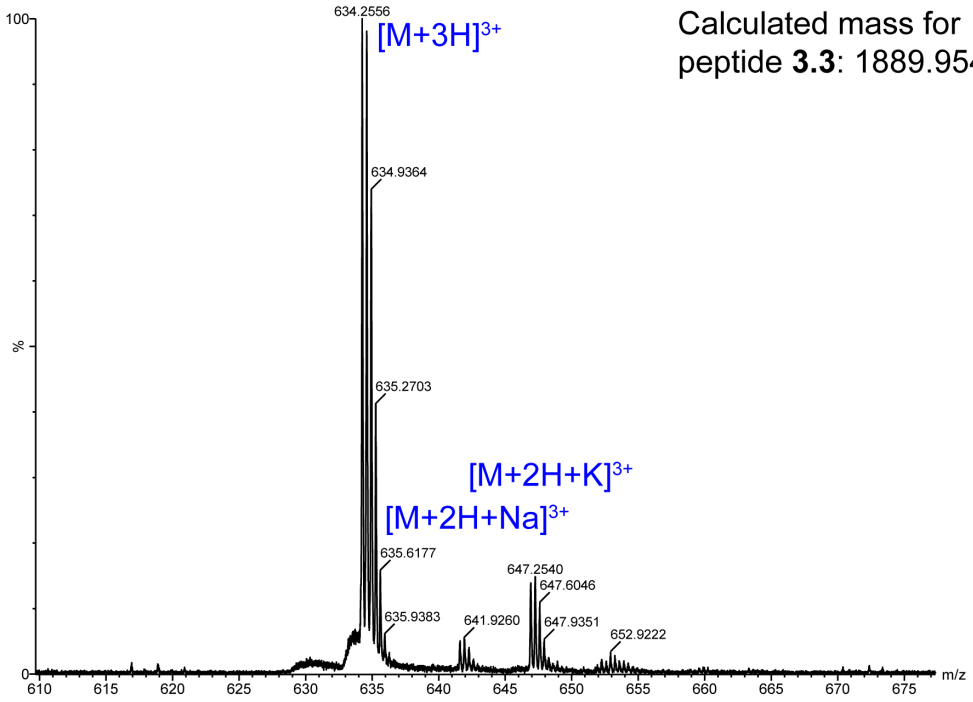

Calculated mass for peptide **3.3**: 1889.9546

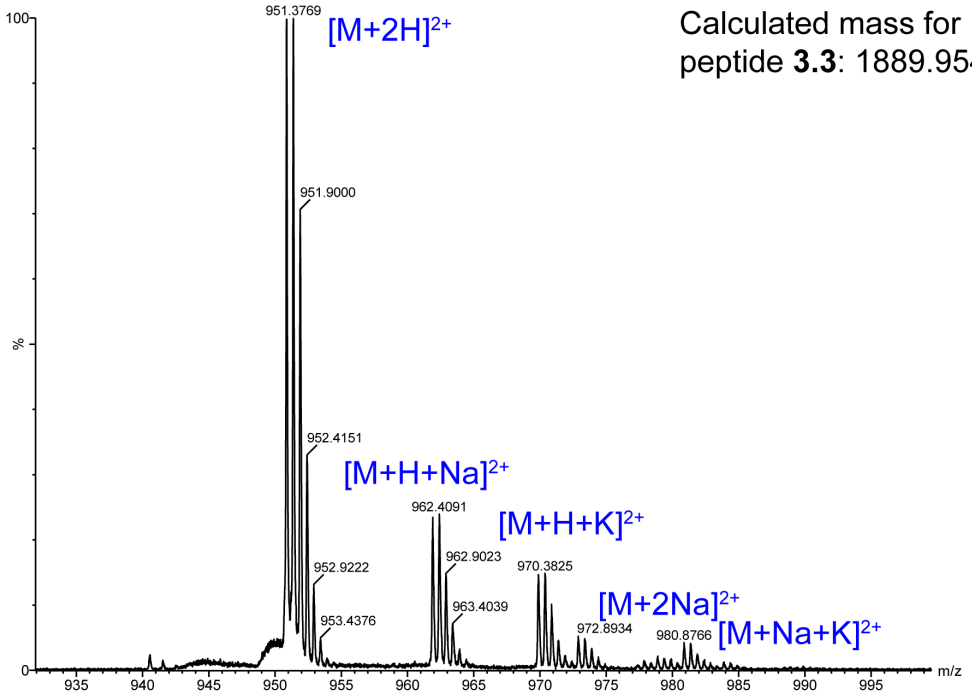

Calculated mass for peptide **3.3**: 1889.9546

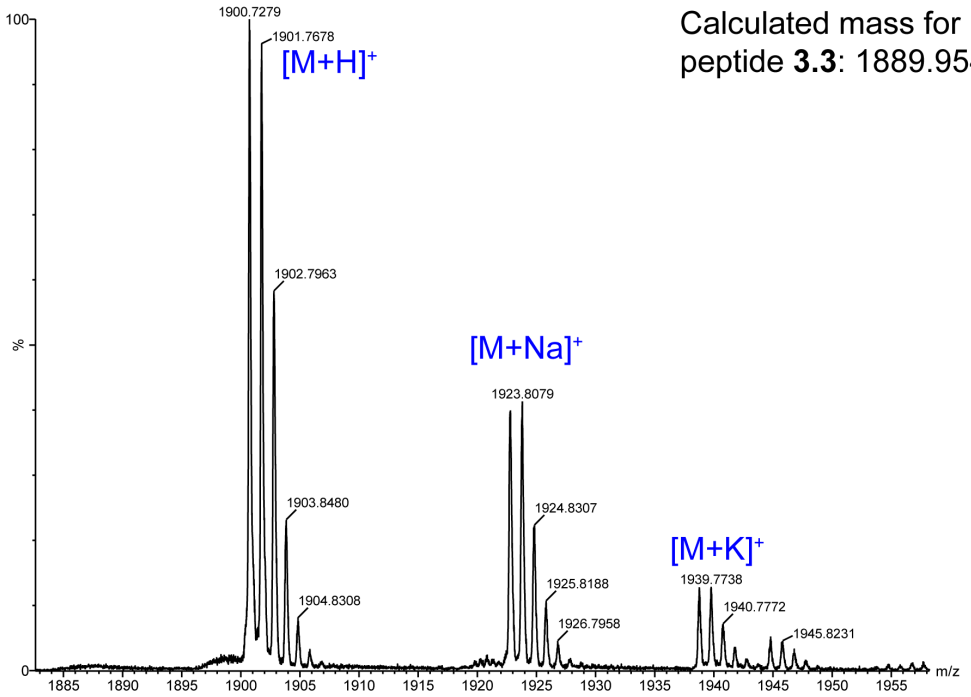

Calculated mass for peptide **3.3**: 1889.9546

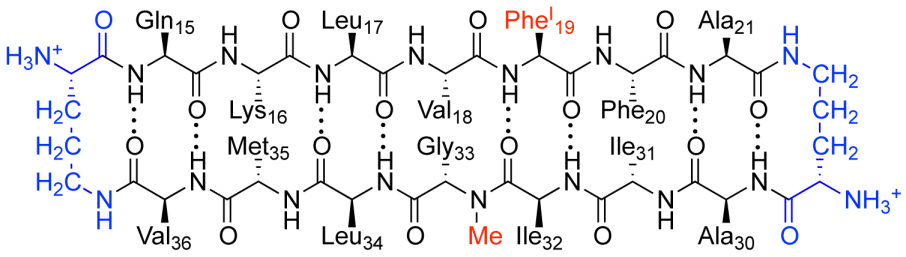

peptide **3.4**

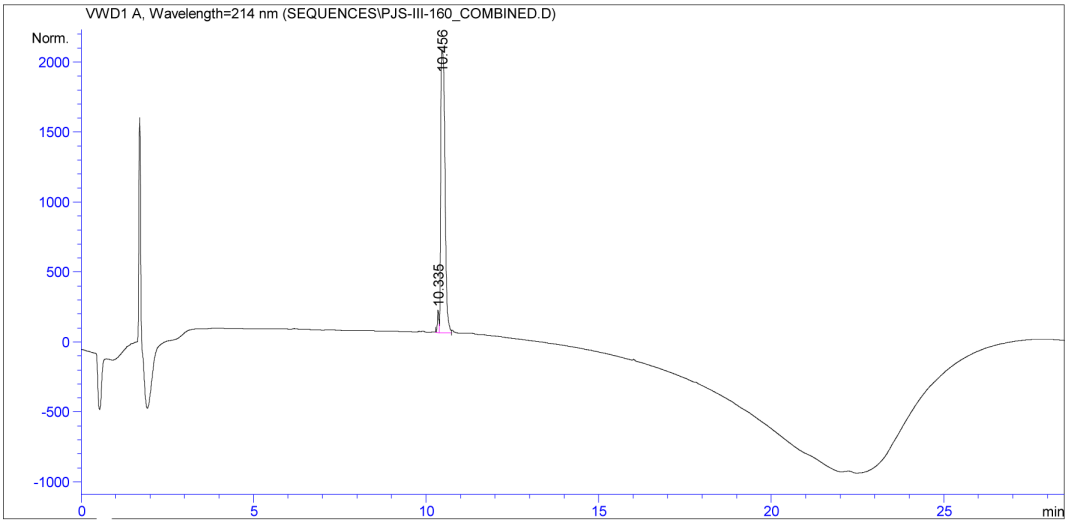

Peak #	RetTime [min]	Type	Width [min]	Area mAU *s	Height [mAU]	Area %
1	10.335	VV	0.0465	466.45056	156.11461	2.6690
2	10.456	VV	0.1363	1.70100e4	2015.18176	97.3310

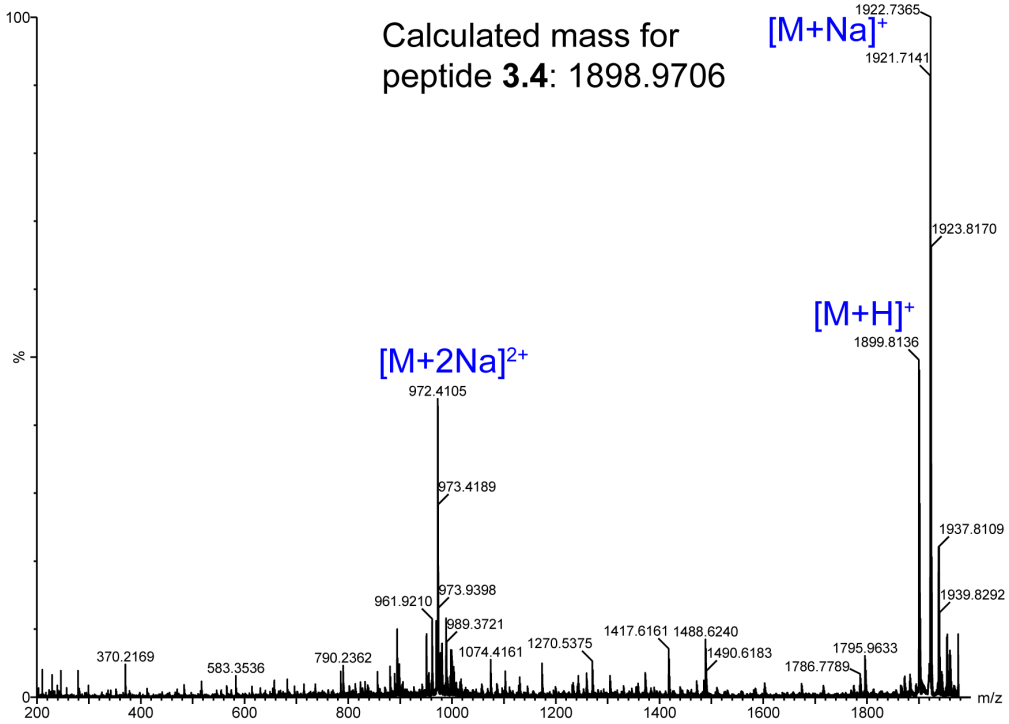

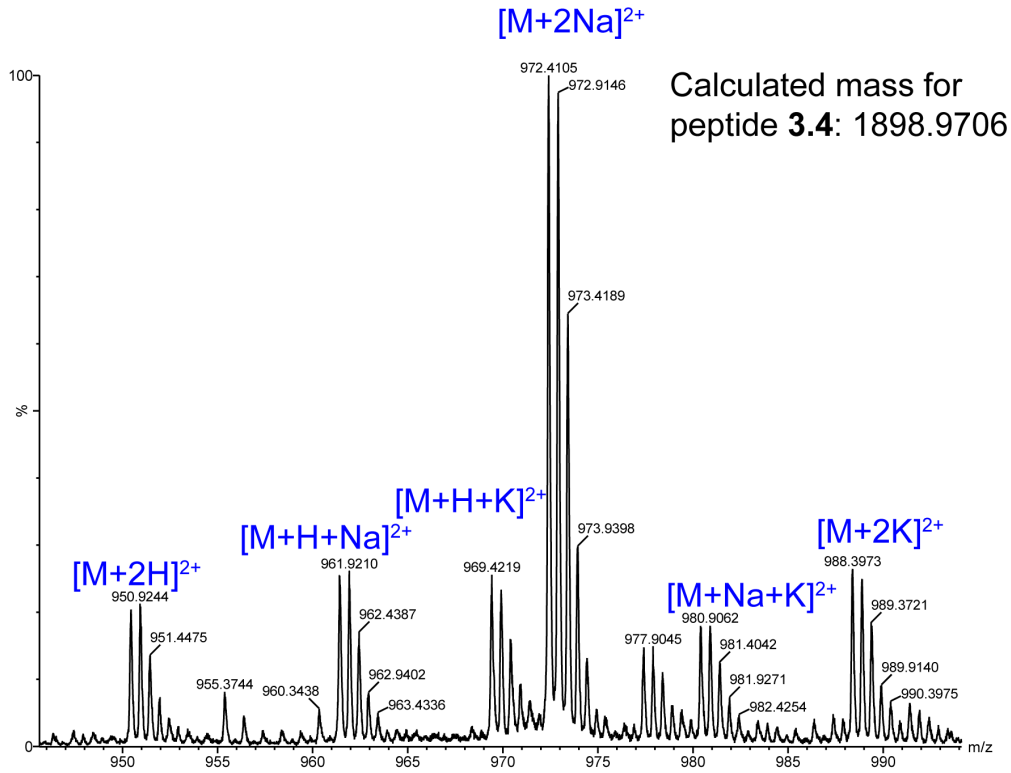
[M+2Na]2+
Calculated mass for peptide 3.4: 1898.9706
[M+2H]2+
[M+H+Na]2+
[M+H+K]2+
[M+Na+K]2+
[M+2K]2+
950.9244
951.4475
955.3744
960.3438
961.9210
962.4387
962.9402
963.4336
969.4219
972.4105
972.9146
973.4189
973.9398
977.9045
980.9062
981.4042
981.9271
982.4254
988.3973
989.3721
989.9140
990.3975
%
m/z

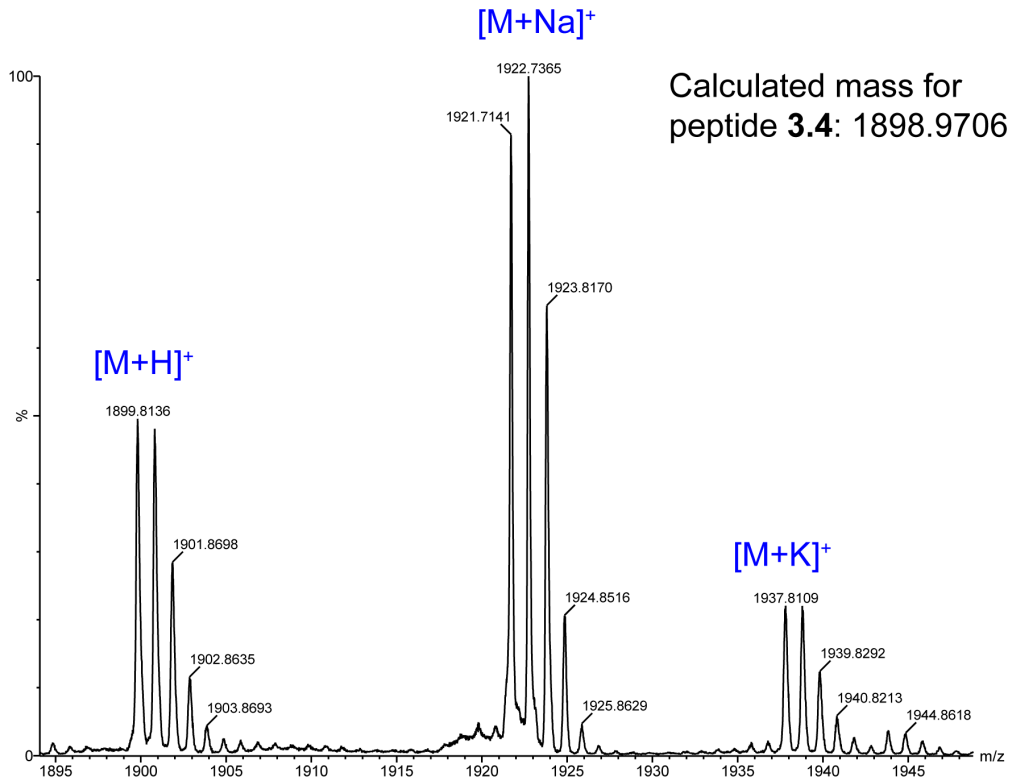
[M+Na]+
Calculated mass for peptide 3.4: 1898.9706
[M+H]+
[M+K]+
1899.8136
1901.8698
1902.8635
1903.8693
1921.7141
1922.7365
1923.8170
1924.8516
1925.8629
1937.8109
1939.8292
1940.8213
1944.8618
%
m/z

Chapter 4

Controlling the oligomerization state of Aβ-derived peptides with light

4.1 Introduction

Photolabile protecting groups have enabled the control of myriad biological properties by allowing the release of biologically active molecules at precise times and locations.[133–136] These protecting groups have revealed hitherto unknown biology through the precise control afforded by light. Photocaged neurotransmitters have enabled the selective activation of signaling pathways in subpopulations of neurons.[137–139] The control gained using photolabile protecting groups has been leveraged in other applications, including protein dimerization, immune cell activation, transcription, and hydrogel formation.[41,140–150] Expanding the control afforded by photolabile protecting groups to oligomers of Aβ may help dissect the biological properties of these enigmatic species associated with Alzheimer's disease.

Soluble oligomers of Aβ are closely associated with neurodegeneration in Alzheimer's disease. The oligomers are heterogeneous and polymorphic, ranging in size from dimers,

trimers, and dodecamers to large annular protofibrils weighing 100–150 kDa.[151] The large Aβ oligomers are thought to comprise multiple copies of smaller oligomers, further complicating the Aβ oligomer landscape. A putative Aβ dodecamer, termed Aβ*56, is thought to comprise multiple trimeric subunits of Aβ.[132] Annular protofibrils have been proposed to comprise multiple hexameric assemblies of Aβ.[129] These differently sized Aβ oligomers, prepared or isolated in different fashions, have different biological properties such as cytotoxicity, synaptotoxicity, and membrane permiabilization.[152,153] The structural heterogeneity of Aβ oligomers renders them intractable to high-resolution structural characterization by X-ray crystallography or NMR spectroscopy. Methods that limit the structural heterogeneity of Aβ oligomers enable the dissection of their structures and biological properties. Thus far, studies of photocaged amyloid-forming peptides and proteins have focused on controlling the aggregation and disaggregation of fibrils.[154–157] To our knowledge, photocaged amyloid-forming peptides have not been used to study amyloid oligomers.

Chemical model systems derived from amyloidogenic peptides and proteins are attractive for exploring the ability of photolabile protecting groups to control the formation of amyloid oligomers. Chemical model systems can limit the structural heterogeneity of amyloid oligomers and provide insights into the assemblies and the biology of amyloid-forming proteins, including Aβ.[52,53,57,60–62,64,158] Our research group has developed chemical model systems that provide insights into the structures and assembly of Aβ oligomers.[57,60–62,64] These model systems are based on macrocyclic β-hairpins derived from Aβ. β-Hairpins have emerged as key building blocks of Aβ oligomers.[59,123,126,127,129,159–161] We have crystallized a number of these macrocyclic β-hairpins and elucidated their structures through X-ray crystallography. The X-ray crystallographic structures have revealed a hierarchical assembly of the macrocyclic β-hairpins into oligomers. These structures have led us to propose models in which Aβ folds into β-hairpins that assemble into triangular trimers and related higher-order oligomers.[55,60]

The chemical model systems that our laboratory has developed to study the oligomerization of Aβ-derived peptides contain two heptapeptide β-strands from Aβ connected by two δ-linked ornithine ($^{\delta}$Orn) β-turn mimics.[87] These macrocyclic β-hairpin peptides contain *N*-methyl groups, which limit the uncontrolled aggregation of the hydrophobic peptides.[56] Our laboratory recently reported β-hairpin peptides **4.1** and **4.2**, which are designed to mimic β-hairpins adopted by $A\beta_{17–36}$ and $A\beta_{16–36}$ (Chart 4.1).[57,62] Both peptides **4.1** and **4.2** contain the heptapeptide β-strand $A\beta_{30–36}$. In peptide **4.1**, the $A\beta_{30–36}$ β-strand is juxtaposed with $A\beta_{17–23}$; in peptide **4.2**, the $A\beta_{30–36}$ β-strand is juxtaposed with $A\beta_{16–22}$. Both peptides bear a single *N*-methyl group. The *N*-methyl group is on Gly_{33} in peptide **4.1**, and on Phe_{19} in peptide **4.2**. Peptides **4.1** and **4.2** assemble in different fashions. Peptide **4.1** assembles to form triangular trimers, which further assemble to form ball-shaped dodecamers and sandwich-like hexamers.[57] Peptide **4.2** assembles to form a compact hexamer.[62] Photoprotected homologues of peptides **4.1** and **4.2** may allow their assembly and biological properties to be controlled.

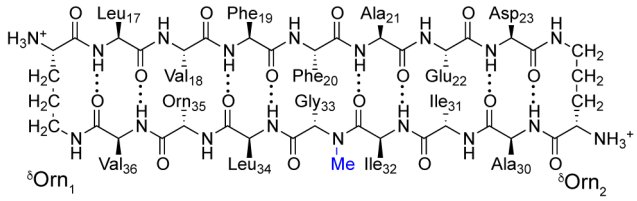

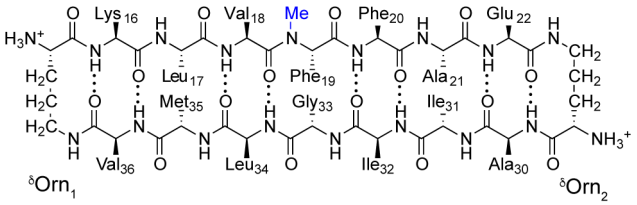

peptide **4.1** cyclo(LVFF AED $^{\delta}$O AIIG$_{Me}$ LOV $^{\delta}$O)
peptide **4.2** cyclo(KLVF$_{Me}$FAE $^{\delta}$O AIIG LMV $^{\delta}$O)

Chart 4.1

In the current paper, we set out to explore the use of light to switch the oligomerization state of β-hairpin peptides derived from Aβ. Our laboratory has previously observed that extensive intermolecular hydrogen-bonding networks stabilize the oligomers formed by both peptides **4.1** and **4.2**. In this study, we hypothesized that photolabile protecting groups installed at locations designed to disrupt these hydrogen-bonding networks would allow the assembly of the peptides to be controlled. We began by determining whether replacing the *N*-methyl group of peptide **4.1** with an *N*-2-nitrobenzyl group would limit aggregation while not altering the assembly into triangular trimers (Figure 4.1A). We then asked if we could apply the *N*-2-nitrobenzyl group to switch on the toxicity of peptide **4.2** by controlling its oligomerization state (Figure 4.1B). Finally, we applied the *N*-2-nitrobenzyl group to trimeric homologues of peptide **4.1**, which assemble to form hexamers or dodecamers depending on the location of the *N*-methyl group (Figure 4.1C). Collectively, these experiments reveal that homologues of peptides **4.1** and **4.2** containing *N*-2-nitrobenzyl groups can readily be prepared and that their photolysis enables the assembly and the biological properties of the peptides to be controlled with light.

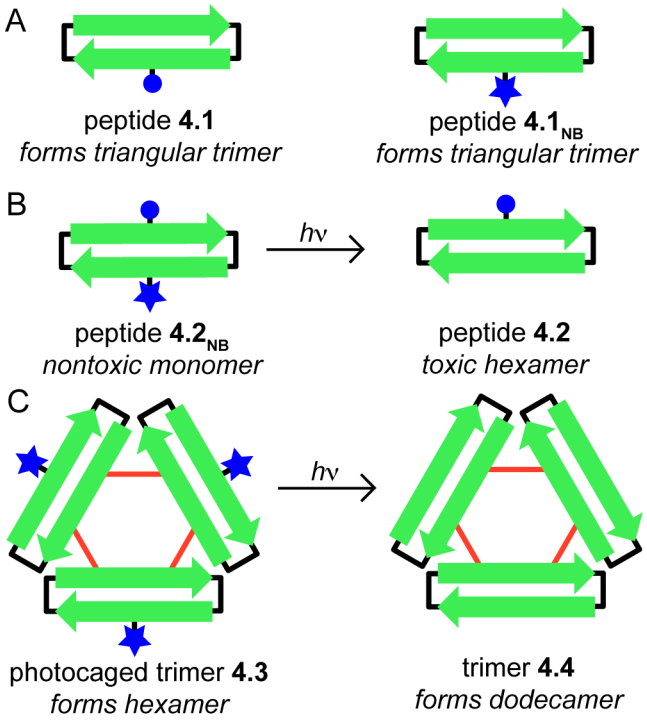

Figure 4.1: Photocaged peptides derived from Aβ. (A) Replacing an *N*-methyl group (blue ball) with an *N*-2-nitrobenzyl group (blue star) does not alter the supramolecular assembly of peptide **4.1**. (B) Adding an *N*-2-nitrobenzyl group to peptide **4.2** allows its assembly and toxicity to be controlled with light. (C) Incorporating *N*-2-nitrobenzyl groups into triangular trimers allows their assembly to be controlled with light.

4.2 Results and Discussion

The following three sections describe and expand upon the experiments outlined in Figure 4.1A, B, and C. In the first set of experiments, we develop a synthetic method to incorporate *N*-2-nitrobenzyl groups into macrocyclic β-hairpin peptides, characterize their assemblies by X-ray crystallography, and demonstrate that we can remove the *N*-2-nitrobenzyl groups with long-wave UV light. In the second set of experiments, we expand on the results from the first set by using the *N*-2-nitrobenzyl group and light to control both the assembly and the biological properties of peptide **4.2**. In the final set of experiments, we expand upon the

findings from the first two sets of experiments, by preparing a covalently crosslinked trimer derived from peptide **4.1$_{NB}$** and altering its assembly with light.

4.1. Developing Macrocyclic β-Hairpin Peptides that Contain an *N*-2-Nitrobenzyl Group. To test whether the *N*-2-nitrobenzyl group would limit uncontrolled assembly of macrocyclic β-hairpin peptides in the same fashion as an *N*-methyl group, we prepared and studied peptide **4.1$_{NB}$**, a homologue of peptide **4.1** (Chart 4.2). We hypothesized that an *N*-2-nitrobenzyl group would be tolerated by the triangular trimer formed by peptide **4.1**, while also limiting the aggregation of the photocaged peptide in the same fashion as an *N*-methyl group (Figure 4.2). We prepared peptide **4.1$_{NB}$** and characterized its assembly by X-ray crystallography to ascertain the effect of replacing the *N*-methyl group with an *N*-2-nitrobenzyl group.

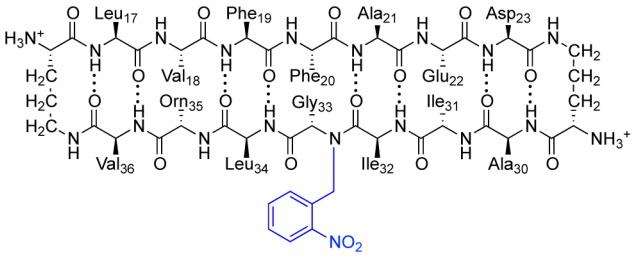

peptide **4.1$_{NB}$**

peptide **4.1**	cyclo(LVF FAED $^{\delta}$O AIIG$_{Me}$LOV $^{\delta}$O)
peptide **4.1$_{NB}$**	cyclo(LVF FAED $^{\delta}$O AIIG$_{NB}$LOV $^{\delta}$O)
peptide **4.1$^{I}_{NB}$**	cyclo(LVF^{I}FAED $^{\delta}$O AIIG$_{NB}$LOV $^{\delta}$O)
peptide **4.1$_{decaged}$**	cyclo(LVF FAED $^{\delta}$O AIIG LOV $^{\delta}$O)

Chart 4.2

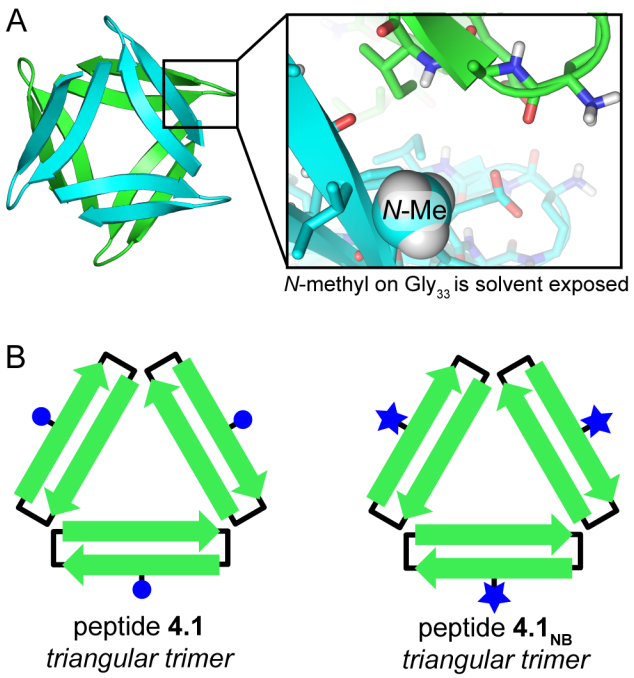

Figure 4.2: Design of a photocaged homologue of peptide **4.1**. (A) X-ray crystallographic structure of the hexamer formed by peptide **4.1** (PDB 4NTR). Inset shows the position of N-methylglycine$_{33}$ within the hexamer. (B) Cartoon of the design of peptide **4.1$_{\mathbf{NB}}$** in which N-2-nitrobenzyl groups replace N-methyl groups.

Synthesis. We synthesized peptide **4.1$_{\mathbf{NB}}$** using solid-phase Fmoc-based peptide synthesis followed by solution-phase macrocyclization. N-2-Nitrobenzylglycine$_{33}$ was not introduced as an Fmoc-protected amino acid, but rather constructed using a submonomer approach, wherein the growing peptide was acylated with bromoacetic acid, and the α-bromo group was then displaced with 2-nitrobenzylamine (Scheme S2).[157,162] Subsequent coupling of Ile$_{32}$ to N-2-nitrobenzylglycine$_{33}$ proved far more difficult than coupling to N-methylglycine$_{33}$ (Figure 4.3). Using HATU and HOAt to activate Fmoc-Ile$_{32}$-OH resulted in multiple products. In contrast, using triphosgene to activate Fmoc-Ile$_{32}$-OH as the acid chloride afforded the Ile$_{32}$-coupled peptide as the single product.[163] Four 1-hour couplings using triphosgene gave 95% conversion to the Ile$_{32}$-coupled product, whereas four 6-hour couplings using HATU and HOAt to activate Fmoc-Ile$_{32}$-OH resulted in little ($< 20\%$) coupling. Triphosgene facilitates this difficult amidation and enables the preparation of 10–30 mg of peptide **4.1$_{\mathbf{NB}}$** from a

0.1-mmol scale synthesis. Approximately 5 mg of each peptide is sufficient to perform the X-ray crystallographic and biological studies described in this chapter. We incorporated 4-iodophenylalanine (Phe^{I}) in place of Phe_{19} in peptide $\mathbf{4.1^{I}_{NB}}$ to facilitate X-ray crystallographic phase determination using single-wavelength anomalous diffraction phasing.[88]

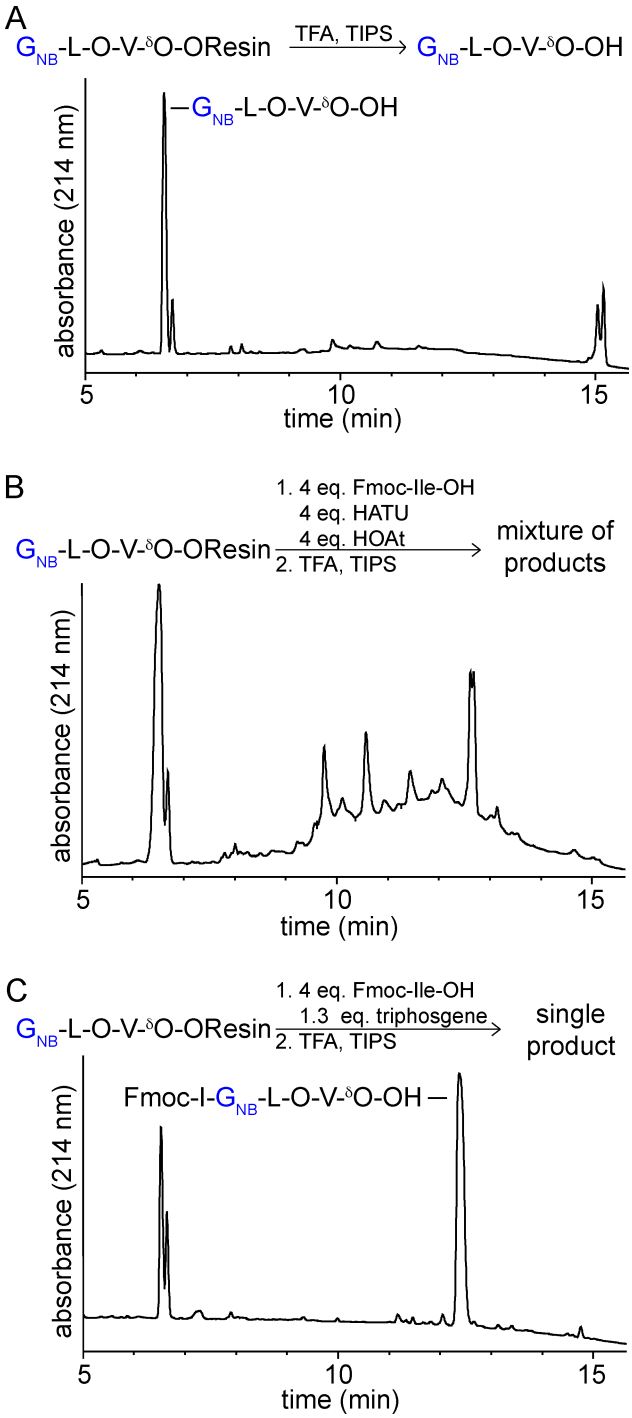

Figure 4.3: Triphosgene enables coupling Fmoc-Ile$_{32}$-OH to *N*-2-nitrobenzylglycine$_{33}$ in solid-phase peptide synthesis. (A) RP-HPLC chromatogram of crude *N*-2-nitrobenzylglycine$_{33}$-Leu$_{34}$-Orn$_{35}$-Val$_{36}$-$^{\delta}$Orn-OH after cleavage from 2-chlorotrityl resin. (B) RP-HPLC chromatogram after coupling with Fmoc-Ile-OH, HATU, and HOAt and cleavage from 2-chlorotrityl resin. (C) RP-HPLC chromatogram after coupling with Fmoc-Ile-OH and triphosgene and cleavage from 2-chlorotrityl resin. Both coupling reactions were performed for 1 hour. The peak that elutes at *ca.* 6.5 minutes is *N*-2-nitrobenzylglycine$_{33}$-Leu$_{34}$-Orn$_{35}$-Val$_{36}$-$^{\delta}$Orn-OH. The peak that elutes at *ca.* 12.5 minutes is Fmoc-Ile$_{32}$-*N*-2-nitrobenzylglycine$_{33}$-Leu$_{34}$-Orn$_{35}$-Val$_{36}$-$^{\delta}$Orn-OH

X-ray crystallography. Peptide $\mathbf{4.1^{I}_{NB}}$ crystalizes in similar conditions as peptide **4.1**: 0.1 M HEPES, buffered at pH 8.75, supplemented with 18% (w/v) Jeffamine M-600. Even though peptides **4.1** and $\mathbf{4.1^{I}_{NB}}$ crystalize in similar conditions, the crystals belong to different space groups. Crystals of peptide $\mathbf{4.1^{I}_{NB}}$ belong to space group $P4_232$ and contain a single copy of peptide $\mathbf{4.1^{I}_{NB}}$ in the asymmetric unit, whereas crystals of peptide **4.1** belong to space group R3 and contain sixteen copies of peptide **4.1** in the asymmetric unit (PDB 4NTR). Peptide $\mathbf{4.1_{NB}}$ also grows crystals with identical morphology to those formed by peptide $\mathbf{4.1^{I}_{NB}}$ in these conditions, however, these crystals do not diffract X-rays. We were therefore unable to solve the X-ray crystallographic structure of peptide $\mathbf{4.1_{NB}}$. Diffraction data were collected to 2.03 Å. The structure of peptide $\mathbf{4.1^{I}_{NB}}$ was solved and refined in space group $P4_232$. The asymmetric unit contains a single copy of peptide $\mathbf{4.1^{I}_{NB}}$, on which the *N*-2-nitrobenzyl group is clearly visible in the electron density map, folded into a β-hairpin (Figures 4.4 and 4.5A). Table 4.1 summarizes the crystallographic properties, crystallization conditions, data collection, and model refinement statistics for peptide $\mathbf{4.1^{I}_{NB}}$.

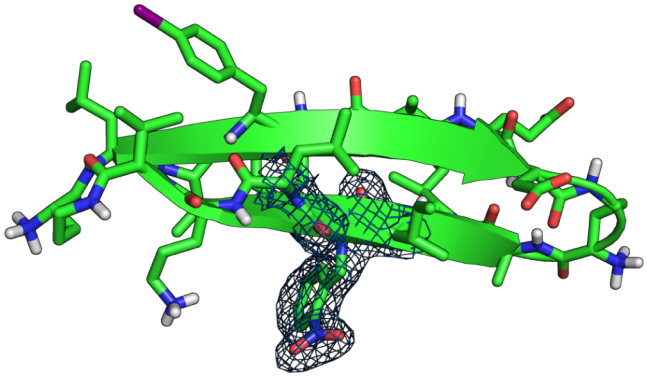

Figure 4.4: The *N*-2-nitrobenzyl group on peptide $\mathbf{4.1^{I}_{NB}}$ is clearly visible in the electron density map. The 2Fo-Fc electron density map is contoured at 1.0 σ.

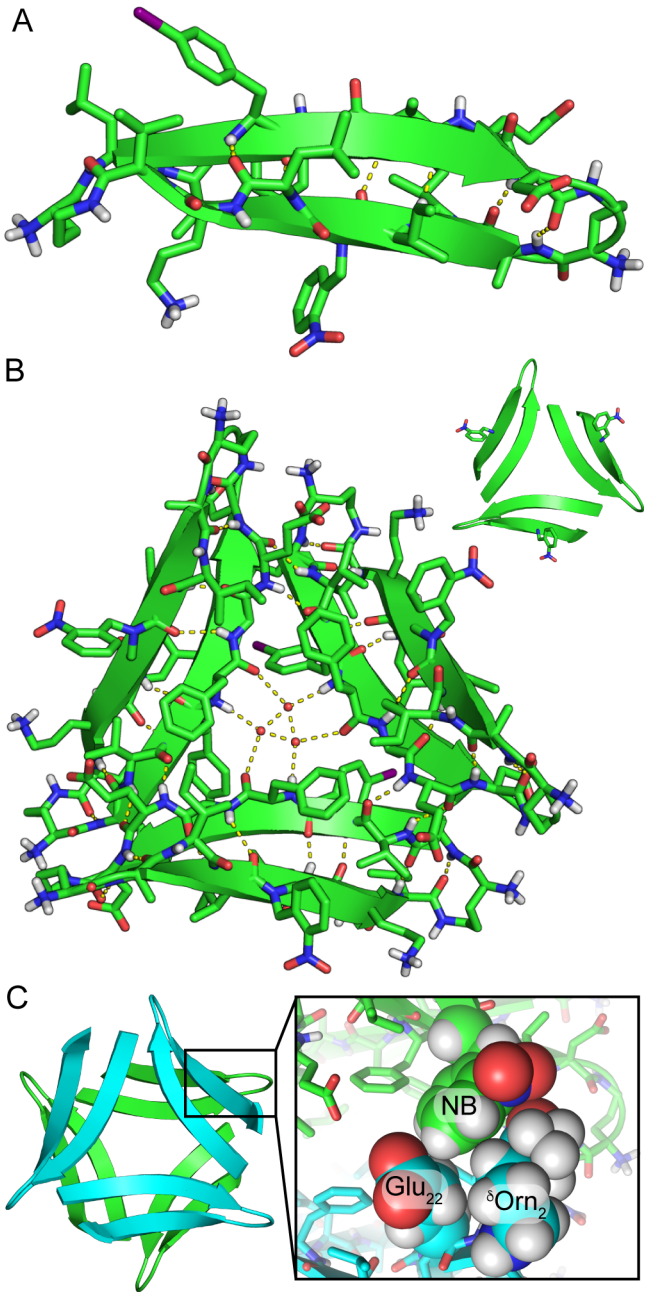

Figure 4.5: X-ray crystallographic structure of peptide $\mathbf{4.1^{I}_{NB}}$ (PDB 6CG3). (A) The asymmetric unit contains a single, folded copy of peptide $\mathbf{4.1^{I}_{NB}}$. (B) Triangular trimer formed by peptide $\mathbf{4.1^{I}_{NB}}$. In the inset, the *N*-2-nitrobenzyl groups are shown as sticks. (C) Hexamer formed by peptide $\mathbf{4.1^{I}_{NB}}$ in the crystal lattice. Inset shows the inter-trimer contacts that the *N*-2-nitrobenzyl group (abbreviated NB) makes within the hexamer.

Peptide $\mathbf{4.1^{I}_{NB}}$ assembles in an identical fashion to peptide **4.1** and several related homologues that our laboratory has previously reported.[57,60,64] The single copy of peptide $\mathbf{4.1^{I}_{NB}}$

within the asymmetric unit is folded into a β-hairpin; three copies of peptide **4.1$^{\mathbf{I}}_{\mathbf{NB}}$** occupy the edges of an equilateral triangle (Figure 4.5B); four copies of this trimer assemble in a tetrahedral fashion to form a ball-shaped dodecamer (Figure 4.6); the interface between dodecamers constitutes a sandwich-like hexamer (Figure 4.5C). The lattice readily accommodates the *N*-2-nitrobenzyl group without substantial changes in structure or assembly, with the *N*-2-nitrobenzyl group from one trimer packing against the side chains of $^{\delta}\text{Orn}_2$ and Glu_{22} from a separate trimer within the sandwich-like hexamer. Thus, the *N*-2-nitrobenzyl group does not prevent peptide **4.1$^{\mathbf{I}}_{\mathbf{NB}}$** from forming triangular trimers and related higher-order oligomers.

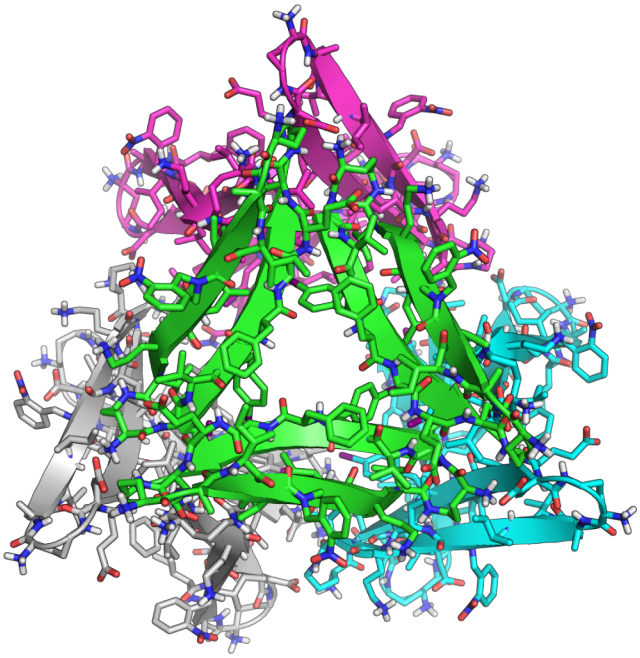

Figure 4.6: Ball-shaped dodecamer formed by peptide **4.1$^{\mathbf{I}}_{\mathbf{NB}}$** in the crystal lattice (PDB 6CG3). The four trimer subunits are colored green, magenta, cyan, and grey.

The assembly of peptide **4.1$^{\mathbf{I}}_{\mathbf{NB}}$** into trimers, hexamers, and dodecamers highlights the proclivity of $\text{A}\beta_{17–36}$ to form triangular trimers when it is constrained into a β-hairpin. Replacing the *N*-methyl group in peptide **4.1** with an *N*-2-nitrobenzyl group does not alter the assembly of the peptide. Our research group has previously observed that a homologue of peptide **4.1** containing the $\text{A}\beta_{24–29}$ loop also assembles into trimers, hexamers, and dodecamers.[60]

Thus, the triangular trimer tolerates substantial modifications and the incorporation of additional residues from Aβ. The formation of triangular trimers appears to be an innate property of β-hairpins encompassing $A\beta_{17–36}$.

Photodecaging. We evaluated the photolysis of peptide $\mathbf{4.1_{NB}}$ using a hand-held long-wave (365 nm) UV lamp. We monitored the photolysis of a 2 mg/mL solution of peptide $\mathbf{4.1_{NB}}$ in a 1 cm quartz cuvette by both RP-HPLC and mass spectrometry (Figure 4.7). Under these conditions, the decaging appears to follow first-order kinetics, reaching approximately 50% completion in 10 minutes. Irradiation of peptide $\mathbf{4.1_{NB}}$ for 1 hour results in the complete photolysis of the *N*-2-nitrobenzyl group. In these studies, we found that the 2-nitrosobenzaldehyde by-product reacts with amine groups of peptide $\mathbf{4.1_{NB}}$. Addition of cysteine to scavenge this by-product eliminates this side reaction.[163]

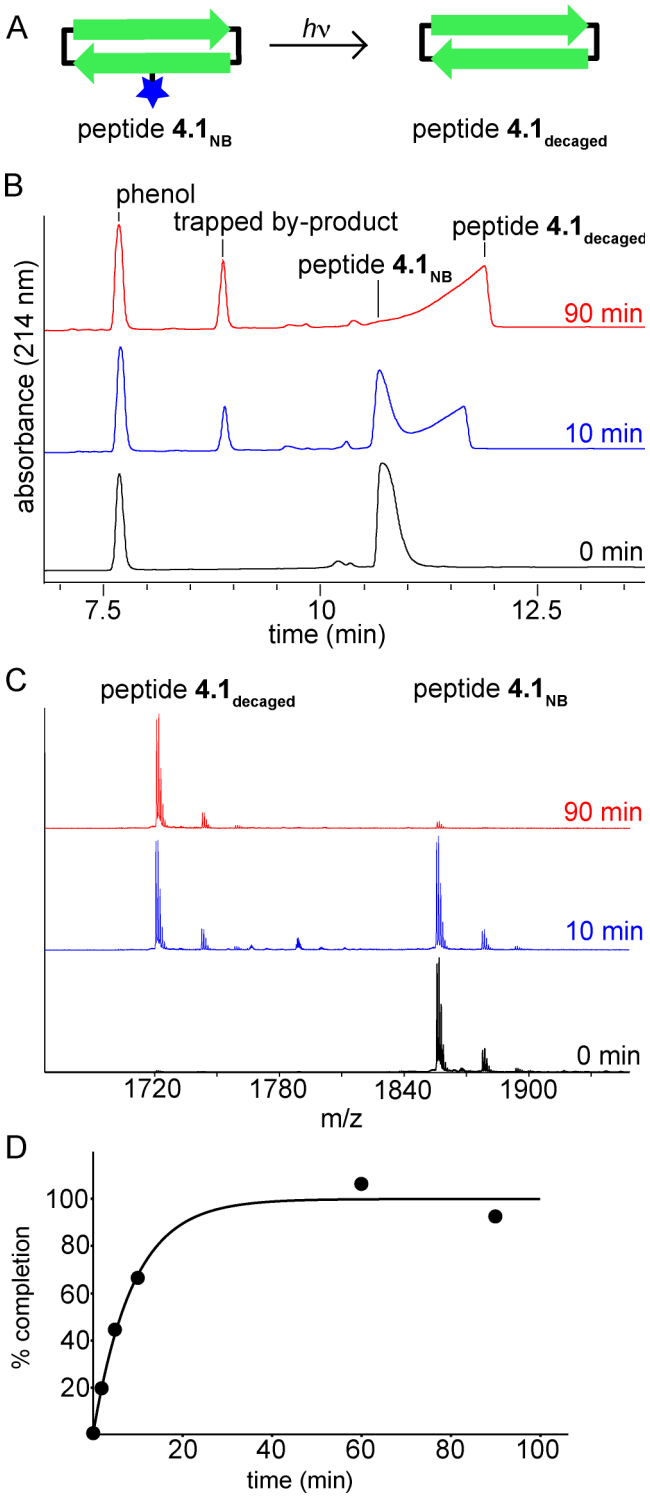

Figure 4.7: Photolysis of the *N*-2-nitrobenzyl group with long-wave UV light. (A) Cartoon representation of the photolysis reaction. (B) RP-HPLC chromatograms illustrating the progress of the photolysis reaction. (C) ESI-MS illustrating the progress of the photolysis reaction. (D) Progress of the photolysis reaction monitored by RP-HPLC. The line represents a 1st-order kinetics fit of the data.

The synthetic, X-ray crystallographic, and photolytic studies of peptides $\mathbf{4.1_{NB}}$ and $\mathbf{4.1^{I}_{NB}}$ establish that the *N*-2-nitrobenzyl group can readily be incorporated into macrocyclic β-hairpin peptides and that it can be removed with light. These studies set the stage for applying the *N*-2-nitrobenzyl group to control the assembly and the biological properties of other macrocyclic β-hairpins.

4.2. Controlling the Biological Properties of a Macrocyclic β-Hairpin Peptide with Light. We next sought to apply the *N*-2-nitrobenzyl group to control the formation of toxic oligomers of a macrocyclic β-hairpin peptide. Our research group has previously shown that peptide **4.2** is toxic towards the neuroblastoma cell-line SH-SY5Y, and that it assembles to form a hexamer, which is observed crystallographically and in SDS-PAGE.[62] The hexamer cannot accommodate *N*-alkylation of Gly_{33}, which hydrogen bonds with Ile_{31} (Figure 4.8). We hypothesized that replacing Gly_{33} with *N*-2-nitrobenzylglycine would disrupt hydrogen bonding and thus disrupt assembly of the toxic hexamer. Photolysis of the *N*-2-nitrobenzyl group would uncage Gly_{33} and allow the hexamer to assemble, thereby switching on the biological properties of the peptide. We synthesized peptide $\mathbf{4.2_{NB}}$ using the submonomer approach described in the preceding section. We studied its assembly in SDS-PAGE, its cytotoxicity, and its interactions with lipid bilayers to test if the *N*-2-nitrobenzyl group can control both the assembly and the biological properties of a macrocyclic β-hairpin peptide (Chart 4.3).

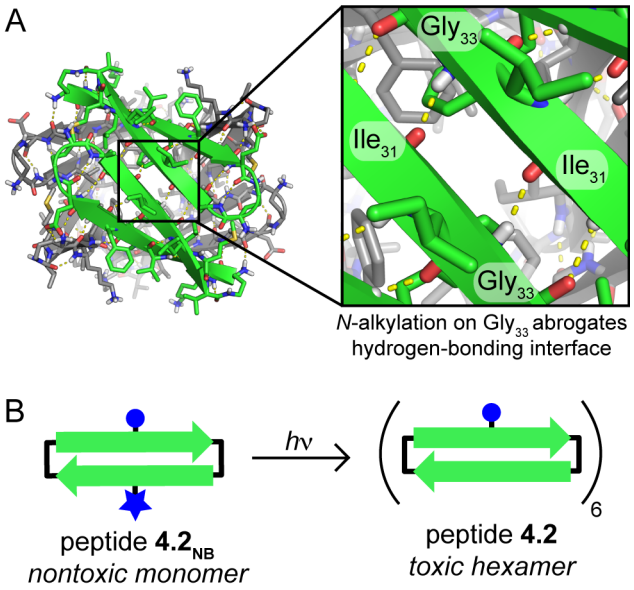

Figure 4.8: Design of peptide **4.2$_{\mathbf{NB}}$**, a photocaged homologue of peptide **4.2**. (A) X-ray crystallographic structure of the hexamer formed by peptide **4.2** (PDB 5W4H). Inset shows the hydrogen-bonding interface between two neighboring monomers in which Gly_{33} hydrogen bonds with Ile_{31}. (B) Cartoon illustrating photolysis and decaging of peptide **4.2$_{\mathbf{NB}}$** to form peptide **4.2**, which assembles into a toxic hexamer.

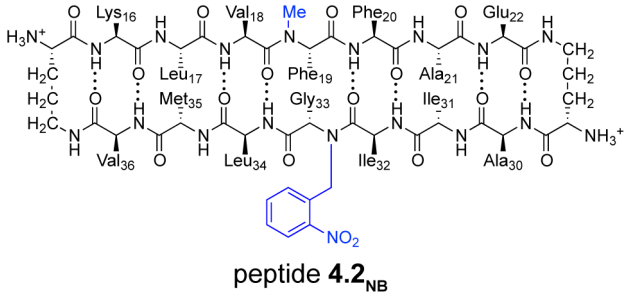

peptide **4.2** cyclo(KLVF_{Me}FAE $^{\delta}$O AIIG LMV $^{\delta}$O)
peptide **4.2$_{\mathbf{NB}}$** cyclo(KLVF_{Me}FAE $^{\delta}$O AIIG_{NB}LMV $^{\delta}$O)
peptide **4.2$_{\mathbf{Me}}$** cyclo(KLVF_{Me}FAE $^{\delta}$O AIIG_{Me}LMV $^{\delta}$O)

Chart 4.3

SDS-PAGE. Unlike peptide **4.2**, peptide **4.2$_{\mathbf{NB}}$** does not assemble to form a hexamer in SDS-PAGE (Figure 4.9). To ascertain the impact of *N*-alkylation of Gly_{33}, we compared the assembly of peptide **4.2** to that of peptide **4.2$_{\mathbf{NB}}$** and peptide **4.2$_{\mathbf{Me}}$**, a homologue bearing an additional *N*-methyl group, on Gly_{33}. In tricine SDS-PAGE, peptide **4.2** migrates with

a similar mobility to the 10 kDa size standard. This mobility is consistent with peptide **4.2** assembling to form a hexamer (10.6 kDa). In contrast, peptides $\mathbf{4.2_{Me}}$ and $\mathbf{4.2_{NB}}$ migrate between the 1.7 and the 4.6 kDa size standards and thus appear to be monomers or dimers. The mobility of peptide $\mathbf{4.2_{NB}}$ shifts after photodecaging with a hand-held UV lamp. The resulting band migrates with a mobility similar to that of peptide **4.2**. Thus, the *N*-2-nitrobenzyl group and its photolysis allows the oligomerization state of peptide **4.2** to be controlled with light.

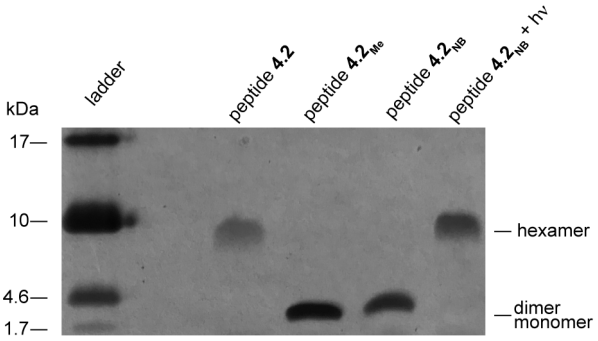

Figure 4.9: An *N*-2-nitrobenzyl group alters the assembly of peptide **4.2**. Silver-stained tricine SDS-PAGE gel. 6 µL aliquots of 0.2 mg/mL solutions of each peptide were loaded into the lanes on the gel.

Cytotoxicity. In addition to altering the assembly of the hexamer, *N*-2-nitrobenzylation alters the biological properties of peptide **4.2**. Peptide $\mathbf{4.2_{NB}}$ is not toxic at concentrations as high as 100 µM as measured by both LDH release and MTT conversion assays against the neuroblastoma cell-line SH-SY5Y (Figure 4.10 and S4). In contrast, peptide **4.2** is toxic at concentrations as low as 50 µM. Irradiating peptide $\mathbf{4.2_{NB}}$ with long-wave UV light switches on the toxicity of the peptide. This toxicity results from the formation of peptide **4.2** and not from the formation of the nitrosobenzaldehyde by-product, as the photolysis of peptide $\mathbf{4.1_{NB}}$ does not result in toxicity.

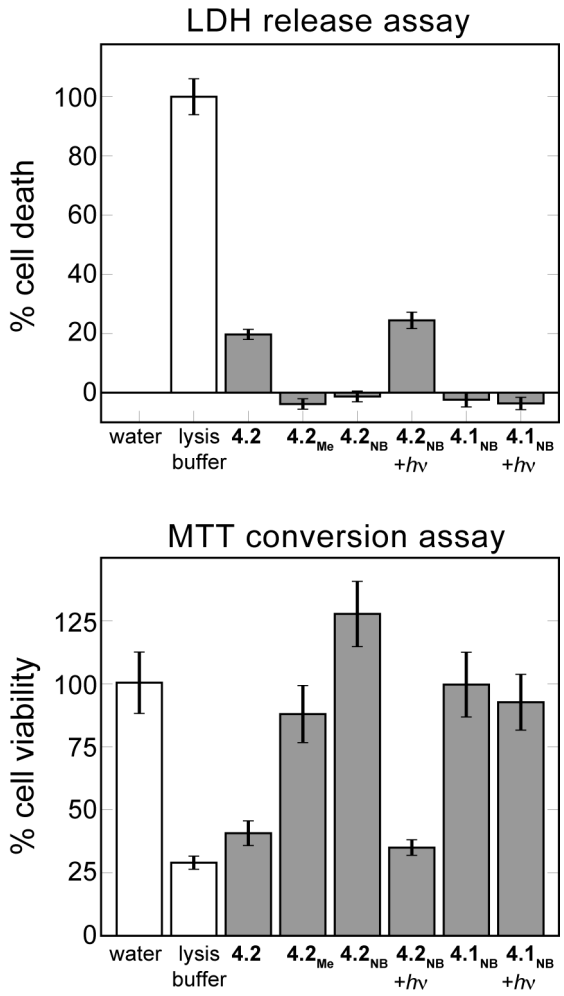

Figure 4.10: An *N*-2-nitrobenzyl group alters the toxicity of peptide **4.2**. LDH release and MTT conversion toxicity assays. SH-SY5Y cells were incubated for 72 hours with 50 µM of the indicated peptide before performing the assay. Error bars represent standard deviations propagated from five replicate runs.

Interactions with liposomes. To evaluate whether the toxicity of peptide **4.2** arrises from its disruption of cell membranes, we studied the effect of peptide **4.2** on liposomes using a dye leakage assay. In this assay, large unilamellar vesicles (LUVs) encapsulating the fluorescent dye calcein were treated with peptide **4.2** and the increase in fluorescence was monitored. Peptide **4.2** induces anionic LUVs to leak their contents (Figure 4.11). Peptide **4.2** induces measurable dye leakage from LUVs composed of a 1:1 mixture of phosphatidylcholine and phosphatidylserine (PC:PS) at concentrations as low as *ca.* 300 nM. Peptide **4.2** induces

50% dye leakage at *ca.* 2 µM. In contrast, peptide **4.2$_{\mathbf{NB}}$** induces comparable leakage at 20 µM. The contrasting activities of peptide **4.2** and peptide **4.2$_{\mathbf{NB}}$** in dye leakage assays indicate that caging peptide **4.2** with the *N*-2-nitrobenzyl group reduces its ability to disrupt membranes.

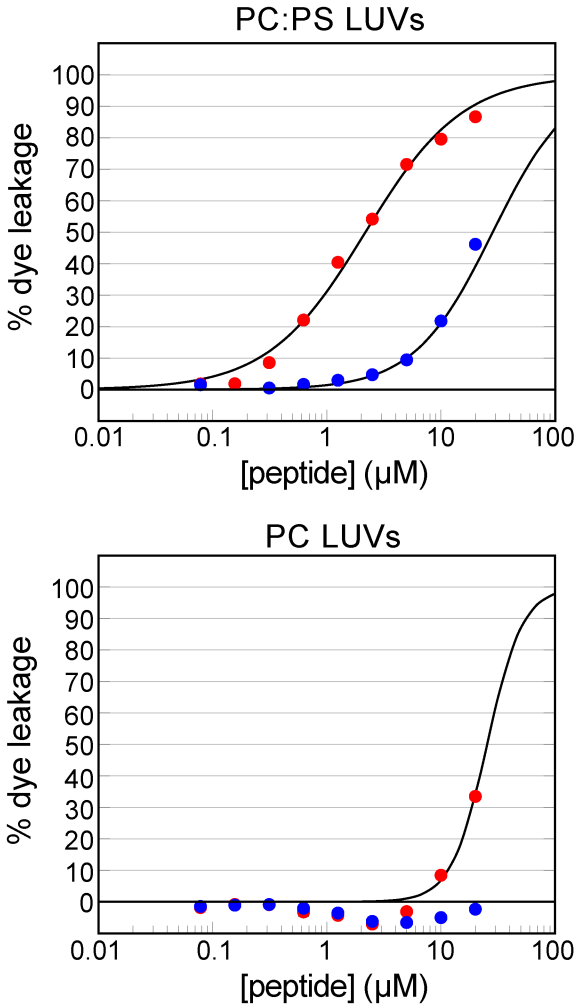

Figure 4.11: Peptide **4.2** disrupts membrane integrity of large unilamellar vesicles. Various concentrations of peptide **4.2** (red) and peptide **4.2$_{\mathbf{NB}}$** (blue) were incubated with LUVs comprising either PC:PS (1:1) or PC encapsulating 70 mM calcein. The percentage of dye leakage was monitored by the increase in fluorescence. Each point is calculated from the average of three replicate runs. Error bars (obscured by the data points) represent standard deviations propagated from three replicate runs.

Both peptides **4.2** and **4.2$_{\mathbf{NB}}$** are substantially less active towards neutral LUVs composed of only phosphatidylcholine (Figure 4.11). Peptide **4.2** induces *ca.* 33% dye leakage at 20 µM

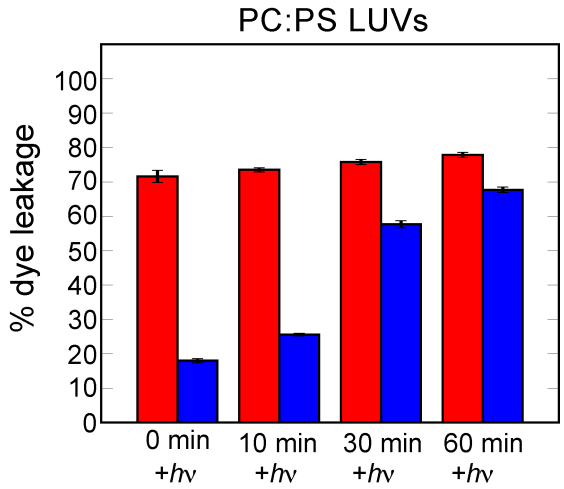

Figure 4.12: Long-wave UV light restores the dye leakage activity of peptide **4.2$_{NB}$**. PC:PS LUVs were incubated with 5 µM of peptide **4.2** (red) or peptide **4.2$_{NB}$** (blue) and irradiated with long-wave UV light. Dye leakage was assessed after 0, 10, 30, and 60 minutes of irradiation. Error bars represent standard deviations propagated from three replicate runs.

(the highest concentration tested), whereas peptide **4.2$_{NB}$** does not induce any measurable dye leakage from PC LUVs. The contrasting behavior of PC:PS LUVs and PC LUVs indicates that electrostatic interactions between the cationic peptides and the anionic liposomes are essential to the dye leakage activity of peptide **4.2**.

Irradiation of peptide **4.2$_{NB}$** with long-wave UV light in the presence of PC:PS LUVs restores the dye leakage activity (Figure 4.12). Photolysis of peptide **4.2$_{NB}$** appears to proceed at a similar rate to the photolysis of peptide **4.1$_{NB}$**. Irradiating 5 µM peptide **4.2$_{NB}$** for 10 minutes results in an increase in dye leakage from PC:PS LUVs. Irradiating peptide **4.2$_{NB}$** for 1 hour restores nearly all of the activity that results from treatment with an equal concentration of peptide **4.2**. Thus, the *N*-2-nitrobenzyl group and its photolysis allows the membrane disrupting activity of peptide **4.2** to be controlled with light.

To evaluate the effect of membranes on the conformations of peptides **4.2** and **4.2$_{NB}$**, we compared the CD spectra of the peptides in aqueous buffer to those of the peptides in the presence of either anionic (PC:PS) or neutral (PC) liposomes (Figure 4.13). The CD spectrum of peptide **4.2** in buffer displays a broad minimum from 207 nm to 216 nm. This

spectrum does not appear to be consistent with predominance of either β-sheets or random coils. Upon mixing peptide **4.2** with anionic liposomes, the minimum sharpens and shifts to 218 nm. In contrast, neutral LUVs have little effect on the CD spectrum. This change in the CD spectrum suggests that interacting with anionic lipids, but not neutral lipids, induces β-sheet folding in peptide **4.2**. These differing effects of PC and PC:PS LUVs on membrane-induced folding are congruent with the role of electrostatic interactions in the dye leakage assays.

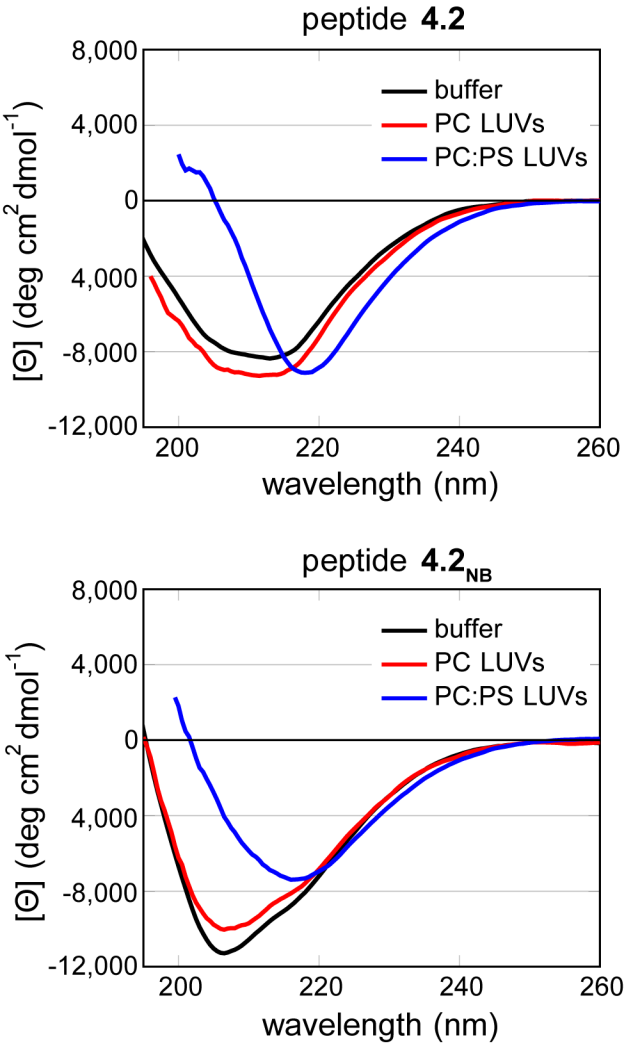

Figure 4.13: Effects of liposomes on the CD spectra of peptides **4.2** and **4.2$_{NB}$**. Spectra of 50 µM peptide in 10 mM sodium phosphate buffer at pH 7.4 were acquired in the presence or absence of 1.0 mM lipids, constituting either phosphatidylcholine (PC) or phosphatidylcholine:phosphatidylserine (PC:PS) liposomes. Data are graphed as mean residue ellipticity. The CD spectra could not be recorded below *ca.* 200 nm in the presence of the liposomes.

Similar conformational changes are observed when peptide **4.2$_{NB}$** is mixed with anionic liposomes. The CD spectra of peptide **4.2$_{NB}$** in buffer and in the presence of neutral liposomes display minima at *ca.* 205 nm. Upon mixing peptide **4.2$_{NB}$** with anionic liposomes, the minimum shifts to *ca.* 218 nm. The *N*-2-nitrobenzyl group does not prevent peptide **4.2$_{NB}$** from interacting with anionic lipids. Taken together, these studies with liposomes support a model in which *N*-2-nitrobenzylation disrupts the assembly of peptide **4.2** into oligomers that cause dye leakage.

The SDS-PAGE, cytotoxicity, and liposome studies establish that the *N*-2-nitrobenzyl group can be incorporated into macrocyclic peptides to control both their assembly and their biological properties. The *N*-2-nitrobenzyl group in peptide **4.2$_{NB}$** disrupts its assembly into hexamers in SDS-PAGE, markedly reduces its toxicity, and decreases its ability to induce membrane leakage. Removal of the *N*-2-nitrobenzyl group with long-wave UV light restores hexamer formation, toxicity, and membrane leakage. Collectively these studies suggest that peptide **4.2** is toxic to SH-SY5Y cells through a mechanism that involves membrane disruption, mediated by oligomers of the peptide.

4.3. Controlling the Assembly of Triangular Trimers with Light. The ability of the *N*-2-nitrobenzyl group to control the assembly of peptide **4.2** suggested that we could incorporate *N*-2-nitrobenzyl groups into a covalently crosslinked trimer derived from peptide **4.1$_{NB}$**. Our laboratory has previously developed two crosslinked trimeric homologues of peptide **4.1** to gain insights into the biological properties of the triangular trimer motif (Figure 4.14A).[61] These trimers are identical in amino acid sequence and only differ in the placement of three *N*-methyl groups. The *N*-methyl groups are on Gly_{33} in trimer **4.1**, blocking the $A\beta_{30–36}$ β-strands from further hydrogen bonding, while the *N*-methyl groups are on Phe_{20} in trimer **4.2**, allowing the $A\beta_{30–36}$ β-strands to further hydrogen bond. Trimers **4.1** and **4.2** assemble to form different oligomers due to blocking or exposing the $A\beta_{30–36}$ β-strands. Trimer **4.1** assembles as a hexamer, which is observed crystallographically and in

SDS-PAGE; trimer **4.2** assembles as a dodecamer, which is also observed crystallographically and in SDS-PAGE. Gly_{33} participates in a hydrogen-bonding interface with Ile_{31} within the dodecamer (Figure 4.14B). We hypothesized that replacing the *N*-methyl groups in trimer **4.1** with photolabile *N*-2-nitrobenzyl groups would result in a triangular trimer that forms a hexamer and that photolysis of the *N*-2-nitrobenzyl groups would switch the supramolecular assembly to a dodecamer (Figure 4.14C). To test this hypothesis, we prepared and studied photocaged trimer **4.3**, which contains three *N*-2-nitrobenzyl groups.

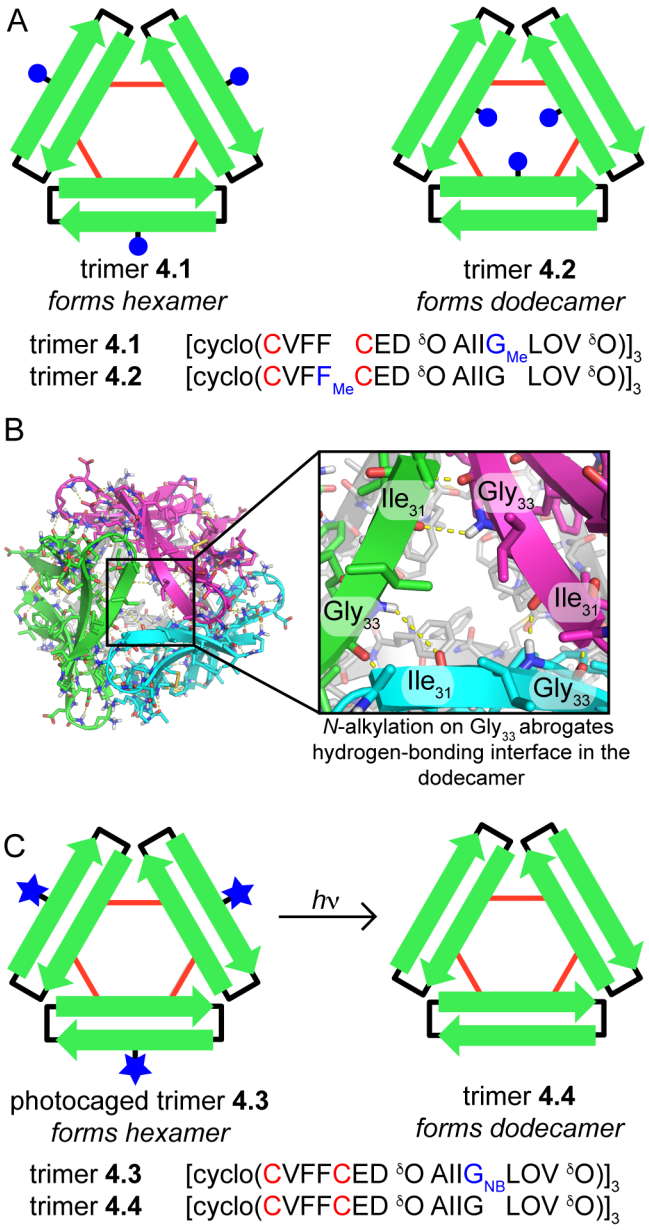

Figure 4.14: Design of a photocaged triangular trimer. (A) Cartoon of two crosslinked trimers derived from peptide **4.1** highlighting the different positions of the *N*-methyl groups. (B) X-ray crystallographic structure of the dodecamer formed by trimer **4.2** (PDB 5SUR). Inset shows the hydrogen-bonding interface between three Aβ_{30-36} β-strands from three neighboring trimers. (C) Cartoon illustrating the photolysis and decaging of trimer **4.3** to form trimer **4.4**.

Synthesis. The X-ray crystallographic structure of peptide **4.1$^{\mathbf{I}}_{\mathbf{NB}}$** suggests a strategy for forming a covalently crosslinked trimer and testing the ability of the *N*-2-nitrobenzyl group

to control assembly. At the three vertices of the triangular trimer, depicted in Figure 4.5B, the side chains of Leu_{17} and Ala_{21} pack against one another. Mutation of these two residues to Cys permits the formation of the *tris*-disulfide crosslinked photocaged trimer **4.3**, in an analogous fashion to the formation of trimers **4.1** and **4.2** that our laboratory has previously reported.[61] With the goal of forming trimer **4.3**, we prepared peptide $\mathbf{4.3_{NB}}$, which bears the L17C and A21C mutations (Chart 4.4).

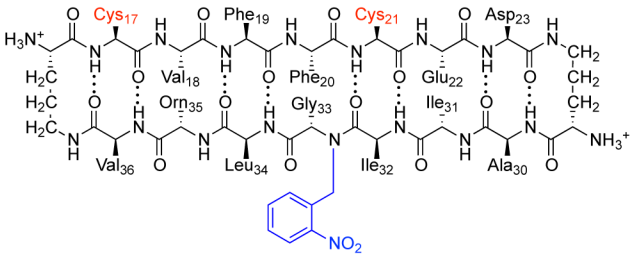

peptide $\mathbf{4.3_{NB}}$

peptide $\mathbf{4.3_{NB}}$ cyclo(CVFFCED $^{\delta}$O AllG$_{NB}$LOV $^{\delta}$O)
peptide **4.4** cyclo(CVFFCED $^{\delta}$O AllG LOV $^{\delta}$O)

Chart 4.4

Oxidation of peptide $\mathbf{4.3_{NB}}$ with 20% aqueous DMSO produces three species: a *tris*-disulfide crosslinked trimer, a *bis*-disulfide crosslinked dimer, and a monomer containing an intramolecular disulfide bond (Figure 4.15).[164,165] The identities of the trimer, dimer, and monomer were established by examining the isotope patterns of the multiply charged ions in the electrospray ionization mass spectrum. We purified trimer **4.3** using RP-HPLC followed by lyophilization of pure fractions. From the oxidation of *ca.* 60 mg of peptide $\mathbf{4.3_{NB}}$, we were able to prepare 14 mg of trimer **4.3** (*ca.* 23% yield). Photolysis of trimer **4.3** for two hours with long-wave UV light readily affords deprotected trimer **4.4**. As with the photolysis of peptide $\mathbf{4.1_{NB}}$, cysteine is added to the photolysis reaction to scavenge the nitrosobenzaldehyde by-product.[163] We purified trimer **4.4** using RP-HPLC followed by lyophilization of pure fractions. From the photolysis of 10 mg of trimer **4.3**, we were able to isolate 5 mg of trimer **4.5** (*ca.* 50% yield).

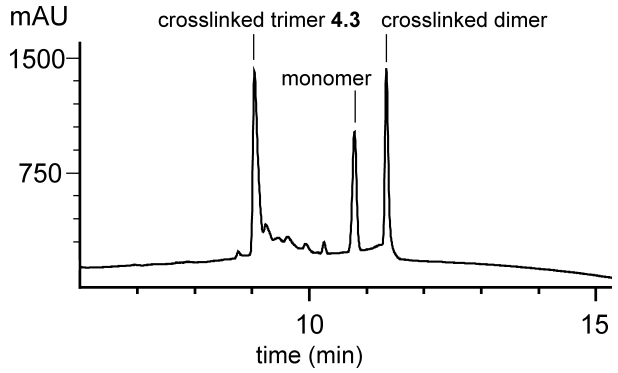

Figure 4.15: Oxidation of peptide $\mathbf{4.3_{NB}}$ produces three major species. Analytical RP-HPLC was performed on a C18 column with an elution gradient of 5–100% CH_3CN over 20 min.

It is not possible to prepare trimer **4.4** by directly oxidizing peptide **4.4** (Chart 4.4). Peptide **4.4**, which contains neither an *N*-methyl group nor an *N*-2-nitrobenzyl group, does not form a crosslinked trimer upon oxidation in aqueous DMSO. Instead, peptide **4.4** only forms a disulfide monomer (Figures 4.16). The *N*-2-nitrobenzyl group enables the synthesis of trimer **4.4** by acting as a traceless aggregation-blocking group that can be removed with light.

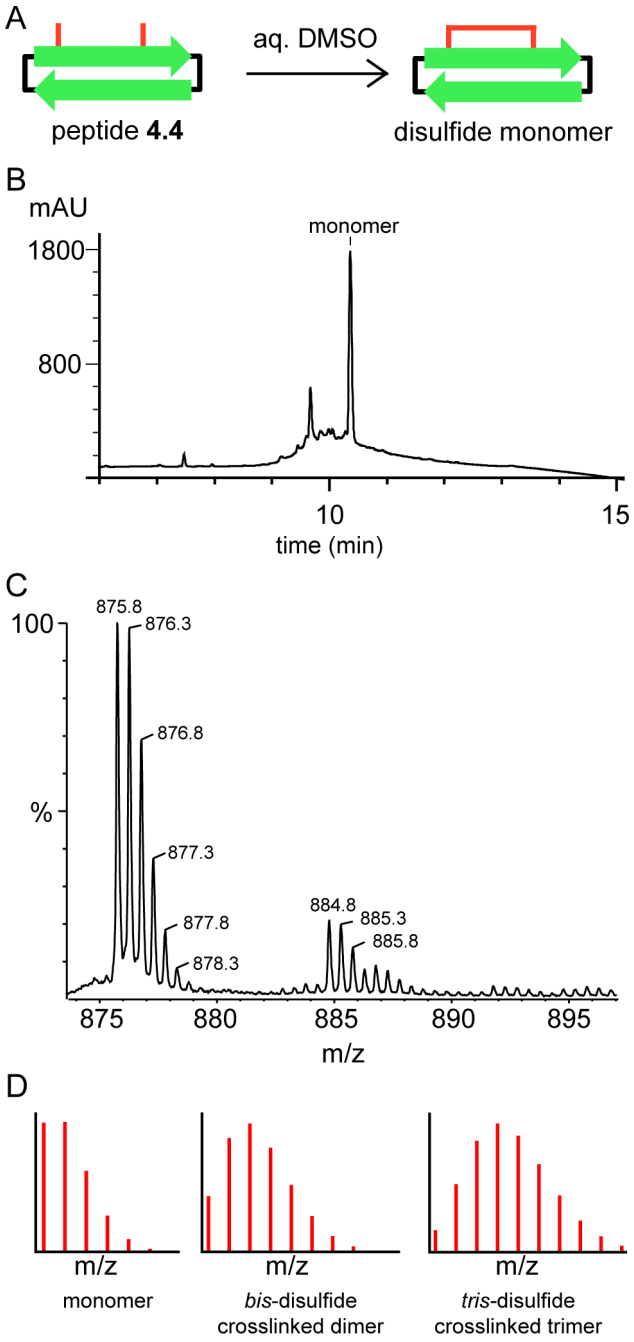

Figure 4.16: Oxidation of peptide **4.4**, which contains neither an *N*-methyl group nor an *N*-2-nitrobenzyl group, does not produce trimer **4.4**. A 6 mM solution of peptide **4.4** in 20% aqueous DMSO was stirred for 48 hours, after which it was diluted 20-fold with water and stirred for an additional 48 hours. (A) Cartoon representation of the oxidation of peptide **4.4** where the only isolable product is a disulfide monomer. (B) RP-HPLC chromatogram of the oxidation reaction of peptide **4.4**. (C) ESI-MS mass spectrum of the crude oxidation reaction. The calculated m/z for the $[M+2H]^{2+}$ isotope for the disulfide monomer is 876.0 while the calculated m/z for the $[M+2H]^{2+}$ isotope for peptide **4.4** is 877.0. The isotope pattern observed is that of the disulfide monomer, not the *tris*-disulfide crosslinked trimer **4.3**. (D) Simulated isotope pattens for a monomer, a *bis*-disulfide crosslinked dimer, and a *tris*-disulfide crosslinked trimer.

SDS-PAGE. The *N*-2-nitrobenzyl group serves as a switch that alters the supramolecular assembly of the triangular trimer motif upon photolysis and liberation of the $A\beta_{30–36}$ β-strands (Figure 4.17). Trimer **4.1** and photocaged trimer **4.3** contain blocked $A\beta_{30–36}$ β-strands and migrate in SDS-PAGE at similar mobilities to the 10 kDa size standard. These mobilities are consistent with trimer **4.1** and trimer **4.3** assembling to form hexamers (10.6 and 11.3 kDa). In contrast, trimer **4.2** and trimer **4.4** contain exposed $A\beta_{30–36}$ β-strands and migrate in SDS-PAGE between the 17 and 26 kDa size standards. These mobilities are consistent with trimer **4.2** and trimer **4.4** assembling to form dodecamers (21.2 and 21.0 kDa). Both dodecamer bands show pronounced downward streaking, indicating an equilibrium with smaller oligomers, such as hexamers or nonamers. In contrast, peptide $\mathbf{4.1_{NB}}$ does not assemble into higher-order oligomers and instead migrates between the 1.7 and 4.6 kDa size standards and thus appears to be a monomer or a dimer.

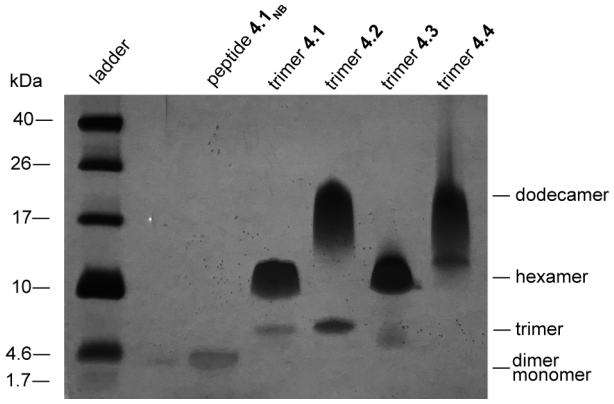

Figure 4.17: Silver-stained SDS-PAGE gel illustrating the assembly of trimers **4.1**–**4.3**. 6 µL of a 0.1 mg/mL solution of each trimer was loaded into the corresponding lanes on the gel.

X-ray crystallography. We turned to X-ray crystallography to gain insights into the assembly of trimers **4.3** and **4.4** into the hexamers and dodecamers observed in SDS-PAGE. Trimer **4.3** does not grow crystals in similar conditions as either trimer **4.1** or trimer **4.2**. Instead, trimer **4.3** crystalizes from a mixture of 0.1 M sodium acetate, buffered at pH 4.5, 0.2 M NaCl, and 28% (w/v) 2-methyl-2,4-pentanediol. We determined the X-ray crystallographic phases by

soaking a crystal for 1 hour in a mixture of 0.1 M potassium iodide (KI) and crystallization buffer. We used the program BLEND to merge multiple data sets from a single crystal and found that doing so allowed single-wavelength anomalous diffraction phasing.[166] The X-ray crystallographic structure of the KI-soaked trimer **4.3** (PDB 6CG4) was then used as a search model in molecular replacement to determine the X-ray crystallographic phases of a data set collected from a crystal that had not been soaked in KI (PDB 6CG5). Both structures of trimer **4.3** were solved and refined in space group $I4_1$ at 2.03 Å resolution. Table 4.1 summarizes the crystallographic properties, crystallization conditions, data collection, and model refinement statistics.

Trimer **4.4** does not grow crystals in similar conditions as trimers **4.1**–**4.3**. Screening trimer **4.4** in 288 conditions yielded a single condition in which crystals grow: a mixture of 0.1 M HEPES, buffered at pH 7.25, and 20% (v/v) Jeffamine M-600. These conditions are similar to those used to crystalize peptides **4.1** and $\mathbf{4.1^{I}_{NB}}$. Unfortunately, our attempts to optimize these conditions have thus far only yielded crystals that diffract X-rays weakly. We have been unable to process the resulting data sets and thus have been unable to solve the X-ray crystallographic structure of trimer **4.4**.

The crystals of trimer **4.3** contain a single copy of trimer **4.3** in the asymmetric unit (Figure 4.18A). The X-ray crystallographic structure of trimer **4.3** reveals a symmetrical trimer composed of three folded β-hairpins. The trimer is stabilized by three disulfide bonds wherein Cys_{17} of one monomer is linked to Cys_{21} of another monomer at the three vertices of the triangular trimer. The *N*-2-nitrobenzyl groups pack against the Phe_{20} side chains on the bottom surface of trimer **4.3** (Figure 4.18B). The three *N*-2-nitrobenzyl groups are clearly visible in the electron density map (Figure 4.19). The *N*-2-nitrobenzyl groups also make intermolecular contacts with neighboring trimers in the crystal lattice, packing against the $^{\delta}Orn_1$ turns from other trimers and interacting with other *N*-2-nitrobenzyl groups. Unlike

the discrete oligomers formed by trimers **4.1** and **4.2**, no discrete oligomers exist in the crystal lattice formed by trimer **4.3**.

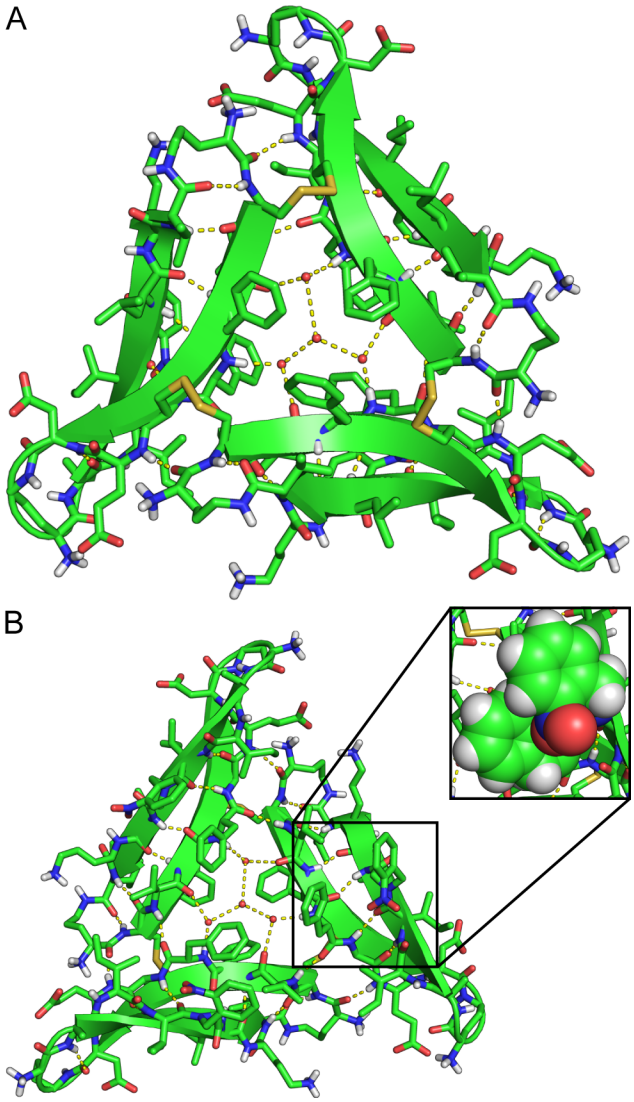

Figure 4.18: X-ray crystallographic structure of photocaged trimer **4.3** (PDB 6CG5). (A) Top surface of trimer **4.3** which displays the three disulfide crosslinks. (B) The bottom surface of trimer **4.3** on which the three *N*-2-nitrobenzyl groups pack against Phe_{20}. In the inset, the side chain of Phe_{20} and the adjacent *N*-2-nitrobenzyl group are shown as spheres.

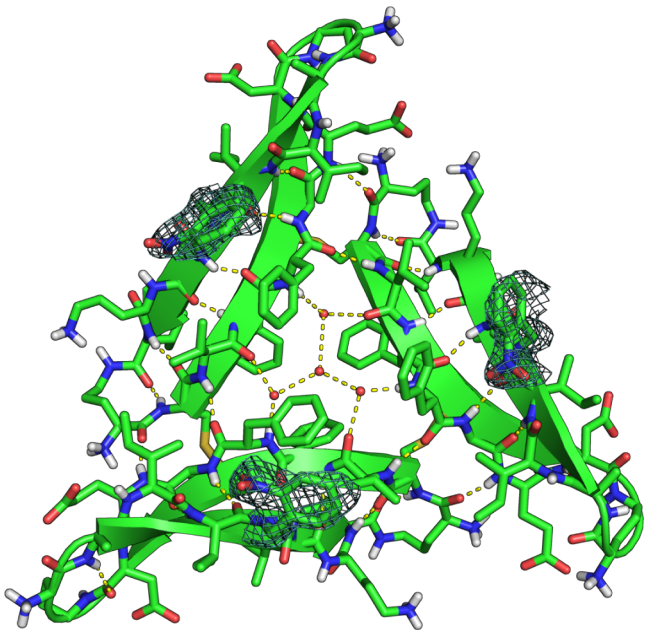

Figure 4.19: The three *N*-2-nitrobenzyl groups on trimer **4.3** are clearly visible in the electron density map. The 2Fo-Fc electron density map is contoured at 1.0 σ.

The assembly of trimer **4.3** in the crystal lattice differs from the assemblies of trimers **4.1** and **4.2**. Trimer **4.1** assembles into stacks of sandwich-like hexamers, which resemble the sandwich-like hexamer formed by peptide $\mathbf{4.1^{I}_{NB}}$ (Figure 4.20A). Trimer **4.2** assembles into ball-shaped dodecamers (Figure 4.20B). We anticipated that trimer **4.3** would assemble in a similar fashion to trimer **4.1**, as the $A\beta_{30–36}$ β-strands in both trimers are blocked from hydrogen bonding. Instead, trimer **4.3** assembles into conjoined dodecamers in which each trimer subunit is shared between two dodecamers in the crystal lattice. These conjoined dodecamers do not resemble the dodecamers formed by trimer **4.2**. The dodecamers formed by trimer **4.3** assemble through heterofacial packing of the composite trimer subunits. In contrast, the dodecamers formed by trimer **4.2** assemble through homofacial packing of the composite trimer subunits. Sequestration of the *N*-methyl groups within trimer **4.2** exposes the $A\beta_{30–36}$ β-strands to further hydrogen-bonding interactions within the trimer **4.2** dodecamer. The *N*-2-nitrobenzyl groups in trimer **4.3** do not permit this mode of

hydrogen bonding. As a result, the hydrogen-bonding network in the trimer **4.2** dodecamer is more extensive than that in the trimer **4.3** dodecamer.

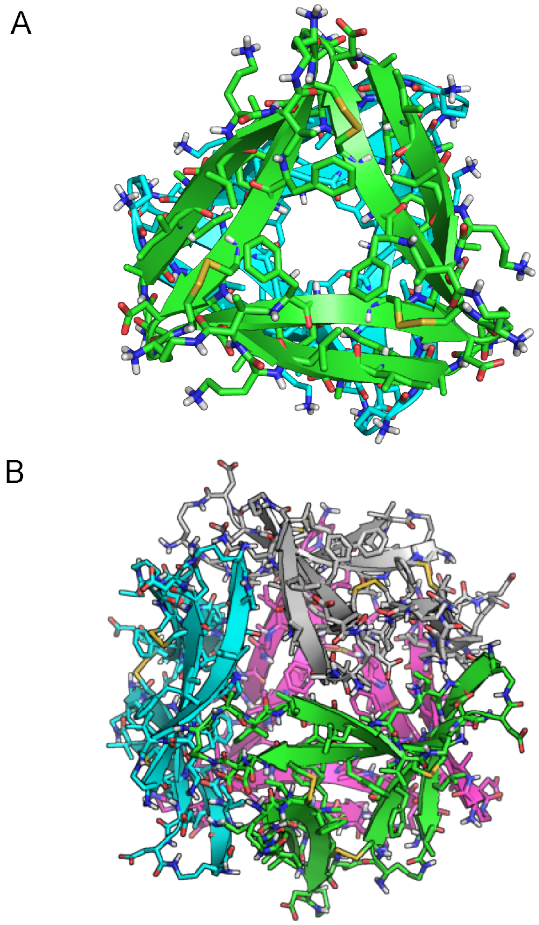

Figure 4.20: X-ray crystallographic structures of trimers **4.1** and **4.2**. (A) Sandwich-like hexamer formed by trimer **4.1** (PDB 5SUT). (B) Ball-shaped dodecamer formed by trimer **4.2** (PDB 5SUR). Each trimer subunit is colored green, cyan, magenta, or grey.

The X-ray crystallographic structure of the conjoined dodecamers formed by trimer **4.3** offers little insight into the hexamers that it forms in SDS-PAGE, because these dodecamers do not contain discrete hexamer subunits. The sandwich-like hexamers formed by trimer **4.1** (PDB 5SUT), on the other hand, support a working model for the structures of these hexamers. In this working model, two trimers sandwich together. Such a model is consistent with other sandwich-like hexamers we have observed in the crystal lattices of other macrocyclic β-hairpin peptides.[57,58,60,61,64]

We have not been able to determine the X-ray crystallographic structure of trimer **4.4** and thus lack a structure to help illuminate the dodecamers it forms in SDS-PAGE. The ball-shaped dodecamers formed by trimer **4.2** (PDB 5SUR) provide a working model for these dodecamers. In this working model, four trimers wrap together to form a ball. Such a model is consistent with other ball-shaped dodecamers we have observed in the crystal lattices of other macrocyclic β-hairpin peptides.[64] Such a model is also consistent with the differing oligomerization states observed for trimers **4.3** and **4.4** in SDS-PAGE.

The synthetic, SDS-PAGE, and X-ray crystallographic studies of trimers **4.3** and **4.4** establish that the *N*-2-nitrobenzyl group is sufficiently robust to be incorporated into covalently crosslinked oligomers containing multiple peptides and *N*-2-nitrobenzyl groups. These studies further establish that the *N*-2-nitrobenzyl group can allow light to switch the peptide from one oligomerization state to another.

4.3 Conclusion

The *N*-2-nitrobenzyl photolabile protecting group allows the oligomerization state of Aβ-derived macrocyclic peptides to be controlled with light. Depending on their positions, the *N*-2-nitrobenzyl groups can either be accommodated by or disrupt the higher-order assemblies of the macrocyclic peptides. Disrupting intermolecular hydrogen bonds that stabilize the oligomers observed by X-ray crystallography disrupts the assembly of the peptides in solution. Their assembly can be recovered by irradiating the peptides with long-wave UV light, which removes the *N*-2-nitrobenzyl groups. In the case of peptide $\mathbf{4.2_{NB}}$, the *N*-2-nitrobenzyl group also alters the biological properties of the peptide. Removing the *N*-2-nitrobenzyl group from peptide $\mathbf{4.2_{NB}}$ restores both the assembly and the biological properties of peptide **4.2**. The *N*-2-nitrobenzyl group offers the promise of controlling when and where macrocyclic β-hairpin peptides assemble in cells. In the case of trimer **4.3**, the

N-2-nitrobenzyl group enables the synthesis of trimer **4.4**, which lacks any *N*-alkyl groups. Trimer **4.4** should better model the types of trimers that full-length Aβ may form and thus allow us to better probe the biology of Aβ oligomers.

We envision that *N*-2-nitrobenzyl groups could be applied to chemical model systems of other amyloid oligomers. The αB crystallin-derived cylindrin oligomers and the SOD1-derived corkscrew oligomers reported by Eisenberg and co-workers, as well as the hPrP-dervied hexameric oligomers reported by Surewicz and co-workers, are all amenable to the strategy described here.[52,54,158] Controlling the assembly of these chemical model systems may enable the biological properties of these oligomers to be probed. The aforementioned structures may even guide the installation of photolabile protecting groups into full-length amyloid-forming peptides and proteins. We envision that the *N*-2-nitrobenzyl group will enable a more rigorous dissection of the relationship between the assembly and the biological properties of amyloid-derived peptides. Studies in this direction are currently underway in our laboratory.

4.4 Materials and Methods

4.4.1 General information

All chemicals were used as received except where otherwise noted. Methylene chloride was passed through alumina under argon prior to use in a solvent purification system. Anhydrous, amine free dimethylformamide (DMF) was purchased from Alfa Aesar. All reactions were performed at ambient temperature (*ca.* 20 °C), unless otherwise noted. Peptide synthesis was performed on a Protein Technologies PS3 synthesizer. Analytical reverse-phase HPLC was performed on an Agilent 1200 equipped with a Aeris PEPTIDE 2.6u XB-C18 column (Phenomonex). Preparative reverse-phase HPLC was performed on a Rainin Dynamax equipped with a ZORBAX SB-C18 column (Agilent). HPLC grade acetonitrile and 18

MΩ deionized water, each containing 0.1% trifluoroacetic acid, were used for analytical and preparative reverse-phase HPLC. All peptides were prepared and used as the trifluoroacetate salts and were assumed to have one trifluoroacetate ion per ammonium group present in each peptide.

The synthesis of peptides **4.2** and $\mathbf{4.2_{Me}}$ were performed using techniques previously described by our laboratory.[56–58,63] Scheme 4.1 illustrates the synthesis of peptide **4.2**. Peptides $\mathbf{4.1_{NB}}$, $\mathbf{4.1^{I}_{NB}}$, $\mathbf{4.2_{NB}}$, and **4.3** were prepared in an identical fashion to peptides **4.2** and $\mathbf{4.2_{Me}}$, with exception of *N*-2-nitrobenzylglycine$_{33}$ and Ile$_{32}$, which were installed via the submonomer approach followed by coupling with triphosgene. After the installation of the *N*-2-nitrobenzyl group, the peptides were protected from light with black felt (purchased from Amazon.com) in subsequent steps. The procedures for these steps are detailed below.

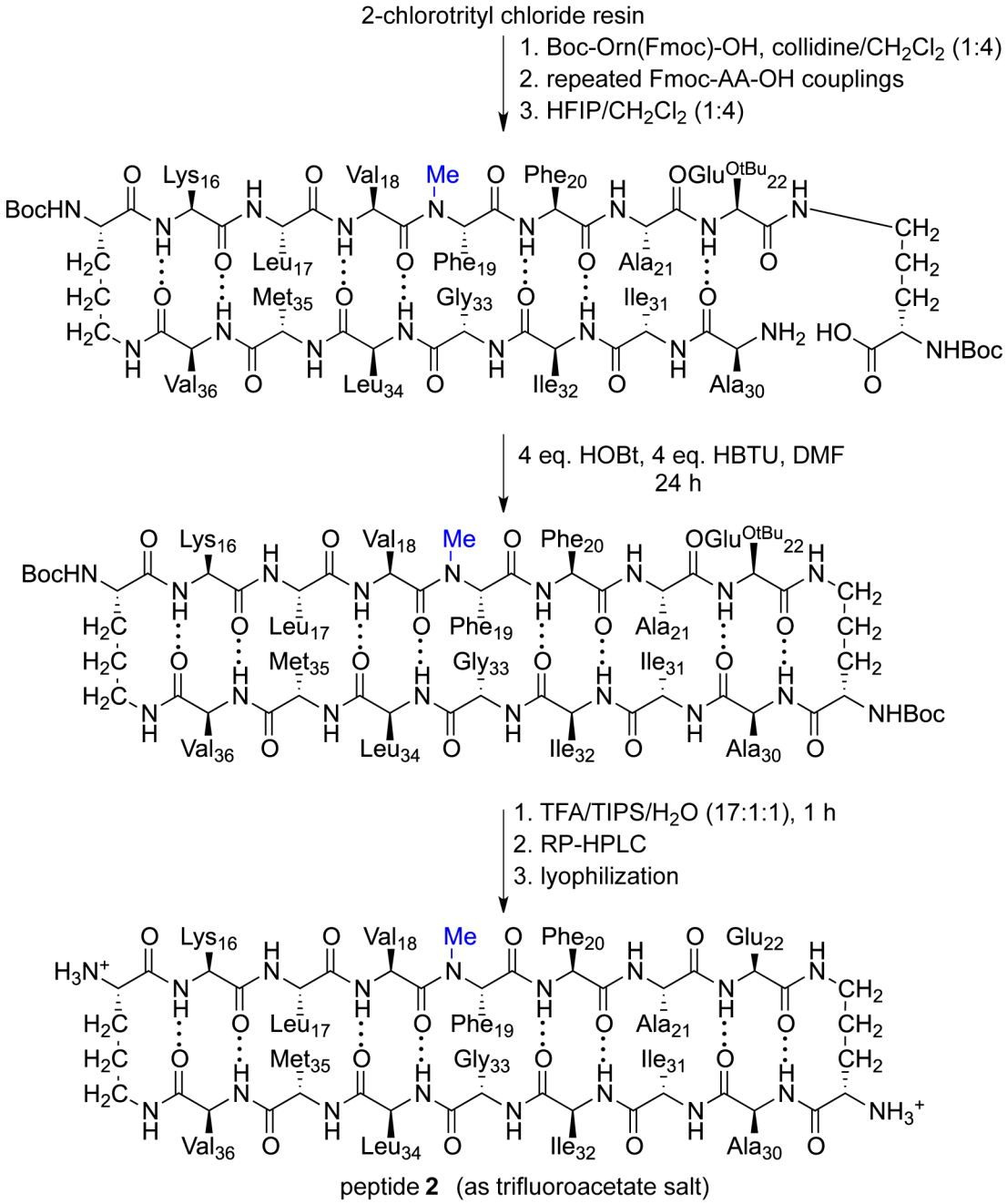
2-chlorotrityl chloride resin
1. Boc-Orn(Fmoc)-OH, collidine/CH2Cl2 (1:4)
2. repeated Fmoc-AA-OH couplings
3. HFIP/CH2Cl2 (1:4)
4 eq. HOBt, 4 eq. HBTU, DMF
24 h
1. TFA/TIPS/H2O (17:1:1), 1 h
2. RP-HPLC
3. lyophilization
peptide 2 (as trifluoroacetate salt)

Scheme 4.1

4.4.2 Submonomer incorporation of *N*-2-nitrobenzylglycine$_{33}$

Scheme 4.2 illustrates the steps involved in the submonomer incorporation of *N*-2-nitrobenzylglycine$_{33}$. After automated solid-phase peptide synthesis, the *N*-terminal Fmoc was deprotected with 20% piperidine in DMF for 5 minutes. The resin was transferred to a peptide synthesis vessel equipped with nitrogen and vacuum, and washed three times with 5 mL DMF. Bromoacetic acid (750 mg, 5 equiv) was dissolved in *ca.* 4 mL of DMF. *N*,*N*-Diisopropylcarbodiimide (DIC, 750 µL, 5 equiv) was added to the solution of bromoacetic acid. This solution was allowed to mix for 1 minute, at which point it was added to the resin via a Pasteur pipette. The coupling reaction was allowed to proceed for 20 minutes, after which the solution was drained, and the resin was washed three times with DMF.

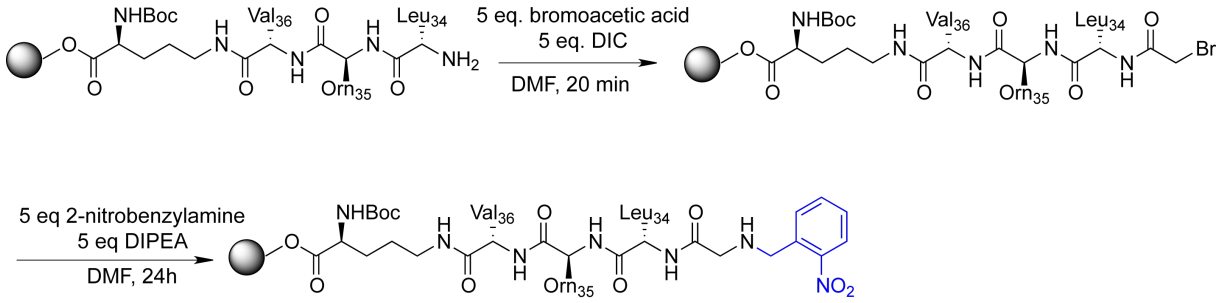

Scheme 4.2

o-Nitrobenzylamine hydrochloride (750 mg) and diisopropylethylamine (DIPEA, 750 µL) were dissolved in 4 mL of DMF. This solution was added to the resin via a Pasteur pipette, and allowed to mix overnight by bubbling nitrogen. The resin was then washed three times with 5 mL DMF. During this reaction, and all subsequent steps in peptide synthesis, the resin was protected from light with black felt.

4.4.3 Triphosgene coupling of Ile$_{32}$

Scheme 4.3 illustrates the steps involved in the triphosgene-mediated coupling of Ile$_{32}$ to *N*-2-nitrobenzylglycine$_{33}$. The resin was washed three times with dry THF, then allowed to

swell in 2 mL of dry THF for 5 minutes. 2 mL of dry THF was added to a vial containing triphosgene (47.5 mg, 1.3 equiv) and Fmoc-Ile-OH (170 mg, 4 equiv) to form a clear solution. 2,4,6-Collidine (220 µL) was added to the mixture of triphosgene and Fmoc-Ile-OH and allowed to mix until a white precipitate formed (*ca.* 1 minute). This suspension was added to the resin via a Pasteur pipette and mixed for one hour by bubbling nitrogen, protected from light. The resin was then washed with 5 mL dry THF, 5 mL dry CH_2Cl_2, and then 5 mL dry THF. This sequence was repeated until coupling of Ile_{32} was completed, as judged by RP-HPLC. Typically, four repititions of this process were performed. Resin was washed three times with 5 mL DMF prior to continuing the traditional solid-phase peptide synthesis protocols.

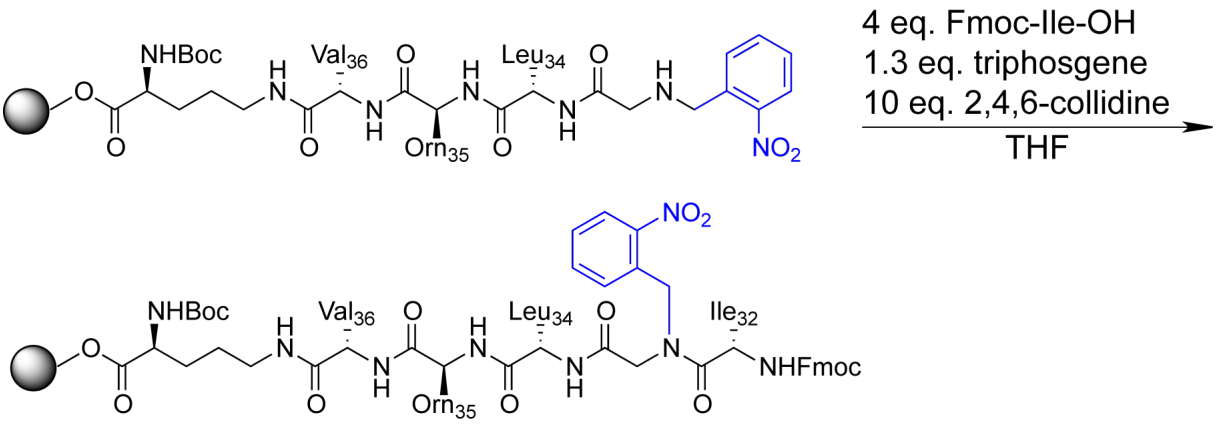

Scheme 4.3

4.4.4 Oxidation of peptide $\mathbf{4.3_{NB}}$ to form trimer 4.3

Peptide $\mathbf{4.3_{NB}}$ was prepared using the protocols described above. After purification and lyophilization of peptide $\mathbf{4.3_{NB}}$, a 6 mM solution of peptide $\mathbf{4.3_{NB}}$ in 20% aqueous DMSO was prepared in a 20-mL glass scintillation vial. This vial was protected from light with aluminum foil and rocked for 48 hours. After 48 hours, the solution was transferred to a 1-L round bottom flask equipped with a stir bar and diluted 20-fold with 18 MΩ deionized water. This diluted solution was allowed to stir for an additional 48 hours. After this second 48-hour

period, the solution was removed using rotary evaporation. The white residue was dissolved in *ca.* 10 mL of 20% aqueous acetonitrile and purified by RP-HPLC using a gradient of 20–30% acetonitrile in water over 15 minutes, followed by a gradient of 30–60% acetonitrile in water over 60 minutes. The purity of fractions were judged by analytical RP-HPLC and ESI-MS. Pure fractions were combined and lyophilized, yielding trimer **4.3** as a white solid.

4.4.5 Photolysis of trimer 4.3 and purification of trimer 4.4

Trimer **4.4** was prepared by photolysis of trimer **3**. The procedure is described briefly here and in more detail in the section on photolysis that follows, below. A 3.2 mg/mL solution of trimer **3** was prepared gravametrically in 10 mg/mL L-cysteine. This solution was transferred into quartz cuvettes placed *ca.* 1 cm from a hand-held UV lamp. The cuvettes were irradiated for 3 hours with long-wave UV light (*ca.* 365 nm). The solution of irradiated trimer **3** was filtered through a 0.2 µm filter, and purified by RP-HPLC using a gradient of 20–30% acetonitrile in water over 15 minutes, followed by a gradient of 30–60% acetonitrile in water over 60 minutes. The purity of fractions were judged by analytical RP-HPLC and ESI-MS. Pure fractions were combined and lyophilized, yielding trimer **4** as a white solid.

4.4.6 X-ray crystallography

X-ray crystallographic studies of peptide $\mathbf{4.1^{I}_{NB}}$ and trimer **4.3** were performed using the protocols previously published by our laboratory with minor modifications. These procedures are slightly modified, and in some cases taken verbatim, from Salveson et *al. J. Am. Chem. Soc.* **2016**, *139*, 4458–4467.[63]

4.4.7 Crystallization of peptide 4.1_{NB} and trimer 4.3

Peptide ***4.1***$_{NB}$: Crystal growth was optimized using conditions similar to those we had previously reported for peptide **4.1**.[57] In the optimization, the pH and cryoprotectant concentrations were varied across the 4x6 matrix of a Hampton VDX 24-well plate to generate crystals that diffracted well. The hanging drops for these optimizations were prepared on glass slides by combining 1 or 2 µL of peptide solution with 1 or 2 µL of well solution in ratios of 1:1, 2:1, and 1:2. Crystals that formed were checked for diffraction using a Rigaku Micromax-007 HF diffractometer with a Cu rotating anode at 1.54 Å.

Trimer ***4.3***: Conditions were identified in 96-well plates. Three kits from Hampton Research (Crystal Screen, Index, and PEG/ION) were used to screen trimer **4.3**, for a total of 288 separate crystallization experiments (three 96-well plates). Each well in the 96-well plates was loaded with 100 µL of a solution from the kits. The hanging drops were set up using a TTP Labtech Mosquito pipetting robot. For each well, three hanging drops were prepared comprising either 50, 75, or 100 nL of well solution mixed with either 100, 75, or 50 nL of a 10 mg/mL solution of trimer **4.3**. Crystal growth was further optimized in 24-well plates in an analogous fashion described for the optimization of peptide $\mathbf{1_{NB}}$ crystal growth.

4.4.8 X-ray diffraction data collection, data processing, and refinement for peptide 4.1_{NB} and trimer 4.3

Data collection: Prior to data collection, crystals of trimer **4.3** were transferred with a nylon loop to a new hanging drop comprising a 1:1 mixture of well-solution and 0.1 M potassium iodide (KI). Crystals were soaked in this condition for 1 hour to incorporate iodide ions into the lattice.

Data were collected from crystals of peptide **4.1$_{NB}$** and trimer **4.3** using a Rigaku Micromax-007 HF diffractometer with a Cu rotating anode at 1.54 Å with 0.5° rotation per image. The program CrystalClear 2.0 was used to design collection strategies with multiplicities exceeding 20. This high multiplicity facilitates single-wavelength anomalous diffraction phasing. This collection strategy results in multiple data sets from a single crystal that need to be merged with one another.

Data processing: Each individual data set was integrated and scaled using XDS.[89] The multiple data sets were then merged using BLEND.[118,166] Hybrid structure search (HySS) in the Phenix software suite was used to determine the coordinates of the anomalous signal for peptide **4.1$_{NB}$** and the KI-soaked trimer **4.3**.[90] The initial electron density maps were generated using the coordinates of the anomalous signal as initial positions in Autosol. For the dataset from the unsoaked crystal of trimer **4.3**, the structure of the KI-soaked trimer **4.3** was used as a search model in Phaser.[119]

Refinement and model manipulation: Phenix.refine was used to refine the models of peptide **4.1$_{NB}$** and trimer **4.3**. Coot was used to manipulate the coordinates for both peptides.[120] Table 4.1 summarizes the crystal properties, data collection, and data processing for peptide **4.1$_{NB}$** and trimer **4.3**.

4.4.9 Photolysis

The rate of decaging was monitored by irradiating a 2 mg/mL solution of peptide **4.1$_{NB}$** with a hand-held UV lamp (model UVGL-58) producing 365 nm light. The solution of peptide **4.1$_{NB}$** was prepared gravametically by dissolving 2 mg in 0.99 mL of a 10 mg/mL solution of L-cysteine. 10 µL of a 5% (w/v) solution of aqueous phenol was added, bringing the total volume of the peptide **4.1$_{NB}$** solution to 1 mL. This solution was placed in a quartz cuvette with a 1 cm x 2 mm chamber. This cuvette was placed *ca.* 1 cm away from

Table 4.1: Crystallographic properties, crystallization conditions, data collection, and model refinement statistics for peptide **4.1$^{\mathbf{I}}_{\mathbf{NB}}$** and trimer **4.3**

	peptide **4.1$^{\mathbf{I}}_{\mathbf{NB}}$**	trimer **4.3** + KI	trimer **4.3**
PDB ID	6CG3	6CG4	6CG5
space group	$P4_232$	$I4_1$	$I4_1$
a, *b*. *c* (Å)	47.5, 47.5, 47.5	39.3, 39.3, 58.4	39.3, 39.3, 58.9
α, β, γ (^{o})	90, 90, 90	90, 90, 90	90, 90, 90
peptide/trimer per asymmetric unit	1	1	1
crystallization conditions	0.1 M HEPES pH 8.75 18% Jeffamine M-600	0.1 M NaOAc pH 4.5 0.2 M NaCl 28% MPD 0.1 M KI soak	0.1 M NaOAc pH 4.5 0.2 M NaCl 28% MPD
Data Collection[a]			
wavelength (Å)	1.54	1.54	1.54
resolution (Å)	19.4–2.03 (2.1–2.03)	32.8–2.08 (2.1–2.08)	37.8–2.08 (2.16 –2.08)
total reflections	39938 (6708)	90671 (7956)	53152 (4449)
unique reflections	1388 (312)	2742 (313)	2728 (301)
multiplicity	28.8 (21.5)	33.1 (25.4)	19.5 (14.8)
completeness (%)	99.5 (98.5)	100.0 (100.0)	100 (99.7)
mean I/σ	18.4 (5.4)	33.1 (14.1)	36.5 (15.6)
R_{merge}	0.166 (0.654)	0.096 (0.241)	0.06 (0.168)
$R_{measure}$	0.171	0.098	0.063
$CC_{1/2}$	0.998 (0.954)	0.999 (0.994)	0.999 (0.994)
CC*	0.999 (0.988)	0.998 (0.995)	1 (0.997)
Refinement			
R_{work}	23.0	22.9	19.7
R_{free}	26.5	27.7	24.2
number of non-hydrogen atoms	145	440	416
number of non-peptide atoms	16	40	20
RMS_{bonds}	0.02	0.005	0.007
RMS_{angles}	2.72	0.93	1.03
Ramachandran favored (%)	100	100	100
outliers (%)	0	0	0
clashscore	11.0	9.52	2.98
average B-factor	22.4	24.0	30.0

[a]Values for the highest resolution shell are show in parentheses.

the UV lamp such that light shown through the 2 mm path length, rather than the 1 cm path length of the cuvette. 150 µL aliquots of this reaction were removed at various time points and diluted with 150 µL of 18 MΩ deionized water. These samples were analyzed by RP-HPLC using a gradient of 0–100 % acetonitrile in water over 20 minutes. Each peak was integrated manually. The integrated values for peptide $\mathbf{4.1_{NB}}$, the photolysis product, and the nitrosobenzaldehyde by-product were divided by the integrated value of the phenol internal control. These ratios were plotted vs time.

Irradiating peptides $\mathbf{4.1_{NB}}$ and $\mathbf{4.2_{NB}}$ prior to treating cells (see below) was accomplished in a similar fashion. Briefly, a 500 µM solution of either peptide $\mathbf{4.1_{NB}}$ or $\mathbf{4.2_{NB}}$ in 0.625 mg/mL L-cysteine was placed into a cuvette and irradiated for 1 hour, as described above.

4.4.10 SDS-PAGE

The oligomerizaiton of trimers **4.1**, **4.2**, **4.3**, and **4.4** as well as peptides $\mathbf{4.1_{NB}}$, **4.2**, $\mathbf{4.2_{Me}}$, and $\mathbf{4.2_{NB}}$ were studied by tricine SDS-PAGE. Reagents and gels for tricine SDS-PAGE were prepared according to recipes reported previously.[61,167]

2X samples of each peptide or trimer were prepared by diluting 10 mg/mL solutions of the peptides or timers with 18 MΩ deionized water to the appropriate concentration. 2X samples of peptides $\mathbf{4.1_{NB}}$ and $\mathbf{4.2_{NB}}$ exposed to UV light were prepared from a 1 mg/mL solution of the corresponding peptide that was irradiated in the presence of 10 mg/mL L-cysteine for 1 hour, as described in the Photolysis section of this document. The 2X samples were then diluted with 2X SDS-PAGE loading buffer (100 mM Tris buffer at pH 6.8, 20% (w/v) glycerol, and 4% (w/v) SDS) to create the 1X samples which were loaded into the gel. 6 µL of the 1X samples were loaded into the gel, in addition to 1 µL of Spectra^{TM} Multicolor Low Range Protein Ladder (Thermo Scientific part no.: 26628). Samples were run through a 16% polyacrylamide gel with a 4% stacking polyacrylamide gel at a constant 80 V at 23

°C. Silver-staining was used to visualize peptide and trimer bands in the SDS-PAGE gel as described previously.[61,168]

4.4.11 Cell culture

SH-SY5Y cell cultures were maintained in 1:1 mixture of Dubelcco's modified Eagle medium and Ham's F12 (DMEM:F12) media supplemented with 10% heat-inactivated fetal bovine serum (FBS), 100 U/mL penicillin and 100 µg/mL streptomycin at pH 7.4 in a humidified 5% CO_2 atmosphere at 37 °C. All experiments were performed using *ca.* 60–80% confluent cells on passages ranging from 3–12.

4.4.12 MTT and LDH assays

These procedures are slightly modified, and in some cases taken verbatim, from Salveson et *al.*, *J. Am. Chem. Soc.*, **2016**, *139*, 4458–4467.[63]

SH-SY5Y cells were plated into 96-well plates at 15,000 cells per well in 100 µL 1:1 DMEM/F12 medium supplemented with 10% FBS, 100 U/mL penicillin and 100 µg/mL streptomycin at pH 7.4 and incubated in a humidified 5% CO_2 atmosphere at 37 °C for 24 h. Prior to treatment, the medium was aspirated and replaced with 90 µL serum-free, phenol-red free DMEM/F12 media. Solutions of the peptides were prepared gravimetrically by dissolving the lyophilized peptide in the appropriate amount of 18 MΩ deionized water to achieve a 10 mg/mL stock. From the 10 mg/mL stock solutions, 10X solutions were made by dilution with 18 MΩ deionized water. 10X samples of peptides $\mathbf{4.1_{NB}}$ and $\mathbf{4.2_{NB}}$ were irradiated for 1 hour in a quartz cuvette in the presence of 0.625 mg/mL cysteine prior to treating cells, as outlines in the Photolysis section. 10 µL of the 10X solutions were added to the wells on the 96-well plates, bringing the total volume of each well to 100 µL. Cells were treated and

incubated in replicates of five in the presence of each compound for 72 hours in a humidified 5% CO_2 atmosphere at 37 °C prior to performing both MTT and LDH assays.

Both MTT (Sigma) and LDH (Thermo Scientific) assays were performed on the each plate. A 50-µL aliquot of supernatant media was transferred to a new 96-well plate and spectrophotometrically analyzed for LDH content according to the manufacturer's instructions. The remainder of the media was aspirated and replaced with 100 µL of serum free, phenol-red free DMEM/F12 medium supplemented with 0.2 mg/mL MTT. The cells were incubated for 24 hours in a humidified 5% CO_2 atmosphere at 37 °C in the presence of the MTT containing media. Formazan crystals from the MTT reaction were dissolved in 10% SDS in 10 mM HCl for 4 h in a humidified 5% CO_2 atmosphere at 37 °C. MTT plates were read spectrophotometrically at 570 nm.

MTT data were graphed as a percentage versus the water treatment control, whereas LDH data were analyzed and plotted as previously described.[103]

4.4.13 Liposome preparation

Large unilamelar vesicles (LUVs) were prepared as previously described.[63] Chicken egg-derived L-α-phosphatidylcholine (PC, product number: 840051C) and porcine brain-derived L-α-phosphatidylserine (PS, product number: 840032) were purchased from Avanti Polar Lipids as 10 mg/mL solutions in chloroform. Liposomes were prepared using 2.6 micromoles of lipids, either solely PC or as a 1:1 molar ratio of PC and PS. For circular dichroism studies, LUVs were prepared in 10 mM sodium phosphate buffer (pH 7.4) by extrusion through 100 nm filters.

4.4.14 Dye leakage assay

For dye leakage assays, LUVs were prepared in leakage buffer, comprising 10 mM Tris (pH 7.4), 150 mM NaCl and 1 mM EDTA supplemented with 70 mM calcein by extrusion through 100 nm filters. The LUVs were separated from free calcein by passage through a 10 x 1 cm column of Spehadex G-50 and collection of the yellow fractions that did not fluoresce under long-wave UV light. After removal of free calcein from LUVs encapsulating calcein, the concentration of lipids was determined using a modified phosphorus assay, as follows.[169] 50 µL of the LUV suspension was added to a 12 x 75 mm disposable culture tube. 30 µL of a 10% (w/v) solution of $Mg(NO_3)_2$ in ethanol was added to the culture tube. This mixture was ashed over a hot flame resulting in the formation of a grey precipitate. 300 µL of 0.5 M HCl was added to dissolve the precipitate. This solution was heated for 15 minutes in a boiling water bath. After cooling to room temperature, 700 uL of a mixture of 1% (w/v) ascorbic acid and 0.378% (w/v) ammonium molybdate tetrahydrate dissolved in 0.45 M H_2SO_4 was added to the boiled solution. This mixture was heated for 1 hour at 37 °C. Over this time the solution develops a faint blue color. This solution was then transferred to a 1 cm quartz cuvette, and the OD_{820} was measured. The concentration of phosphate was determined using a molar extinction coefficient of 120 $M^{-1}cm^{-1}$. The concentration of total lipid is assumed to be equal to the concentration of phosphate measured in this assay, as one mole of phospholipid contains one mole of phosphate.

The stock LUV suspension was diluted in leakage buffer to a final concentration of 11 µM lipid. 10X solutions of the peptides where prepared from 10 mg/mL stock solutions prepared in 18 MΩ deionized water. 20 uL of these 10X stock solutions were added to the wells of a 96-well plate. 20 µL of 10X lysis buffer was used as the 100% leakage controls. 20 µL of 18 MΩ deionized water was used as the 0% leakage control. Each treatment was done in triplicate. 180 uL of the 11 µM lipid LUV suspension was added to every well. The fluorescence was immediately recorded on a Spectra Max Gemini XPS fluorescent plate

reader. The excitation wavelength was set to 490 nm. Emission was recorded at 520 nm. Data was averaged across the three replicate wells. Data is plotted using the below equation:

$$\% \text{ leakage} = 100 * (F_{\text{peptide}} - F_{\text{water}})/(F_{\text{lysis buffer}} - F_{\text{water}})$$

Where F_{peptide} is the average fluorescence of the given peptide treatment, F_{water} is the average fluorescence of the water treatments, and $F_{\text{lysis buffer}}$ is the average fluorescence of the lysis buffer treatment.

4.4.15 Circular dichroism spectroscopy

CD spectra were acquired on a Jasco J-810 circular dichroism spectropolarimeter at ambient temperature (*ca.* 20 °C). A 50 µM solution of each peptide was prepared by diluting an appropriate amount of a 10 mg/mL stock solution of peptide with either 10 mM sodium phosphate buffer at pH 7.4 or 10 mM sodium phosphate buffer at pH 7.4 containing 1 mM lipids in a 1 mm quartz cuvette. Data were collected using 0.2 nm intervals from 260 nm to 190 nm and averaged over 5 accumulations.[99] Spectra were smoothed using Savitsky-Golay smoothing with a 21 point window. Data are graphed as mean residue ellipticity, [Θ], which is calculated as follows:[98,99]

$$[\Theta] = \text{millidegrees}/(\text{path length(mm)} \times [\text{peptide}]\ (\text{M}) \times \text{number of residues})$$

Data were omitted below wavelengths at which the voltage in the photomultiplier tube exceeded 600 V.

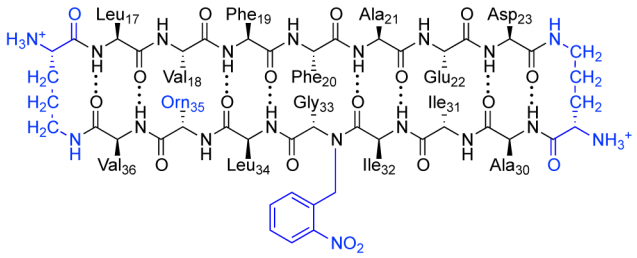

peptide **4.1**$_{NB}$

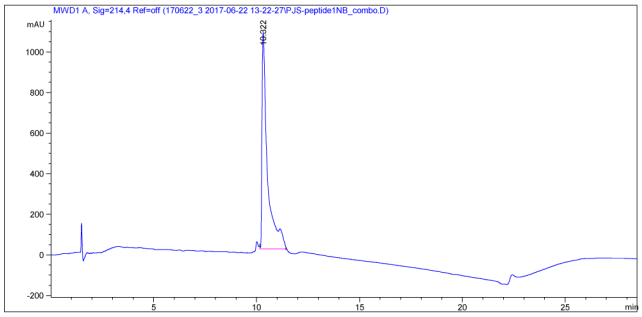

Calculated mass for peptide **4.1**$_{NB}$: 1865.0451

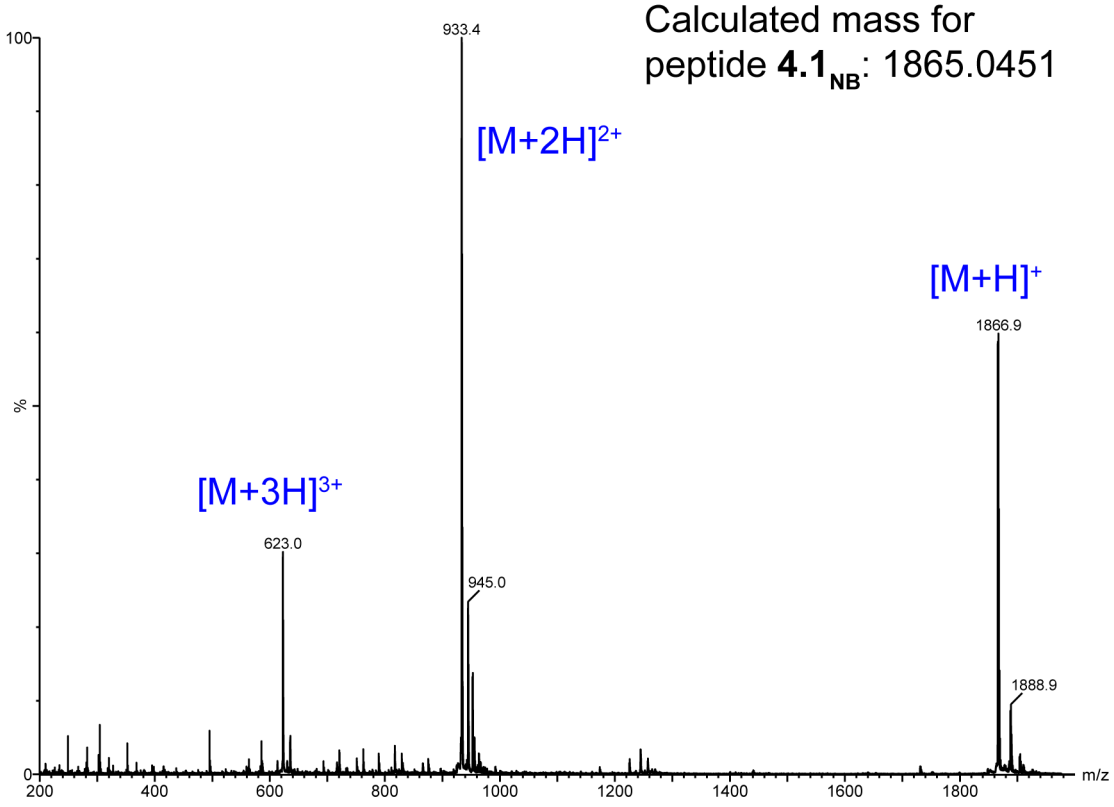

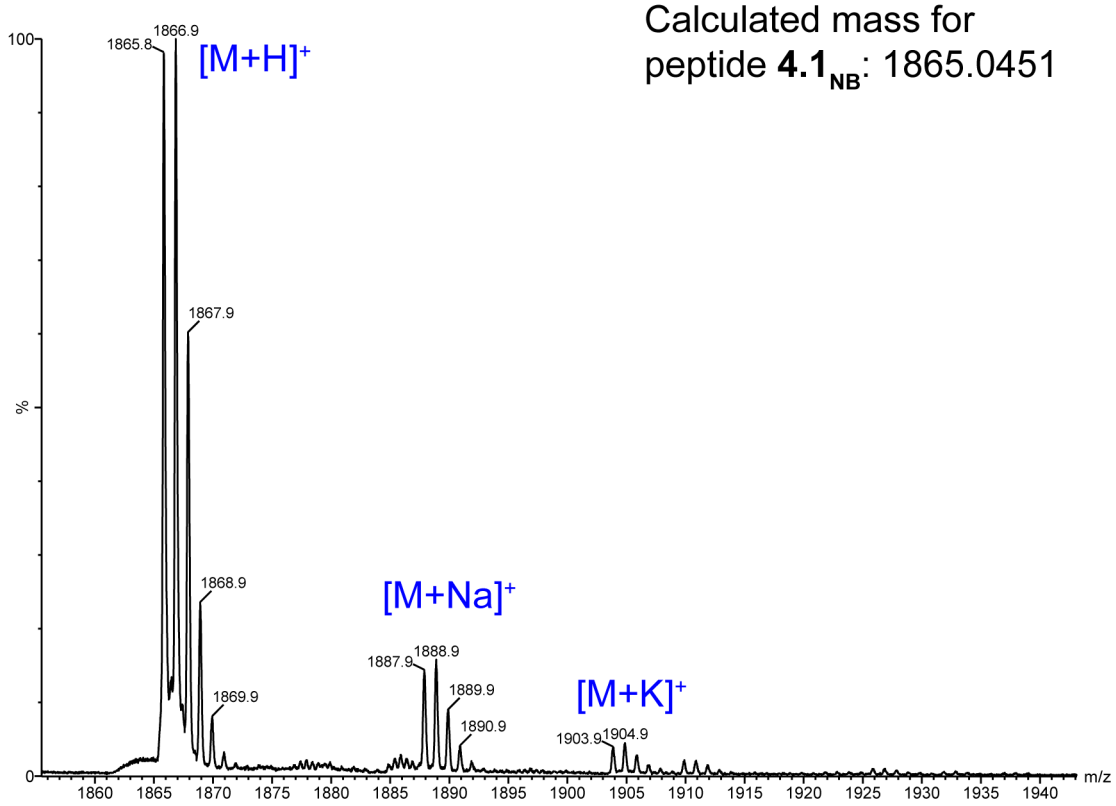
Calculated mass for peptide 4.1NB: 1865.0451
[M+H]+
[M+Na]+
[M+K]+
1865.8
1866.9
1867.9
1868.9
1869.9
1887.9
1888.9
1889.9
1890.9
1903.9
1904.9
100
%
0
m/z
1860
1865
1870
1875
1880
1885
1890
1895
1900
1905
1910
1915
1920
1925
1930
1935
1940

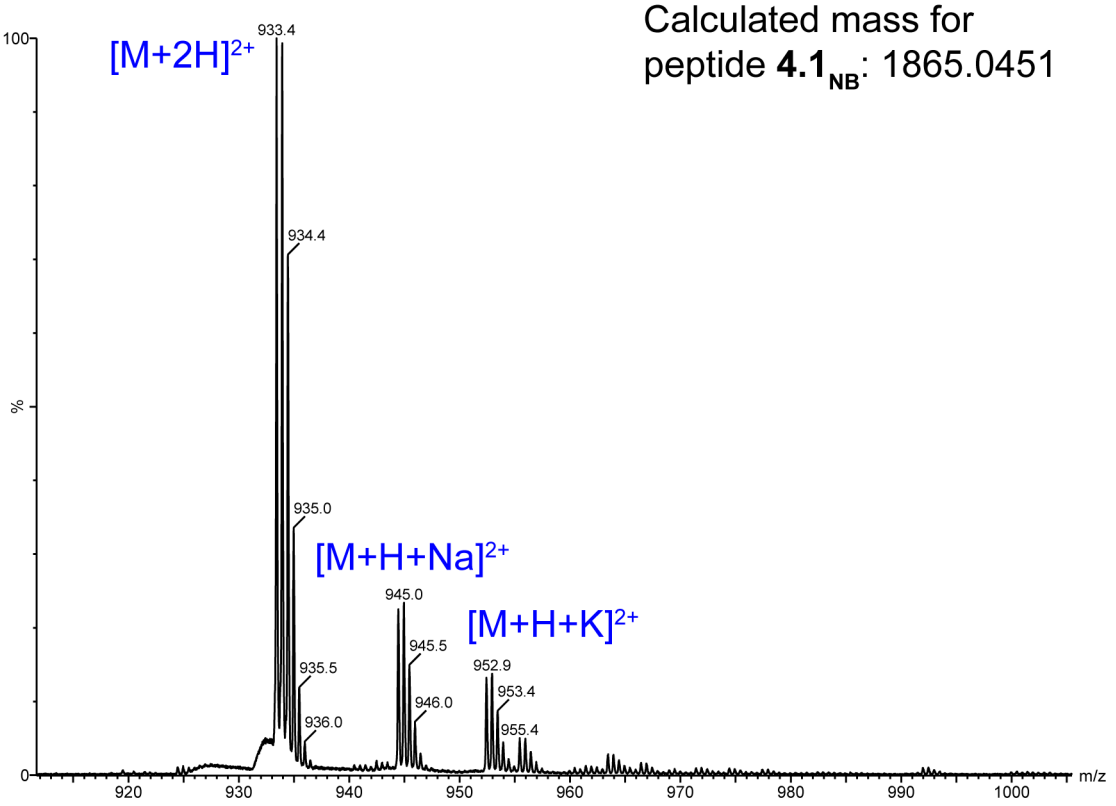
Calculated mass for peptide 4.1NB: 1865.0451
[M+2H]2+
[M+H+Na]2+
[M+H+K]2+
933.4
934.4
935.0
935.5
936.0
945.0
945.5
946.0
952.9
953.4
955.4
100
%
0
m/z
920
930
940
950
960
970
980
990
1000

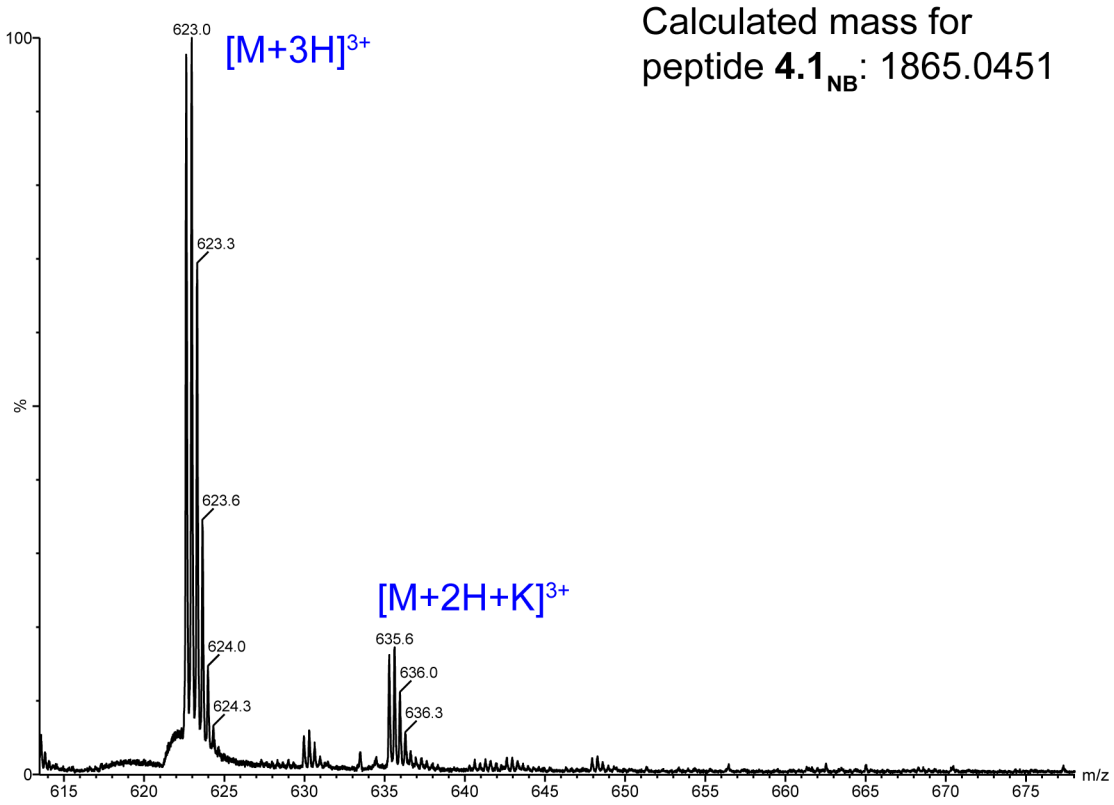
Calculated mass for peptide 4.1NB: 1865.0451
[M+3H]3+
[M+2H+K]3+
623.0
623.3
623.6
624.0
624.3
635.6
636.0
636.3
100
%
0
615
620
625
630
635
640
645
650
655
660
665
670
675
m/z

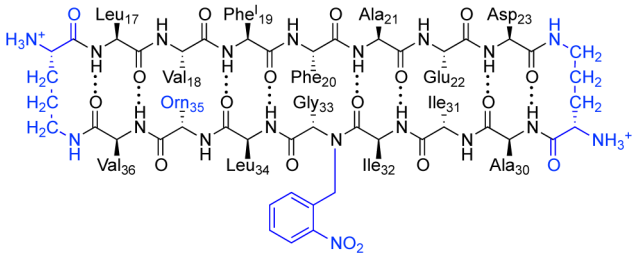

peptide **4.1$^{I}_{NB}$**

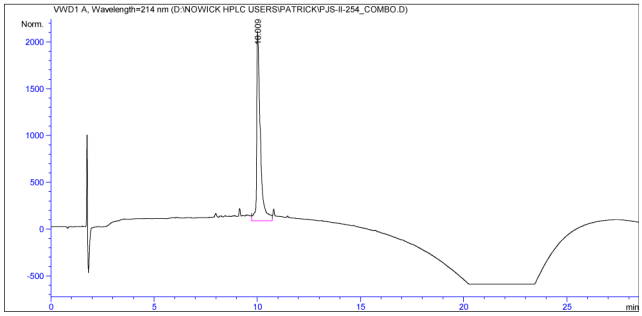

Calculated mass for peptide **4.1$^{I}_{NB}$**: 1990.9418

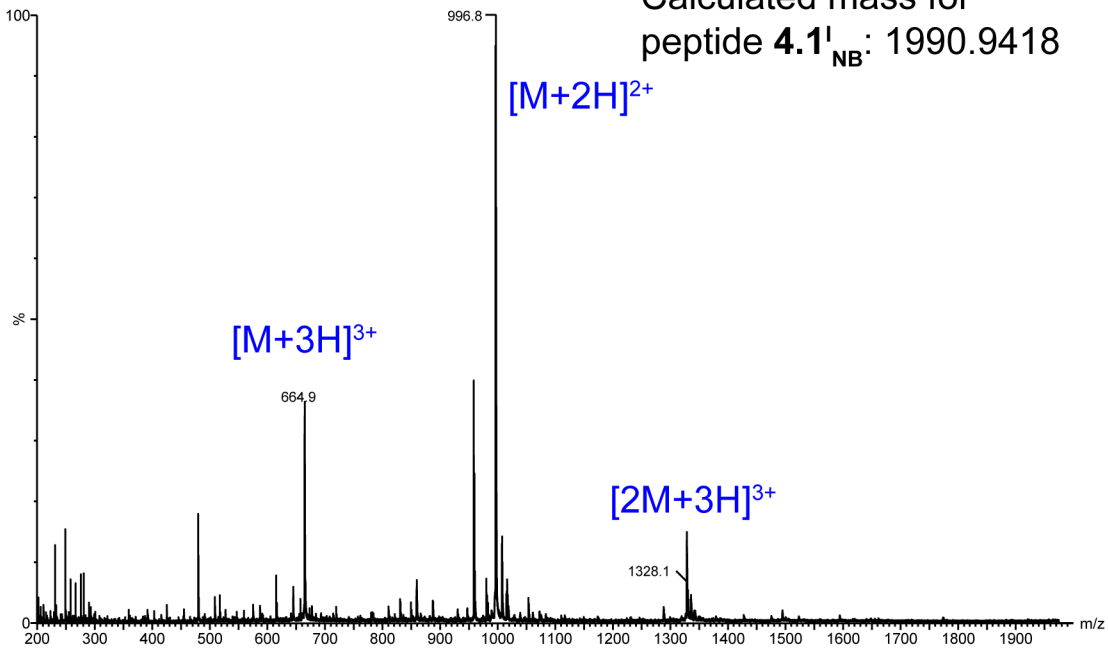

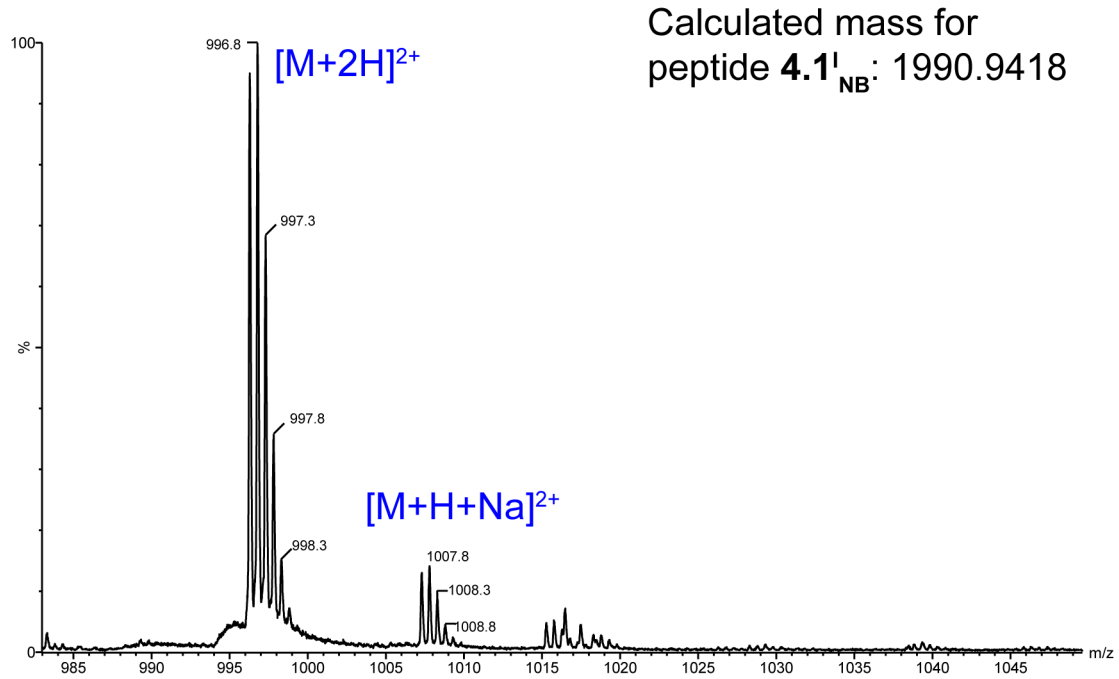
Calculated mass for peptide 4.1I NB: 1990.9418
[M+2H]2+
996.8
997.3
997.8
998.3
[M+H+Na]2+
1007.8
1008.3
1008.8
100
%
0
985 990 995 1000 1005 1010 1015 1020 1025 1030 1035 1040 1045
m/z

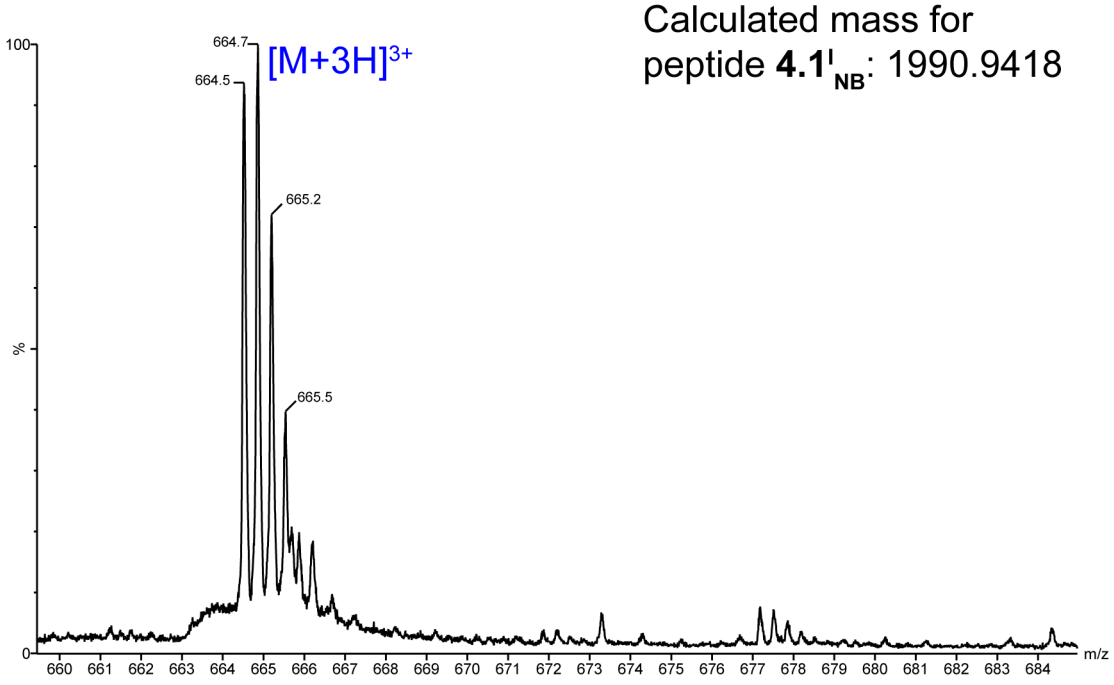
Calculated mass for peptide 4.1I NB: 1990.9418
[M+3H]3+
664.7
664.5
665.2
665.5
100
%
0
660 661 662 663 664 665 666 667 668 669 670 671 672 673 674 675 676 677 678 679 680 681 682 683 684
m/z

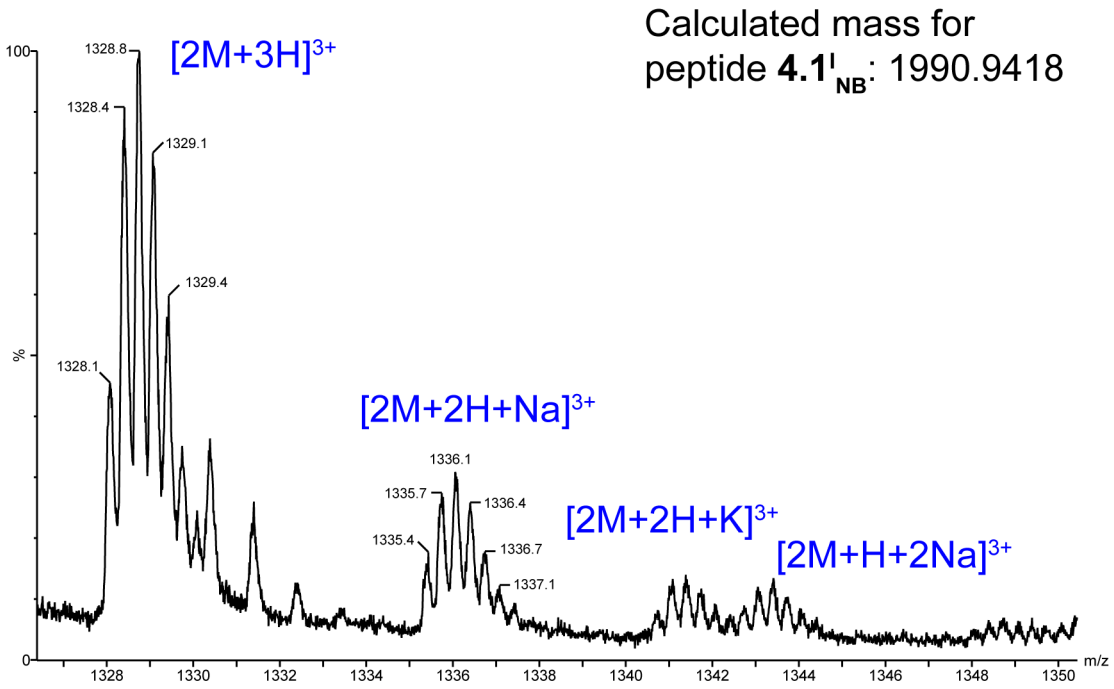
Calculated mass for peptide 4.1I NB: 1990.9418
[2M+3H]3+
[2M+2H+Na]3+
[2M+2H+K]3+
[2M+H+2Na]3+
1328.8
1328.4
1329.1
1329.4
1328.1
1336.1
1335.7
1336.4
1335.4
1336.7
1337.1
100
%
0
1328
1330
1332
1334
1336
1338
1340
1342
1344
1346
1348
1350
m/z

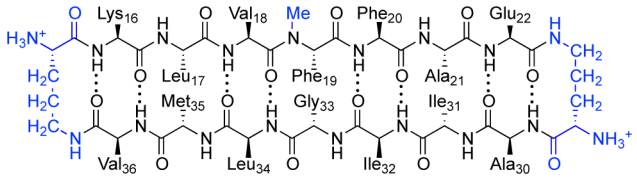

peptide **4.2**

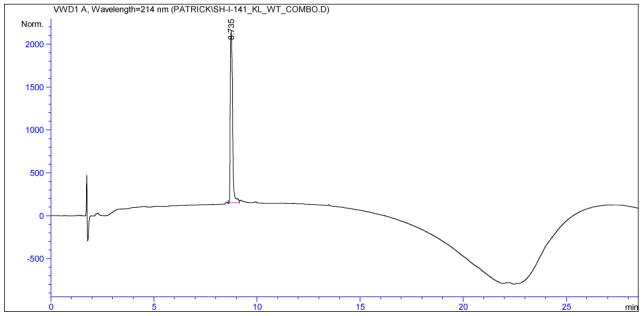

Calculated mass for peptide **4.2**: 1774.0579

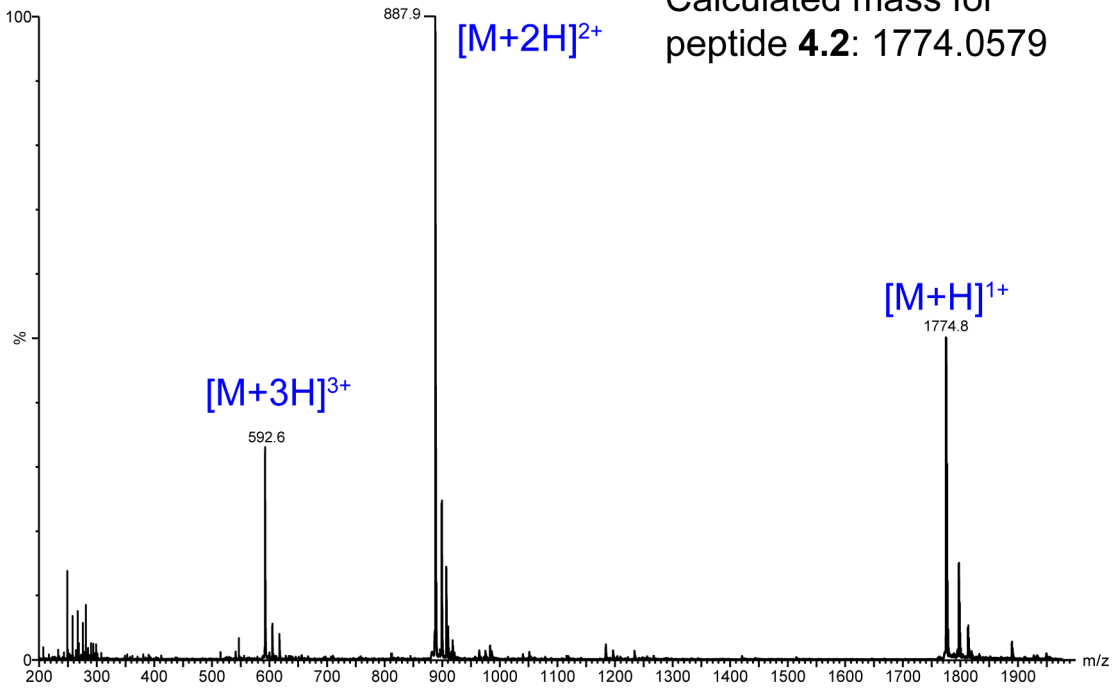

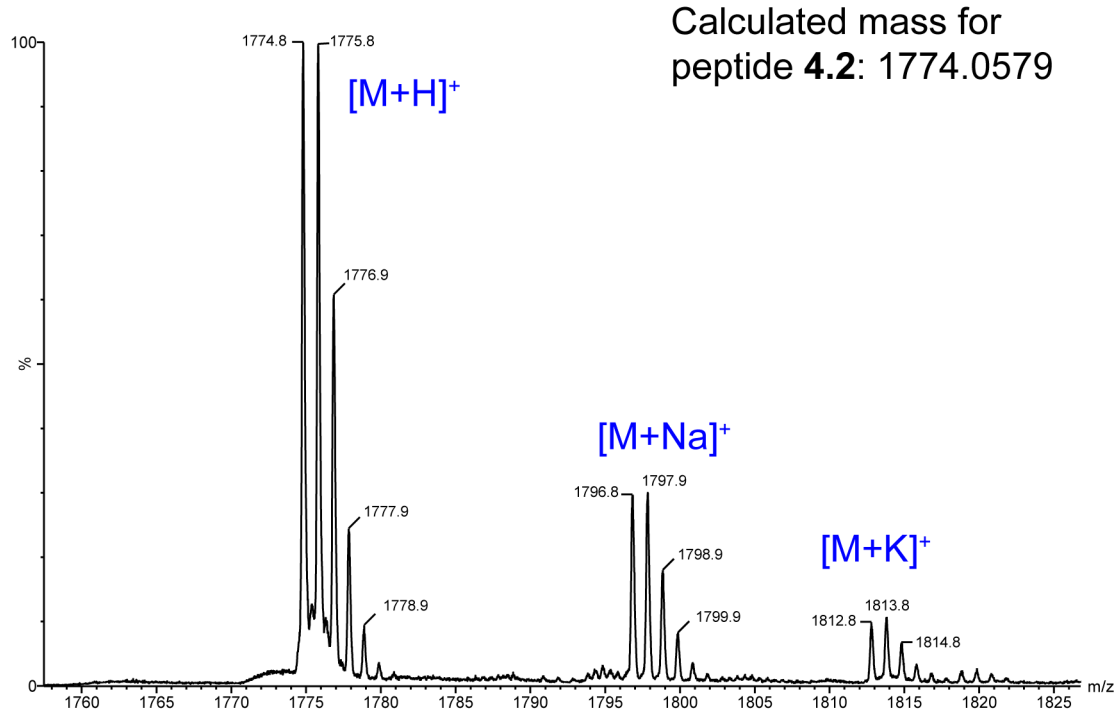
Calculated mass for peptide **4.2**: 1774.0579
[M+H]+
[M+Na]+
[M+K]+
1774.8
1775.8
1776.9
1777.9
1778.9
1796.8
1797.9
1798.9
1799.9
1812.8
1813.8
1814.8
100
%
0
m/z
1760
1765
1770
1775
1780
1785
1790
1795
1800
1805
1810
1815
1820
1825

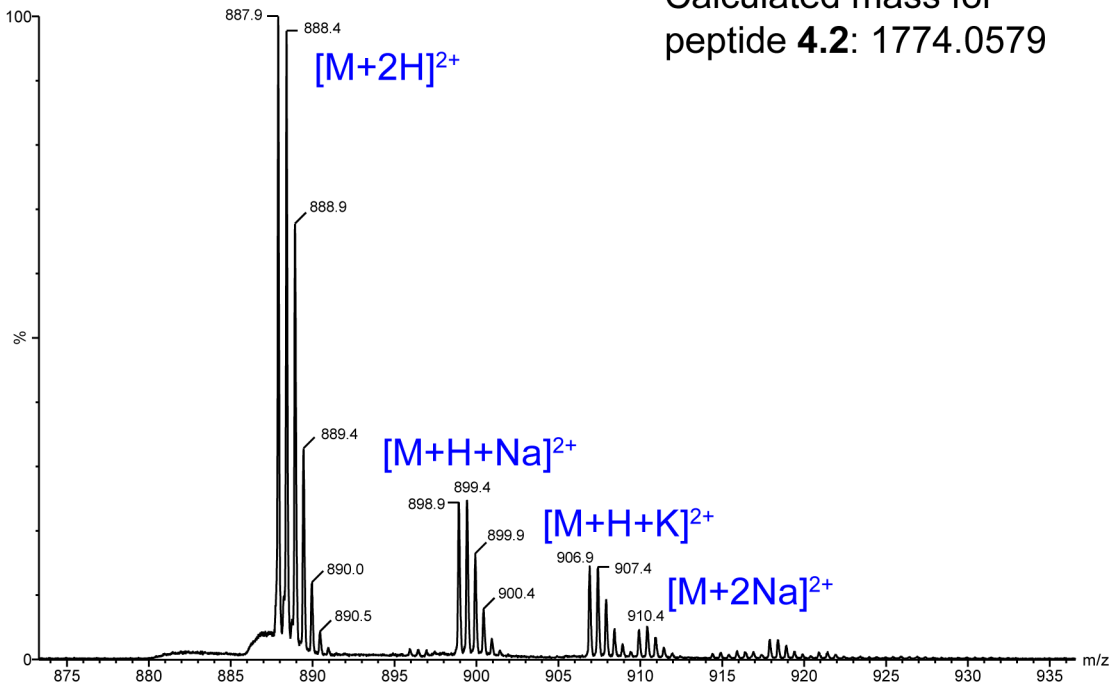
Calculated mass for peptide **4.2**: 1774.0579
[M+2H]2+
[M+H+Na]2+
[M+H+K]2+
[M+2Na]2+
887.9
888.4
888.9
889.4
890.0
890.5
898.9
899.4
899.9
900.4
906.9
907.4
910.4
100
%
0
m/z
875
880
885
890
895
900
905
910
915
920
925
930
935

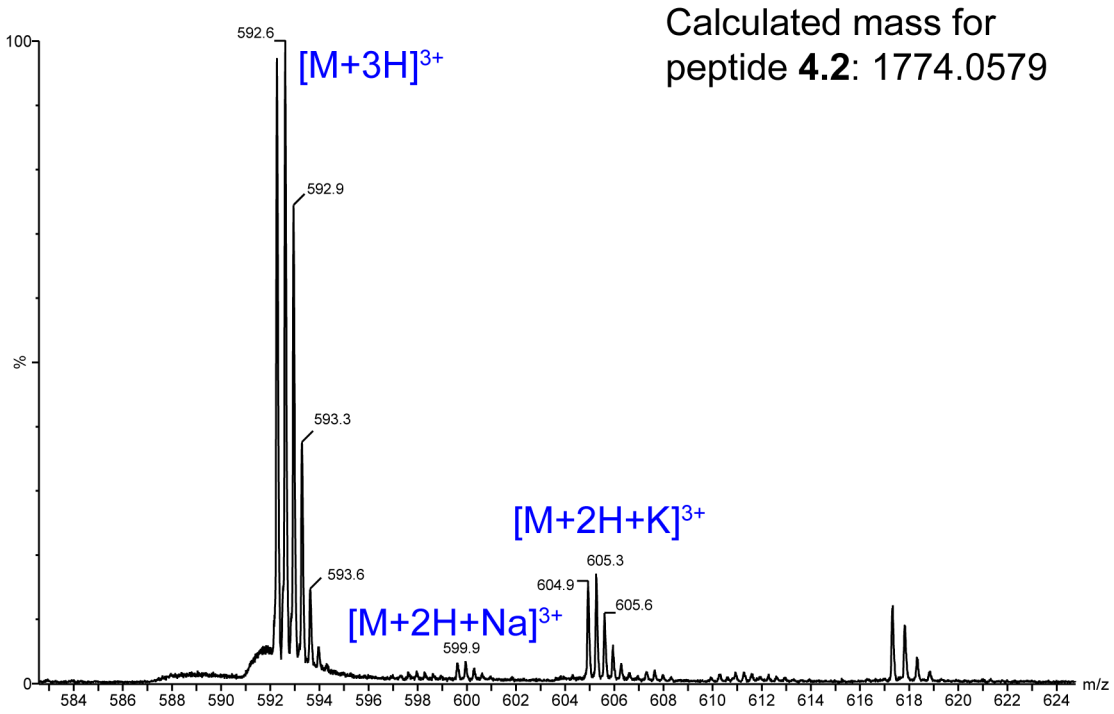
Calculated mass for peptide **4.2**: 1774.0579
[M+3H]3+
[M+2H+K]3+
[M+2H+Na]3+
592.6
592.9
593.3
593.6
599.9
604.9
605.3
605.6
100
%
0
584 586 588 590 592 594 596 598 600 602 604 606 608 610 612 614 616 618 620 622 624
m/z

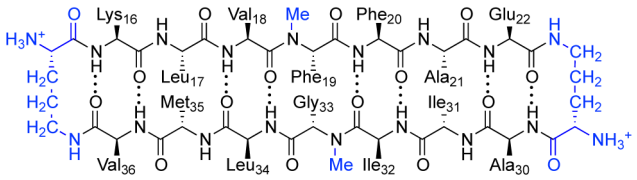

peptide **4.2**$_{\mathbf{Me}}$

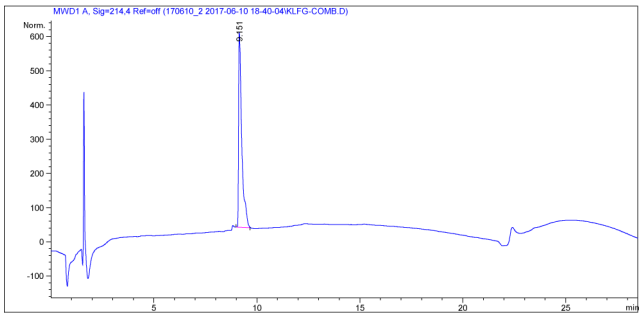

Calculated mass for peptide **4.2**$_{\mathbf{Me}}$: 1788.0736

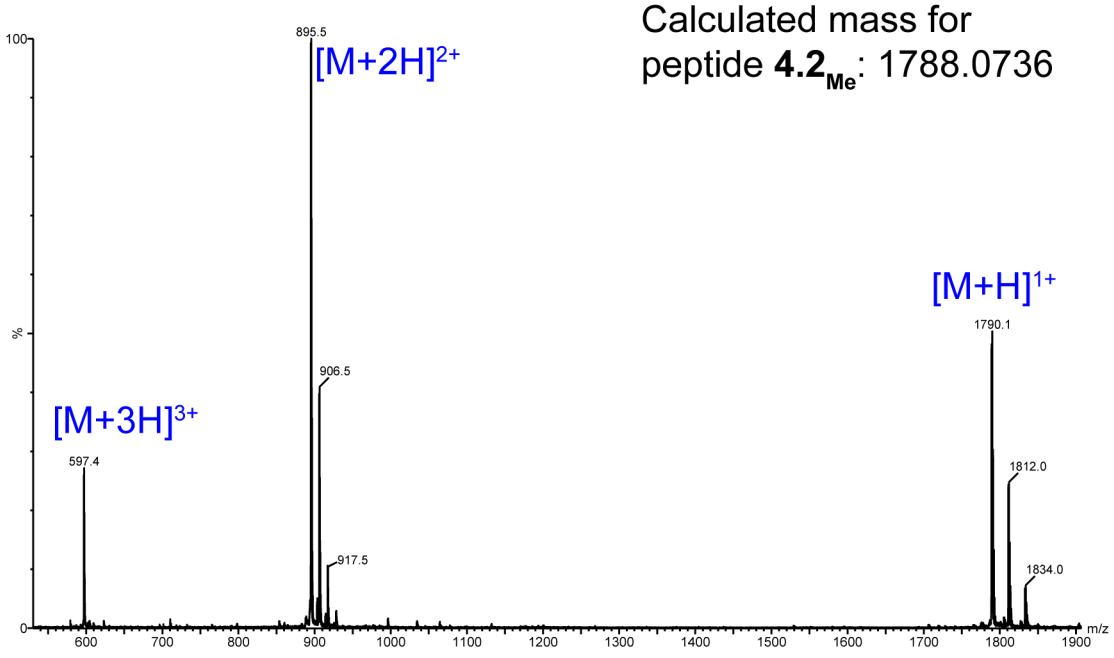

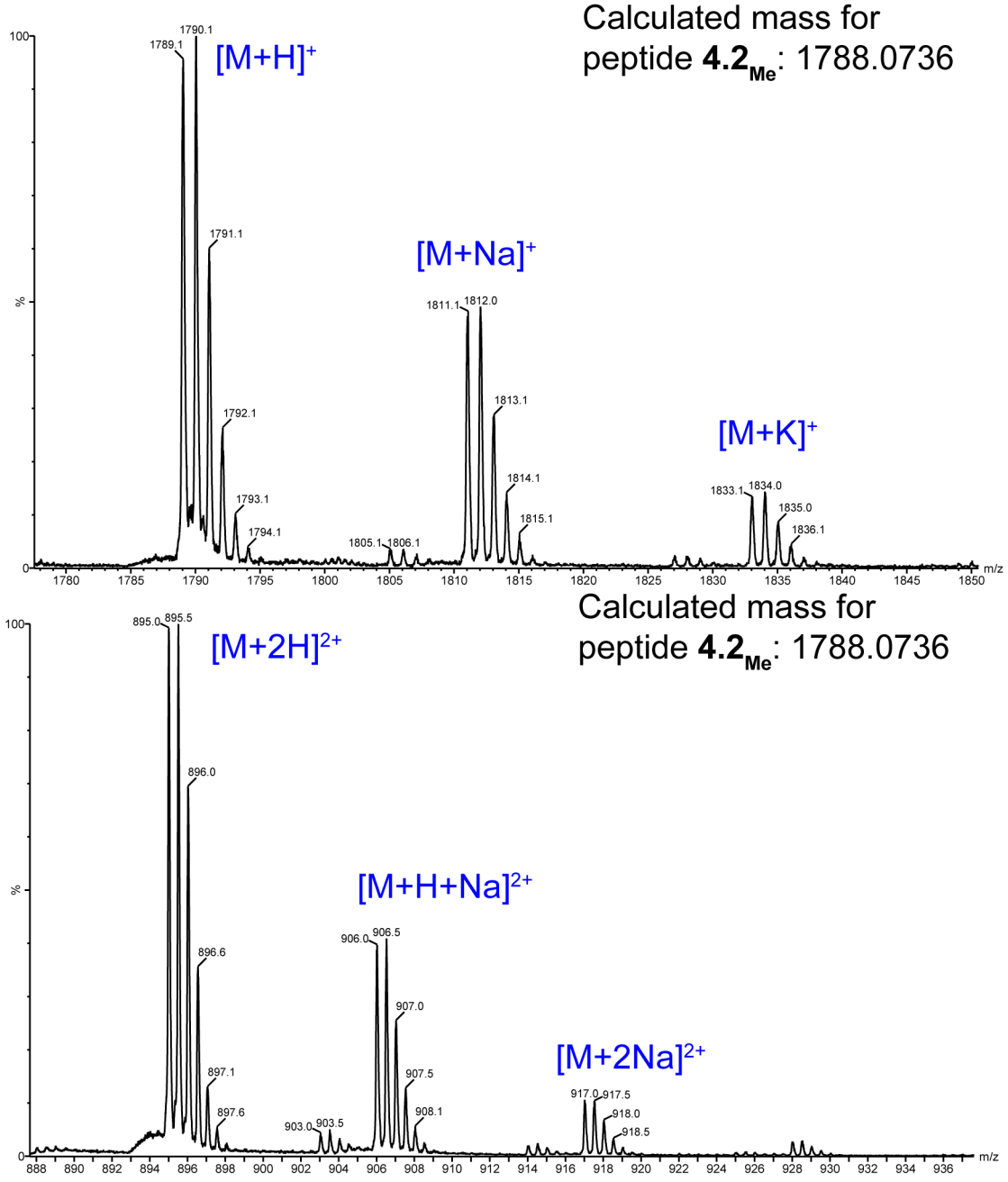
Calculated mass for peptide 4.2Me: 1788.0736
[M+H]+
[M+Na]+
[M+K]+
[M+2H]2+
[M+H+Na]2+
[M+2Na]2+
m/z
%

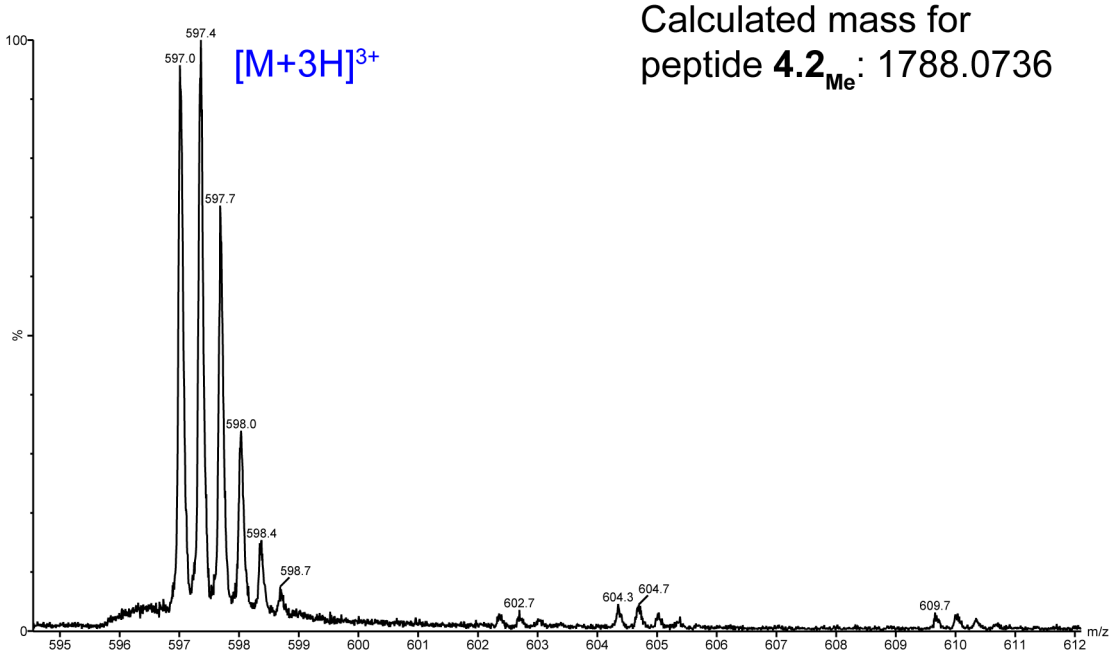

Calculated mass for peptide **4.2**$_{\mathbf{Me}}$: 1788.0736

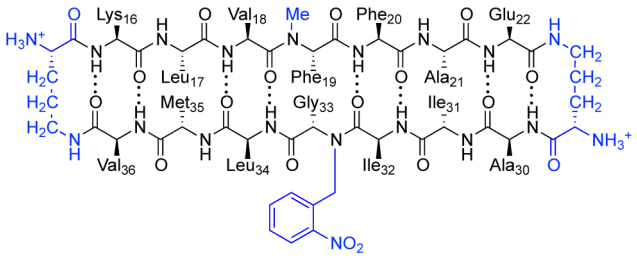

peptide **4.2**$_{NB}$

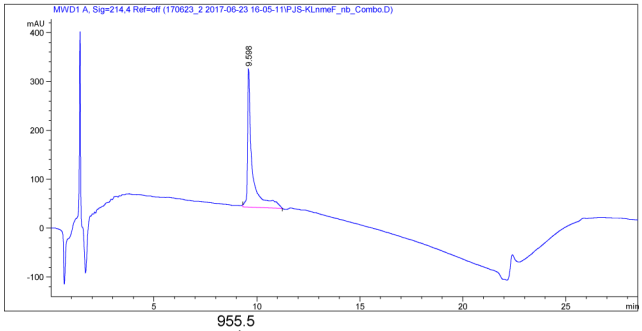

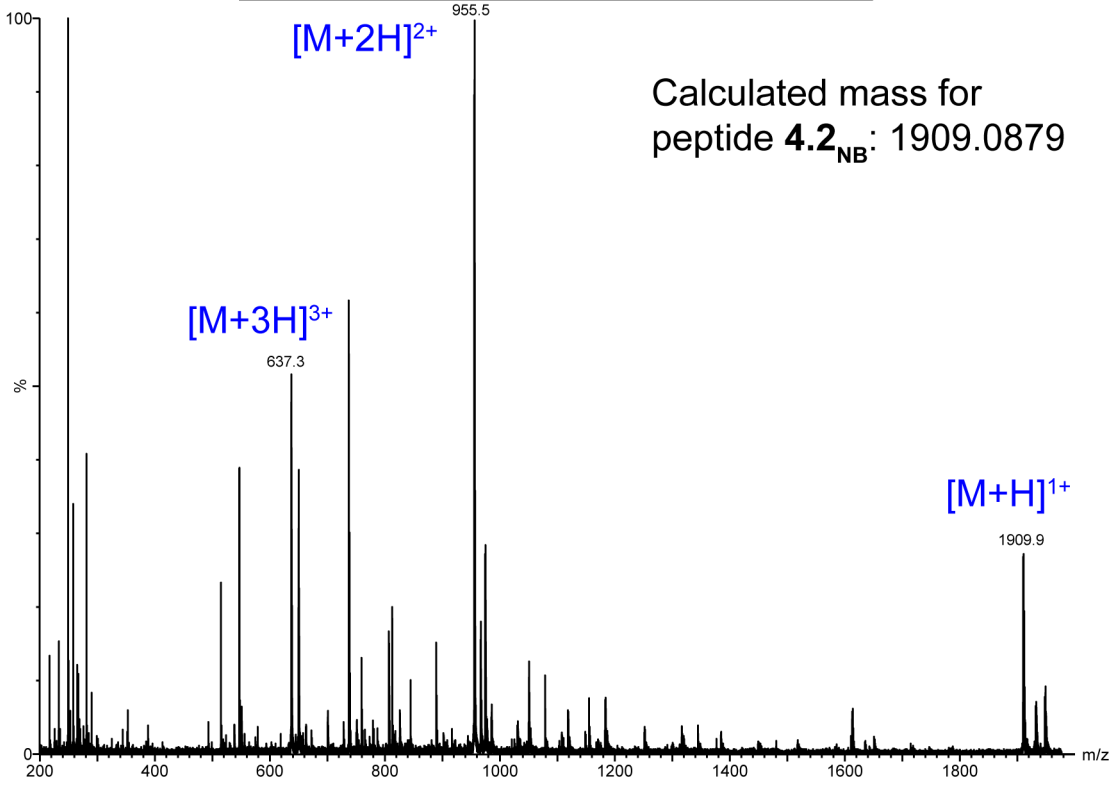

Calculated mass for peptide **4.2**$_{NB}$: 1909.0879

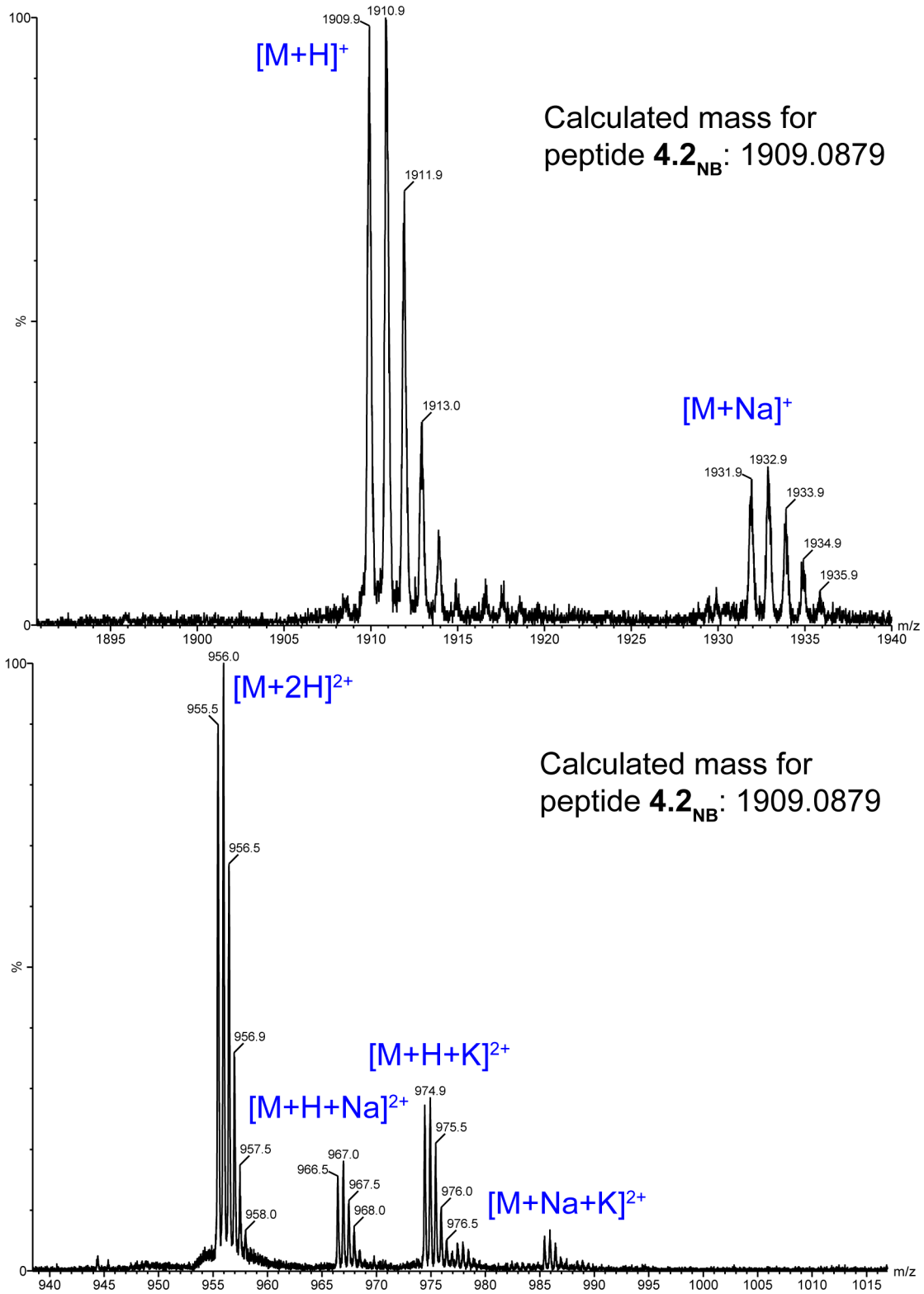
[M+H]+
Calculated mass for peptide 4.2NB: 1909.0879
[M+Na]+
[M+2H]2+
Calculated mass for peptide 4.2NB: 1909.0879
[M+H+K]2+
[M+H+Na]2+
[M+Na+K]2+
m/z
%

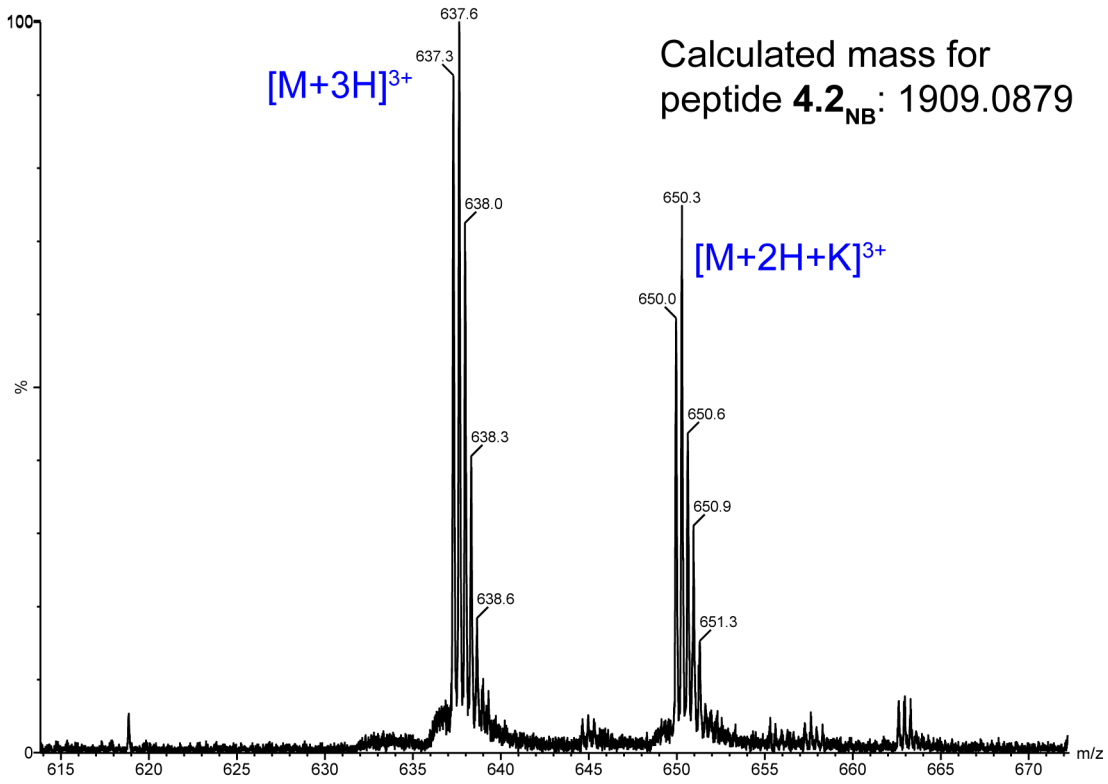
100
%
0
637.6
637.3
[M+3H]3+
638.0
638.3
638.6
650.3
[M+2H+K]3+
650.0
650.6
650.9
651.3
Calculated mass for
peptide 4.2NB: 1909.0879
615
620
625
630
635
640
645
650
655
660
665
670
m/z

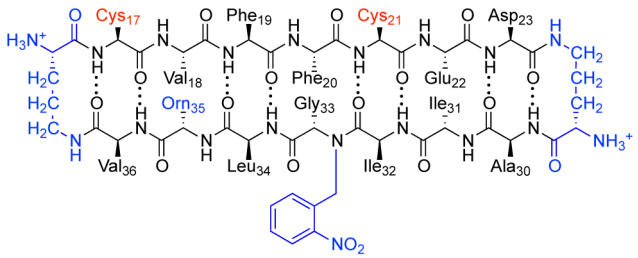

peptide **4.3**$_{NB}$

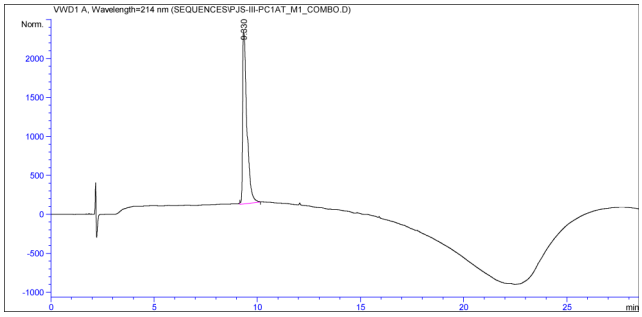

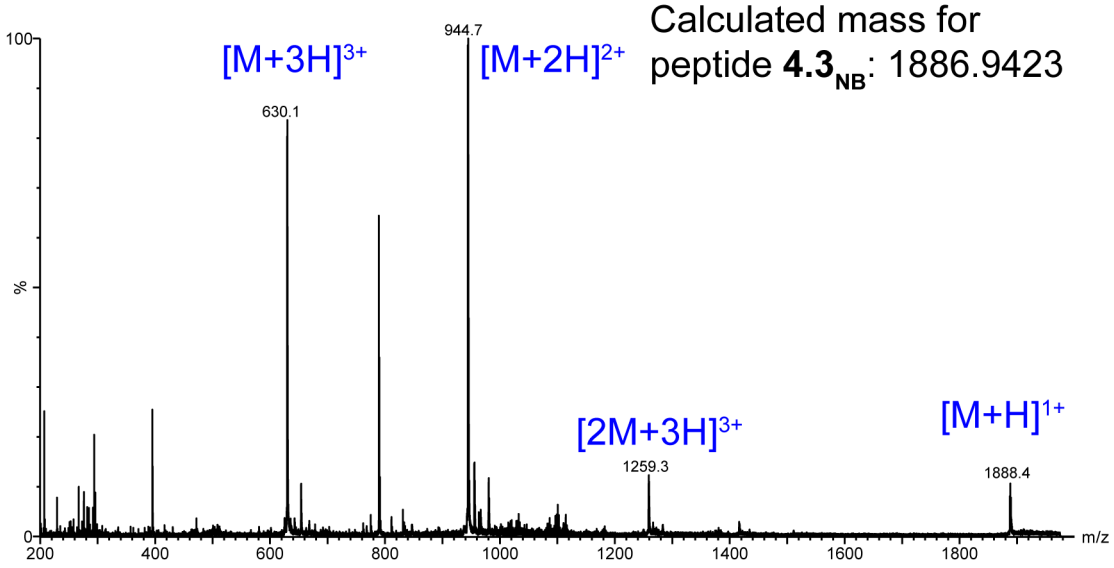

Calculated mass for peptide **4.3**$_{NB}$: 1886.9423

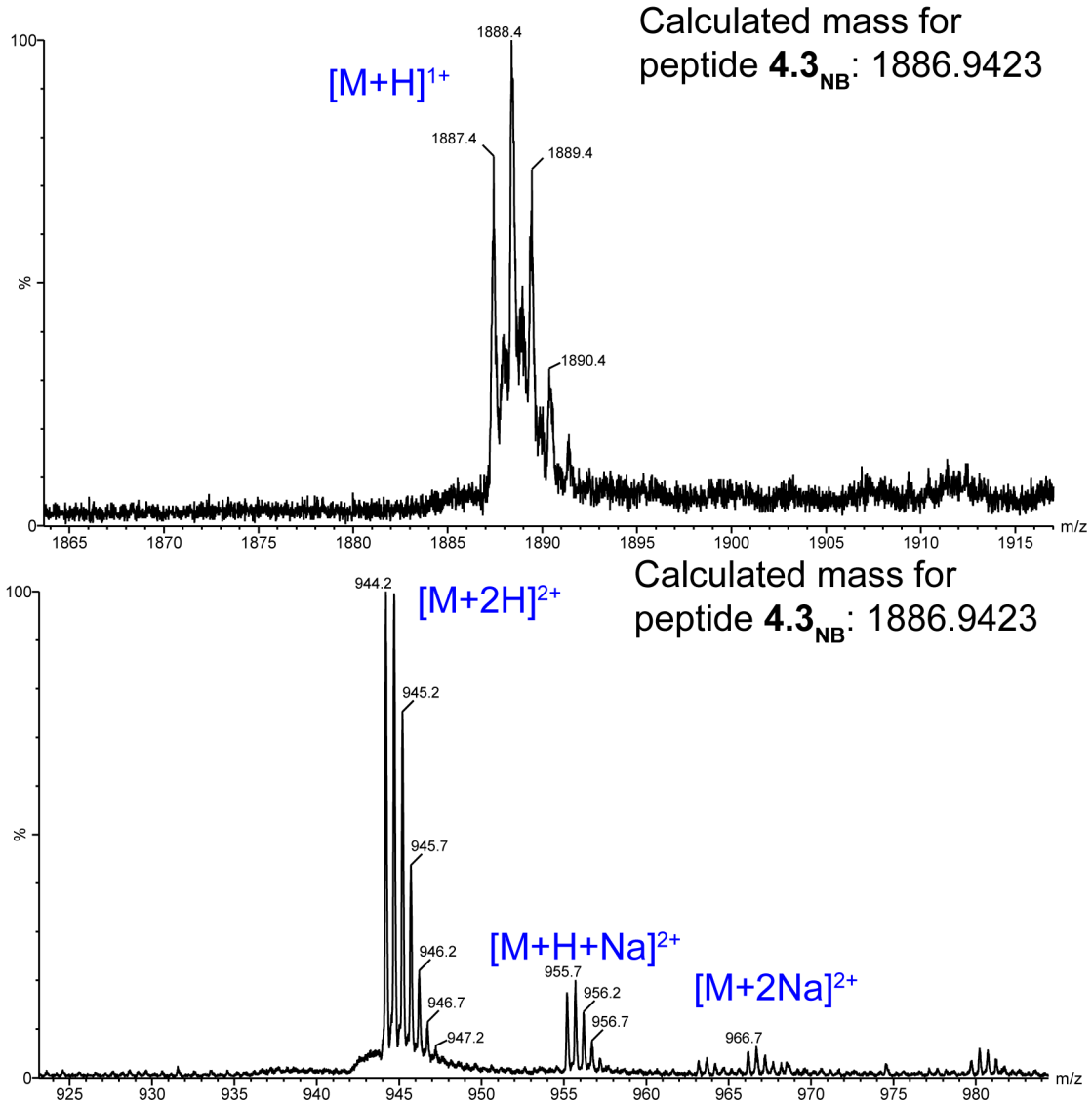
Calculated mass for peptide 4.3NB: 1886.9423
[M+H]1+
1888.4
1887.4
1889.4
1890.4
100
%
0
1865
1870
1875
1880
1885
1890
1895
1900
1905
1910
1915
m/z
Calculated mass for peptide 4.3NB: 1886.9423
[M+2H]2+
944.2
945.2
945.7
946.2
946.7
947.2
[M+H+Na]2+
955.7
956.2
956.7
[M+2Na]2+
966.7
100
%
0
925
930
935
940
945
950
955
960
965
970
975
980
m/z

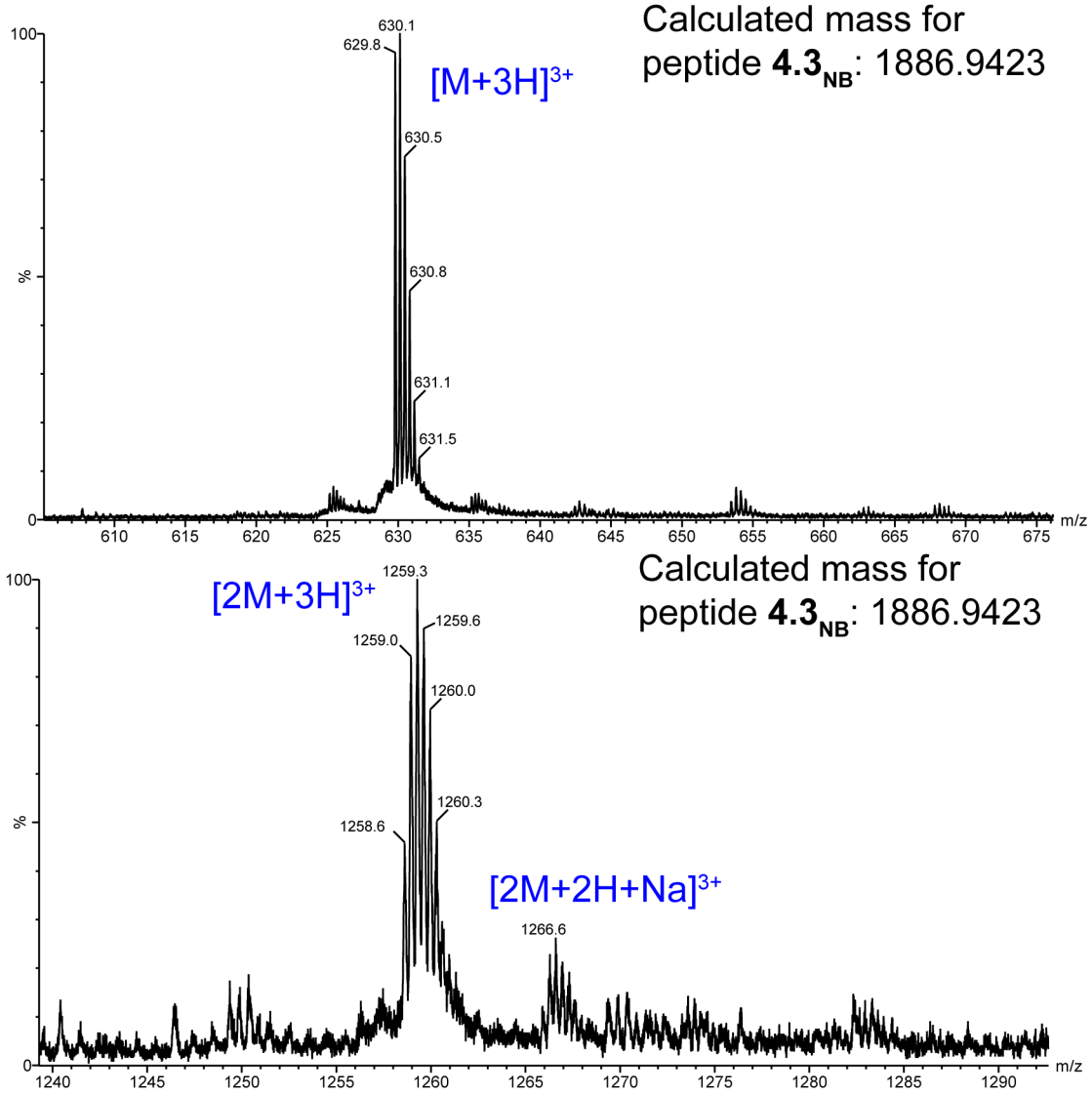
Calculated mass for peptide 4.3NB: 1886.9423
[M+3H]3+
630.1
629.8
630.5
630.8
631.1
631.5
100
%
0
610
615
620
625
630
635
640
645
650
655
660
665
670
675
m/z
[2M+3H]3+
Calculated mass for peptide 4.3NB: 1886.9423
1259.3
1259.6
1259.0
1260.0
1260.3
1258.6
[2M+2H+Na]3+
1266.6
100
%
0
1240
1245
1250
1255
1260
1265
1270
1275
1280
1285
1290
m/z

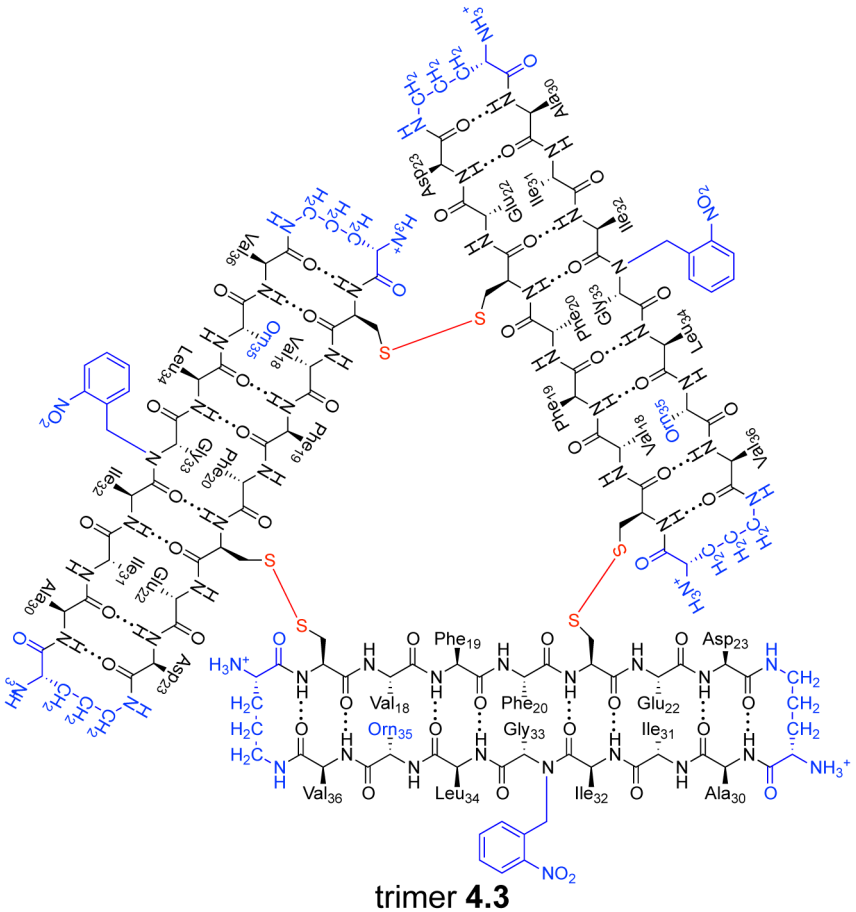

trimer **4.3**

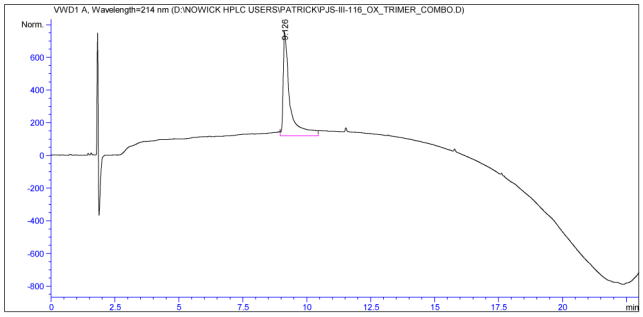
VWD1 A, Wavelength=214 nm (D:\NOWICK HPLC USERS\PATRICK\PJS-III-116_OX_TRIMER_COMBO.D)
Norm.
600
400
200
0
-200
-400
-600
-800
0
2.5
5
7.5
10
12.5
15
17.5
20
min

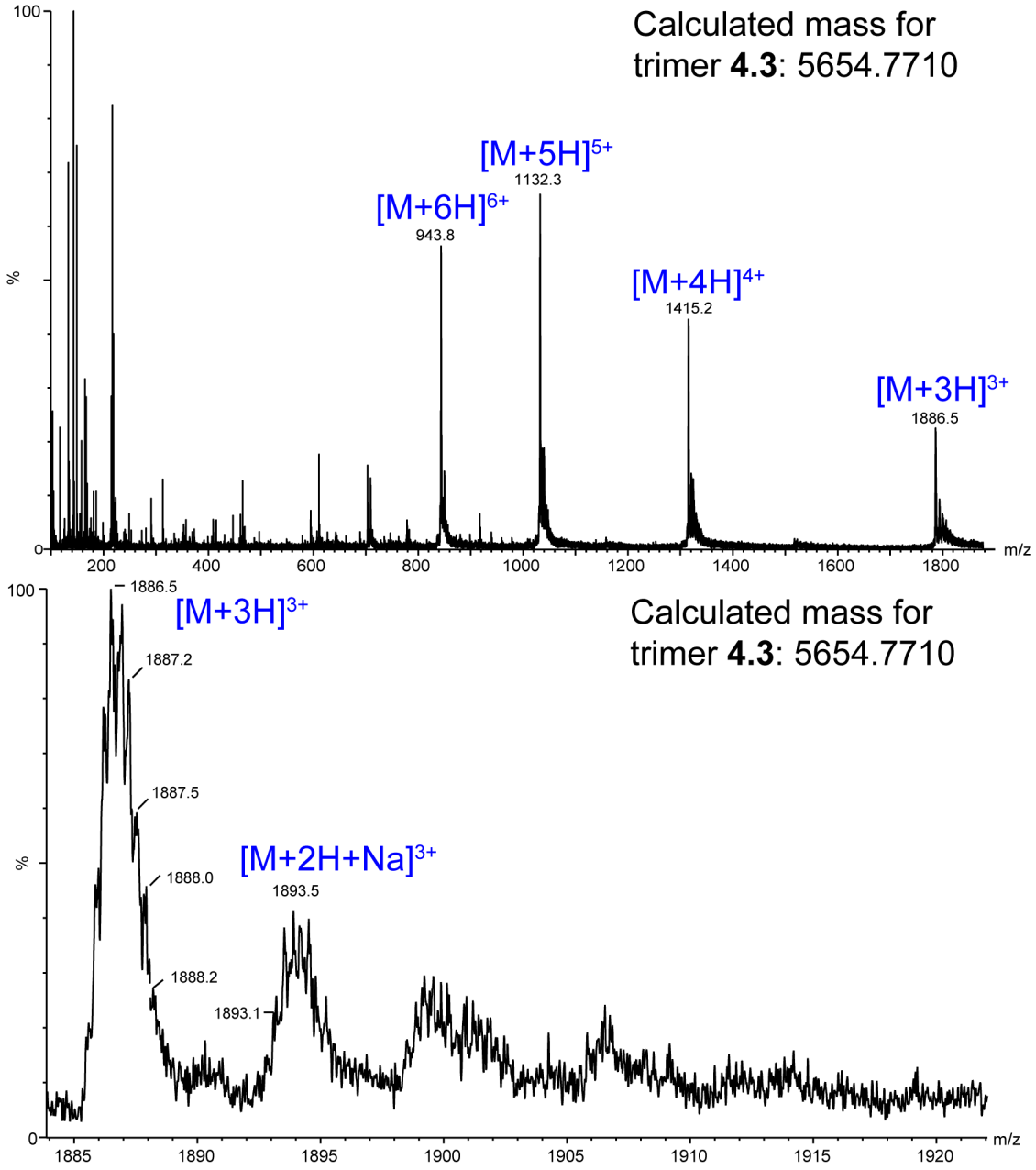
Calculated mass for
trimer **4.3**: 5654.7710
[M+6H]6+
943.8
[M+5H]5+
1132.3
[M+4H]4+
1415.2
[M+3H]3+
1886.5
100
%
0
200
400
600
800
1000
1200
1400
1600
1800
m/z
[M+3H]3+
1886.5
1887.2
1887.5
1888.0
1888.2
[M+2H+Na]3+
1893.5
1893.1
Calculated mass for
trimer **4.3**: 5654.7710
100
%
0
1885
1890
1895
1900
1905
1910
1915
1920
m/z

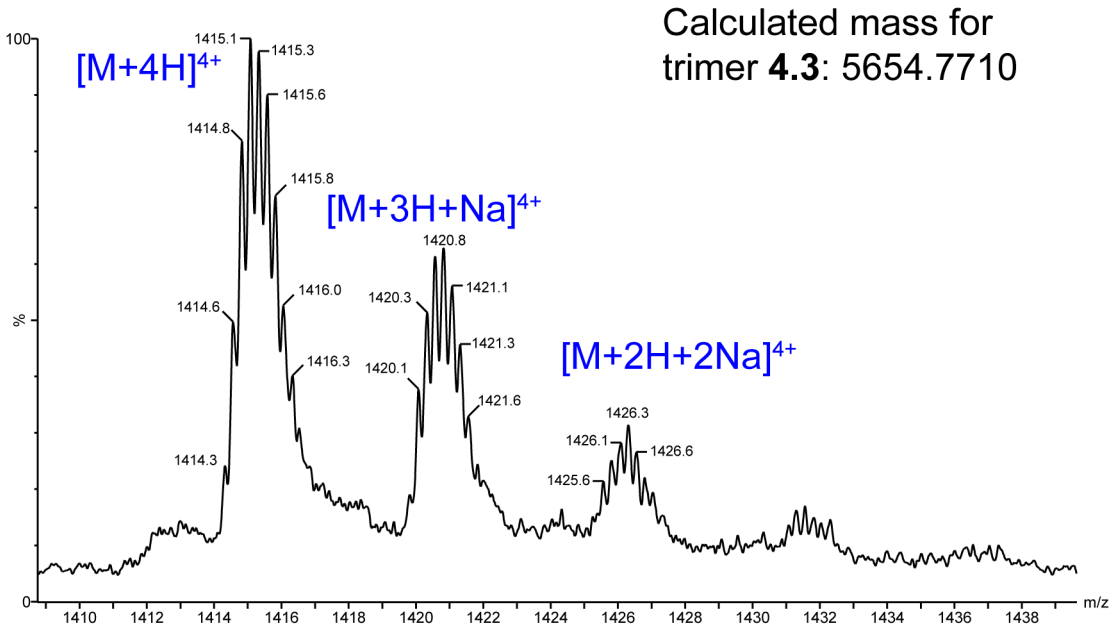
Calculated mass for
trimer **4.3**: 5654.7710
[M+4H]4+
[M+3H+Na]4+
[M+2H+2Na]4+
1415.1
1415.3
1415.6
1414.8
1415.8
1416.0
1414.6
1416.3
1414.3
1420.8
1420.3
1421.1
1421.3
1420.1
1421.6
1426.3
1426.1
1426.6
1425.6
100
%
0
1410
1412
1414
1416
1418
1420
1422
1424
1426
1428
1430
1432
1434
1436
1438
m/z

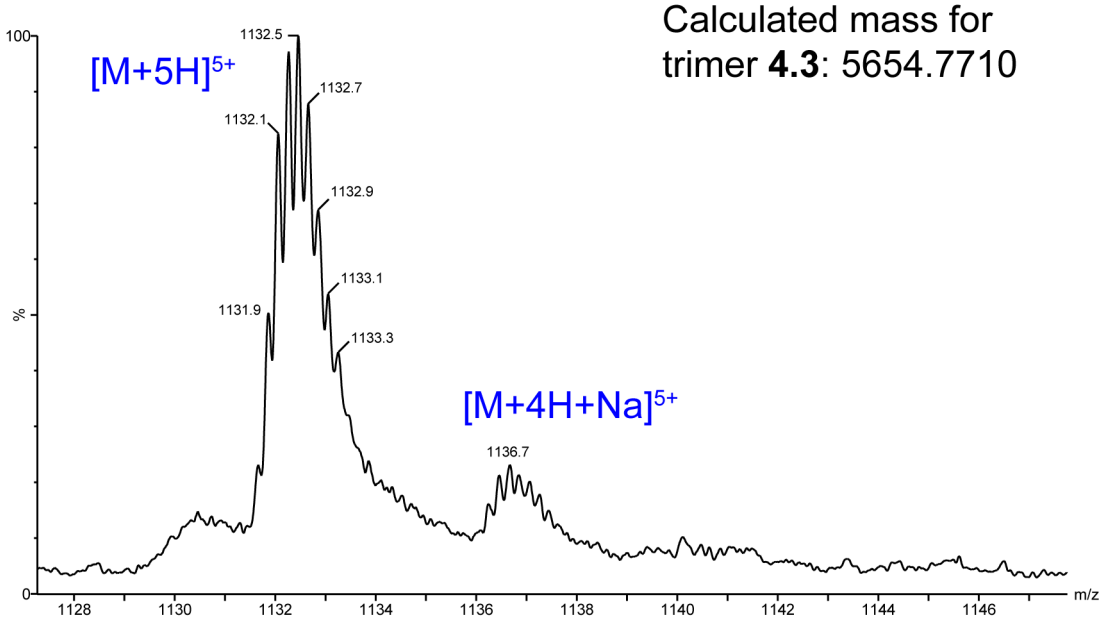
Calculated mass for
trimer **4.3**: 5654.7710
[M+5H]5+
[M+4H+Na]5+
1132.5
1132.7
1132.1
1132.9
1133.1
1131.9
1133.3
1136.7
100
%
0
1128
1130
1132
1134
1136
1138
1140
1142
1144
1146
m/z

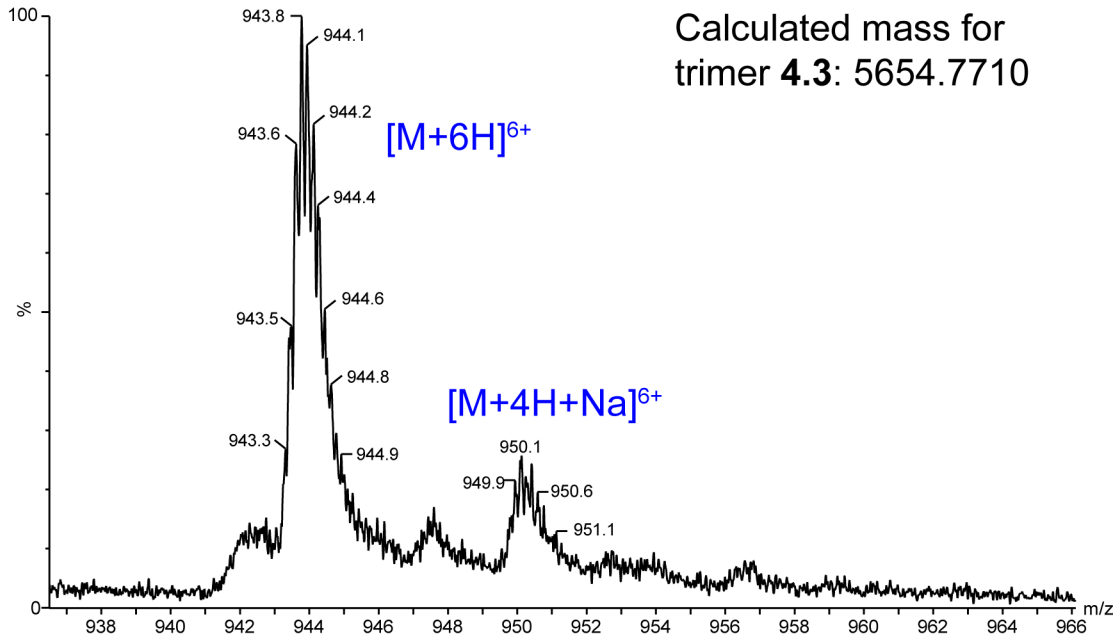
Calculated mass for
trimer **4.3**: 5654.7710
[M+6H]6+
[M+4H+Na]6+
943.8
944.1
944.2
943.6
944.4
944.6
943.5
944.8
943.3
944.9
950.1
949.9
950.6
951.1
100
%
0
938
940
942
944
946
948
950
952
954
956
958
960
962
964
966
m/z

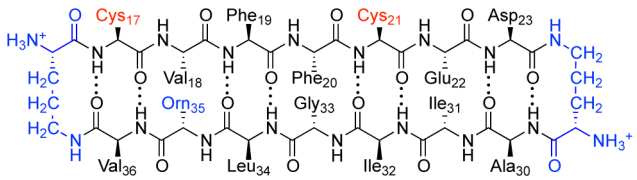
Cys17
Phe19
Cys21
Asp23
Val18
Phe20
Glu22
Orn35
Gly33
Ile31
Val36
Leu34
Ile32
Ala30

peptide **4.4**

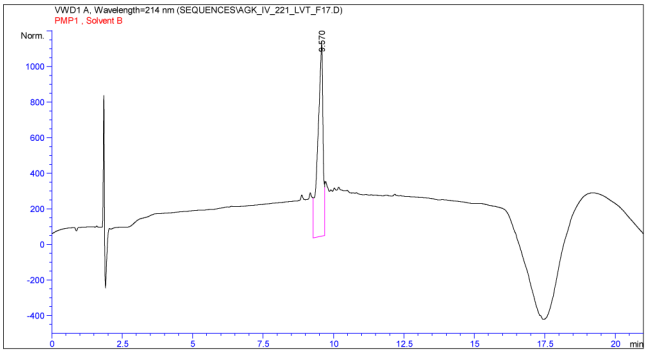
VWD1 A, Wavelength=214 nm (SEQUENCES\AGK_IV_221_LVT_F17.D)
PMP1 , Solvent B
Norm.
min

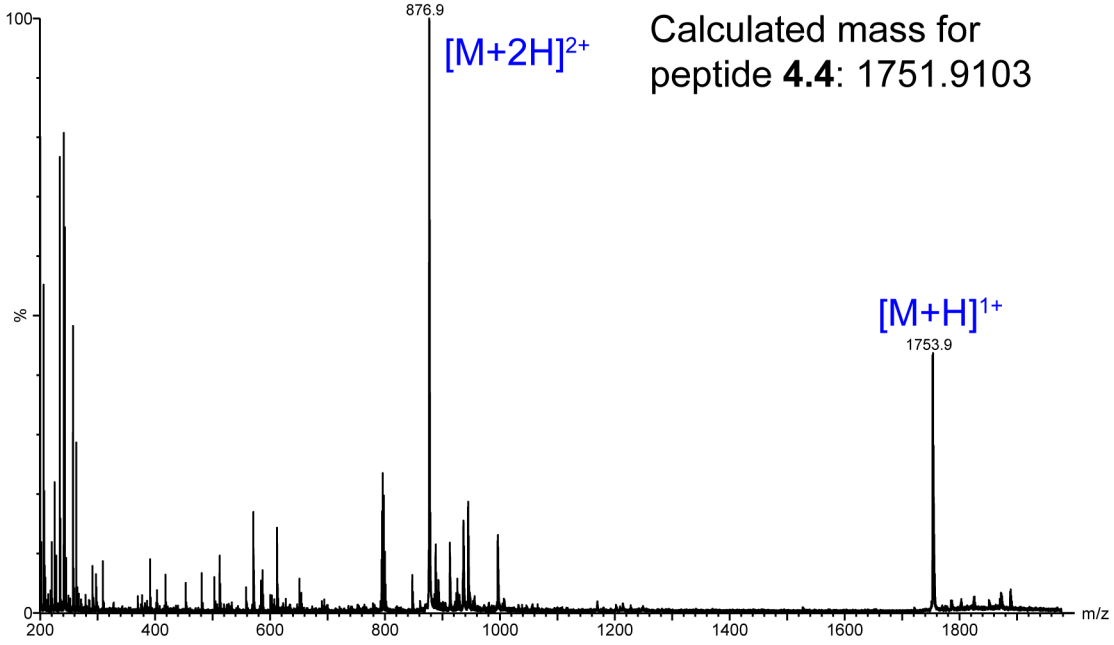
876.9
[M+2H]2+
Calculated mass for peptide 4.4: 1751.9103
[M+H]1+
1753.9
%
m/z

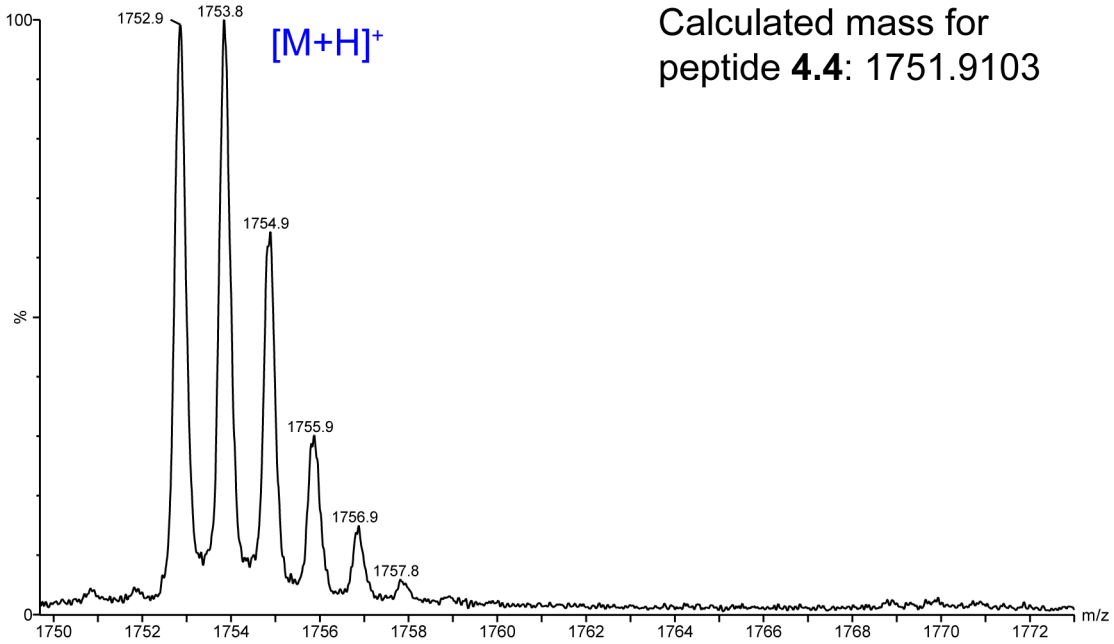
[M+H]+
Calculated mass for peptide 4.4: 1751.9103
1752.9
1753.8
1754.9
1755.9
1756.9
1757.8
100
%
0
1750
1752
1754
1756
1758
1760
1762
1764
1766
1768
1770
1772
m/z

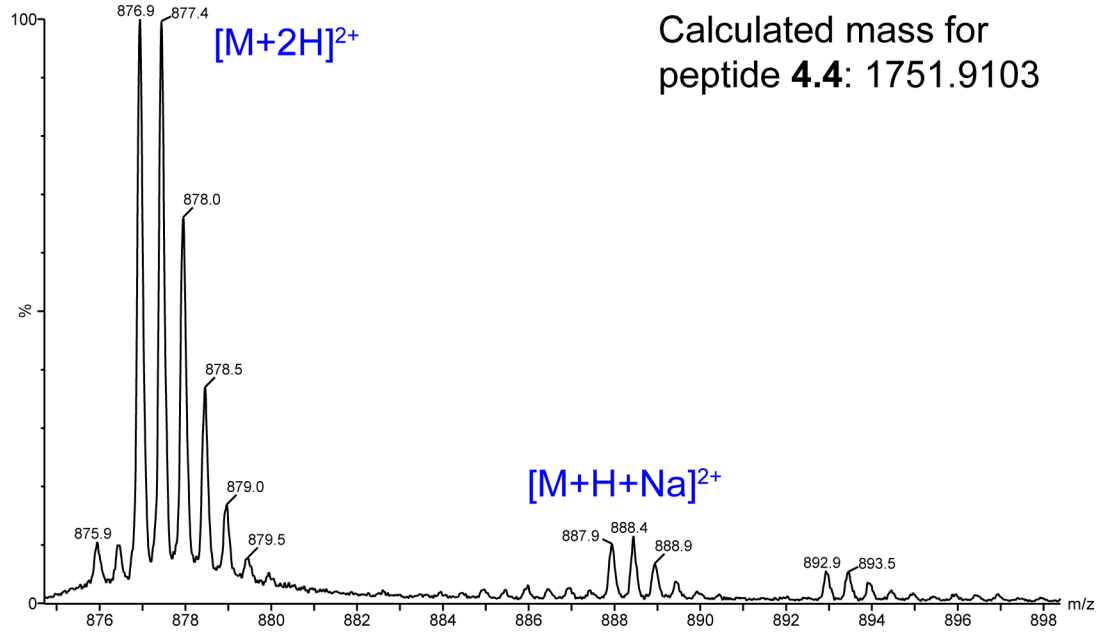
[M+2H]2+
Calculated mass for peptide 4.4: 1751.9103
[M+H+Na]2+
876.9
877.4
878.0
878.5
879.0
879.5
875.9
887.9
888.4
888.9
892.9
893.5
100
%
0
876
878
880
882
884
886
888
890
892
894
896
898
m/z

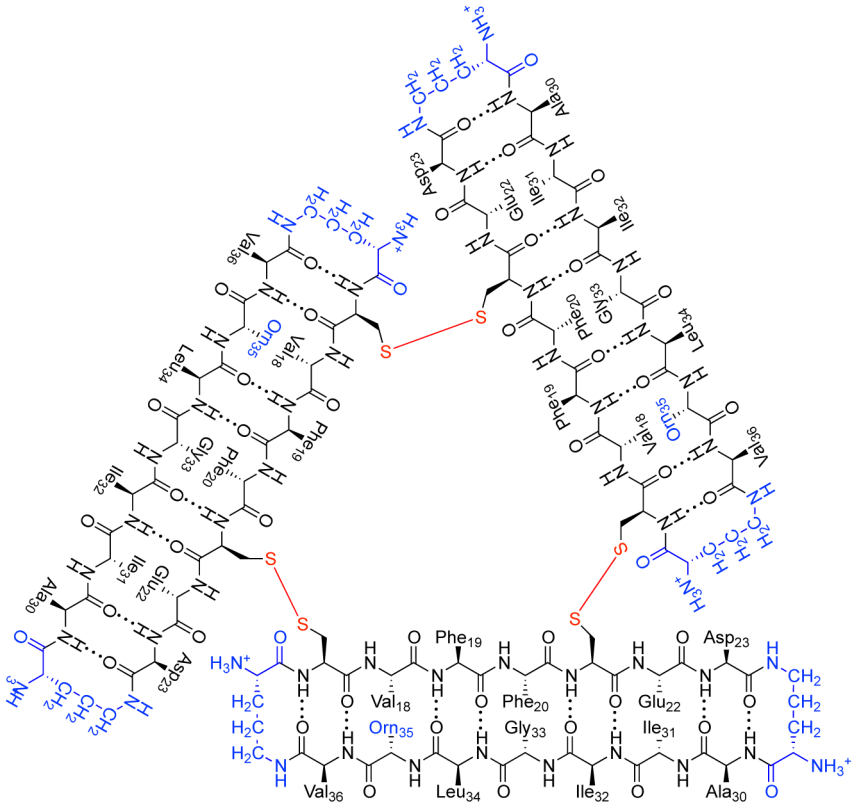

trimer **4.4**

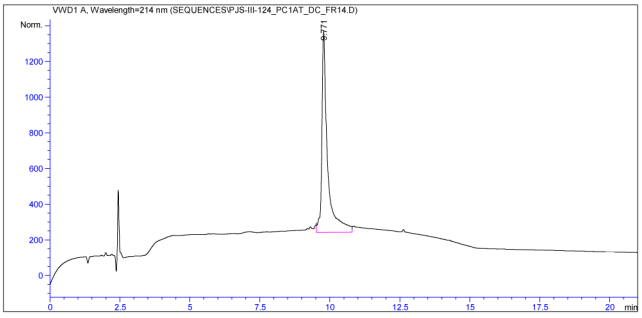
VWD1 A, Wavelength=214 nm (SEQUENCES\PJS-III-124_PC1AT_DC_FR14.D)
Norm.
8.771
1200
1000
800
600
400
200
0
0
2.5
5
7.5
10
12.5
15
17.5
20
min

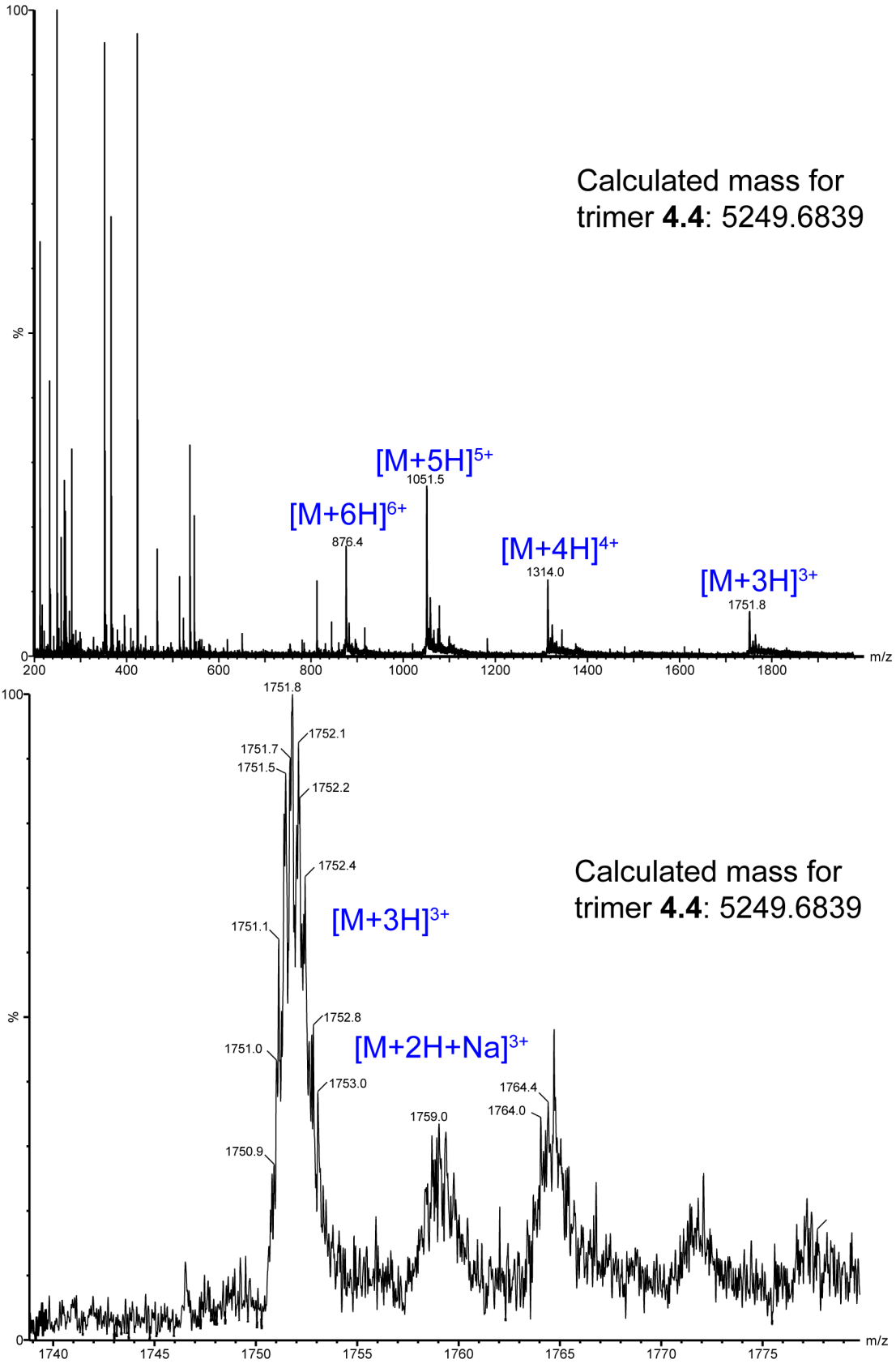
Calculated mass for trimer **4.4**: 5249.6839
[M+5H]5+
1051.5
[M+6H]6+
876.4
[M+4H]4+
1314.0
[M+3H]3+
1751.8
%
m/z
Calculated mass for trimer **4.4**: 5249.6839
[M+3H]3+
[M+2H+Na]3+
1751.8
1752.1
1751.7
1751.5
1752.2
1752.4
1751.1
1752.8
1751.0
1753.0
1764.4
1764.0
1759.0
1750.9

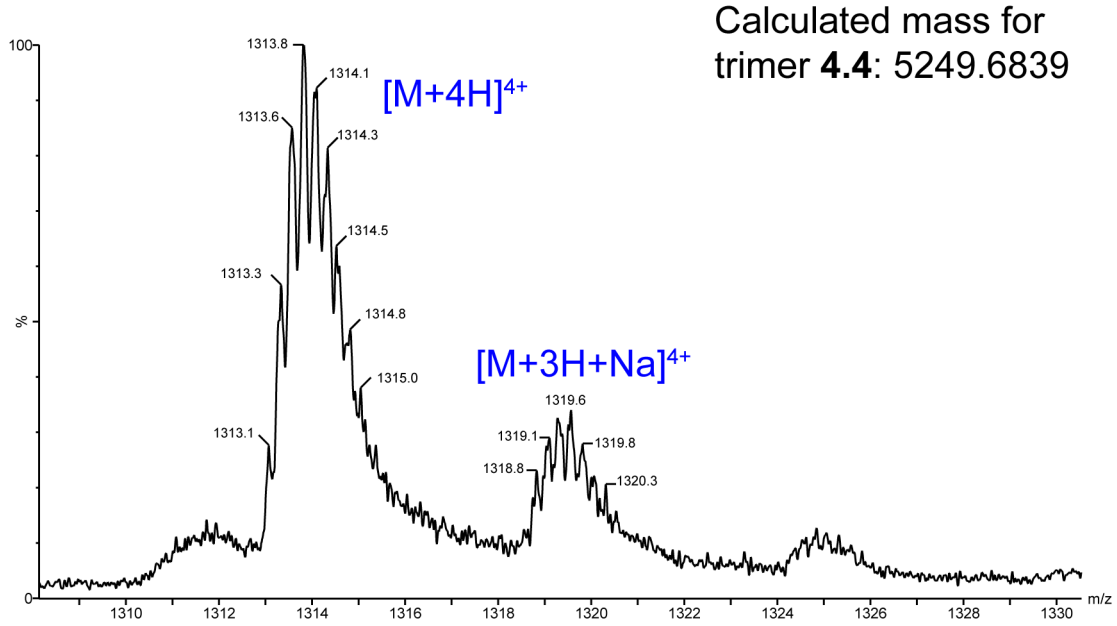
Calculated mass for trimer **4.4**: 5249.6839
[M+4H]4+
[M+3H+Na]4+
1313.8
1314.1
1313.6
1314.3
1314.5
1313.3
1314.8
1315.0
1313.1
1319.6
1319.1
1319.8
1318.8
1320.3
100
%
0
1310
1312
1314
1316
1318
1320
1322
1324
1326
1328
1330
m/z

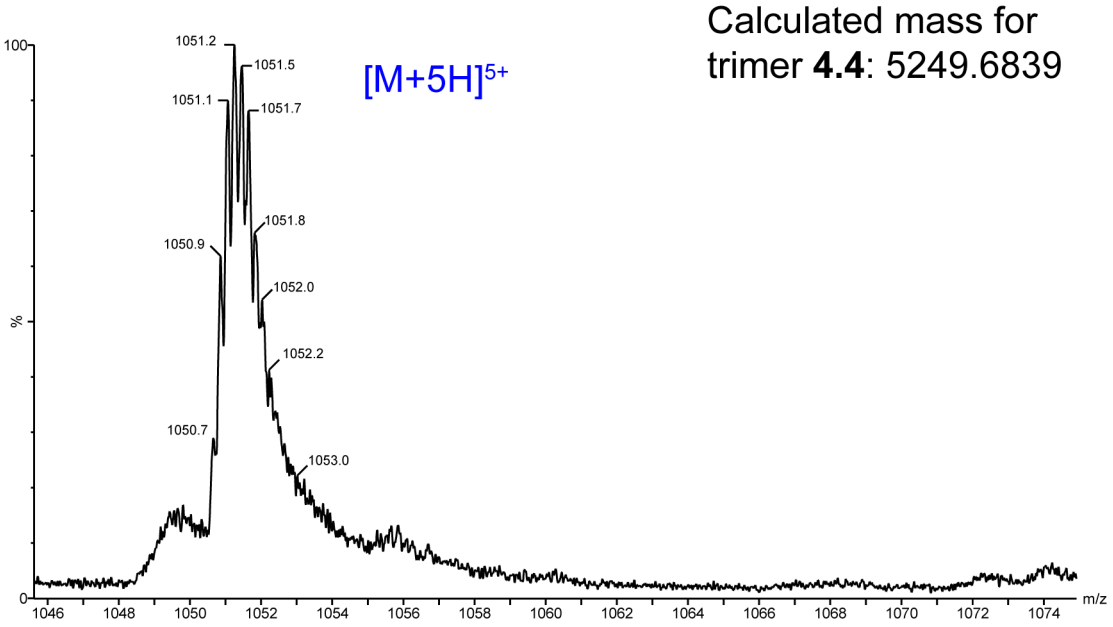
Calculated mass for trimer **4.4**: 5249.6839
[M+5H]5+
1051.2
1051.5
1051.1
1051.7
1051.8
1050.9
1052.0
1052.2
1050.7
1053.0
100
%
0
1046
1048
1050
1052
1054
1056
1058
1060
1062
1064
1066
1068
1070
1072
1074
m/z

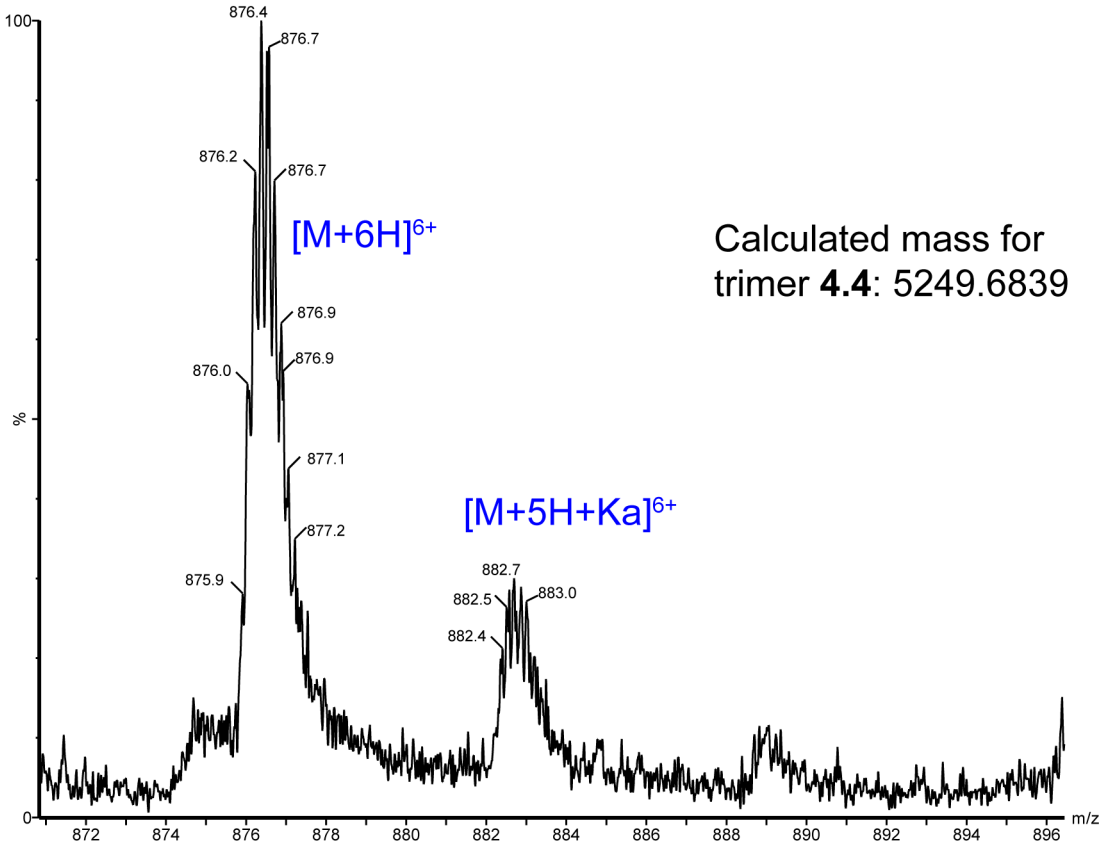
100
%
0
876.4
876.7
876.2
876.7
[M+6H]6+
876.9
876.9
876.0
877.1
877.2
[M+5H+Ka]6+
875.9
882.7
882.5
883.0
882.4
872
874
876
878
880
882
884
886
888
890
892
894
896
m/z
Calculated mass for
trimer **4.4**: 5249.6839

Chapter 5

Repurposing triphenylmethane dyes to bind to triangular trimers derived from Aβ

5.1 Introduction

Fluorescent dyes have longstanding history as probes to study the molecular basis of amyloid disorders, such as Alzheimer's disease, Parkinson's disease, and type 2 diabetes. The dye Congo red has been used to stain amyloid plaques in tissue for nearly a century, while thioflavin T and thioflavin S have been used for several decades as both probes of amyloid plaques and tools to monitor the aggregation of amyloid-forming proteins into fibrils.[170–174] New life has been breathed into these chemical probes through the creative application of their selectivity for amyloid plaques. For example, homologues of Congo red have been used to block amyloid fibril formation, radio-labeled homologues of thioflavin T are currently used in PET imaging diagnostic tests of Alzheimer's disease, and combinatorial flu-

orescent molecular sensors based around thioflavin T have enabled differentiation among aggregates of Aβ.[175–178] High-resolution structures of fibrils and fibril-dye complexes, coupled with molecular dynamics simulations, have revealed structural bases of this molecular recognition, wherein planer aromatic dyes lie parallel to the fibril axis and pack against hydrophobic residues displayed on the fibril surface.[179–188] These structures have guided the design of other small molecules that bind to amyloid fibrils.[189]

Although a handful of chemical probes are used to study the formation of the biologically inert amyloid fibrils, there are few that specifically detect neurotoxic oligomers.[190–196] The specific oligomer structures that these chemical probes recognize remain unknown. Chemical probes that detect amyloid oligomers are urgently needed to help study the structures and function of amyloid oligomers.[197,198] The current lack of high-resolution structures of amyloid oligomers hinders the design of chemical probes that detect these assemblies[199].

While studying the self-assembly of peptides derived from the β-amyloid peptide, Aβ, we have discovered that triphenylmethane dyes bind to assemblies of covalently stabilized oligomers formed by peptides derived from $A\beta_{17–36}$.[61] This discovery was guided by the complementary shape and symmetry of triphenylmethane dyes and the oligomeric assemblies our laboratory has characterized by X-ray crystallography.[61] This binding produces marked changes to the color of the dyes, from purple in the unbound state to blue in the bound state. Binding also induces pronounced red fluorescence upon excitation with green light. Here we report the discovery of triphenylmethane dyes that bind to triangular trimers derived from Aβ.

Our laboratory previously synthesized macrocyclic β-hairpin peptide **5.1** to mimic a β-hairpin formed by $A\beta_{17–36}$ (Figure 5.1).[57] Peptide **5.1** contains the heptapeptide β-strands $A\beta_{17–23}$ and $A\beta_{30–36}$ connected by two δ-linked ornithine turn units. Peptide **5.1** bears a single *N*-methyl group, on Phe_{20}, which limits uncontrolled aggregation of the peptide. The X-ray crystallographic structure of peptide **5.1** revealed a triangular trimer motif wherein three copies of peptide **5.1** assemble to form an equilateral triangle (PDB 4NW9). To ascertain the

biological and biophysical properties of this triangular trimer, we covalently stabilized this oligomer, resulting in trimer **5.2**.[61] Trimer **5.2** is stabilized by disulfide crosslinks, which we engineered into the three vertices of the triangular trimer. Trimer **5.2** induces apoptosis in the human neuroblastoma SH-SY5Y cell line and reacts with the amyloid oligomer-specific antibody A11,[200] thus mimicking the biological properties of oligomers formed by full-length Aβ.[153]

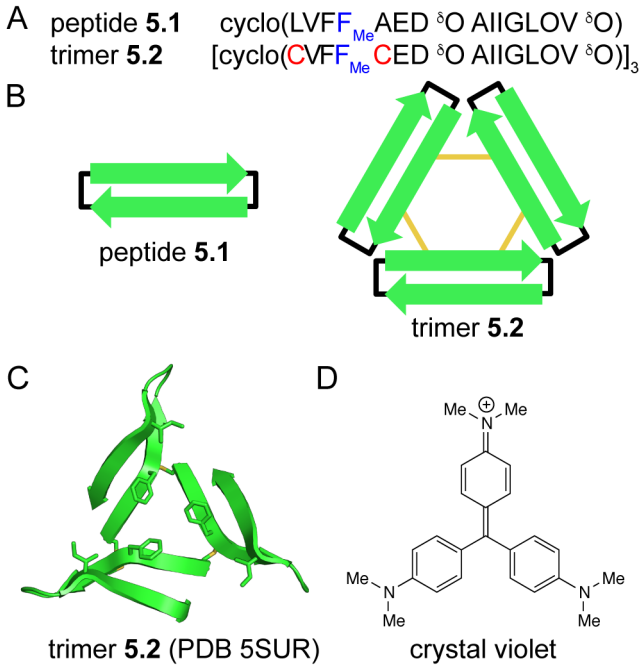

Figure 5.1: Chemical models of oligomers formed by Aβ. (A) Amino acid sequences of peptide **5.1** and trimer **5.2**. (B) Cartoon of peptide **5.1** and trimer **5.2**. Black lines represent δ-linked ornithine turn units; yellow lines represent disulfide bonds. (C) X-ray crystallographic structure of trimer **5.2** (PDB 5SUR). The side chains of Cys_{17}, Phe_{20}, Cys_{21}, and Ile_{31} are shown as sticks. (D) Chemical structure of crystal violet.

The discovery and development of compounds that interact with fibrils have been guided by high resolution structures of fibrils and fibril-like assemblies.[186,189,201,202] The X-ray crystallographic structure of trimer **5.2** (PDB 5SUR) provided us with a starting point for discovering chemical probes that bind the triangular trimers that we have observed crystallographically and that we postulate to be formed by Aβ. We hypothesized that $C3$ symmetric dyes would interact with the $C3$ symmetric trimer. Specifically, we envisioned that the three side chains

of Phe_{20}, arrayed around the $C3$ symmetry axis of trimer **5.2**, would interact with $C3$ symmetric small molecules (Figure 5.1C). We began our exploration with crystal violet, a $C3$ symmetric triphenylmethane dye (Figure 5.1D).

5.2 Results and Discussion

Trimer **5.2** forms a complex with crystal violet in aqueous solution (Figure 5.2). The visible absorption spectrum of crystal violet is sensitive to changes in the local environment surrounding the dye.[203] The resulting color change has been used to measure complexation of crystal violet by proteins, including bovine serum albumin.[204–206] We also observe color changes, from violet to blue, upon addition of trimer **5.2** to crystal violet. The visible spectrum of crystal violet displays an absorption maximum at 590 nm and a shoulder at *ca.* 530 nm in 100 mM aqueous acetate buffer (pH 4.6). When trimer **5.2** is added to crystal violet at low micromolar concentrations, the maximum shifts to longer wavelengths and becomes more intense, while the shoulder disappears (Figure 5.2B). The spectra that result from titration of crystal violet with trimer **5.2** do not exhibit a well defined isosbestic point, suggesting the formation of multiple trimer **5.2**-crystal violet complexes in solution. The complexation also enhances the fluorescence spectra of crystal violet, causing it to fluoresce red when irradiated with green light (Figure 5.2C). Crystal violet is largely non-fluorescent in aqueous solution due to non-irradiative modes of relaxation that result from bond rotations in the excited state.[203] Complexation by trimer **5.2** likely restricts these rotations, resulting in the enhanced fluorescence of crystal violet.[207,208]

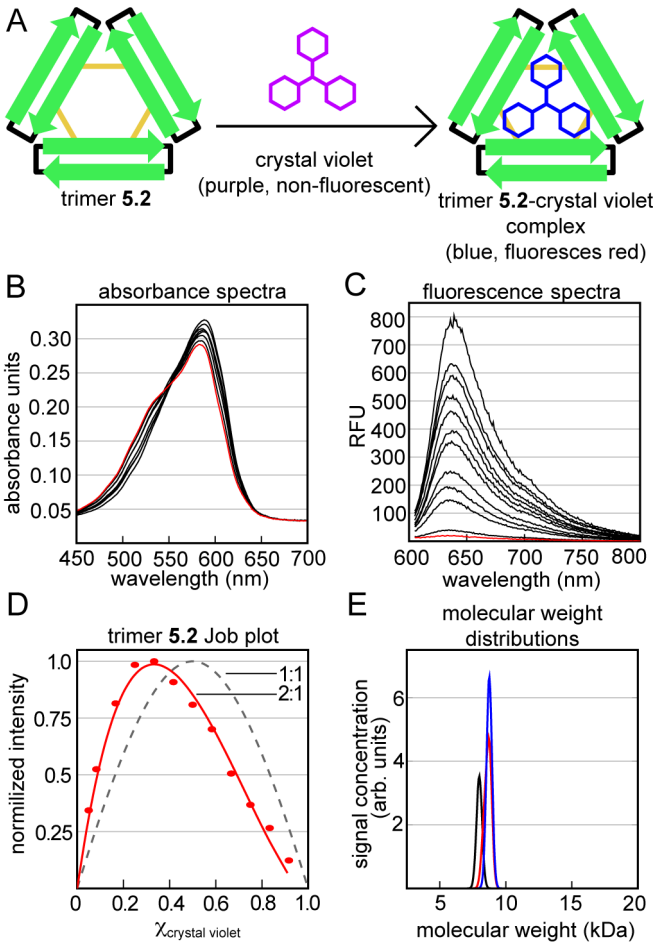

Figure 5.2: Crystal violet binds to trimer **5.2** in aqueous buffer. (A) Cartoon of the color and fluorescence changes that occur upon binding. (B and C) Absorbance and fluorescence spectra of crystal violet (red) titrated with increasing amounts of trimer **5.2** (black) in buffer comprising 50 mM sodium acetate and 50 mM acetic acid (pH 4.6). Fluorescence spectra were acquired with a 590 nm excitation wavelength. (D) Job plot analysis of the stoichiometry of the trimer **5.2**-crystal violet complex. The dashed line is a 1:1 (trimer **5.2**-crystal violet) fit of the data, while the solid line is a 2:1 fit of the data. (E) Molecular weight distributions calculated from sedimentation velocity analytical ultracentrifugation experiments. The distributions are calculated from mixtures of 7 µM crystal violet with 14 µM (black), 42 µM (red), and 56 µM (blue) trimer **5.2**.

To determine the stoichiometry of the complex between crystal violet and trimer **5.2**, we used Job's method of continuous variation (Figure 5.2D).[209–212] In this experiment, we mixed crystal violet and trimer **5.2** at varying ratios while maintaining the total concentration of the two components, and we measured the fluorescence intensities of the resulting mixtures. The resulting fluorescence spectra display a maximum intensity at a 0.33 mole fraction (χ) of

crystal violet, which suggests that two molecules of trimer **5.2** bind to one molecule of crystal violet. The data do not fit a simple 1:1 trimer-dye binding model, wherein the maximum fluorescence intensity would occur at a 0.5 mole fraction of crystal violet. From the 2:1 fit of the data, the dissociation constant is *ca.* $0.94 \cdot 10^{-9}$ M^2, which corresponds to a complex that dissociates around 30 µM. The 2:1 stoichometry is consistent with our laboratory's previously reported observation that trimer **5.2** assembles to form a dimer in solution.[61]

To corroborate the apparent 2:1 stoichiometry, we performed sedimentation velocity analytical ultracentrifugation (AUC) experiments. In these experiments, we mixed 7 µM crystal violet with one, two, four, six, or eight molar equivalents of trimer **5.2** in sodium acetate buffer, and monitored the sedimentation of crystal violet by measuring the visible absorbance at 593 nm. Crystal violet does not sediment upon ultracentrifugation in the absence of trimer **5.2**, because it is too low in molecular weight (Figure 5.3). When crystal violet is mixed with two or more equivalents of trimer **5.2**, it sediments as a *ca.* 9 kDa species (Figure 5.2E). This molecular weight is largely consistent with crystal violet binding to two molecules of trimer **5.2**, each weighing 5.3 kDa. These experiments support the Job plot analysis that trimer **5.2** forms a 2:1 complex with crystal violet.

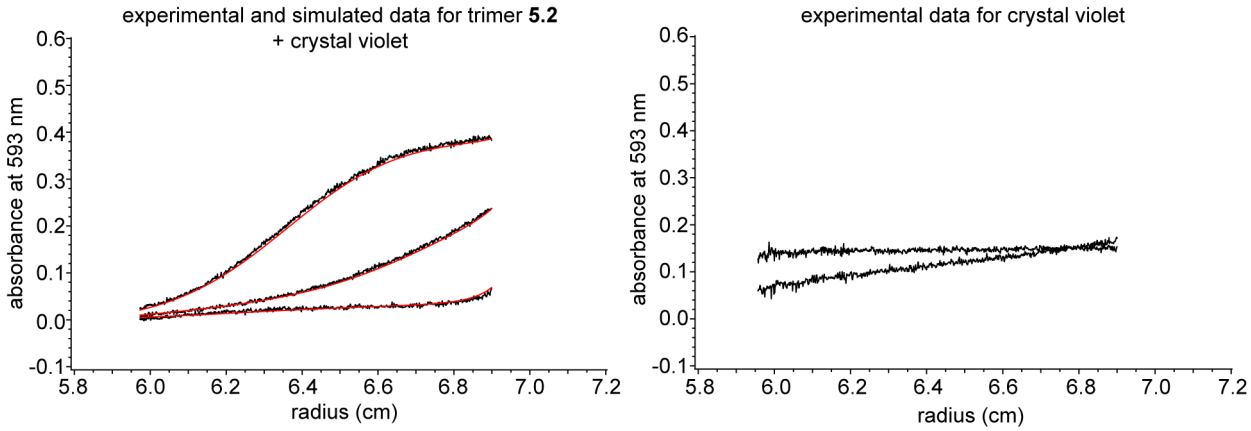

Figure 5.3: Sedimentation velocity analytical ultracentrifugation experiments for 7 µM crystal violet with (left) and without (right) 28 µM trimer **5.2**. Sedimentation velocity data (black) fitted using 2DSA[213] analysis (red). For clarity, only the first and last scan are shown for crystal violet, while three scans, ranging from the 100th to the last, are shown for the crystal violet and trimer **5.2** mixture.

To further corroborate the formation of the 2:1 trimer **5.2**-crystal violet complex, we performed isothermal titration calorimetry (ITC) experiments. In these experiments, we added aliquots of a 500-µM crystal violet solution to a solution of 100 µM trimer **5.2** and recorded the heat of association. Although the reaction is clearly exothermic, the association constant is too low to permit precise analysis of the titration data (Figure 5.4). The limited solubility of trimer **5.2** in sodium acetate buffer and the propensity of crystal violet and trimer **5.2** to self-associate at higher concentrations complicate a rigorous analysis of binding constants and thermodynamic parameters by ITC. At the concentrations used in the titration, the data fit well to a 2:1 binding model, with a dissociation constant of *ca.* $1.4 \cdot 10^{-9}$ M^2 (Figure S2B and C). This dissociation constant is similar to that estimated by Job's method of continuous variation. The data deviate from a simple 1:1 binding model, where the residuals display sinusoidal deviation similar to the deviation in the attempted 1:1 fit of the Job plot data in Figure 5.2D.[214] The fit to a 2:1 binding model shows substantially smaller deviations.

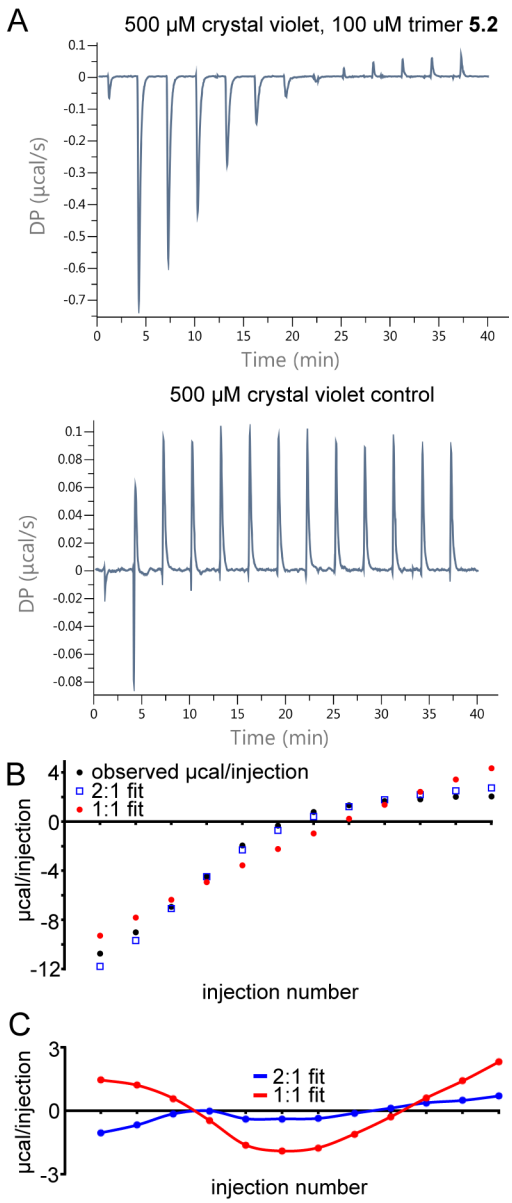

Figure 5.4: Isothermal titration calorimetry experiments with crystal violet and trimer **5.2**. (A) Raw data for the titration of 500 µM crystal violet into 100 µM trimer **5.2** (top) or into acetate buffer (bottom). (B) Integrated heat per injection (black circles) fitted to a 2:1 (blue squares) and 1:1 (red circles) trimer **5.2**-crystal violet binding model. (C) Residuals for the 2:1 and 1:1 binding models.

Crystal violet is known to interact with numerous proteins, such as BSA and acetylcholine receptors.[204–206,215–219] For these reasons, we were concerned that the interaction of crystal violet and trimer **5.2** might not reflect the specific recognition of the three-fold symmetric

dye by the triangular trimer motif. To determine if the association of crystal violet with trimer **5.2** requires the triangular trimer motif, we studied the interaction of crystal violet with peptide **5.1** (Figure 5.5). Peptide **5.1** does not assemble into a triangular trimer at the low micromolar concentrations (5–150 μM) at which trimer **5.2** complexes crystal violet.[61] No significant changes occur in the absorbance or fluorescence spectra of crystal violet upon addition of peptide **5.1** (Figure 5.5B and C). ITC experiments further corroborate that peptide **5.1** does not bind crystal violet at concentrations where trimer **5.2** does (Figure 5.6). The association of crystal violet with macrocyclic β-hairpins derived from Aβ appears to require a binding site that is unique to the triangular trimer.

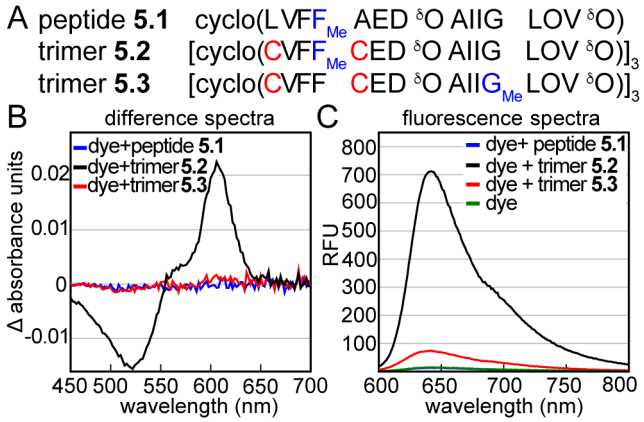

Figure 5.5: Interaction of other Aβ-derived peptides with crystal violet. (A) Amino acid sequences of peptide **5.1**, trimer **5.2**, and trimer **5.3**. Residues bearing *N*-methyl groups are highlighted in blue. (B) Difference absorbance spectra of 25 μM crystal violet with 75 μM peptide **5.1**, 25 μM trimer **5.2**, or 25 μM trimer **5.3**. Difference spectra are calculated by subtracting the absorbance spectrum of 25 μM crystal violet from the absorbance spectra of the mixed samples. (C) Fluorescence spectra of 25 μM crystal violet or 25 μM crystal violet with 75 μM peptide **5.1**, 25 μM trimer **5.2**, or 25 μM trimer **5.3**. Fluorescence spectra were acquired with a 550 nm excitation wavelength. Crystal violet exhibits near-baseline fluorescence alone or with peptide **5.1**. Experiments were performed in buffer comprising 50 mM sodium acetate and 50 mM acetic acid (pH 4.6).

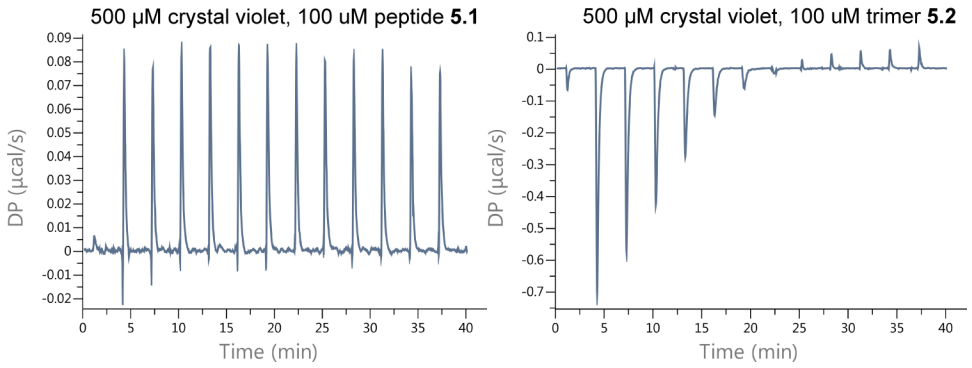

Figure 5.6: ITC titrations of 500 µM crystal violet into 100 µM peptide **5.1** (left) or 100 µM trimer **5.2** (right).

To further test if the interaction between crystal violet and trimer **5.2** results from specific molecular recognition of the trimer **5.2** surface, we studied the interaction between crystal violet and trimer **5.3** (Figure 5.5). Trimer **5.3** is almost identical to trimer **5.2**, differing only in the location of the three *N*-methyl groups. The *N*-methyl groups are on Phe_{20} in trimer **5.2**, while they are on Gly_{33} in trimer **5.3**. The surfaces of trimer **5.3** differ from those of trimer **5.2** because the two trimers have different hydrogen-bonding patterns between the cross-linked monomers that comprise the trimers (Figure 5.7). Absorbance spectroscopy, fluorescence spectroscopy, and ITC experiments indicate that trimer **5.3** does not appreciably associate with crystal violet at low micromolar concentrations. No significant changes occur to the absorbance spectrum of crystal violet when crystal violet and trimer **5.3** are mixed at 25 µM concentrations (Figure 5.5B). In contrast, trimer **5.2** visibly alters the color of crystal violet under the same conditions. A small enhancement does occur to the fluorescence spectrum of crystal violet when mixed with trimer **5.3**, but this enhancement is far smaller than that which occurs when crystal violet is mixed with trimer **5.2** (Figure 5.5C). ITC experiments further corroborate that trimer **5.3** does not bind crystal violet under conditions wherein trimer **5.2** does (Figure 5.8). These titration data do suggest that trimer **5.3** weakly associates with crystal violet, with an association constant that corresponds to a complex that dissociates in the hundred-micromolar regime. However, the limited solubility

of trimer **5.3** precludes the accurate measurement of this weak association constant by ITC. The interaction of crystal violet with trimer **5.2** but not trimer **5.3**, under these conditions, suggests that the surfaces displayed by trimer **5.2** are primed to interact with crystal violet.

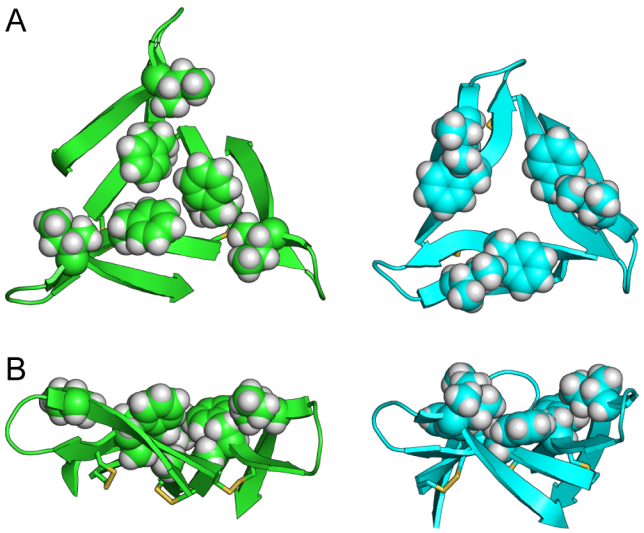

Figure 5.7: Comparison of the surfaces of trimer **5.2** (PDB 5SUR, green) and trimer **5.3** (PDB 5SUT, cyan). (A) Top view. (B) Side view. The side chains of Phe_{20} and Ile_{31} are depicted as spheres; the side chains of Cys_{17} and Cys_{21} are depicted as sticks.

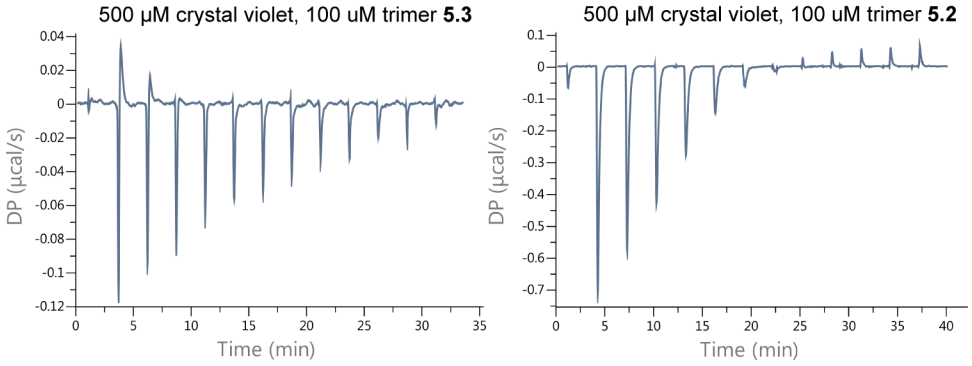

Figure 5.8: ITC titrations of 500 µM crystal violet into 100 µM trimer **5.3** (left) or 100 µM trimer **5.2** (right).

To understand why trimer **5.2** interacts with crystal violet while other Aβ-derived peptides we have studied do not, we performed docking simulations. In these simulations, we used AutoDock to propose a model for the recognition of crystal violet by trimer **5.2**.[220] We performed these docking studies because X-ray crystallography and NMR spectroscopy have

been unsuccessful in illuminating the details of the trimer **5.2**-crystal violet complex: We have been unable to co-crystalize crystal violet with trimer **5.2**, and the NMR spectra of trimer **5.2** in the presence or absence of crystal violet are broad and uninterpretable. Docking simulations, on the other hand, have enabled us to generate testable models for the molecular recognition between trimer **5.2** and crystal violet (Figure 5.9). In these simulations, we docked crystal violet to a single copy of trimer **5.2**, extracted from the X-ray crystallographic structure of trimer **5.2** (PDB 5SUR). These simulations suggest that the three side chains of Phe_{20} complement the three aryl rings of crystal violet, and that the three side chains of Ile_{31} are positioned to pack against the three *N*,*N*-dimethylamino substituents on crystal violet. We proceeded to probe this model by studying the association of crystal violet homologues with trimer **5.2**, as well as the association of crystal violet with trimer **5.2** homologues.

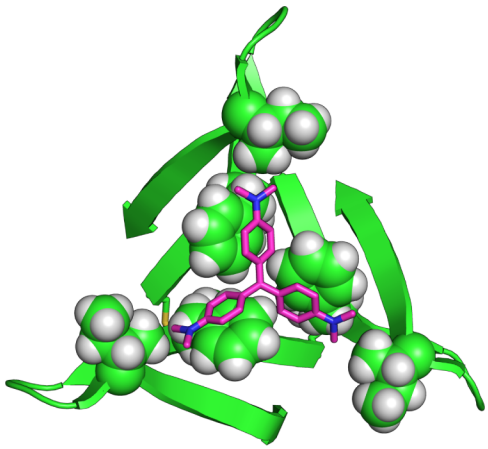

Figure 5.9: Representative molecular model of the trimer **5.2**-crystal violet complex generated in AutoDock. The side chains of Phe_{20} and Ile_{31} are depicted as spheres.

The model proposed in Figure 5.9 suggests that the *N*,*N*-dimethylamino substituents of crystal violet pack against the side chains of Ile_{31}. To test the role of the *N*,*N*-dimethylamino substituents on complex formation, we studied the association of crystal violet homologues with trimer **5.2** (Figures 5.10 and 5.11). We studied two dyes with smaller substituents than crystal violet and two dye with larger substituents than crystal violet (Figure 5.10A): malachite green contains only two *N*,*N*-dimethylamino groups; pararosaniline contains three

amino groups; ethyl violet contains three *N*,*N*-diethylamino groups; propyl violet contains three *N*,*N*-dipropylamino groups. No significant changes occur in the visible spectrum of either malachite green or pararosaniline upon mixing with trimer **5.2** (Figure 5.10B). No enhancement occurs to the fluorescence spectrum of pararosaniline upon mixing with trimer **5.2** (Figure 5.11A). A small enhancement does occur to the fluorescence spectrum of malachite green, but it is much smaller than that which occurs to the fluorescence spectrum of crystal violet. ITC experiments corroborate that malachite green does not associate with trimer **5.2** at concentrations that crystal violet does (Figure 5.11B).

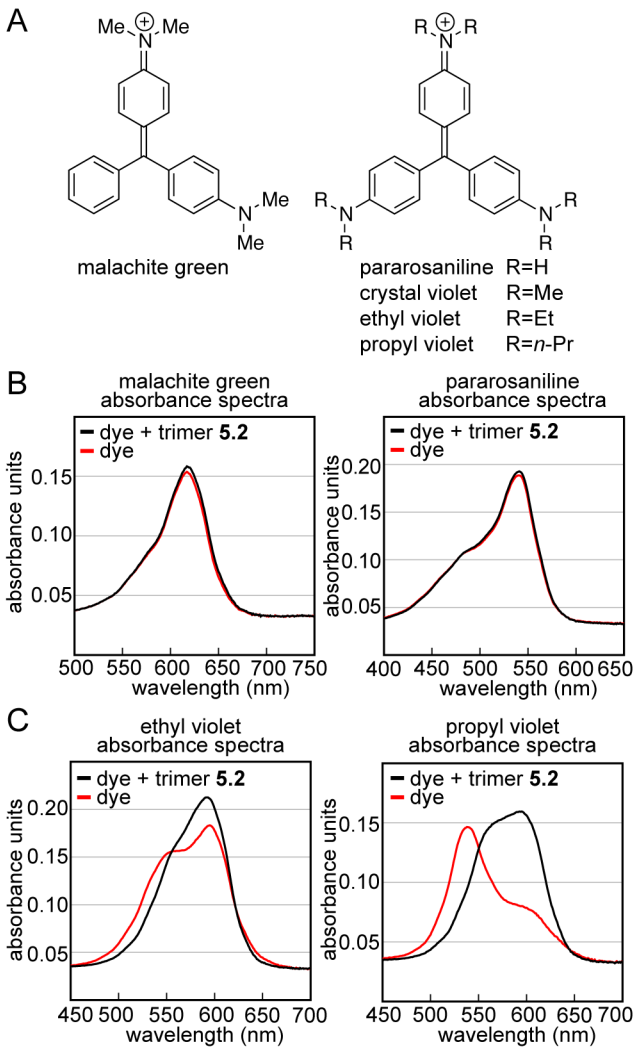

Figure 5.10: Interaction of other triphenylmethane dyes with trimer **5.2**. (A) Chemical structures of crystal violet and related triphenylmethane dyes. (B) Absorbance spectra of 25 µM malachite green and 25 µM pararosaniline in the presence (black) or absence (red) of equimolar trimer **5.2**. (C) Absorbance spectra of 25 µM ethyl violet and 20 µM propyl violet in the presence (black) or absence (red) of equimolar trimer **5.2**. Experiments were performed in buffer comprising 50 mM sodium acetate and 50 mM acetic acid (pH 4.6).

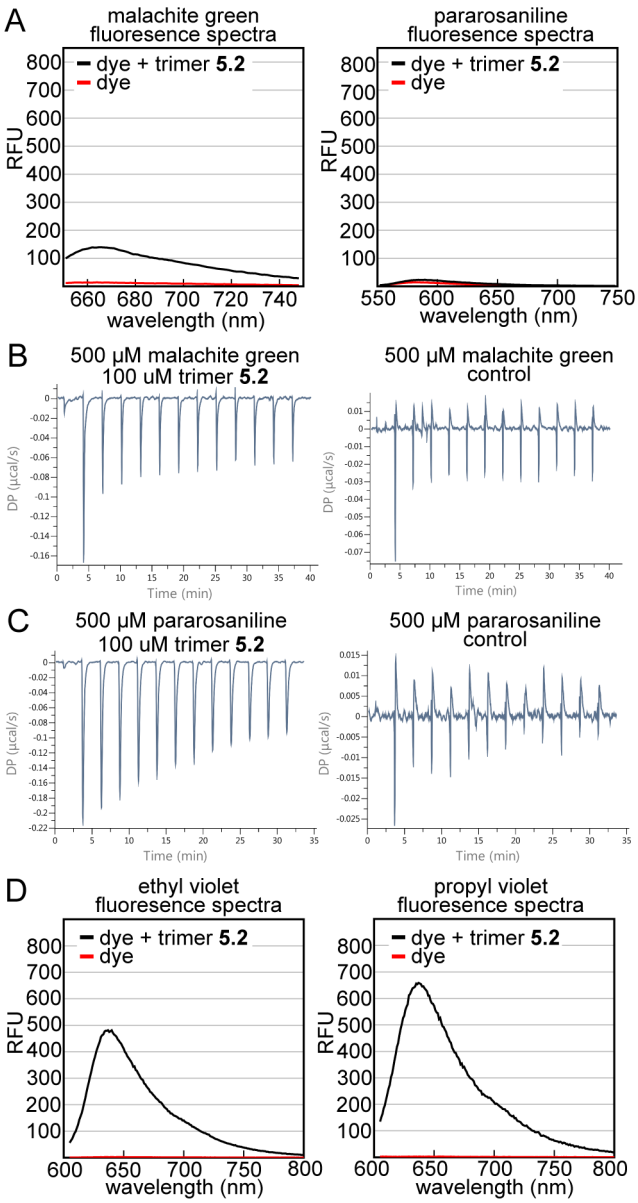

Figure 5.11: Fluorescence spectra of malachite green, pararosaniline, ethyl violet, and propyl violet in the presence and absence of trimer **5.2** and ITS titrations of malachite green or pararosaniline into trimer **5.2**. (A) Fluorescence spectra of 25 µM malachite green or pararosaniline in the presence (black) or absence (red) of equimolar trimer **5.2** (black). (B) ITC Titration of 500 µM malachite green into 100 µM trimer **5.2** (left) or into acetate buffer (right). (C) ITC titration of 500 µM pararosaniline into 100 µM trimer **5.2** (left) or into acetate buffer (right). (D) Fluorescence spectra of 20 µM ethyl violet (red) or 5 µM propyl violet in the presence (black) or absence (red) of 20 µM or 10 µM trimer **5.2**.

ITC experiments suggest that pararosaniline associates weakly with trimer **5.2**, with an association constant that corresponds to a complex that dissociates in the hundred-micromolar

regime (Figure 5.11C). The limited solubility of trimer **5.2** precludes the accurate measurement of this association constant by ITC. In contrast to malachite green and pararosaniline, dramatic changes occur to both the visible and fluorescence spectra of ethyl violet and propyl violet upon mixing with trimer **5.2** (Figures 5.10C and 5.11D). It is difficult to characterize the complexes of ethyl violet and propyl violet with trimer **5.2** using Job's method of continuous variation, AUC, and ITC, because the dyes aggregate strongly in aqueous solution. Collectively these studies with crystal violet homologues suggest that three *N*,*N*-dialkylamino substituents are required for complexation.

To further test the molecular model proposed in Figure 5.9, we prepared five homologues of trimer **5.2** containing cyclohexylalanine (Cha), valine, and cyclohexylglycine (Chg) at positions 19, 20, and 31. Cha is the fully reduced (non-aromatic) analogue of phenylalanine; Chg is a bulkier analogue of both valine and isoleucine. We prepared trimers $\mathbf{5.2_{I31V}}$ and $\mathbf{5.2_{I31Chg}}$ to test if crystal violet packs against the side chain of Ile_{31}, and we prepared trimers $\mathbf{5.2_{F19Cha}}$, $\mathbf{5.2_{F20Cha}}$, and $\mathbf{5.2_{F19,F20Cha}}$ to test if crystal violet packs against the side chain of Phe_{20} (Figure 5.12A). We prepared these trimer **5.2** homologues using the same procedures our laboratory has previously used to prepare other crosslinked trimers.[61,65]

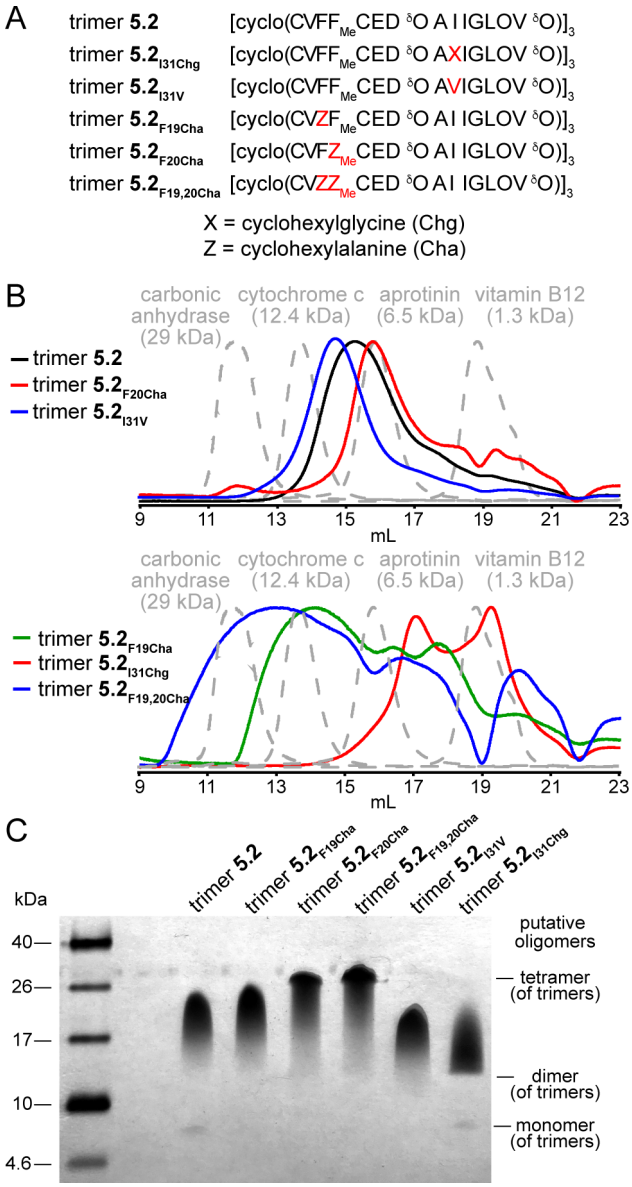

Figure 5.12: Trimer **5.2** homologues. (A) Amino acid sequence of trimer **5.2** homologues. Mutations relative to trimer **5.2** are colored red. (B) SEC chromatograms of trimer **5.2** and its homologues. SEC was performed on 1 mg/mL (*ca.* 150 µM) solutions of trimer dissolved in buffer comprising 50 mM sodium acetate and 50 mM acetic acid on a Superdex 75 10/300 column. (C) Silver-stained SDS-PAGE gel of trimer **5.2** and its homologues. Aliquots (5 µL) of 0.1 mg/mL solutions of each trimer were loaded into the corresponding lanes in the gel.

To determine the impact of these five mutations on the oligomerization state of trimer **5.2**, we compared the oligomerization state of these trimer **5.2** homologues to that of trimer **5.2** using size exclusion chromatography (SEC) and SDS-PAGE. In SEC, we found that some of the

trimer **5.2** homologues elute as well defined oligomers, while others elute as broad peaks that contain multiple features, some of which suggest adsorption to the column (Figure 5.12B). In 100 mM acetate buffer (pH 4.6), trimer **5.2** elutes between the cytochrome C (12.4 kDa) and aprotinin (6.5 kDa) size standards, which elute at 13.6 and 15.8 mL, respectively. The retention volume (15.6 mL) is consistent with the assembly of trimer **5.2** into a dimer (10.6 kDa).[61] Trimer **5.2** shows pronounced tailing in its elution, which suggests that trimer **5.2** may adsorb to the column. Trimer $\mathbf{5.2_{F20Cha}}$ and trimer $\mathbf{5.2_{I31V}}$ both elute with retention volumes similar to that of trimer **5.2**, and exhibit tailing similar to that present in the elution of trimer **5.2** (14.6 and 15.7 mL). These retention volumes suggest that both of these trimer **5.2** homologues assemble into dimers, like that formed by trimer **5.2**.

In contrast, trimers $\mathbf{5.2_{F19Cha}}$, $\mathbf{5.2_{F19,20Cha}}$, and $\mathbf{5.2_{I31Chg}}$, elute as broad peaks with multiple distinct features. Trimer $\mathbf{5.2_{I31Chg}}$ elutes as two peaks with retention volumes of 17.0 and 19.1 mL. It is possible that these two peaks correspond to a dimer and monomer that both adsorb to the column. In contrast, trimers $\mathbf{5.2_{F19Cha}}$ and $\mathbf{5.2_{F19,20Cha}}$ elute as broad heavily-featured bands with retention volumes as early as *ca.* 12 and 14 mL and as late as 22 mL. The early retention volumes are consistent with these hydrophobic mutations promoting the solution-phase assembly of oligomers larger than the dimers formed by trimers **5.2**, $\mathbf{5.2_{F20Cha}}$, and $\mathbf{5.2_{I31V}}$, while the late retention volumes are consistent with the adsobption of these hydrophobic trimers to the column. Mutating Phe_{19} to cyclohexylalanine in full-length $A\beta_{40}$ also enhances its propensity to aggregate.[221]

In contrast to the SEC studies, SDS-PAGE studies indicate that the trimer **5.2** homologues assemble in a fashion similar to that of trimer **5.2** (Figure 5.12C). These 5.0–5.4 kDa trimers migrate as bands between the 17 and 26 kDa size standards, consistent with the trimers forming tetramers under these conditions. These putative tetramer bands show pronounced downward streaking, indicating an equilibrium with lower weight oligomers. The degree of this downward streaking varies among the mutants, likely reflecting the mutations stabilizing

or destabilizing the tetrameric assemblies in SDS. Mutating Phe_{20} to Cha (trimers $\mathbf{5.2_{F20Cha}}$ and $\mathbf{5.2_{F19,20Cha}}$) appears to stabilize the putative tetrameric assemblies. In contrast, mutating Phe_{19} to Cha (trimer $\mathbf{5.2_{F19Cha}}$) or mutating Ile_{31} to Val (trimer $\mathbf{5.2_{I31V}}$) appears to have little impact on the stabilities of the tetramers relative to trimer **5.2**. Mutating Ile_{31} to Chg (trimer $\mathbf{5.2_{I31Chg}}$) appears to disrupt the tetramer and instead stabilize a putative dimer in the presence of SDS. This dimer band shows pronounced upward streaking, rather than downward streaking, suggesting an equilibrium with higher weight oligomers such as trimeric and tetrameric assemblies.

To further characterize the impact of these mutations on the structure and assembly of trimer **5.2**, we determined their structures using X-ray crystallography. Of the five trimer **5.2** homologues, only trimer $\mathbf{5.2_{F19,20Cha}}$ failed to grow crystals. The four other trimer **5.2** homologues grew crystals with hexagonal morphologies, similar to crystals of trimer **5.2**. To remove any possible model bias from using molecular replacement to generate the electron density maps, we determined the X-ray crystallographic phases of each mutant using sulfur single-wavelength anomalous diffraction (S-SAD) phasing.[222–227] Table 5.1 summarizes the crystallographic properties, crystallization conditions, data collection, and model refinement statistics for trimers $\mathbf{5.2_{I31V}}$, $\mathbf{5.2_{I31Chg}}$, and $\mathbf{5.2_{F20Cha}}$[228].

Table 5.1: Crystallographic properties, crystallization conditions, data collection, and model refinement statistics for trimers **5.2$_{\mathbf{I31V}}$**, **5.2$_{\mathbf{I31Chg}}$**, and **5.2$_{\mathbf{F20Cha}}$**

	trimer **5.2$_{\mathbf{I31V}}$**	trimer **5.2$_{\mathbf{I31Chg}}$**	trimer **5.2$_{\mathbf{F20Cha}}$**
PDB ID	6DR4	6DR5	6DR6
space group	$P6_322$	$P3_121$	$P6_322$
a, *b*. *c* (Å)	57.7, 57.7, 94.7	57.8, 57.8, 61.8	58.0, 58.0, 95.6
α, β, γ (^{o})	90, 90, 120	90, 90, 120	90, 90, 120
monomers per asymmetric unit	4	6	4
crystallization conditions	0.1 M tris pH 9.0 0.2 M $MgCl_2$ 2.7 M 1,6-hexanediol	0.2 M NH_4OAc 0.1 M bis-tris pH 5.0 47% (w/v) MPD	0.1 M tris pH 7.5 0.2 M $MgCl_2$ 3.9 M 1,6-hexanediol
Data Collection[a]			
wavelength (Å)	1.54	1.54	1.54
resolution (Å)	47.34–2.10 (2.17–2.10)	38.9–2.08 (2.14–2.08)	34.6–2.61 (2.72–2.62)
total reflections	103768 (6426)	186775 (9988)	245931 (30168)
unique reflections	5880 (461)	7543 (577)	3263 (384)
multiplicity	17.6 (13.9)	24.8 (17.3)	75.4 (78.6)
completeness (%)	99.9 (99.1)	99.9 (99.5)	100 (100)
mean I/σ	35.7 (2.7)	73.3 (27.9)	57.4 (13.1)
R_{merge}	0.055 (0.926)	0.034 (0.093)	0.069 (0.483)
$R_{measure}$	0.057	0.032	0.070
$CC_{1/2}$	1.0 (0.886)	0.993 (0.998)	1.0 (0.993)
CC*	1.0 (0.969)	0.998 (0.999)	1 (0.998)
Refinement			
R_{work}	22.0	17.0	24.2
R_{free}	26.4	21.0	27.7
number of non-hydrogen atoms	532	828	499
number of non-peptide atoms	36	66	7
RMS_{bonds}	0.01	0.03	0.012
RMS_{angles}	1.2	1.55	1.25
Ramachandran favored (%)	100	100	100
outliers (%)	0	0	0
clashscore	3.8	3.1	21.2
average B-factor	58.6	33.6	70.0

[a]Values for the highest resolution shell are show in parentheses.

The X-ray crystallographic structures of trimer $\mathbf{5.2_{I31V}}$ (PDB 6DR4), trimer $\mathbf{5.2_{I31Chg}}$ (PDB 6DR5), and trimer $\mathbf{5.2_{F20Cha}}$ (PDB 6DR6) are nearly identical to that of trimer **5.2** (PDB 5SUR, Figure 5.13). The mutations do not appear to alter the proposed crystal violet binding site, depicted in Figure 5.9. The mutant trimers differ mainly in the conformations of Asp_{23}, Ala_{30}, and the δ-linked ornithine turn that connects them[229]. These mutations do not significantly alter the supramolecular assembly of the cross-linked trimers; the three trimer **5.2** homologues assemble into ball-shaped tetramers which resemble the ball-shaped tetramer formed by trimer **5.2** (Figure 5.13B). The tetramers pack together in the lattice to form dimer interfaces. Although the specific details of these dimer interfaces vary amongst the trimer **5.2** homologues, the modes of assembly are similar to that of trimer **5.2**, which forms tetramers that pack in the lattice through dimer interfaces.[61]

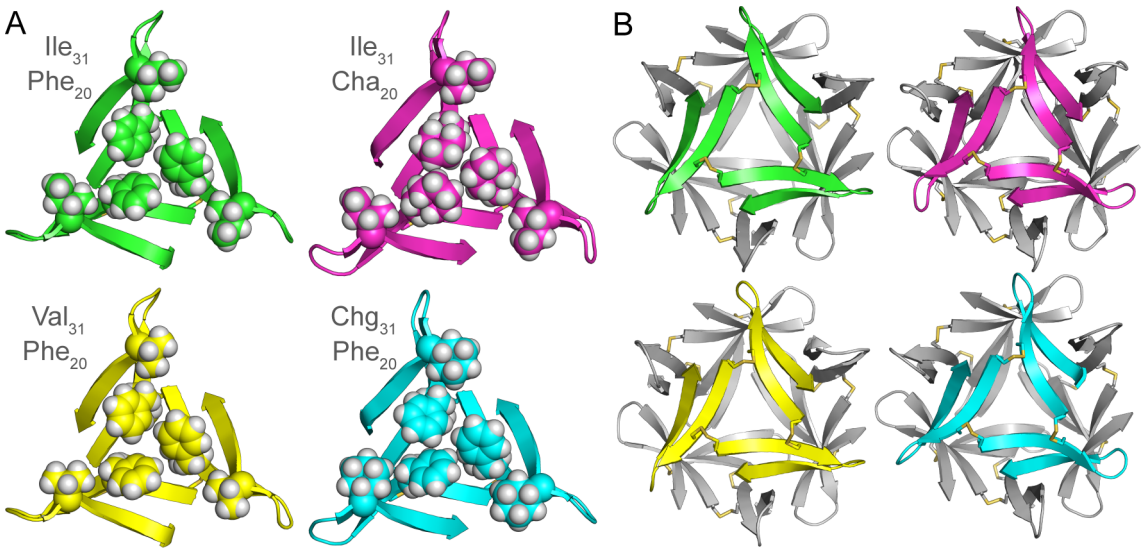

Figure 5.13: X-ray crystallographic structures of trimer **5.2** (PDB 5SUR, green), trimer $\mathbf{5.2_{F20Cha}}$ (PDB 6DR6, magenta), trimer $\mathbf{5.2_{I31V}}$ (6DR4, yellow), and trimer $\mathbf{5.2_{I31Chg}}$ (PDB 6DR5, cyan). (A) Comparison of the triangular trimers. The side chains of Phe_{20}, Cha_{20}, Ile_{31}, Val_{31}, and Chg_{31} are shown as spheres; the side chains of Cys_{17} and Cys_{21} are shown as sticks. (B) Comparison of the ball-shaped tetramers formed by trimer **5.2** and its homologues in the crystal lattices.

To ascertain the impact of these mutations on the molecular recognition of crystal violet, we studied the interaction of crystal violet with the five trimer **5.2** homologues using fluo-

rescence spectroscopy (Figure 5.14). We compared the fluorescence spectra of crystal violet in the presence of the five trimer **5.2** homologues to the fluorescence spectrum of crystal violet in the presence of trimer **5.2**. Fluorescence spectroscopy reveals that the side chains of Phe_{20} and Ile_{31} are important for the recognition of crystal violet (Figure 5.14A). The fluorescence enhancements that occur upon mixing crystal violet with trimer $\mathbf{5.2_{F20Cha}}$ or $\mathbf{5.2_{F19,F20Cha}}$ are far smaller than those which occur upon mixing crystal violet with trimers **5.2** or $\mathbf{5.2_{F19Cha}}$ (Figure 5.14A, left). These results indicate that the aromatic surface formed by the Phe_{20} side chains is involved in the association of trimer **5.2** with crystal violet. The fluorescence enhancement that occurs upon mixing crystal violet with trimer $\mathbf{5.2_{I31Chg}}$ is greater than that which occurs upon mixing crystal violet and trimer **5.2**, while the fluorescence enhancement that occurs upon mixing trimer $\mathbf{5.2_{I31V}}$ is far smaller that that which occurs upon mixing crystal violet with trimer **5.2** (Figure 5.14A, right). These results indicate that the steric bulk provided by the Ile_{31} side chains is involved in the association of trimer **5.2** with crystal violet and suggest that the bulkier Chg stabilizes the 2:1 trimer-dye complex while the smaller Val destabilizes the 2:1 trimer-dye complex.

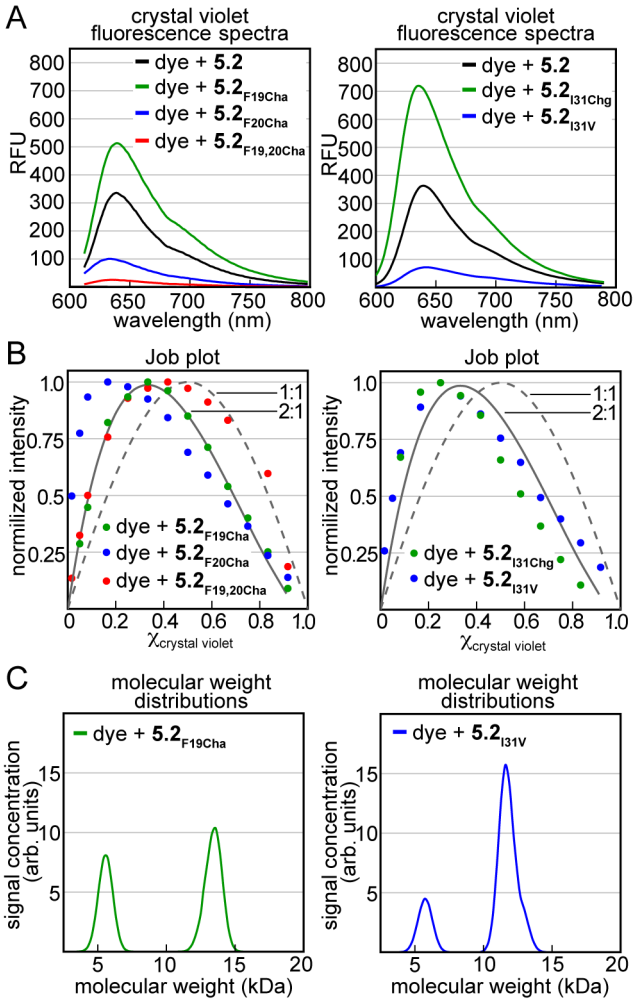

Figure 5.14: Complexation of crystal violet by trimer **5.2** homologues. (A) Fluorescence spectra from mixtures of crystal violet and trimers **5.2**, **5.2$_{\mathbf{F19Cha}}$**, **5.2$_{\mathbf{F20Cha}}$**, and **5.2$_{\mathbf{F19,20Cha}}$** (left) and trimers **5.2**, **5.2$_{\mathbf{I31Chg}}$**, and **5.2$_{\mathbf{I31V}}$** (right). Fluorescence spectra where acquired from samples comprising 20 µM crystal violet and 20 µM of the indicated trimer using an excitation wavelength of 550 nm. (B) Job plot analyses for trimers **5.2$_{\mathbf{F19Cha}}$**, **5.2$_{\mathbf{F20Cha}}$**, and **5.2$_{\mathbf{F19,20Cha}}$** (left) and trimers **5.2$_{\mathbf{I31Chg}}$** and **5.2$_{\mathbf{I31V}}$** (right). The dashed line is a 1:1 binding model, while the solid line is a 2:1 binding model. Job plot experiments where conducted with a total concentration of 30 µM crystal violet and the indicated trimer. (C) Molecular weight distributions calculated from sedimentation velocity analytical ultracentrifugation experiments for trimer **5.2$_{\mathbf{F19Cha}}$** (left) and trimer **5.2$_{\mathbf{I31V}}$** (right). the distributions are calculated from samples comprising 10 µM crystal violet and 60 µM of the indicated trimer. All experiments were performed in buffer comprising 50 mM sodium acetate and 50 mM acetic acid (pH 4.6).

We used Job's method of continuous variation to determine the stoichiometry of the five trimer **5.2** homologue-crystal violet complexes.[209–212] All five homologues deviate from a

simple 1:1 trimer-dye binding model (Figure 5.14B). The Job plot for trimer $\mathbf{5.2_{F19Cha}}$ fits well to a 2:1 binding model, with a dissociation constant of *ca.* $0.92 \cdot 10^{-9}$ M^2. This dissociation constant is similar to that of the trimer **5.2**-crystal violet dissociation constant determined by Job's method of continuous variation (above). The Job plots for the other four trimer **5.2** homologues do not fit well to either a 2:1 or a 1:1 binding model. The deviations from these models may reflect more complex associations of crystal violet with these trimer **5.2** homologues. The maxima in these Job plots occur at $\chi_{\text{crystal violet}}$ ranging from 0.2–0.4, and suggest that multiple molecules of the trimer **5.2** homologues associate with one molecule of crystal violet. Alternatively, the deviations may reflect unavoidable errors that result from the lower fluorescence intensity of these complexes coupled with the absorption of the emitted light by the dye in samples that contain higher concentrations of crystal violet (e.g., $\chi_{\text{crystal violet}} > 0.3$).

To corroborate the apparent stoichiometries of the trimer **5.2** homologue-crystal violet complexes, we performed sedimentation velocity analytical ultracentrifugation experiments (Figure 5.15). In these experiments, we monitored the sedimentation of 10 µM crystal violet in the presence of 60 µM of each of the trimer **5.2** homologues. When mixed with trimers $\mathbf{5.2_{F19Cha}}$ and $\mathbf{5.2_{I31V}}$, crystal violet sediments as a mixture of *ca.* 5 and 13 kDa species (Figure 5.14C). These molecular weights are largely consistent with crystal violet associating with one and two molecules of trimer $\mathbf{5.2_{F19Cha}}$ or trimer $\mathbf{5.2_{I31V}}$. When mixed with trimer $\mathbf{5.2_{I31Chg}}$, crystal violet sediments as high molecular weight aggregates (Figure 5.15A). In contrast, crystal violet does not sediment when mixed with trimers $\mathbf{5.2_{F20Cha}}$ or $\mathbf{5.2_{F19,20Cha}}$ (Figure 5.15E and F). This lack of sedimentation reflects the weak association of crystal violet with either of these mutants, as also seen in the reduction in fluorescence intensity relative to trimer **5.2** (Figure 5.14A).

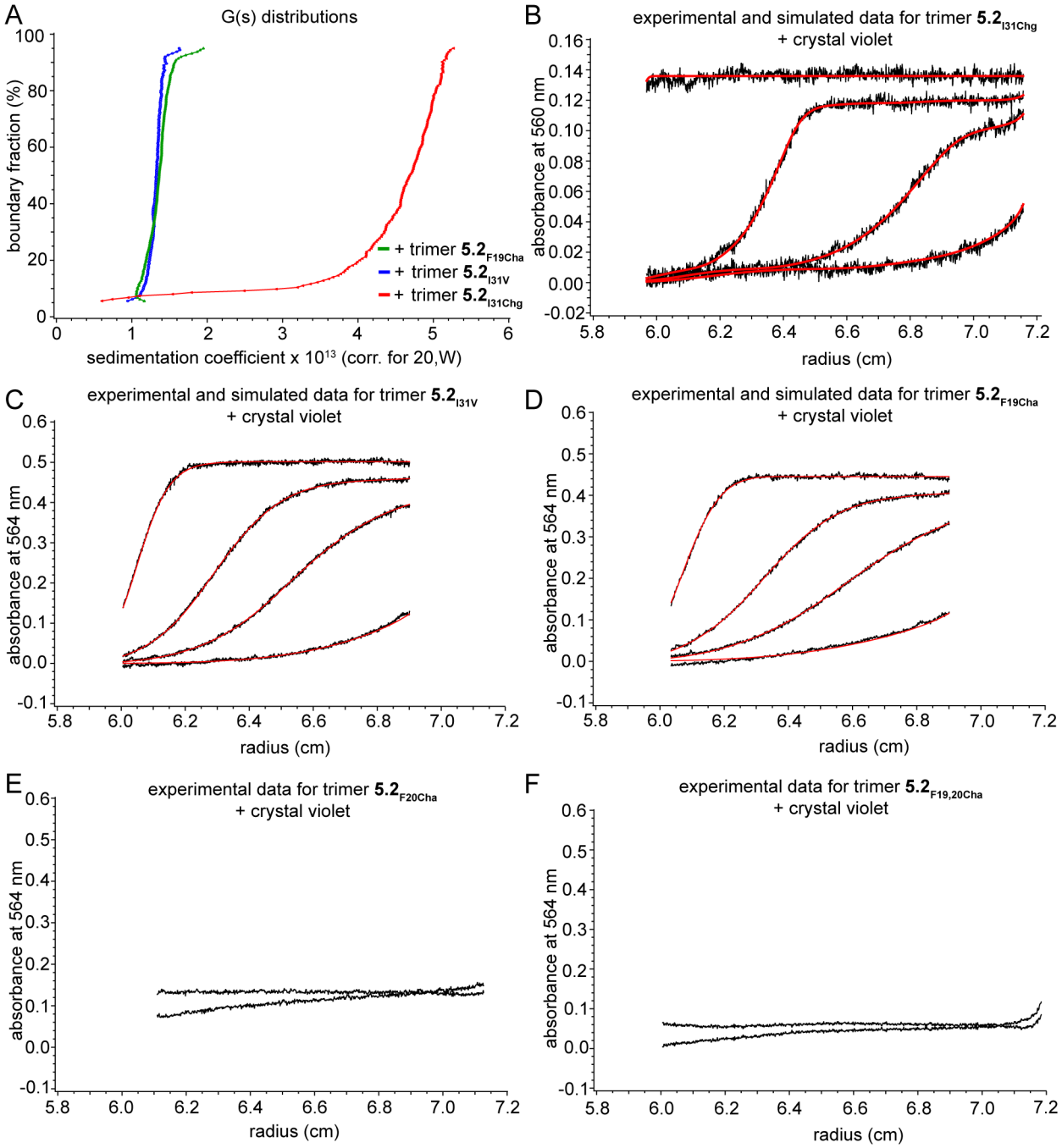

Figure 5.15: Sedimentation velocity analytical ultracentrifugation experiments for mixtures of crystal violet and the trimer **5.2** homologues. (A) Sedimentation coefficient distributions. (B–F) Sedimentation velocity data (black) fitted using 2DSA[213] analysis (red). Data are from sedimentation velocity experiments acquired from samples comprising 10 µM crystal violet and 60 µM of the indicated trimer **5.2** homologue. For clarity, only the first and last scan are shown for trimers $\mathbf{5.2_{F20Cha}}$ and $\mathbf{5.2_{F19,20Cha}}$, while four scans, ranging from the first to the last, are shown for trimers $\mathbf{5.2_{F19Cha}}$, $\mathbf{5.2_{I31V}}$, and $\mathbf{5.2_{I31Chg}}$.

Collectively, these studies support the model depicted in Figure 5.9, wherein the three aryl rings of crystal violet pack against the side chains of Phe_{20} and the three *N*,*N*-dimethylamino substituents pack against the side chains of Ile_{31}. The complex likely resembles a sandwich, in which two copies of trimer **5.2** sandwich around crystal violet through the interactions described above. Such a model is consistent with the observation that two molecules of trimer **5.2** bind to one molecule of dye. This sandwich is likely in equilibrium with an "open-faced" sandwich, wherein only one molecule of trimer **5.2** binds crystal violet. Such an equilibrium is consistent with the lack of an isosbestic point in the transition from free to bound dye (Figure 5.2B), and the observation of crystal violet sedimenting as *ca.* 5 and 13 kDa species in the presence of trimers $\mathbf{5.2_{F19Cha}}$ and $\mathbf{5.2_{I31V}}$ (Figure 5.14C).

We used a combination of docking and molecular mechanics to construct a model for the sandwich complex (Figure 5.16). In this model, two molecules of trimer **5.2** envelop one molecule of crystal violet. The side chains from the six Phe_{20} residues sandwich the three aryl rings of crystal violet, and the side chains from two Ile_{31} residues clasp each *N*,*N*-dimethylamino group. These interactions are similar to the interactions between crystal violet and other proteins observed in high resolution X-ray crystallographic structures.[216,218,219] These structures show that the aryl rings of crystal violet pack against aromatic residues and that the *N*,*N*-dimethylamino groups pack against hydrophobic residues. These co-crystal structures do not indicate that the three-fold symmetry of crystal violet is important for recognition, unlike the trimer **5.2**-crystal violet model. The association of ethyl violet with an insulin hexamer does suggest that symmetry of the triphenylmethane dye can be important in complexation of an oligomer.[230]

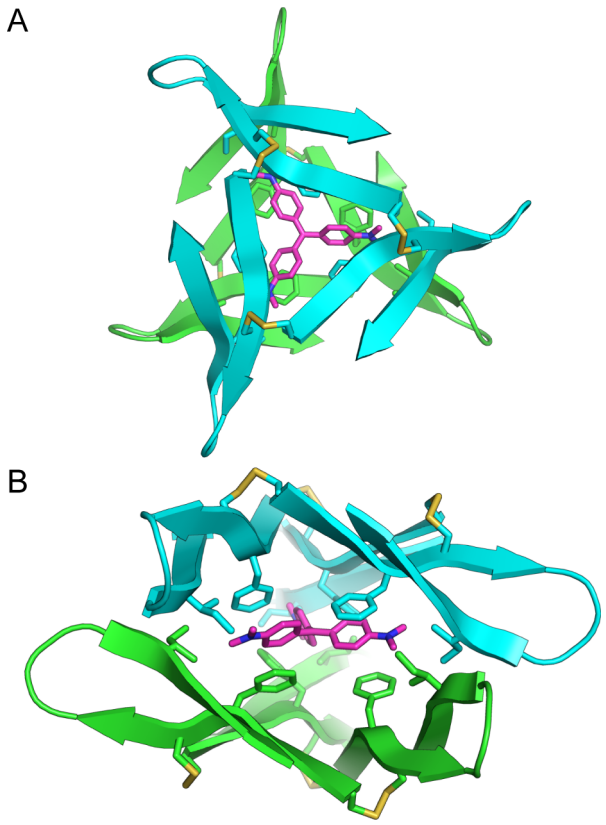

Figure 5.16: Molecular model of the 2:1 trimer **5.2**-crystal violet complex. (A) Top view. (B) Side view. Crystal violet and the side chains of Cys_{17}, Phe_{20}, Cys_{21}, and Ile_{31} are shown as sticks.

This working model of the trimer **5.2**-crystal violet complex may explain the interaction of other triphenylmethane dyes with full-length Aβ. The triphenylmethane dye coomassie brilliant blue G associates with neurotoxic trimers and tetramers formed by Aβ.[231] This triphenylmethane dye differs from those studied here in the substitution of the three nitrogen atoms and in methylation of the triphenylmethane core. Formation of these complexes detoxifies these neurotoxic oligomers[232]. This triphenylmethane dye also alters the *in vitro* aggregation of Aβ and is neuroprotective in animal models of Alzheimer's disease.[233–235] It is possible that coomassie brilliant blue G is recognized by a surface similar to that which recognizes crystal violet in trimer **5.2**. The selectivity of other oligomer-specific dyes has been rationalized through docking studies with the X-ray crystallographic structures of triangular trimers reported by our laboratory.[191–193] BODIPY-based probes,[191] developed by

the Chang group, spiropyran-based probes,[192] developed by the Yi group, and cyanine-based probes,[193] developed by the Wong group, all specifically stain Aβ oligomers. To explain the oligomer-specific reactivity of these probes, all three groups performed docking simulations, in which the probes were docked on a triangular trimer formed by an Aβ-derived peptide (PDB 4NTR). These docking studies suggest that the side chains of three Phe_{19} residues pack against the probes and that the side chains of three Val_{36} residues clasp the probes. These proposed interactions are similar to those that occur between crystal violet and trimer **5.2**, wherein crystal violet packs against an aromatic surface and is clasped by hydrophobic side chains. While these three fluorogenic probes are not $C3$-symmetric, they may recognize a surface similar to that which binds crystal violet in trimer **5.2**.

5.3 Conclusion

Crystal violet and other triphenylmethane dyes have rich history in their use as metachromatic probes for amyloid deposition in tissue.[236] The results described here suggest that these dyes may be repurposed to serve as metachromatic and fluorogenic probes for amyloid oligomers. The X-ray crystallographic structure of trimer **5.2** suggested that $C3$ symmetric small molecules might bind to the triangular trimer. Several different $C3$ symmetric triphenylmethane dyes associate with trimer **5.2** to form supramolecular complexes. Association with trimer **5.2** alters the color of the triphenylmethane dyes, and enhances their fluorescence. These changes and enhancements are specific to trimer **5.2** and several homologues, but do not occur in the presence of the unassembled monomer or in the presence of the related triangular trimer **5.3**. The triphenylmethane dyes appear to pack against the aromatic surface formed by the three Phe_{20} side chains while being clasped by the three Ile_{31} side chains. These triphenylmethane dyes recognize a motif distinct from the amyloid fibrils recognized by planer aromatic dyes.

These studies suggest a blueprint for other small molecules that may bind to Aβ-derived triangular trimers, wherein $C3$-symmetric molecules position three aryl groups around the symmetry axis. We envision that such molecules may be identified in fluorescence- and absorbance-based competition assays in which small molecules compete with crystal violet for the binding site formed by Phe_{20} and Ile_{31}.[237,238] We also envision that the fluorescence enhancements of crystal violet may facilitate imaging trimer **5.2** and related triangular trimers in cellular environments.[239–242] Triphenylmethane dyes, and other $C3$-symmetric small molecules, thus might prove a rich source of chemical probes to explore the structure and function triangular trimers.

5.4 Materials and Methods

5.4.1 General information

All chemicals were used as received except where otherwise noted. Methylene chloride and tetrahydrofuran (THF) were passed through alumina under argon prior to use in a solvent purification system. Anhydrous, amine free dimethylformamide (DMF) was purchased from Alfa Aesar. Diethyl carbonate was dried over magnesium sulfate and distilled prior to use. All reactions were performed at ambient temperature (*ca.* 20 °C), unless otherwise noted. Peptide synthesis was performed on a Protein Technologies PS3 synthesizer. Analytical reverse-phase HPLC was performed on an Agilent 1200 equipped with a Aeris PEPTIDE 2.6u XB-C18 column (Phenomonex). Preparative reverse-phase HPLC was performed on a Rainin Dynamax equipped with a ZORBAX SB-C18 column (Agilent). HPLC grade acetonitrile and 18 MΩ deionized water, each containing 0.1% trifluoroacetic acid, were used for analytical and preparative reverse-phase HPLC. All peptides were prepared and used as

the trifluoroacetate salts and were assumed to have one trifluoroacetate ion per ammonium group present in each peptide.

5.4.2 Synthesis of trimer 5.2, its homologues, and trimer 5.3

Trimer **5.2**, its homologues, and trimer **5.3** were prepared using protocols our laboratory has previously described.[61,65] Macrocyclic β-hairpin peptides containing the heptapeptide β-strands $A\beta_{17–23}$ and $A\beta_{30–36}$ were prepared on a 0.1-mmol scale using the protocols our laboratory has previously described.[63] Peptides **I31V**, **I31Chg**, **F19Cha**, **F20Cha**, and **F19,20Cha** all contained the L17C and A21C point mutations, which are required for the covalent stabilization of the cross-linked trimer. After purification and lyophilization, these monomeric peptides were oxidized into cross-linked trimers as follows: A 6 mM solution of the cysteine-bearing peptide in 20% aqueous DMSO was prepared in a 20-mL glass scintillation vial. [We routinely oxidize 10–50 mg of the cysteine-bearing peptides at a time.] The 6 mM solution was rocked for 48 hours. After 48 hours, the solution was transferred to a 1-L round bottom flask equipped with a magnetic stirring bar and diluted 20-fold with 18 MΩ deionized water. This diluted solution was allowed to stir for an additional 48 hours. After this second 48-hour period, the solution concentrated to dryness using rotary evaporation. The white residue was dissolved in *ca.* 10 mL of 20% aqueous acetonitrile and purified by RP-HPLC using a gradient of 20–30% acetonitrile in water over 15 minutes, followed by a gradient of 30–60% acetonitrile in water over 60 minutes. During these purifications, the column was heated to 60 °C in a water bath. The fractions were analyzed by analytical RP-HPLC and ESI-MS, and pure fractions were combined and lyophilized. This protocol yields trimer **5.2**, its homologues, and trimer **5.3** as a white solids. These procedures typically afford 3–7 mg of the crosslinked trimer from each 0.1-mmol scale synthesis of the corresponding monomeric peptide.

5.4.3 Synthesis of propyl violet

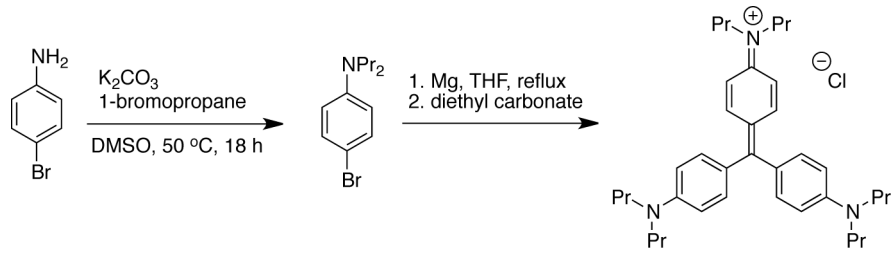

Scheme 5.1

A mixture of anhydrous potassium carbonate (1 g, 7 mmol), *p*-bromoaniline (3.4 g, 20 mmol), 1-bromopropane (4 mL, 44 mmol), and 0.5 mL DMSO was stirred at 50 °C overnight (*ca.* 18 h), and then cooled to room temperature and poured into *ca.* 10 mL of water. This mixture was extracted with *ca.* 30 mL of methylene chloride. The organic layer was washed with saturated aqueous sodium chloride, dried with magnesium sulfate, and filtered. Solvent was removed under reduced pressure and the resulting oil was purified by silica gel column chromatography (0–10 % EtOAc:hexanes) to afford 1.42 g of *N*,*N*-dipropyl-*p*-bromoaniline. ^{1}H-NMR (400 MHz, $CDCl_3$) δ 7.25 (d, J=8.7 Hz, 3 H, includes $CHCl_3$), δ 6.50 (d, J=8.8 Hz, 2 H), δ 3.20 ppm (appar. t, J=7.6 Hz, 4 H), δ 1.59 (sex, J=7.3 Hz, 5 H, includes H_2O), δ 0.92 (t, J=7.2 Hz, 6 H). ^{13}C-NMR (125 MHz, $CDCl_3$) δ 147.2, δ 131.8, δ 113.4, δ 106.8, δ 53.0, δ 20.3, δ 11.4.

A flame-dried 250-mL round bottom flask equipped with a magnetic stirring bar and a reflux condenser was charged with *ca.* 50 mL anhydrous THF. To this reaction vessel, ground magnesium turnings (*ca.* 200 mg, 8.3 mmol), and *N*,*N*-dipropyl-*p*-bromoaniline (1.42 g, 6.2 mmol), and an iodine crystal were added. This mixture was heated to reflux under an atmosphere of N_2 until the mixture had a murky brown color. The reaction vessel was allowed to cool to room temperature at which point dry diethyl carbonate (0.23 mL, 2 mmol) was added via syringe. The reaction mixture turned yellow upon addition of dry diethyl carbonate. The reaction mixture was heated at reflux for *ca.* 5 min at which point

it was allowed to cool to room temperature. Upon exposure to air, the reaction mixture gradually turned a deep violet color. A 6-mL aliquot of 6 M HCl was added, and the THF was removed under reduced pressure by rotary evaporation. The resulting greenish purple residue was suspended in *ca.* 20 mL of water, heated to boiling, and recrystallized. The resulting green paste was filtered, washed with diethyl ether, and dried under reduced pressure overnight to afford 300 mg of propyl violet. ^{1}H-NMR (500 MHz, DMSO-d6) δ 7.30 (d, J=9.1 Hz, 6 H), δ 7.00 (d, J=6.8 Hz, 6 H), δ 3.50 (t, J=7.1 Hz, 18 H, includes H_2O), δ 1.67 (sex, J= 7.2 Hz, 12 H), δ 0.95 (t, J=7.3 Hz, 18 H). ^{13}C-NMR (125 MHz, DMSO-d6) δ 175.8, δ 154.2, δ 139.8, δ 125.9, δ 113.0, δ 52.3, δ 20.8, δ 11.5. Calcd for $C_{37}H_{54}N_3^+$ $[M]^+$: 540.4318; found 540.4311.

5.4.4 Sample preparation

The triphenylmethane dye stocks were prepared gravimetrically by dissolving *ca.* 1.5 mg of triphenylmethane dye in buffer comprising 50 mM acetic acid and 50 mM sodium acetate (pH 4.6) to achieve 500 µM dye. We found that the triphenylmethane dyes adsorb onto glass and plastic containers used to prepare the stock solutions. For these reasons, the stocks were prepared fresh for each experiment, and used for no longer than 24 hours.

The peptide and trimer stock solutions were prepared gravimetrically by dissolving *ca.* 1.0 mg of lyophilized peptide or trimer in 18 MΩ water to achieve 10 mg/mL. The molarity of the peptide and trimer stock solutions was calculated using the molecular weight of the peptides and trimers, assuming that the peptides and trimers contain one trifluoroacetate ion per ammonium group present in each peptide. These stock solutions were stored at 4 °C degrees when not in use.

All samples were prepared by diluting aliquots of stock peptide/trimer and stock dye solutions with buffer comprising 50 mM acetic acid and 50 mM sodium acetate (pH 4.6). Table

Table 5.2: Representative sample preparation

conc. (µM) trimer **5.2**	conc. (µM) crystal violet	vol (µL) stock trimer **5.2**	vol (µL) stock crystal violet	vol (µL) buffer
0	37.5	0	30.0	370.0
0.95	37.5	0.25	30.0	369.8
4.7	37.5	1.2	30.0	368.8
9.5	37.5	2.4	30.0	367.6
14.2	37.5	3.6	30.0	366.4
19.0	37.5	4.8	30.0	365.2
23.7	37.5	6.0	30.0	364.0
28.4	37.5	7.2	30.0	362.8
35.6	37.5	9.0	30.0	361.0
42.7	37.5	10.8	30.0	359.2
53.3	37.5	13.5	30.0	356.5
61.6	37.5	15.6	30.0	354.4
66.4	37.5	16.8	30.0	353.2
71.1	37.5	18.0	30.0	352.0
75.8	37.5	19.2	30.0	350.8
106.7	37.5	27.0	30.0	343.0

5.2 demonstrates the volumes of stock solutions and buffer required to prepare the samples in Figure 5.2B and C.

5.4.5 Absorption Spectroscopy

Visible absorbance spectra were recorded on a Thermo Scientific MULTISKAN GO instrument equipped with a cuvette reader. Data were acquired from samples in a quartz cuvette with a 0.1 cm path length.

5.4.6 Fluorescence Spectroscopy

Fluorescence data were recorded on a Cary Eclipse fluorimeter. Data were acquired from samples in a quartz cuvette with a 1 cm by 0.2 cm cross section. For all measurements, the sample were excited along the 0.2 cm path and emission was observed from the 10 cm

path. Samples of crystal violet, ethyl violet, and propyl violet were excited at either 550 nm or 590 nm. Samples of pararosaniline and malachite green were excited at 540 nm and 640 nm, respectively. For each experiment, the photomultiplier tube voltage and excitation slit widths were optimized to achieve *ca.* 900 RFU from the brightest sample. Typically, 10 nm excitation and 5 nm emission slit widths were used for the measurements. After this initial optimization of instrument parameters, the remaining samples in the experiment were acquired using the same photomultiplier tube voltage and slit widths. Fluorescence spectra were recorded from 600–800 nm for crystal violet, ethyl violet, and propyl violet. Fluorescence spectra were recorded from 650–750 nm for malachite green, and from 550–750 nm for pararosaniline.

5.4.7 Job Plots

Mixtures of trimer **5.2** and crystal violet were prepared such that the concentration of trimer **5.2** plus the concentration of crystal violet was equal to 30 µM in acetate buffer. In other words, [trimer **5.2**] + [crystal violet] = 30 µM. Mixtures were prepared to span $\chi_{\text{crystal violet}}$ from *ca.* 0.01 to 0.9, where $\chi_{\text{crystal violet}}$ is calculated by the following ratio: [crystal violet] / ([crystal violet] + [trimer **5.2**]). These mixtures were prepared from the 10 mg/mL trimer **5.2** stock solutions and the 500 µM crystal violet stock solutions. This same process was followed for the five trimer **5.2** homologue-crystal violet mixtures as well. Table 5.3 lists the volumes of trimer **5.2** stock solution, crystal violet stock solution, and buffer that are mixed to prepare the samples in Figure 5.2D.

Table 5.3: Representative sample preparation for Job's method of continuous variation

$\chi_{\text{crystal violet}}$	conc. (µM) trimer **5.2**	conc. (µM) crystal violet	vol (µL) stock trimer **5.2**	vol (µL) stock crystal violet	vol (µL) buffer
0.016	29.5	0.5	9.4	0.5	490.1
0.05	28.5	1.5	9.1	1.5	489.4
0.083	27.5	2.5	8.8	2.5	488.7
0.17	25.0	5	8.0	5.0	487.0
0.25	22.5	7.5	7.2	7.5	485.3
0.33	20.0	10	6.4	10.0	483.6
0.42	17.5	12.5	5.6	12.5	481.9
0.50	15.0	15.0	4.8	15.0	480.2
0.58	12.5	17.5	4.0	17.5	478.5
0.67	10.0	20.0	3.2	20.0	476.8
0.75	7.5	22.5	2.4	22.5	475.1
0.83	5.0	25.0	1.6	25.0	473.4
0.92	2.5	27.5	0.8	27.5	471.7

The fluorescence intensity of these mixtures was recorded on a Cary Eclipse fluorimeter. The excitation wavelength was 550 nm, and the emission was monitored from 620–650nm. Prior to recording the intensity from all of the trimer **5.2**-crystal violet mixtures, the excitation slit width and photomultiplier tube voltage was optimized to achieve *ca.* 900 RFU from the brightest sample, as described above. The resulting raw data was normalized to the most intense sample in the series, and graphed versus $\chi_{\text{crystal violet}}$. This same process was followed for the five trimer **5.2** homologue-crystal violet mixtures as well. The resulting data was fitted to a one-to-one trimer-crystal violet binding model and to a two-to-one trimer-crystal violet binding model using OriginPro. See the nonlinear regression analysis section for more detail and the equations used to fit the data.

5.4.8 X-ray crystallography

X-ray crystallographic studies of the trimer **5.2** homologues were performed using the protocols previously published by our laboratory with minor modifications. These procedures are

slightly modified, and in some cases taken verbatim, from Salveson et *al. J. Am. Chem. Soc.* **5.2016**, *139*, 4458–4467 and Salveson et *al. J. Am. Chem. Soc.* **5.2018**, *140*, 5842–5852.[63,65]

5.4.9 Crystallization of trimer 5.2 homologues

Trimers ***5.2$_{I31V}$*** *and* ***5.2$_{F20Cha}$***: Crystal growth was optimized using conditions similar to those we had previously reported for trimer **5.2**.[61] In the optimization, the pH and cryoprotectant concentrations were varied across the 4x6 matrix of a Hampton VDX 24-well plate to generate crystals that diffracted well. The hanging drops for these optimizations were prepared on glass slides by combining 1 or 2 µL of peptide solution with 1 or 2 µL of well solution in ratios of 1:1, 2:1, and 1:2. Crystals that formed were checked for diffraction using a Rigaku Micromax-007 HF diffractometer with a Cu rotating anode at 1.54 Å.

Trimers ***5.2$_{I31Chg}$*** *and* ***5.2$_{F19Cha}$***: Conditions were identified in 96-well plates. Three kits from Hampton Research (Crystal Screen, Index, and PEG/ION) were used to screen trimers **5.2$_{\mathbf{I31Chg}}$** and **5.2$_{\mathbf{F19Cha}}$**, for a total of 288 separate crystallization experiments (three 96-well plates). Each well in the 96-well plates was loaded with 100 µL of a solution from the kits. The hanging drops were set up using a TTP Labtech Mosquito pipetting robot. For each well, three hanging drops were prepared comprising either 50, 75, or 100 nL of well solution mixed with either 100, 75, or 50 nL of a 10 mg/mL solution of trimer **5.2$_{\mathbf{I31Chg}}$** or trimer **5.2$_{\mathbf{F19Cha}}$**. Crystal growth was further optimized in 24-well plates in an analogous fashion described for the optimization of trimers **5.2$_{\mathbf{I31V}}$** and **5.2$_{\mathbf{F20Cha}}$**.

5.4.10 X-ray diffraction data collection, data processing, and refinement

Data collection: Diffraction data were collected using a Rigaku Micromax-007 HF diffractometer with a Cu rotating anode at 1.54 Å with 0.5° rotation per image. The program CrystalClear 2.0 was used to design collection strategies with multiplicities exceeding 20. This high multiplicity facilitates sulfur single-wavelength anomalous diffraction phasing. This collection strategy results in multiple data sets from a single crystal that need to be merged with one another.

Data processing: Each individual data set was integrated and scaled using XDS.[89] The multiple data sets were then merged using BLEND.[118,166] Hybrid structure search (HySS) in the Phenix software suite was used to determine the coordinates of the sulfur atoms.[90] The initial electron density maps were generated using the coordinates of the anomalous signal as initial positions in Autosol.

Refinement and model manipulation: Phenix.refine was used to refine the models of the timer **5.2** homologues. Coot was used to manipulate the coordinates of the models.[120] Table 5.1 summarizes the crystal properties, data collection, and data processing for the trimer **5.2** homologues.

5.4.11 Analytical ultracentrifugation

Trimer **5.2** and its homologues were sedimented in the presence of crystal violet on a Beckman Optima AUC at the Center for Analytical Ultracentrifugation of Macromolecular Assemblies (CAUMA) at the University of Texas Health Science Center at San Antonio (UTHSCSA). Samples were prepared from the 10 mg/mL trimer and 500 µM crystal violet stock solutions, described above, in buffer comprising 50 mM sodium acetate and 50 mM acetic acid buffer

(pH 4.6). All samples were measured at 20 °C at 60 krpm by UV intensity detection at 560 nm, 564 nm, or at 594 nm in the presence of crystal violet. All measurements were performed using an An60Ti rotor and standard 2-channel titanium centerpieces (Nanolytics). All data were analyzed with UltraScan 4.0 release 2470.[243] The partial specific volumes of peptides were determined by UltraScan using the peptide sequence.[243]

Sedimentation velocity data were analyzed as previously described.[244] Optimization was performed by 2-dimensional spectrum analysis (2DSA)[213] with simultaneous removal of time- and radially-invariant noise contributions. 2DSA solutions were further refined using the parametrically constrained spectrum analysis (PCSA)[245] and, where applicable, analyzed by the enhanced van Holde-Weischet analysis.[246] PCSA solutions were further refined using Monte Carlo analysis[247] to determine confidence limits for the determined parameters. The calculations are computationally intensive and are carried out on high-performance computing platforms.

5.4.12 Isothermal titration calorimetry

Isothermal titration calorimetry (ITC) experiments were performed on a Malvern MicroCal PEAQ-ITC. All titrations were performed at 25 °C, using a 750 rpm stirring speed. The reference power for each titration was set to 5 µcal/s. The titrations were performed by titrating 500 µM triphenylmethane dye into 100 µM trimer **5.2**. All samples were prepared in buffer comprising 50 mM acetic acid and 50 mM sodium acetate (pH 4.6), as described above. The syringe was filled with 40 µl of the triphenylmethane dye sample. The sample cell was filled with 280 µL of the trimer **5.2** sample. An initial 60 seconds of baseline was recorded prior to a single 0.2 µL injection, followed by thirteen 3 µL injections. Each injection was spaced by either 120 or 150 seconds to ensure that the signal decayed back to the baseline value. The integrated heats of injection were calculated in the Malvern software. The heat of

dilution for each triphenylmethane dye was measured by titrating 500 µM triphenylmethane dye into acetate buffer, in a similar fashion to titrating triphenylmethane dye into trimer **5.2**. The heat of dilution was then subtracted from the heat of injection measured for the trimer **5.2**-triphenylmethane dye titrations in the Malvern software. Data were fit with a one-to-one trimer **5.2**-triphenylmethane dye binding model and a two-to-one trimer **5.2**-triphenylmethane dye binding model using Solver in Excel. See the nonlinear regression analysis section for more detail and the equations used to fit the data.

5.4.13 SDS-PAGE

The oligomerizaiton of trimers **5.2** were studied by tricine SDS-PAGE. This procedure is slightly modified from Salveson et *al. J. Am. Chem. Soc.* **5.2018**, *140*, 5842–5852.[65] Reagents and gels for tricine SDS-PAGE were prepared according to recipes reported previously.[61,167] 2X samples of each trimer were prepared by diluting 10 mg/mL solutions of the peptides or timers with 18 MΩ deionized water to the appropriate concentration. The 2X samples were then diluted with 2X SDS-PAGE loading buffer (100 mM Tris buffer at pH 6.8, 20% (w/v) glycerol, and 4% (w/v) SDS) to create the 1X samples which were loaded into the gel. 6 µL of the 1X samples were loaded into the gel, in addition to 1 µL of Spectra^{TM} Multicolor Low Range Protein Ladder (Thermo Scientific part no.: 26628). Samples were run through a 16% polyacrylamide gel with a 4% stacking polyacrylamide gel at a constant 80 V at 23 °C. Silver-staining was used to visualize trimer bands in the SDS-PAGE gel as described previously.[61,168]

5.4.14 Size exclusion chromatography

The solution-phase oligomerization of the trimer **5.2** homologues was studied by size exclusion chromatography (SEC). SEC was performed in 50 mM sodium acetate/50 mM acetic

acid buffer at 4 °C on a GE Superdex 75 10/300 GL column. Samples were prepared as follows: Each trimer was dissolved in 18 MΩ water to a concentration of 10 mg/mL. These 10 mg/mL stocks were then diluted to 1 mg/mL by adding 65 µL of the 10-mg/mL solutions to 585 µL of the sodium acetate running buffer. The samples were then loaded into the column and run using a flow rate of 0.85 mL/min. Chromatograms were recorded at 215 nm and normalized to the highest absorbance value. Carbonic anhydrase, cytochrome C, aprotinin, and vitamin B12 were run as size standards, in a similar fashion.

5.4.15 Nonlinear regression analysis

Two models were used for nonlinear regression analysis for data from both Job plot experiments and isothermal titration calorimetry experiments: a 1:1 trimer-dye model and a 2:1 trimer-dye model. The derivation of these two models for both experiments is identical, however, each model is modified slightly to handle the different observables in the Job plot experiments and ITC experiments. The following text first describes the derivation of the functions used to determine the concentration of either the 1:1 or the 2:1 trimer-dye complexes. These functions are then applied to data analysis for both Job plots experiments and ITC experiments.

1:1 trimer-dye model

The association of one molecule of trimer with one molecule of dye can be expressed as the following equilibrium:

$$[trimer]_{\mathrm{f}} + [dye]_{\mathrm{f}} <-> [1:1\ complex] \tag{5.1}$$

where $[\text{trimer}]_\text{f}$ and $[\text{dye}]_\text{f}$ are the free concentrations of the trimer and dye, while [1:1 complex] is the concentration of the 1:1 complex. The corresponding association constant, K_a, and material balance equations for this equilibrium are:

$$K_\text{a} = \frac{[1:1\ complex]}{[trimer]_\text{f}[dye]_\text{f}} \tag{5.2}$$

$$[trimer]_\text{t} = [trimer]_\text{f} + [1:1\ complex] \tag{5.3}$$

$$[dye]_\text{t} = [dye]_\text{f} + [1:1\ complex] \tag{5.4}$$

where $[\text{trimer}]_\text{t}$ and $[\text{dye}]_\text{t}$ are the total concentrations of the trimer and dye. The concentration of the 1:1 trimer-dye complex, [1:1 complex], can be expressed as a function of the association constant K_a, the total concentration of trimer $[\text{trimer}]_\text{t}$, and the total concentration of dye $[\text{dye}]_\text{t}$. This function is derived by rearranging equations 5.3 and 5.4 and substituting them into equation 5.2. The resulting equation is then rearranged into a quadratic equation of the form:

$$a[1:1\ complex]^2 + b[1:1\ complex] + c = 0 \tag{5.5}$$

The roots of quadratic equation can be solved using the quadratic formula, which results in an expression for the concentration of the 1:1 complex:

$$[1:1\ complex] = \frac{[dye]_t + [trimer]_t + K_a{}^{-1} - \sqrt{([dye]_t + [trimer]_t + K_a{}^{-1})^2 - 4[dye]_t[trimer]_t}}{2} \tag{5.6}$$

Equation 5.6 will be modified in the following sections for the analysis of either the Job plot experiments or the ITC titrations.

2:1 trimer-dye model

The association of two molecules of trimer with one molecule of dye can be expressed as the following two equilibriums:

$$[trimer]_f + [dye]_f <-> [1:1\ complex] \tag{5.7}$$

$$[1:1\ complex] + [trimer]_f <-> [2:1\ complex] \tag{5.8}$$

where $[\text{trimer}]_f$ and $[\text{dye}]_f$ are the free concentrations of the trimer and dye, [1:1 complex] is the concentration of the 1:1 complex, and [2:1 complex] is the concentration of the 2:1 complex. In our derivation of an expression for [2:1 complex] as a function of an association constant and the total concentrations of trimer and dye, we treat the concentration of the 1:1 complex as negligible, which greatly simplifies the math for the following steps.

This simplification allows us to express the association of two molecules of trimer with one molecule of dye as a single equilibrium:

$$2[trimer]_{\mathrm{f}} + [dye]_{\mathrm{f}} <-> [2:1\ complex] \tag{5.9}$$

The corresponding association constant, K_a, and material balance equations for this simplified equilibrium are:

$$K_{\mathrm{a}} = \frac{[2:1\ complex]}{([trimer]_{\mathrm{f}})^2[dye]_{\mathrm{f}}} \tag{5.10}$$

$$[trimer]_{\mathrm{t}} = [trimer]_{\mathrm{f}} + 2[2:1\ complex] \tag{5.11}$$

$$[dye]_{\mathrm{t}} = [dye]_{\mathrm{f}} + [2:1\ complex] \tag{5.12}$$

The concentration of the 2:1 complex [2:1 complex] can be written as a function of the association constant K_a, the total concentration of trimer, and the total concentration of dye. This function is derived by rearranging equations 5.11 and 5.12 and substituting them

into equation 5.10. The resulting equation is then rearranged into a cubic equation of the form:

$$a[2:1\ complex]^3 + b[2:1\ complex]^2 + c[2:1\ complex] + d = 0 \tag{5.13}$$

The roots of this cubic equation can be determined using Cardano method with Vieta's substitution, as described elsewhere[248]. This process results in a expression of the concentration of the 2:1 complex as a function of the association constant K_a, total concentration of trimer $[trimer]_t$, and total concentration of dye $[dye]_t$:

$$[2:1\ complex] = ... \tag{5.14}$$

Equation 5.14 is too long to be reproduced here, legibly, with the terms $[dye]_t$, $[trimer]_t$, and K_a substituted into it. Equation 5.14 will be modified in the following sections for the analysis of either the Job plot experiments or the ITC titrations.

Job Plots

In traditional titration experiments, the observable (e.g., fluorescence intensity) is plotted versus the total concentration of titrant added. In Job's method of continuous variation, the observable is instead plotted versus the mole fraction, χ, of one of the species in the equilibrium. For this reason, equations 5.6 and 5.14 were modified to accommodate mol fraction of crystal violet, $\chi_{\text{crystal violet}}$, in place of the total concentrations of trimer and dye.

This modification was achieved by substituting $[\text{trimer}]_t$ and $[\text{dye}]_t$ in equations 5.6 and 5.14 with:

$$[trimer]_t = C - C\chi_{\text{crystal violet}} \tag{5.15}$$

$$[dye]_t = C\chi_{\text{crystal violet}} \tag{5.16}$$

where C is the total concentration used for the Job Plot (in our case, 30 µM). The term, $\chi_{\text{crystal violet}}$, can range from 0–1.

To normalize both the 1:1 and 2:1 Job plot models, (1) evaluate equation 5.6 at $\chi_{\text{crystal violet}} = 0.5$, and evaluate equation 5.14 at $\chi_{\text{crystal violet}} = 0.33$; (2) divide equation 5.6 and equation 5.14 by these values, respectively. This cumbersome process was done in OriginPro using the Fitting Function Organizer. For simplicity, we have included these models below, broken up as simple equations. These equations can be directly incorporated into a user defined function as equations in OriginPro. In this process, the user must specify a constant value for C, and OriginPro will determine the association constant.

For the 1:1 trimer-dye model:

L = C * x

R = C - C * x

a = L + R + (1 / K)

b = 4 * L * R

PP = sqrt(a * a - b)

d = (L + R + (1/ K) - PP) / 2

LL = C * 0.5

RR = C - C * 0.5

e = LL + RR + (1 / K)

f = 4 * LL * RR

QQ = sqrt(e * e - f)

g = (LL + RR + (1/ K) - QQ) / 2

y = d / g

where y is the normalized value of the function, C is the total concentration of trimer + dye used in the experiment, K is the association constant, and x is $\chi_{\text{crystal violet}}$.

For the 2:1 trimer-dye model:

L = C * x

R = C - C * x

a = -4 * K

bo = 4 * K * L + 4 * K * R

c = -1 - 4 * K * L * R - K * R * R

d = K * L * R * R

DO = bo * bo - 3 * a * c

```
D1 = 2 * bo * bo * bo - 9 * a * bo * c + 27 * d * a * a

DD = D1 * D1 - 4 * DO * DO * DO

PP = sqrt(DD)

G = (D1 / 2 + PP / 2)^(1/3)

B = ( -1 / ( 3 * a ) ) * ( bo + G + DO / G )

LL = C * 0.33

RR = C - C * 0.33

aa = -4 * K

boo = 4 * K * LL + 4 * K * RR

cc = -1 - 4 * K * LL * RR - K * RR * RR

dd = K * LL * RR * RR

DOO = boo * boo - 3 * aa * cc

D11 = 2 * boo * boo * boo - 9 * aa * boo * cc + 27 * dd * aa * aa

DDD = D11 * D11 - 4 * DOO * DOO * DOO

PPP = sqrt(DDD)

GG = (D11 / 2 + PPP / 2)^(1/3)

BB = ( -1 / ( 3 * aa ) ) * ( boo + GG + DOO / GG )

y = B/BB
```

where y is the normalized value of the function, C is the total concentration of trimer + dye used in the experiment, K is the association constant, and x is $\chi_{\text{crystal violet}}$.

Isothermal titration calorimetry

In an isothermal titration calorimetry experiment, a series of i injections of small volume, v_i, of a concentrated solution of dye, $[\text{dye}]_{\text{syringe}}$, are added to a sample well with volume V_o containing a solution of trimer, $[\text{trimer}]_{\text{cell, i}}$. In these types of titrations, a sequence of events is assumed to occur for the each injection: (1) a volume v_i of the syringe solution is added to the cell; (2) this addition displaces a volume v_i of the sample cell, which displaces the contents of the cell by a factor v_i/V_o; (3) the system re-equilibrates to the new concentrations of $[\text{trimer}]_{\text{free, cell, i}}$, $[\text{complex}]_{\text{cell, i}}$, $[\text{dye}]_{\text{free, cell, i}}$.

The initial concentration of the trimer in the sample cell prior to the start of the titration is given by $[\text{trimer}]_{\text{initial, cell}}$. The total concentration of trimer in the cell after the 1st injection is given by:

$$[trimer]_{\text{total, 1}} = (1 - \frac{v_1}{V_o})[trimer]_{\text{cell, initial}} \tag{5.17}$$

The total concentration of trimer in the sample cell after the ith injection is then given by:

$$[trimer]_{\text{total, i}} = (1 - \frac{v_i}{V_o})[trimer]_{\text{cell, i-1}} \tag{5.18}$$

The total concentration of dye in the sample cell after the 1st injection is given by:

$$[dye]_{\text{total, 1}} = \frac{v_{\text{i}}}{V_{\text{o}}}[dye]_{\text{syringe}} \tag{5.19}$$

The total concentration of dye in the sample cell after the ith injection is then given by:

$$[dye]_{\text{total, i}} = \frac{v_{\text{i}}}{V_{\text{o}}}[dye]_{\text{syringe}} + (1 - \frac{v_{\text{i}}}{V_{\text{o}}})[dye]_{\text{cell, i-1}} \tag{5.20}$$

Equations 5.17–5.20 are then substituted into equation 5.6 and 5.14 to calculate the concentration of the 1:1 complex, $[\text{1:1 complex}]_{\text{i}}$, and the concentration of the 2:1 complex, $[\text{2:1 complex}]_{\text{i}}$, in the sample cell after the 1st or ith injection of dye. The heat observed from each injection i upon formation of the 1:1 complex is given by:

$$q_{\text{i}} = V_{\text{o}}\Delta H([1:1\ complex]_{\text{i}} - (1 - \frac{v_{\text{i}}}{V_{\text{o}}})[1:1\ complex]_{\text{i-1}}) + q_{\text{i, dilute}} \tag{5.21}$$

and the heat observed from each injection i upon formation of the 2:1 complex is given by:

$$q_{\text{i}} = V_{\text{o}}\Delta H([2:1\ complex]_{\text{i}} - (1 - \frac{v_{\text{i}}}{V_{\text{o}}})[2:1\ complex]_{\text{i-1}}) + q_{\text{i, dilute}} \tag{5.22}$$

In equations 5.21 and 5.22, $q_{\text{i, dilute}}$ is the heat of dilution of the dye. This constant can be measured by titrating dye into buffer. Equations 5.21 and 5.22 were incorporated into excel, and Solver was used to determine values for K_{a}, ΔH, and $q_{\text{i, dilute}}$.

5.4.16 Docking and molecular modeling

The model of the trimer **5.2**-crystal violet interaction depicted in Figure 5.9 was generated as follows: Starting coordinates of trimer **5.2** were generated from the trimer **5.2** crystallographic structure (PDB 5SUR) using PyMOL and saved as a new PDB file. Coordinates of crystal violet were obtained from the RCSB as a PDB file (ligand three letter code CVI). iBabel was used to convert the crystal violet PDB file into a PDBQT file prior to docking. Docking was performed using AutoDock Tools and AutoDock 4.2.[220] In AutoDock Tools, a grid was chosen to encompass the entire molecule of trimer **5.2**. Trimer **5.2** was treated as a rigid receptor in these calculations. Docking was repeated 50 times using the genetic algorithm. The lowest energy cluster, as determined by AutoDock Tool's built-in analysis feature, was chosen to represent the trimer **5.2**-crystal violet model in Figure 4.

The model of the 2:1 trimer **5.2**-crystal violet complex depicted in Figure 5.16 was generated as follows: (1) in PyMOL, create a crude dimer model manually; (2) in Macromodel, generate a hollow dimer model; (3) in AutoDock, dock crystal violet into the hollow dimer model. To generate the crude model of the complex, two copies of the trimer **5.2**-crystal violet model were loaded into PyMOL. The coordinates of one of these models was manipulated manually such that the two trimer **5.2** molecules sandwiched the two molecules of crystal violet. This sandwiching was achieved by manually superimposing the two molecules of crystal violet. The two molecules of crystal violet were deleted, and the resulting crude hollow trimer **5.2** sandwich structure was saved as a new PDB file. This process results in the generation of a crude model of the sandwich complex with a cavity in the center. It is currently not possible to perform minimizations in Macromodel with crystal violet present within the sandwich model, as MacroModel currently does not support atom types for the central carbocation of crystal violet. It is possible to model crystal violet with the positive charge centered on one of three three nitrogens; however, this results in an unrealistic conformation of the triphenylmethane core. For these reasons, we chose to minimize the sandwich model without

crystal violet in MacroModel, then redock crystal violet into the energy-minimized model using AutoDock.

To minimize the crude hollow model, the structure was loaded into MacroModel using the Maestro graphical interface. Bond orders and atom types were edited as needed to correct errors in bond orders (i.e. carbonyl groups becoming hydroxy groups) and atom types (ammonium groups becoming amine groups). Prior to minimization, several constraints were applied to the model. First, all main-chain hydrogen bonds were constrained as a 2.5Å long bond (from amide N-H to carbonyl oxygen). This constraint was applied to every cross-strand hydrogen bond within the macrocyclic β-hairpins that compose the crosslinked trimers. This constraint was also applied to three hydrogen bonds that occur between two macrocyclic β-hairpins at the three vertices of the crosslinked trimers (33 intramolecular hydrogen bond constraints, per molecule of trimer **5.2**). Six intermolecular hydrogen bonds were also enforced between the layers of the sandwich model. These hydrogen bonds were enforced between Ile_{31} of one trimer, and Ile_{31} of the other trimer, at each of the three vertices of the sandwich. We found that six additional intermolecular distant constraints between the side chains of Phe_{20} that line the empty cavity of the sandwich were required to maintain the binding pocket of crystal violet in this minimization. These constraints were chose to ensure that the phenyl rings from one trimer were 7 Å from the phenyl rings from the other trimer. Without these constraints, the minimization collapses this cavity rendering it impossible to redock crystal violet into this energy minimized trimer **5.2** sandwich model. This model was minimized in MacroModel using the MMFFs force field in GB/SA water. After minimization of the crude trimer **5.2** sandwich model with both the hydrogen bond and Phe_{20}–Phe_{20} constraints, the model was again minimized without the hydrogen bond constraints. Crystal violet was then docked into this hollow dimer model using AutoDock 4.2, as described above for the generation of the trimer **5.2**-crystal violet model.

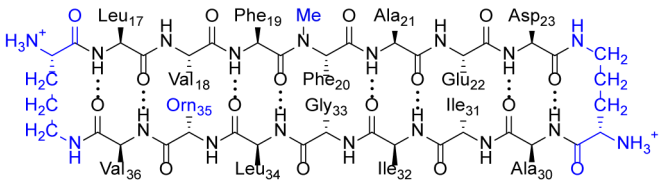
Leu17
Phe19
Me
Ala21
Asp23
Val18
Phe20
Glu22
Orn35
Gly33
Ile31
Val36
Leu34
Ile32
Ala30

peptide **5.1**

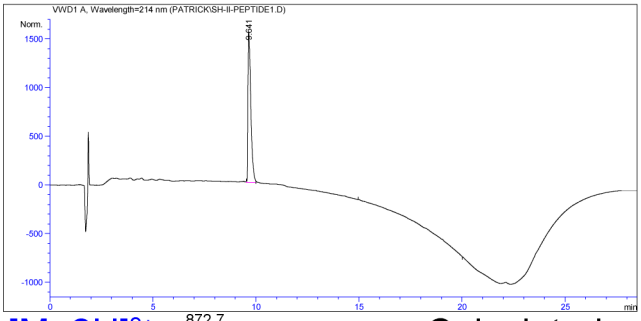
VWD1 A, Wavelength=214 nm (PATRICK\SH-II-PEPTIDE1.D)
Norm.
9.641
min

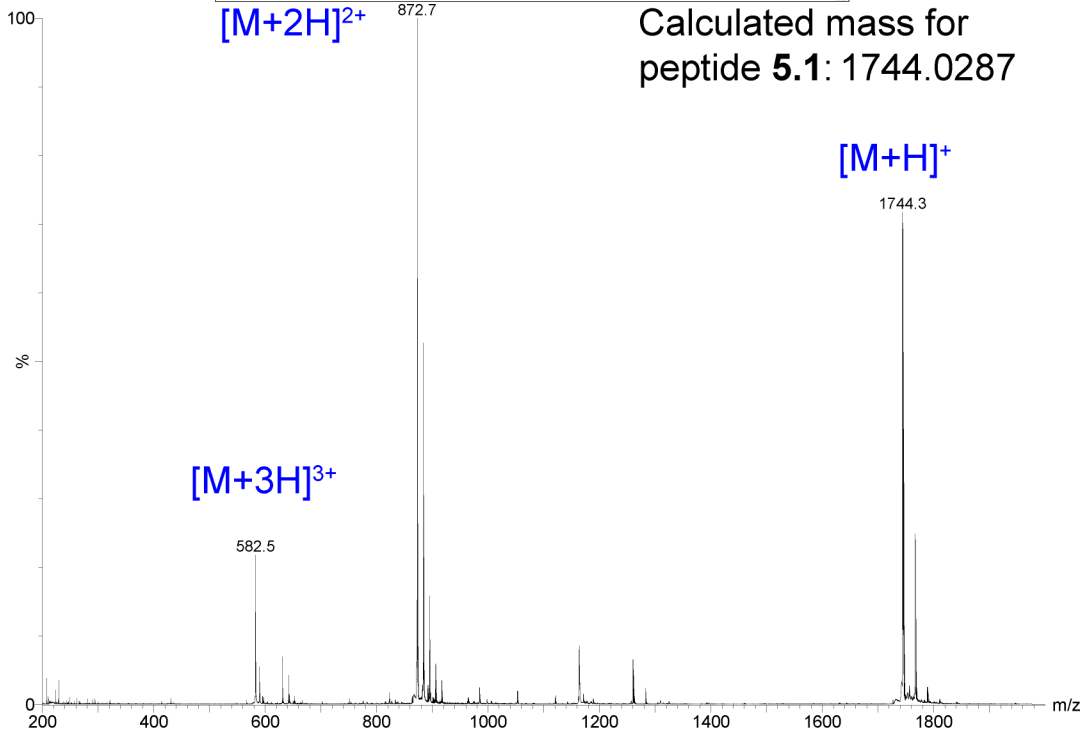
100
%
0
872.7
[M+2H]2+
Calculated mass for peptide 5.1: 1744.0287
[M+H]+
1744.3
[M+3H]3+
582.5
200
400
600
800
1000
1200
1400
1600
1800
m/z

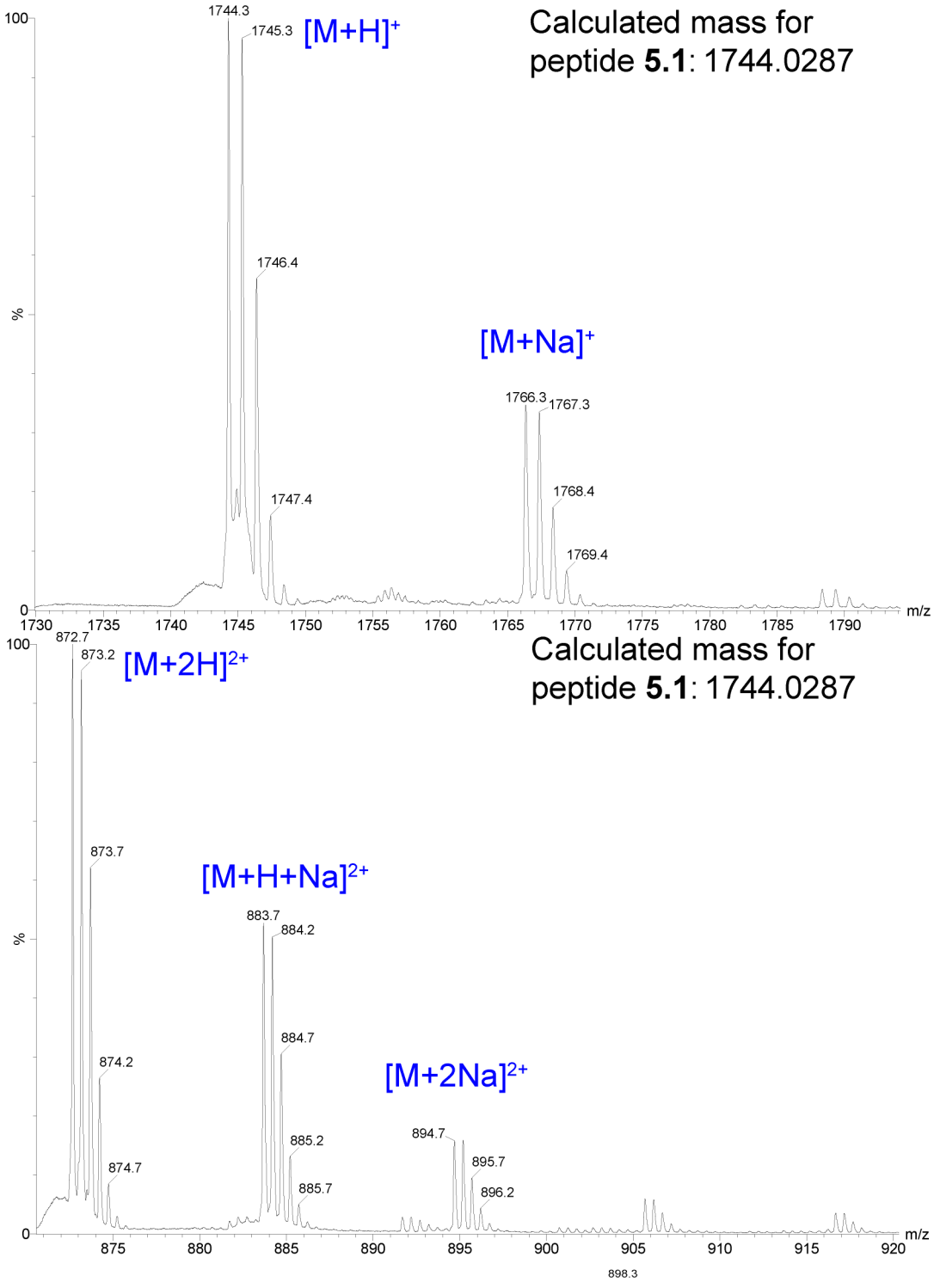
100
%
0
1744.3
1745.3
[M+H]+
Calculated mass for peptide 5.1: 1744.0287
1746.4
[M+Na]+
1766.3
1767.3
1747.4
1768.4
1769.4
1730 1735 1740 1745 1750 1755 1760 1765 1770 1775 1780 1785 1790
m/z
100
%
0
872.7
873.2
[M+2H]2+
Calculated mass for peptide 5.1: 1744.0287
873.7
[M+H+Na]2+
883.7
884.2
884.7
874.2
[M+2Na]2+
894.7
885.2
895.7
874.7
885.7
896.2
875 880 885 890 895 900 905 910 915 920
m/z
898.3

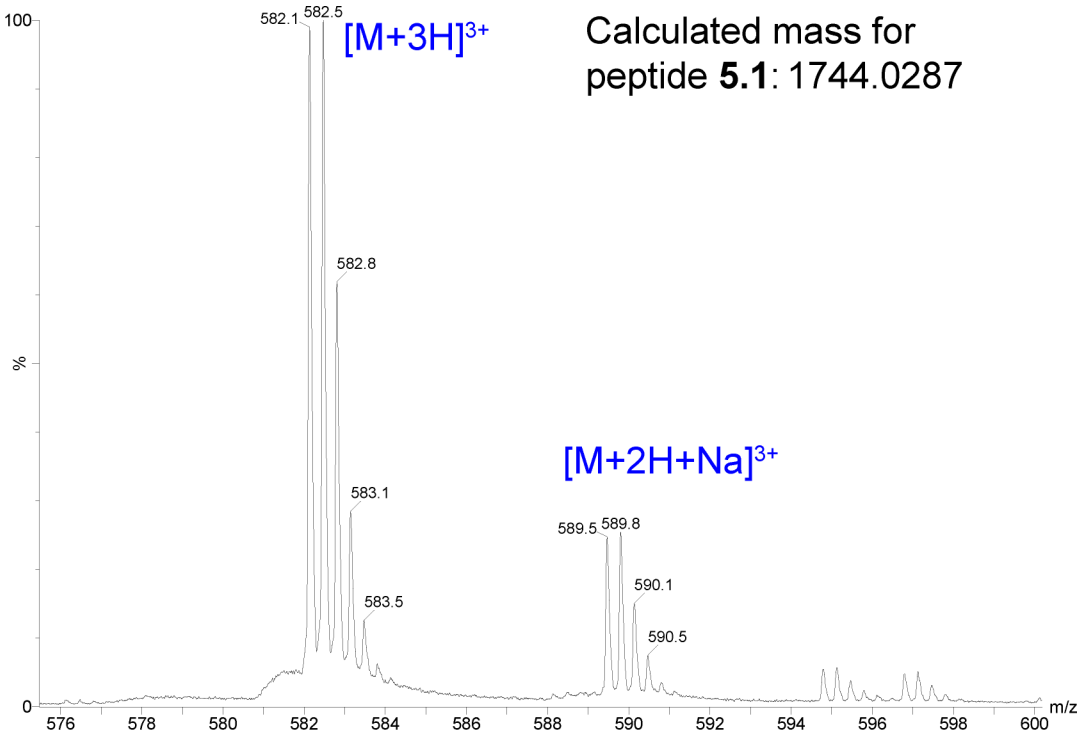
100
%
0
582.1
582.5
582.8
583.1
583.5
[M+3H]3+
Calculated mass for
peptide 5.1: 1744.0287
[M+2H+Na]3+
589.5
589.8
590.1
590.5
576
578
580
582
584
586
588
590
592
594
596
598
600
m/z

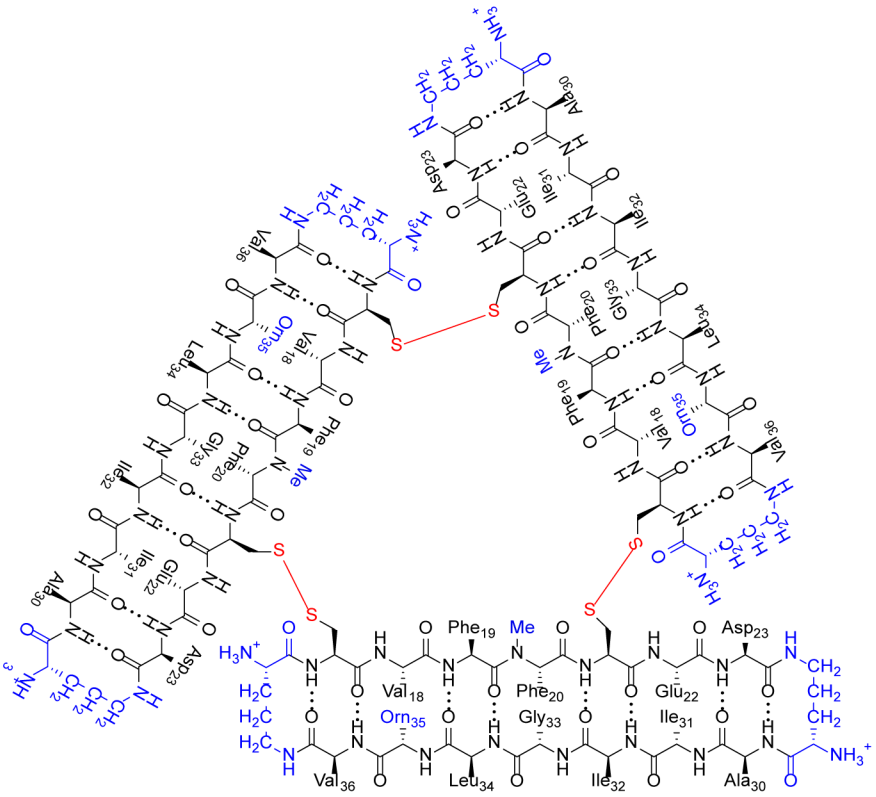

trimer **5.2**

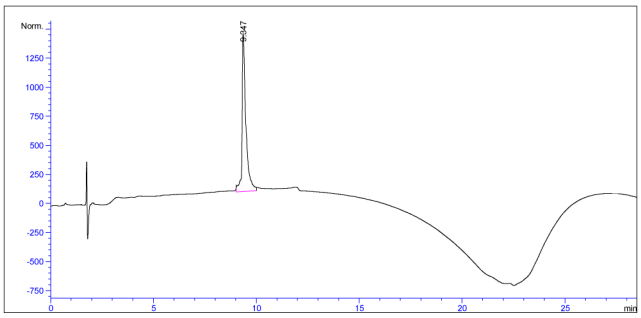

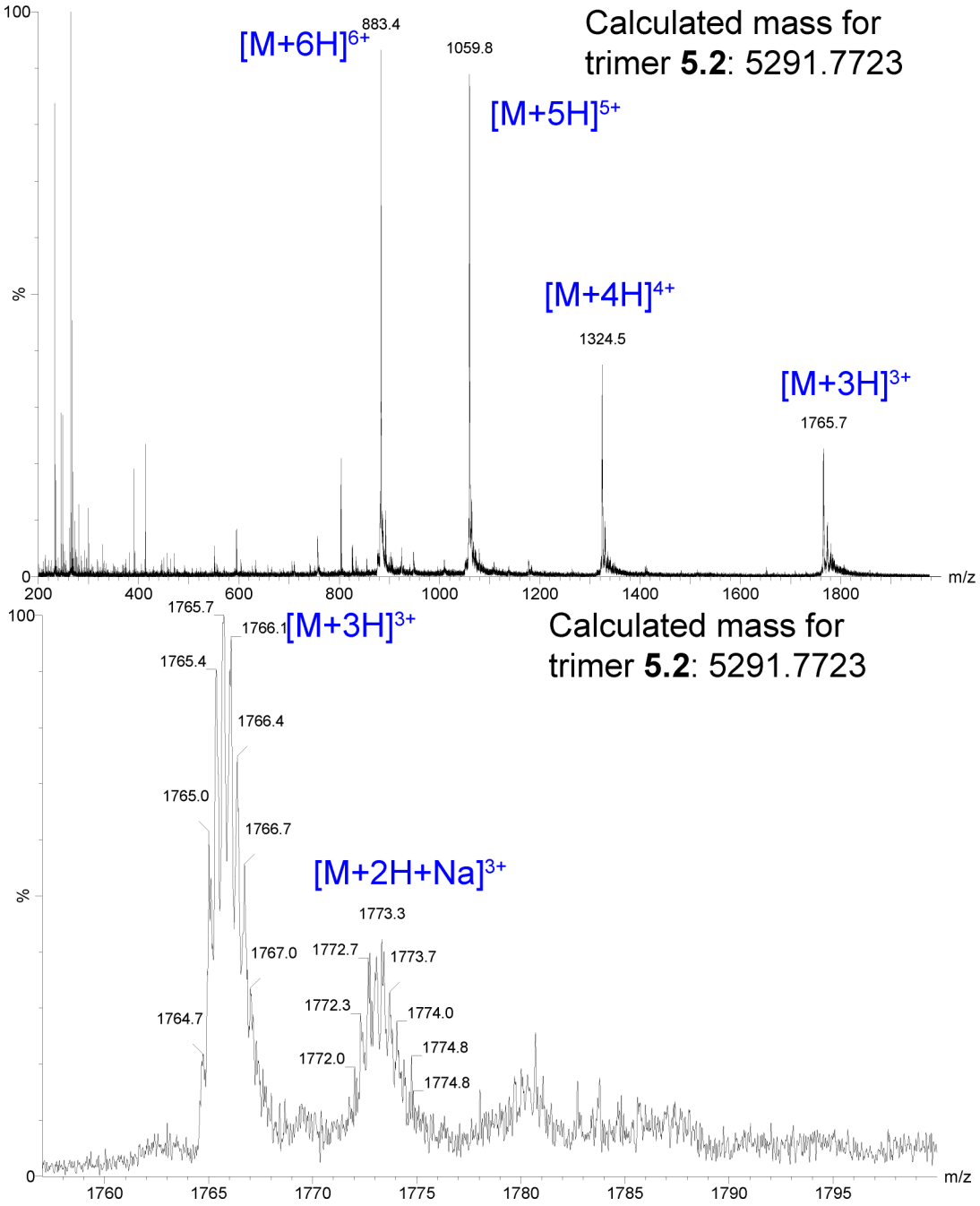
100
%
0
883.4
[M+6H]6+
1059.8
[M+5H]5+
1324.5
[M+4H]4+
1765.7
[M+3H]3+
200
400
600
800
1000
1200
1400
1600
1800
m/z
Calculated mass for
trimer 5.2: 5291.7723
100
%
0
1765.7
1766.1
[M+3H]3+
1765.4
1766.4
1765.0
1766.7
[M+2H+Na]3+
1773.3
1767.0
1772.7
1773.7
1772.3
1774.0
1764.7
1774.8
1772.0
1774.8
1760
1765
1770
1775
1780
1785
1790
1795
m/z
Calculated mass for
trimer 5.2: 5291.7723

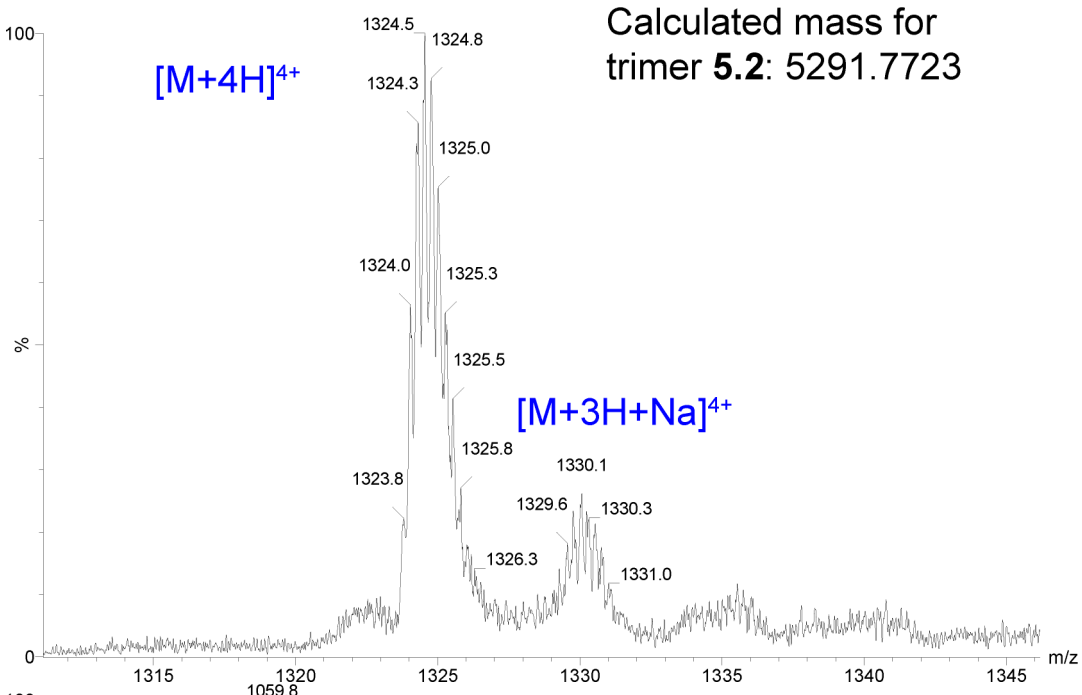
Calculated mass for trimer **5.2**: 5291.7723
[M+4H]4+
[M+3H+Na]4+
1324.5
1324.8
1324.3
1325.0
1324.0
1325.3
1325.5
1325.8
1323.8
1330.1
1329.6
1330.3
1326.3
1331.0
100
%
0
1315
1320
1325
1330
1335
1340
1345
m/z

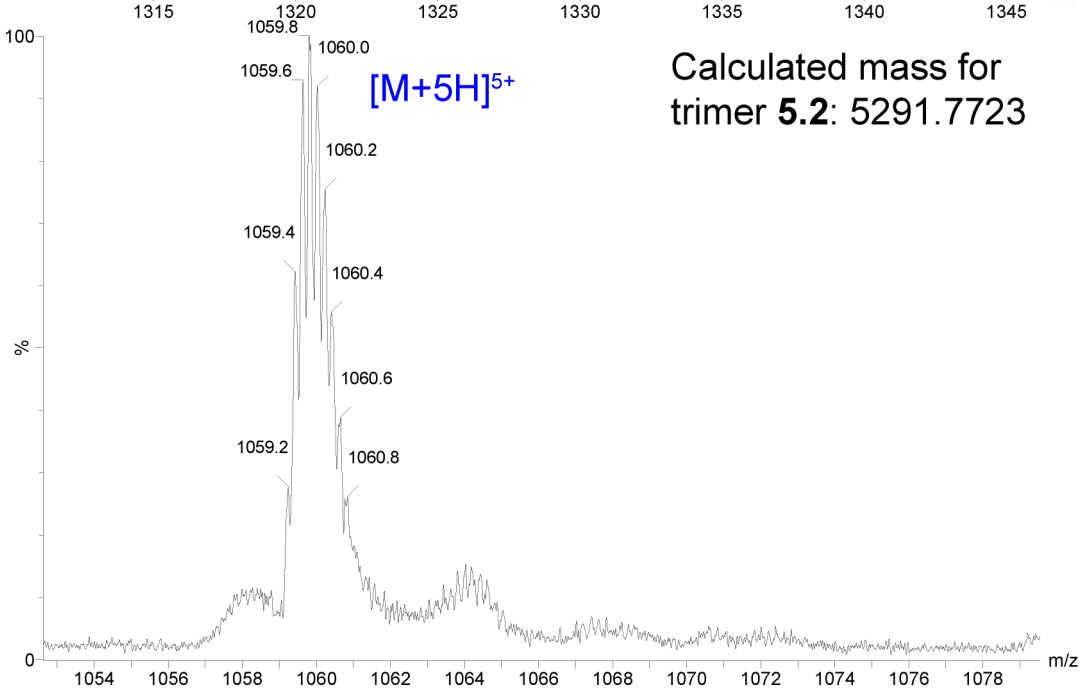
[M+5H]5+
Calculated mass for trimer **5.2**: 5291.7723
1059.8
1060.0
1059.6
1060.2
1059.4
1060.4
1060.6
1059.2
1060.8
100
%
0
1054
1056
1058
1060
1062
1064
1066
1068
1070
1072
1074
1076
1078
m/z

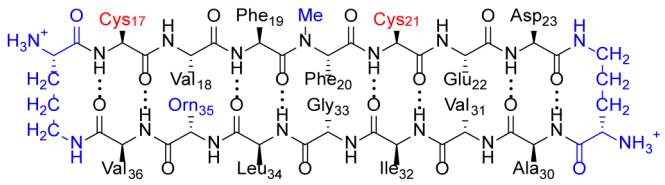

peptide **5.I31V**

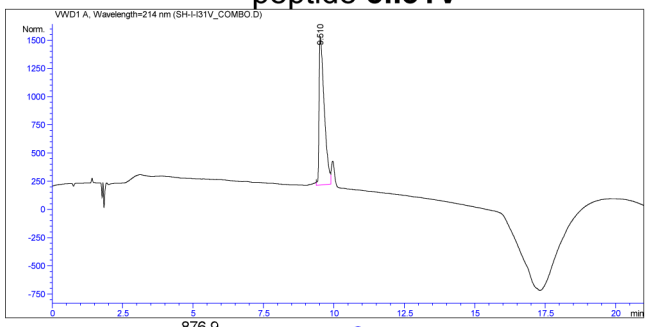

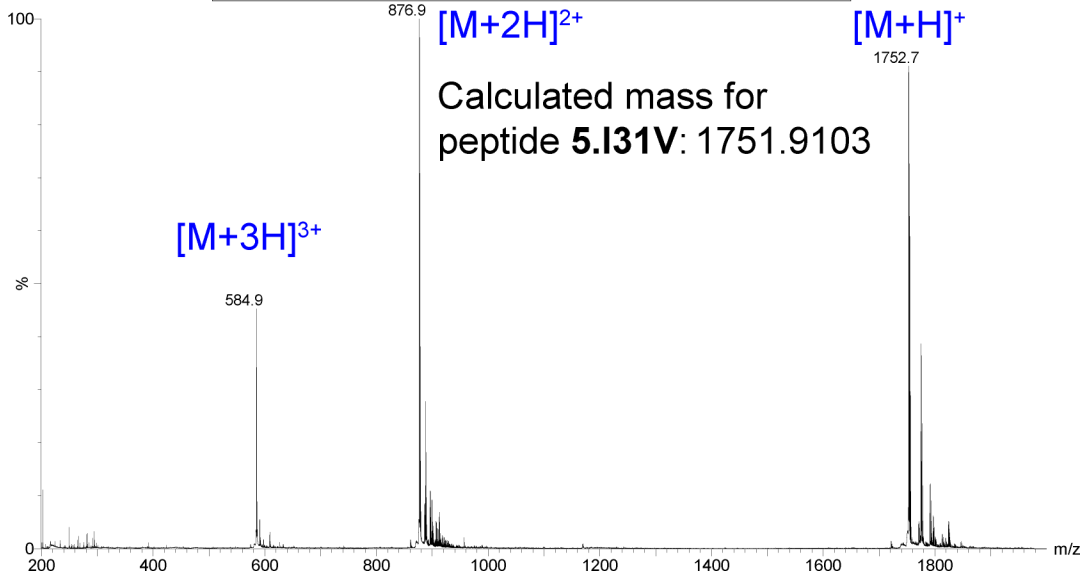

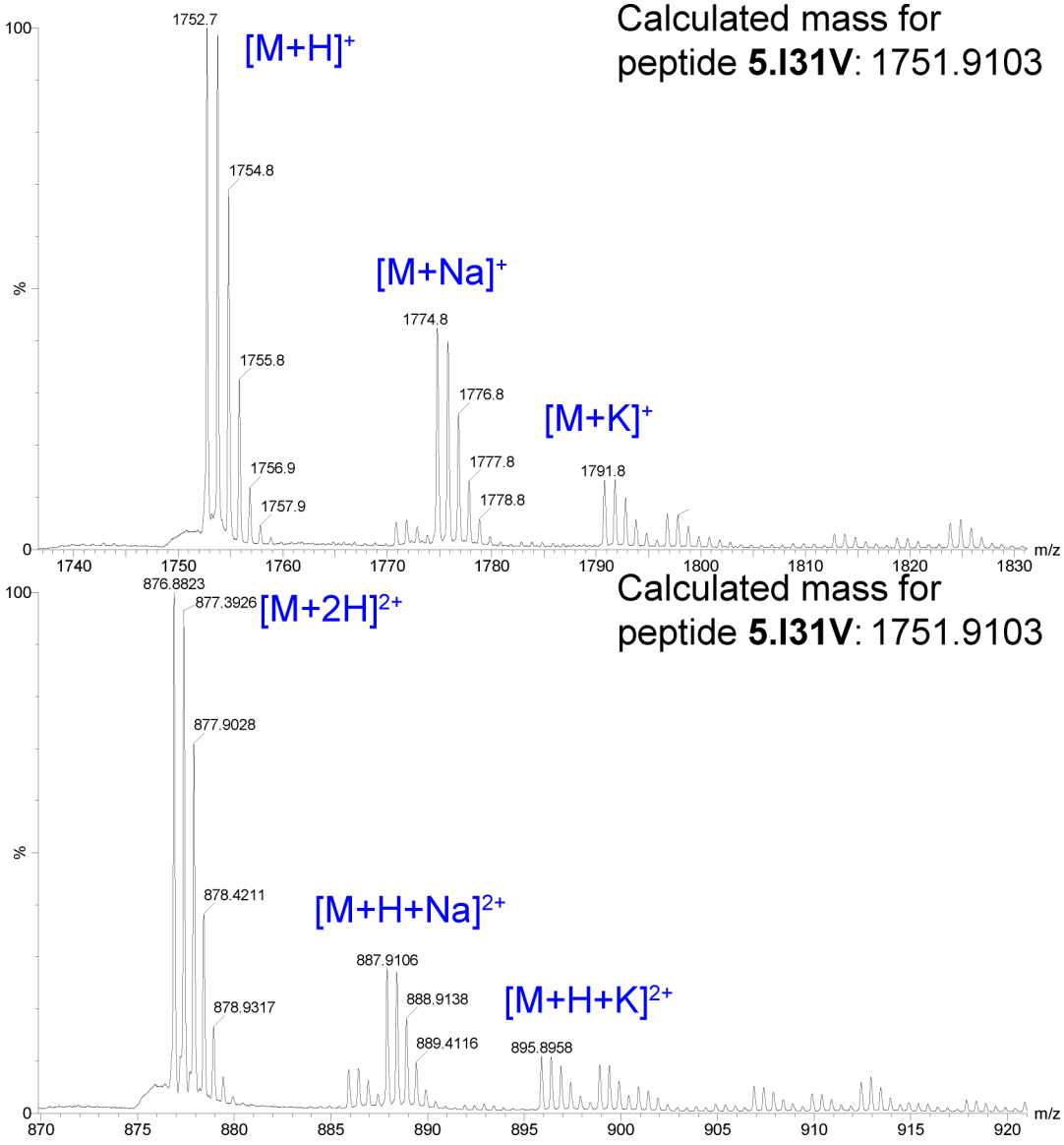
Calculated mass for peptide **5.I31V**: 1751.9103
[M+H]+
[M+Na]+
[M+K]+
1752.7
1754.8
1755.8
1756.9
1757.9
1774.8
1776.8
1777.8
1778.8
1791.8
100
%
0
1740
1750
1760
1770
1780
1790
1800
1810
1820
1830
m/z
Calculated mass for peptide **5.I31V**: 1751.9103
[M+2H]2+
[M+H+Na]2+
[M+H+K]2+
876.8823
877.3926
877.9028
878.4211
878.9317
887.9106
888.9138
889.4116
895.8958
100
%
0
870
875
880
885
890
895
900
905
910
915
920
m/z

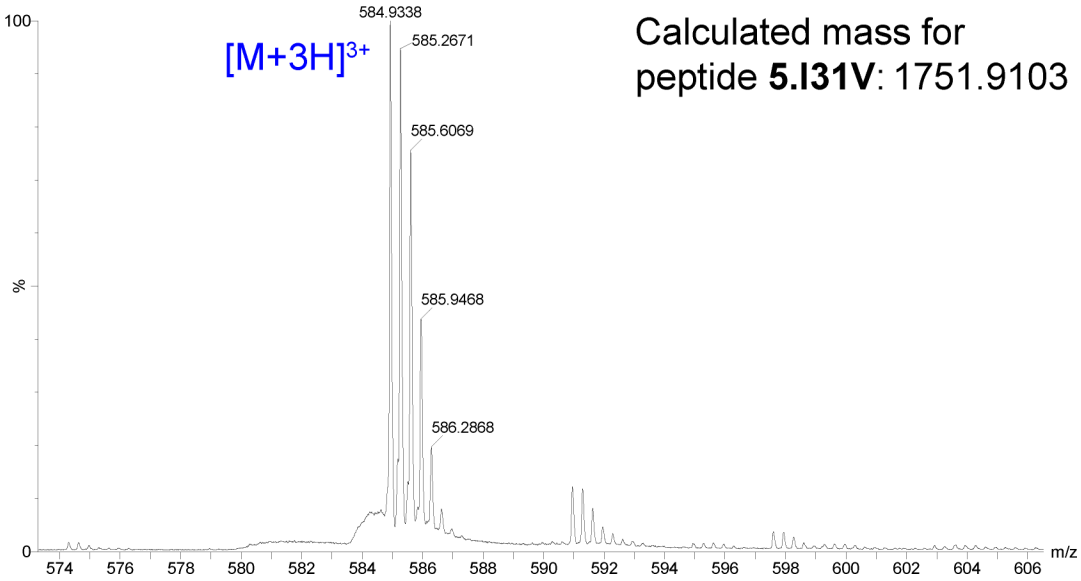
100
%
0
584.9338
585.2671
585.6069
585.9468
586.2868
[M+3H]3+
Calculated mass for
peptide 5.I31V: 1751.9103
574
576
578
580
582
584
586
588
590
592
594
596
598
600
602
604
606
m/z

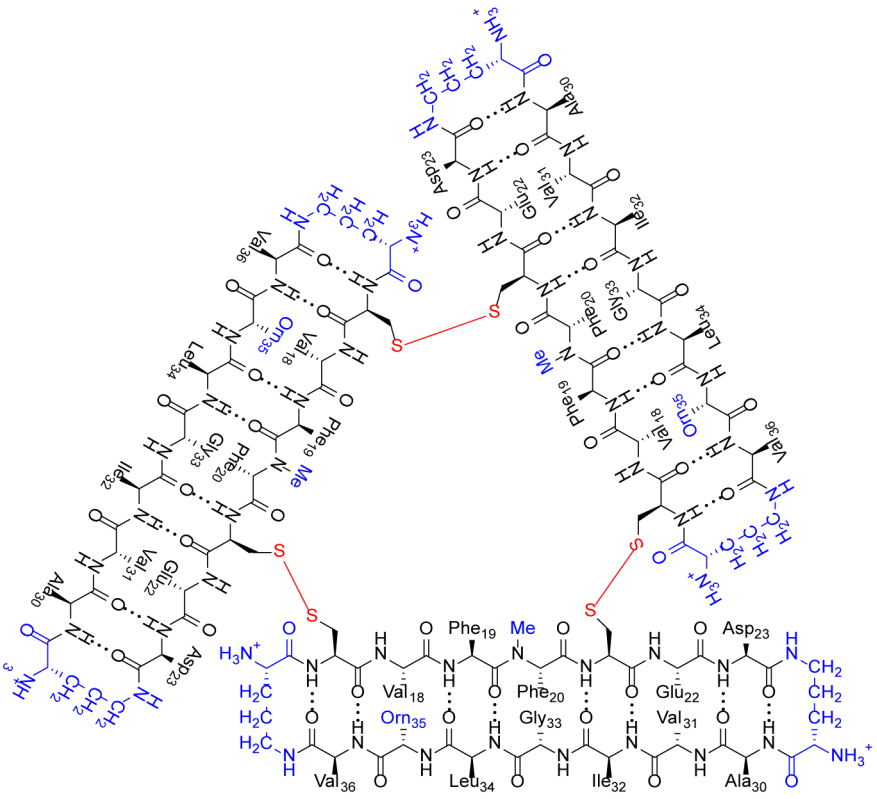

trimer **5.2**$_{\mathbf{I31V}}$

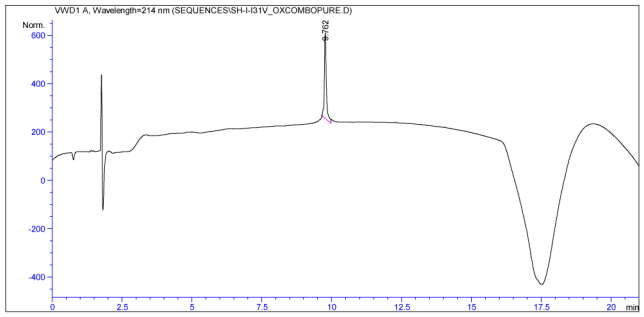

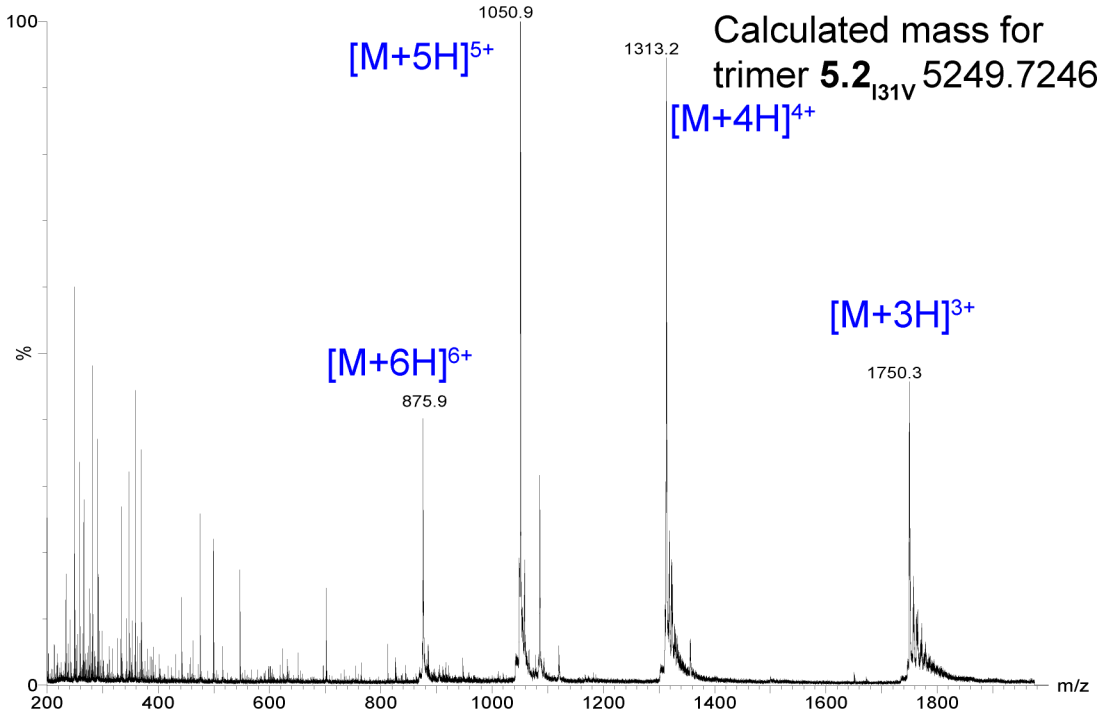

Calculated mass for trimer **5.2**$_{I31V}$ 5249.7246

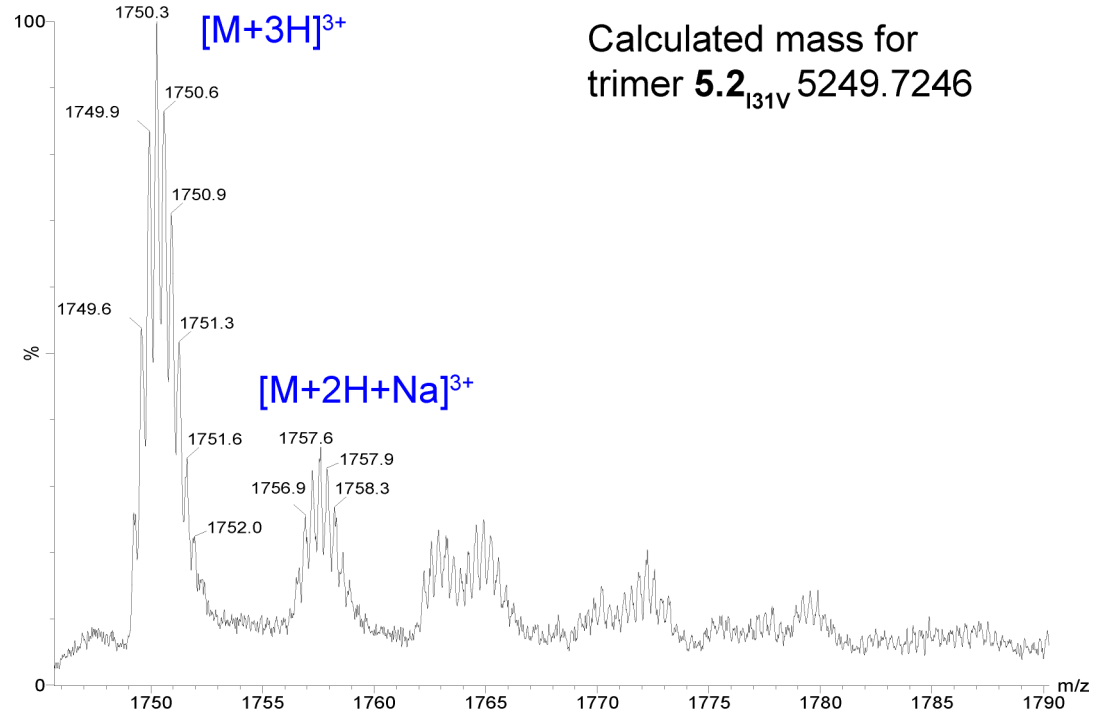

Calculated mass for trimer **5.2**$_{I31V}$ 5249.7246

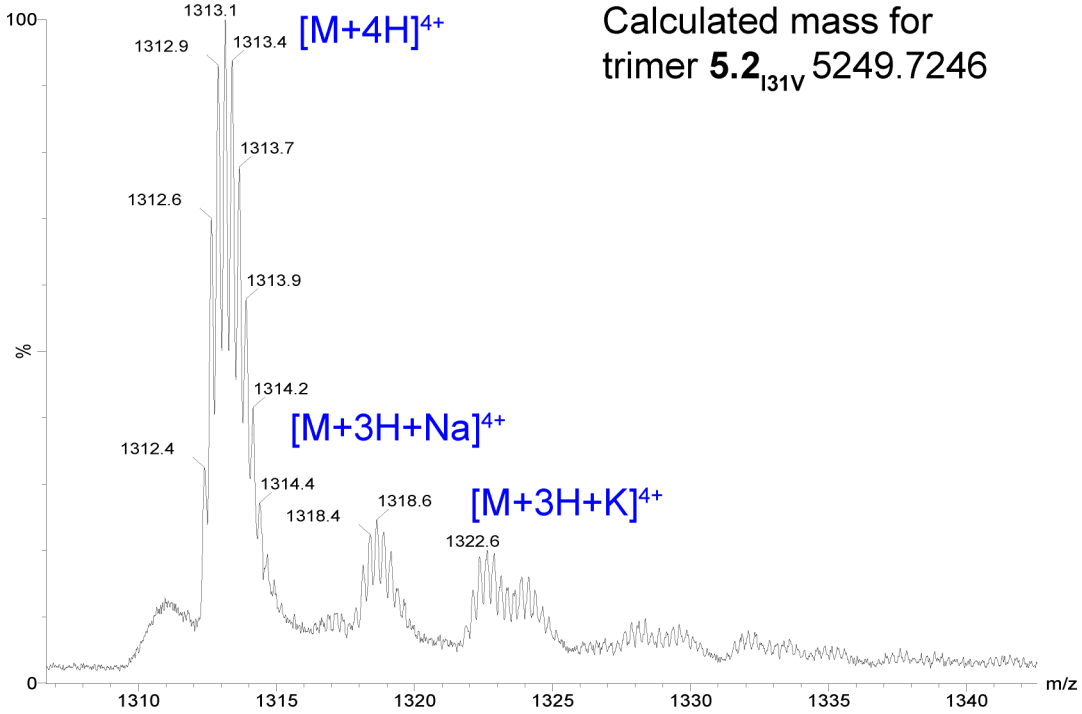
100
%
0
1313.1
1312.9
1313.4
[M+4H]4+
1313.7
1312.6
1313.9
1314.2
[M+3H+Na]4+
1312.4
1314.4
1318.6
1318.4
[M+3H+K]4+
1322.6
1310
1315
1320
1325
1330
1335
1340
m/z
Calculated mass for
trimer 5.2I31V 5249.7246

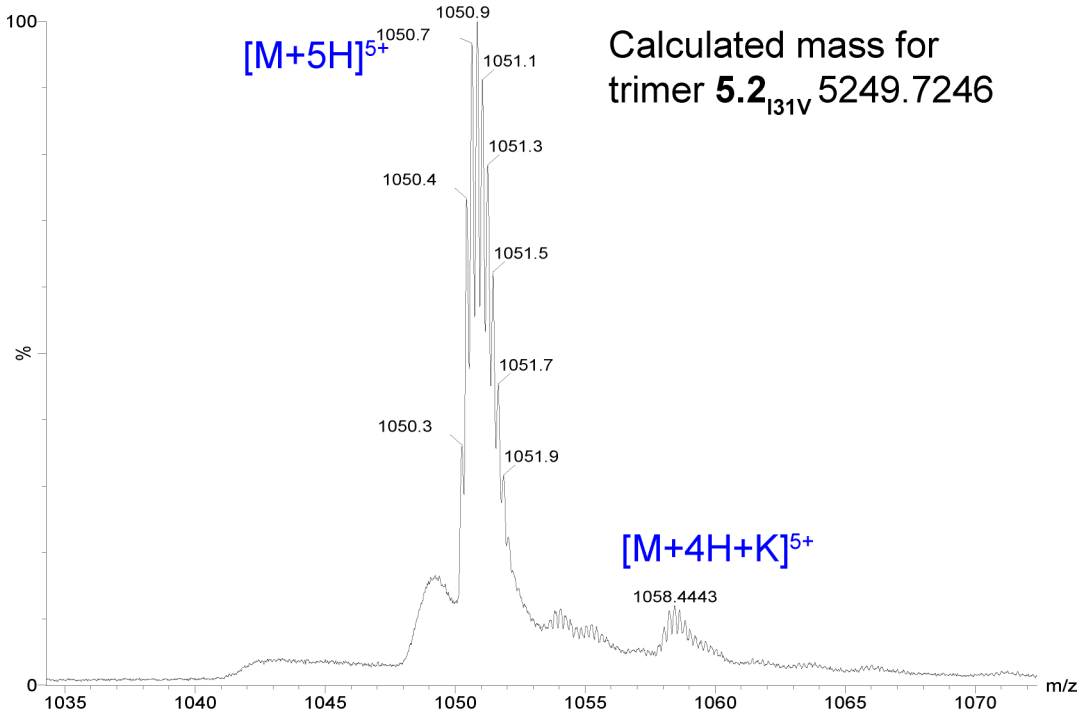
100
%
0
1050.9
[M+5H]5+
1050.7
1051.1
1051.3
1050.4
1051.5
1051.7
1050.3
1051.9
[M+4H+K]5+
1058.4443
1035
1040
1045
1050
1055
1060
1065
1070
m/z
Calculated mass for
trimer 5.2I31V 5249.7246

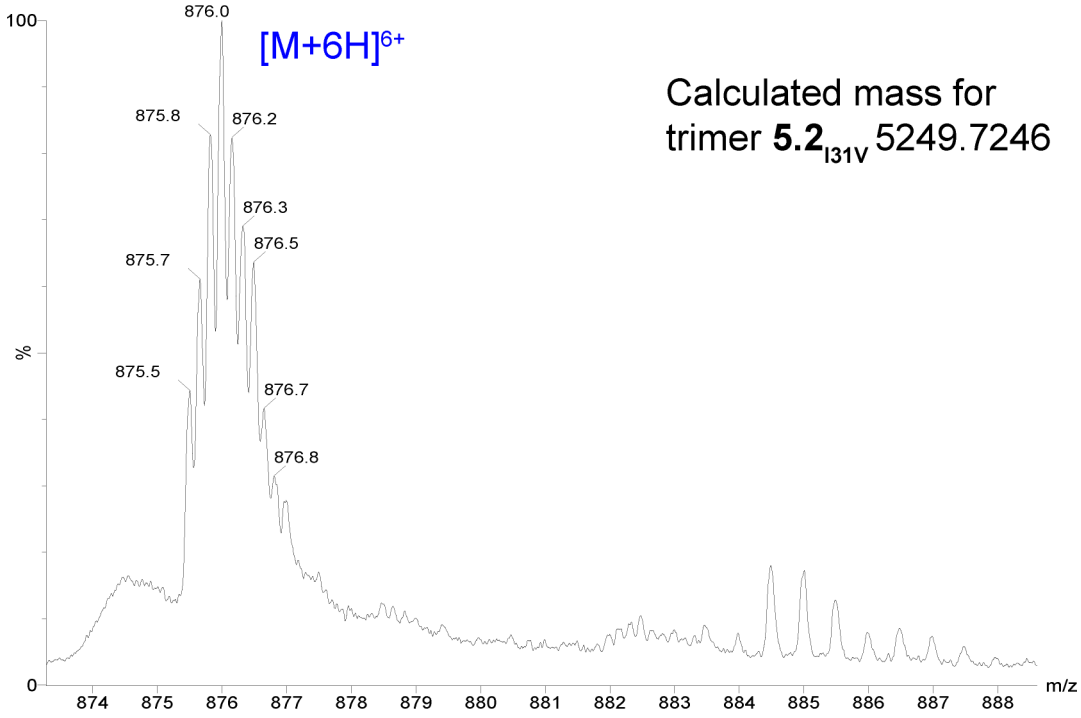
100
%
0
876.0
[M+6H]6+
875.8
876.2
876.3
876.5
875.7
875.5
876.7
876.8
874
875
876
877
878
879
880
881
882
883
884
885
886
887
888
m/z
Calculated mass for
trimer 5.2I31V 5249.7246

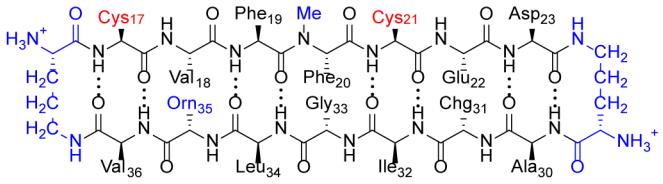

peptide **5.I31Chg**

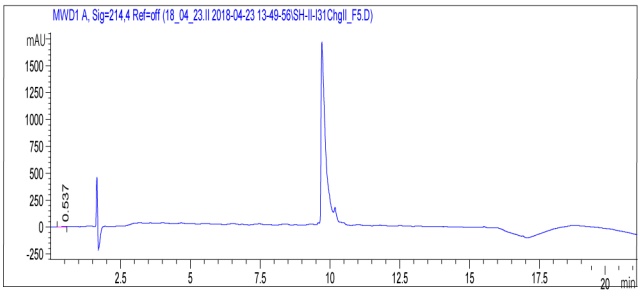

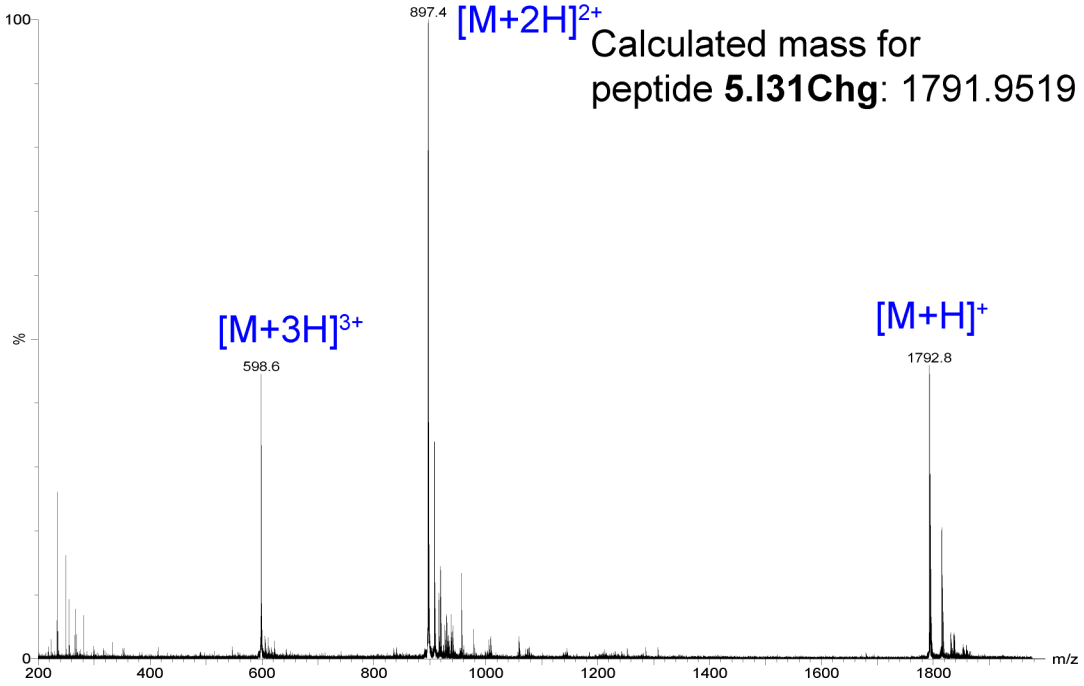

Calculated mass for peptide **5.I31Chg**: 1791.9519

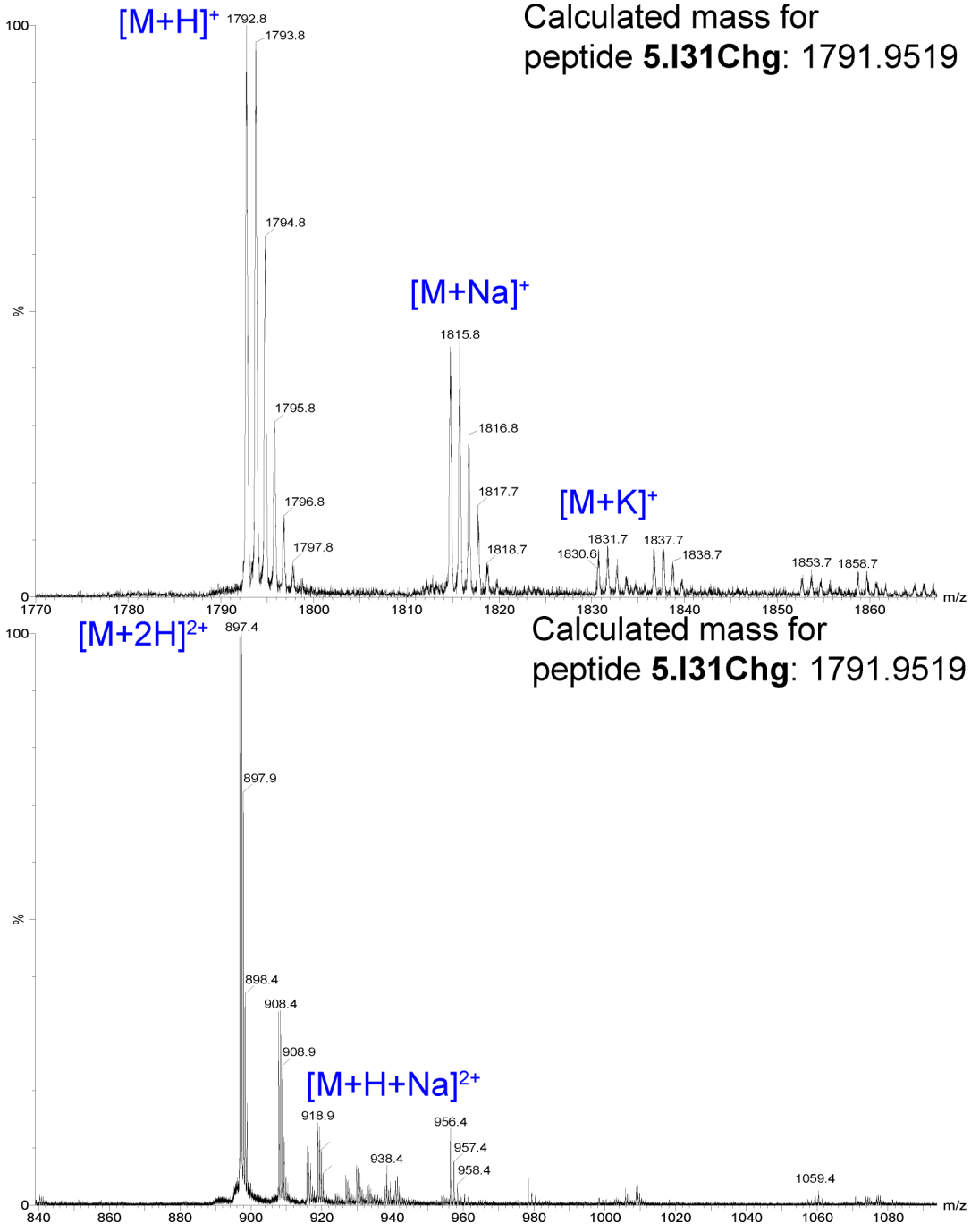
[M+H]+
1792.8
1793.8
1794.8
1795.8
1796.8
1797.8
[M+Na]+
1815.8
1816.8
1817.7
1818.7
[M+K]+
1830.6
1831.7
1837.7
1838.7
1853.7
1858.7
Calculated mass for peptide 5.I31Chg: 1791.9519
m/z
[M+2H]2+
897.4
897.9
898.4
908.4
908.9
[M+H+Na]2+
918.9
938.4
956.4
957.4
958.4
1059.4
Calculated mass for peptide 5.I31Chg: 1791.9519
m/z

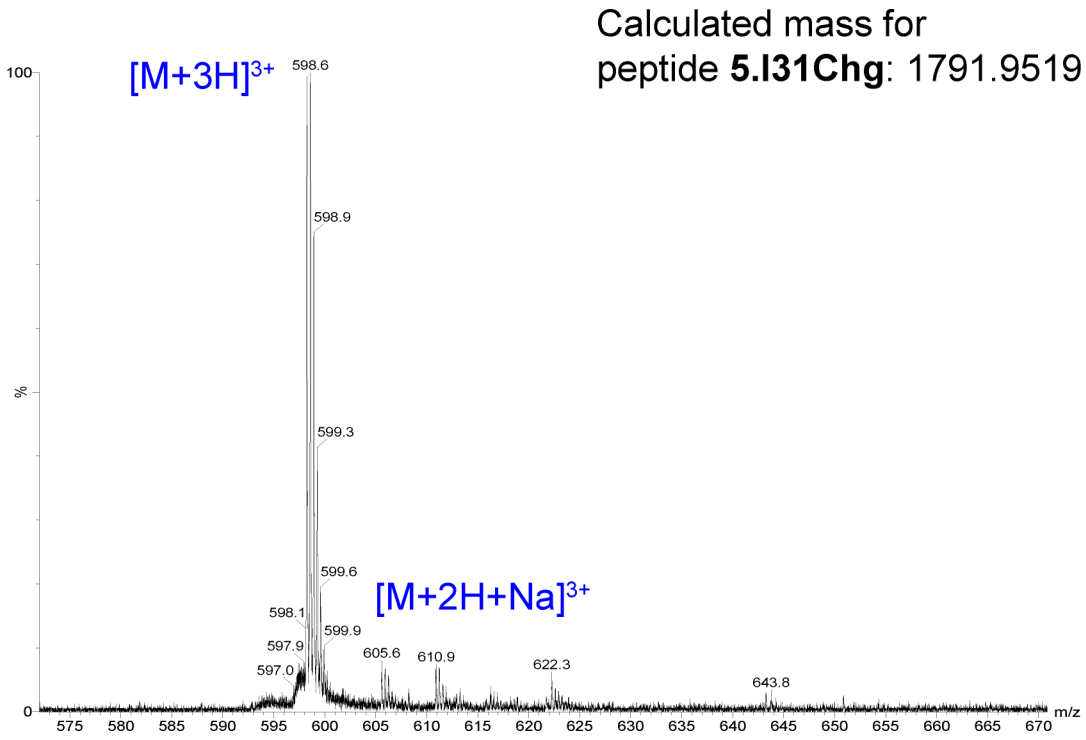
Calculated mass for
peptide **5.I31Chg**: 1791.9519
[M+3H]3+
[M+2H+Na]3+
598.6
598.9
599.3
599.6
598.1
599.9
597.9
597.0
605.6
610.9
622.3
643.8
100
%
0
575 580 585 590 595 600 605 610 615 620 625 630 635 640 645 650 655 660 665 670
m/z

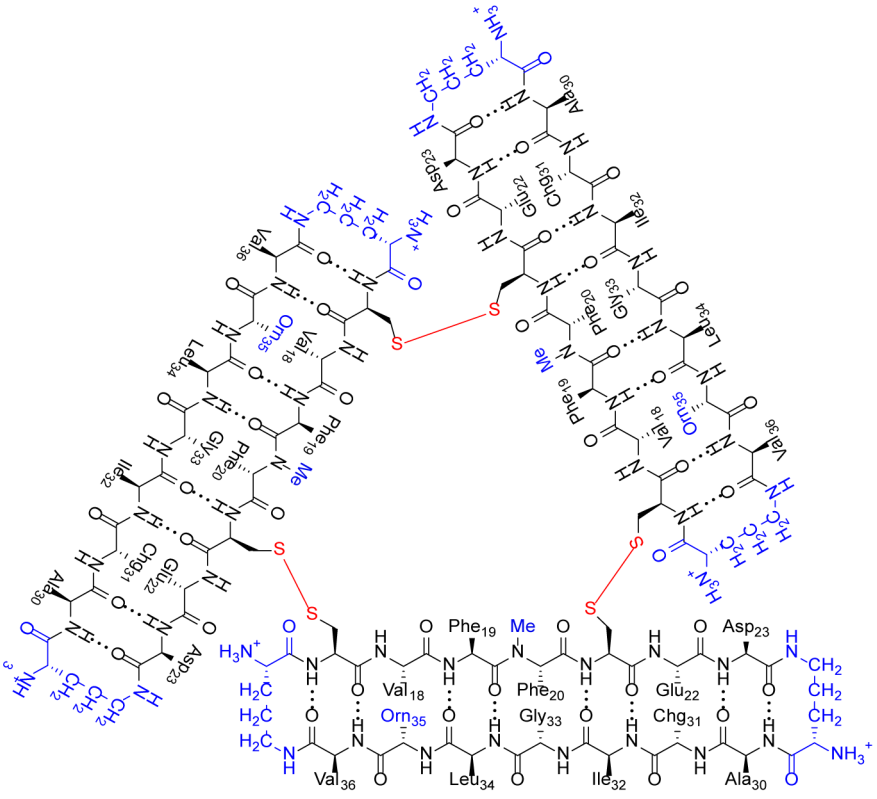

trimer **5.2**$_{\mathbf{I31Chg}}$

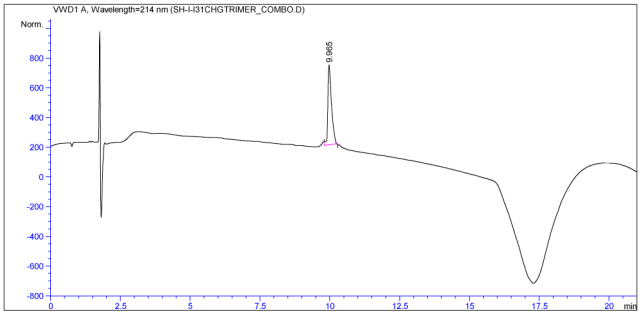

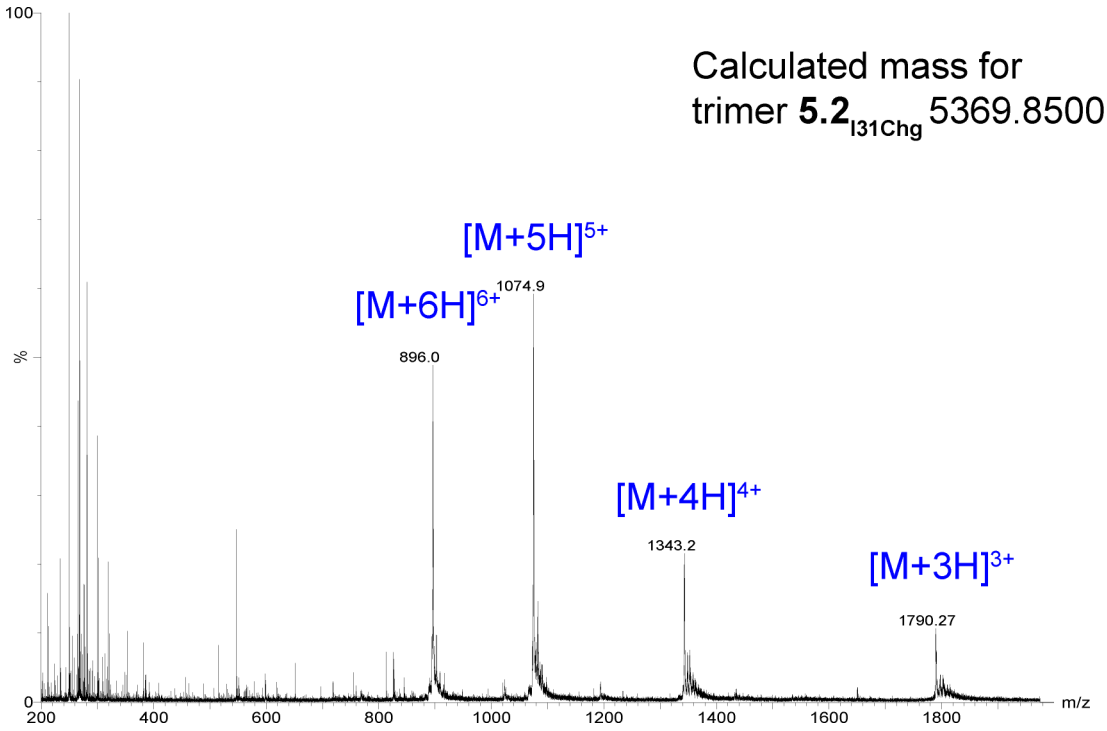
Calculated mass for
trimer **5.2**$_{\text{I31Chg}}$ 5369.8500
[M+5H]$^{5+}$
[M+6H]$^{6+}$
1074.9
896.0
[M+4H]$^{4+}$
1343.2
[M+3H]$^{3+}$
1790.27
100
%
0
200
400
600
800
1000
1200
1400
1600
1800
m/z

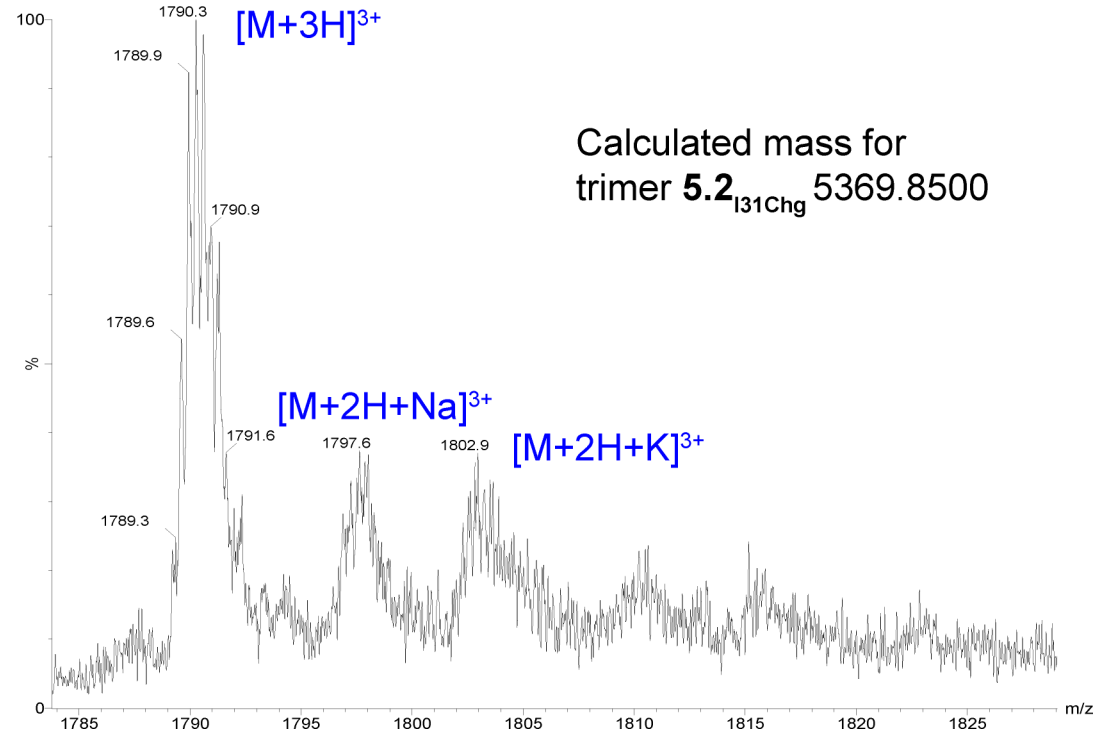
[M+3H]$^{3+}$
1790.3
1789.9
1790.9
1789.6
1789.3
[M+2H+Na]$^{3+}$
1791.6
1797.6
1802.9
[M+2H+K]$^{3+}$
Calculated mass for
trimer **5.2**$_{\text{I31Chg}}$ 5369.8500
100
%
0
1785
1790
1795
1800
1805
1810
1815
1820
1825
m/z

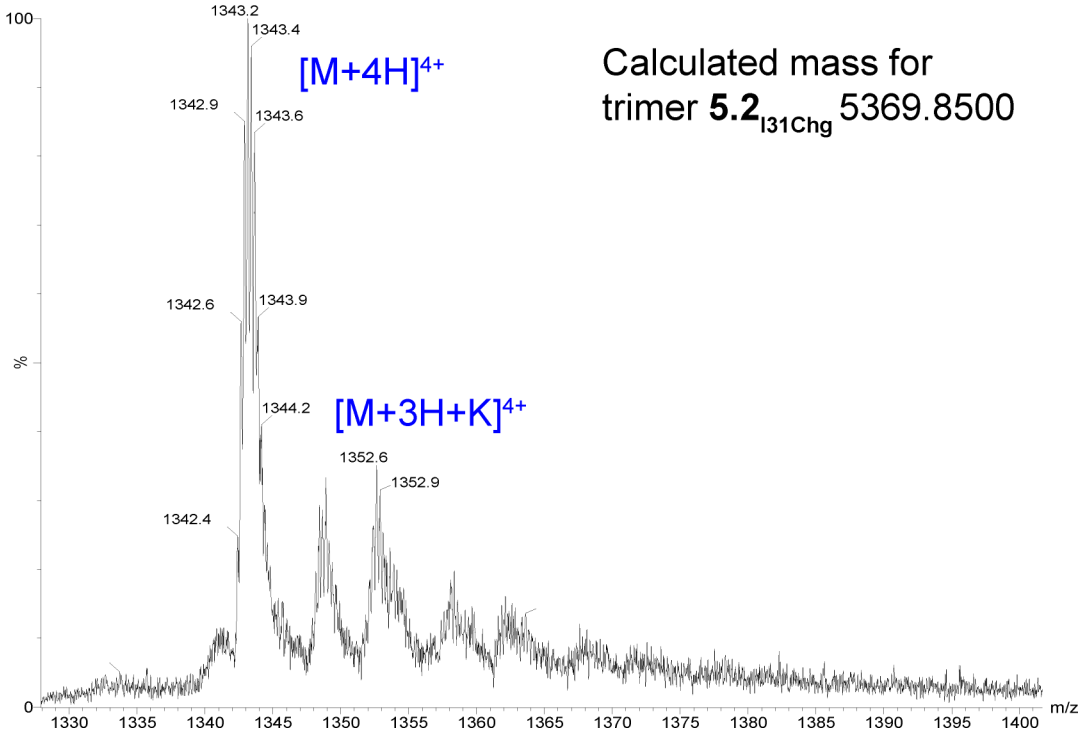

Calculated mass for trimer **5.2**$_{\text{I31Chg}}$ 5369.8500

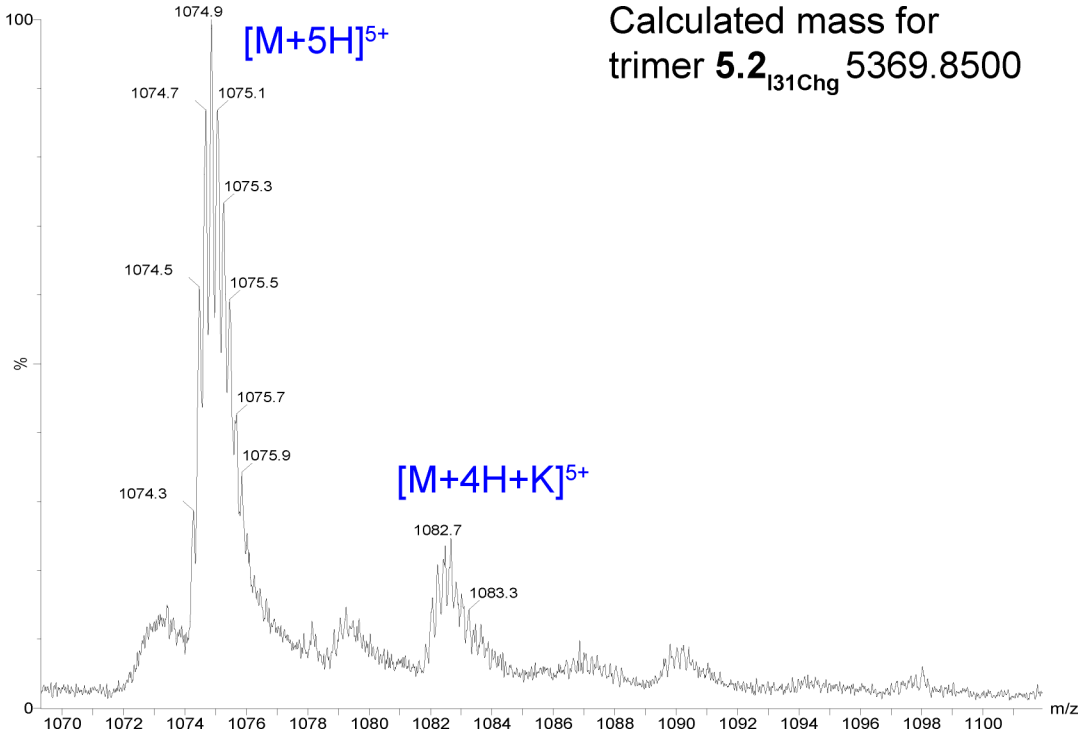

Calculated mass for trimer **5.2**$_{\text{I31Chg}}$ 5369.8500

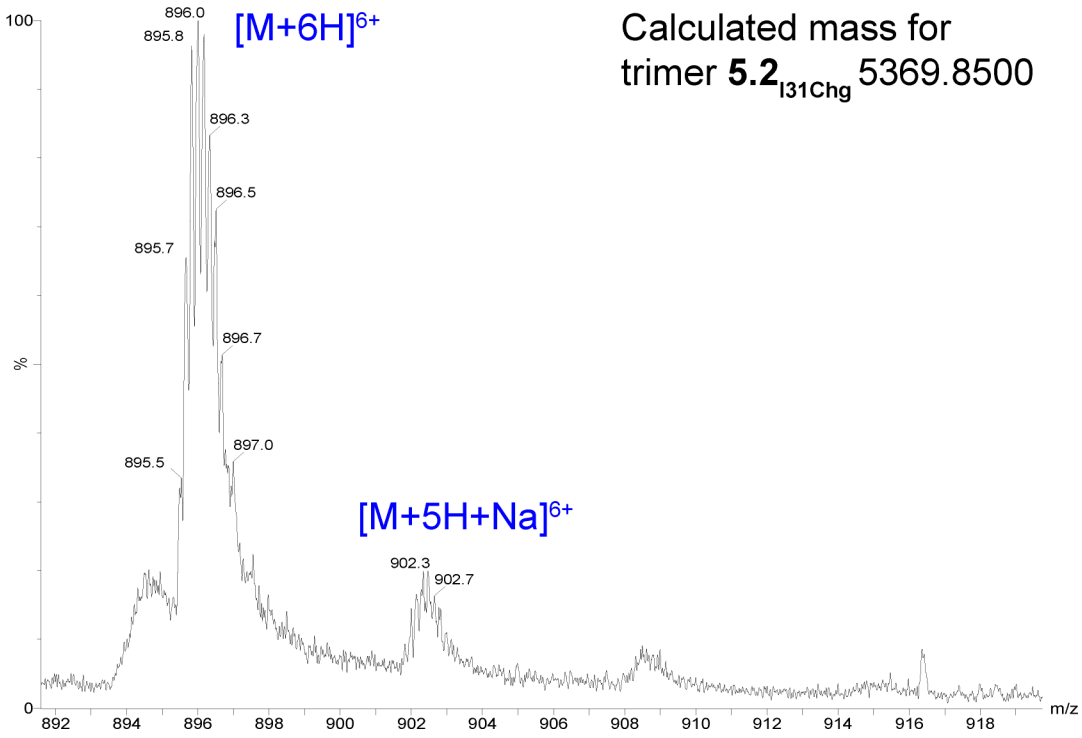
100
%
0
896.0
895.8
896.3
896.5
895.7
896.7
897.0
895.5
[M+6H]6+
[M+5H+Na]6+
902.3
902.7
892
894
896
898
900
902
904
906
908
910
912
914
916
918
m/z
Calculated mass for
trimer 5.2I31Chg 5369.8500

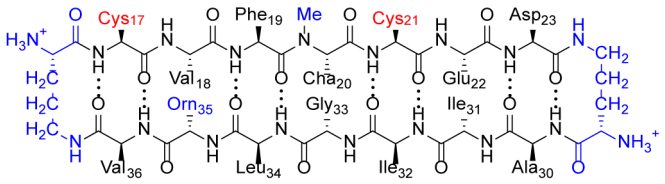

peptide **5.F20Cha**

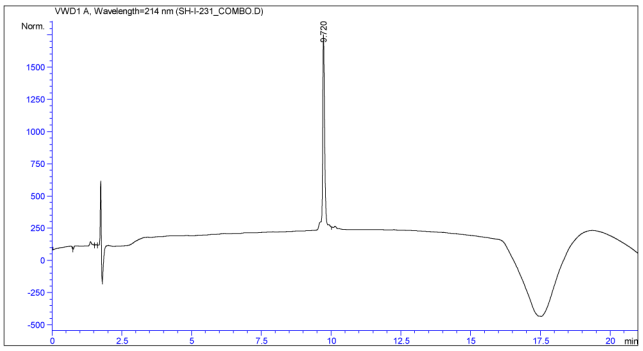

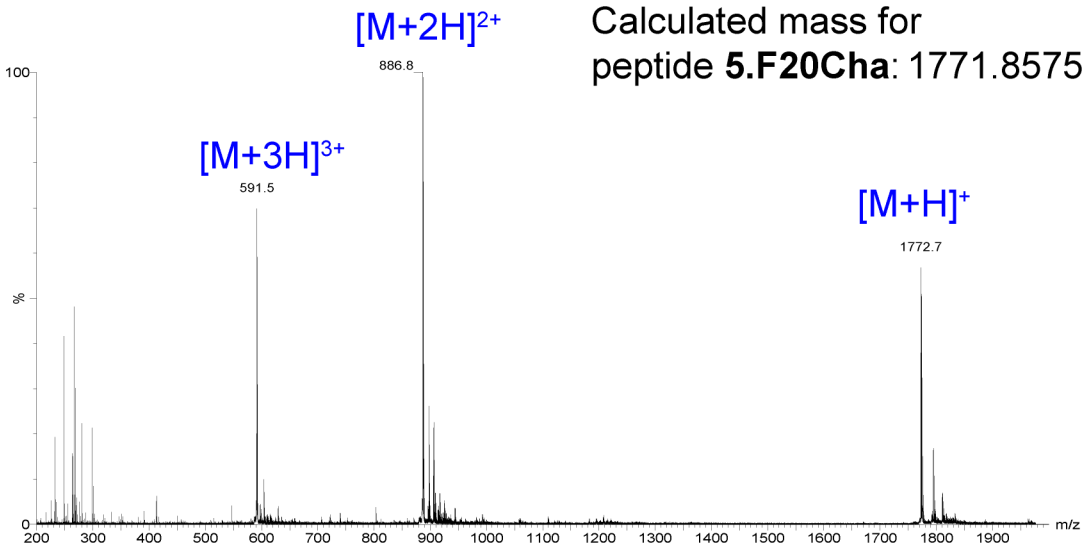

Calculated mass for peptide **5.F20Cha**: 1771.8575

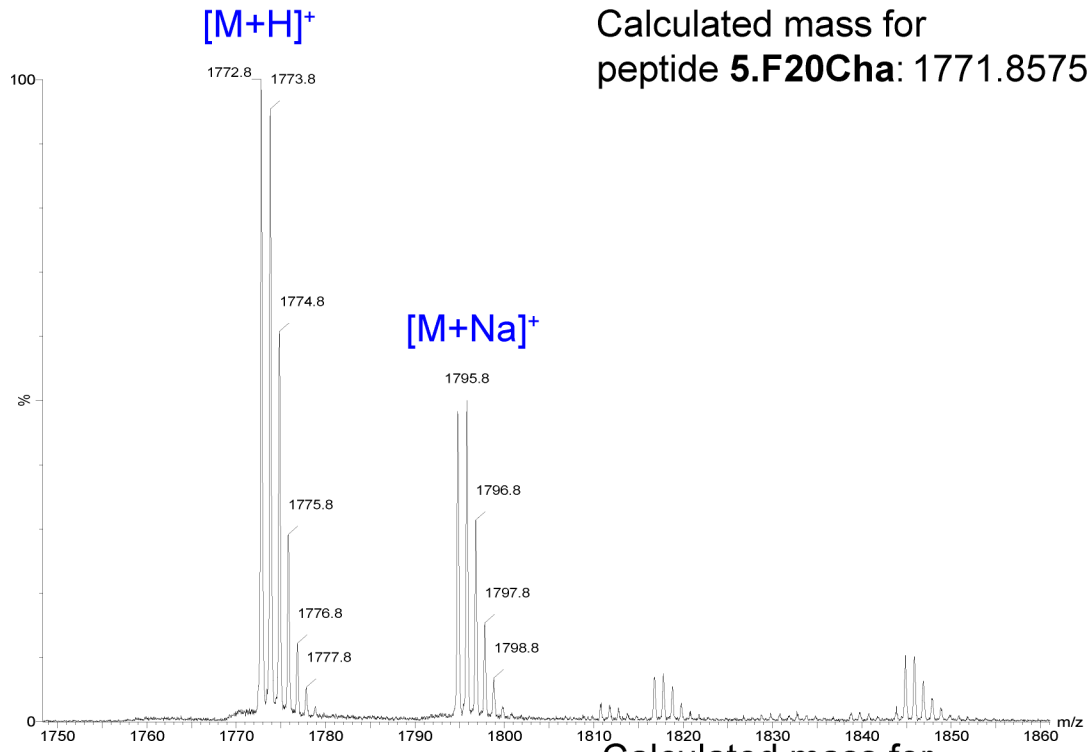
[M+H]+
Calculated mass for peptide **5.F20Cha**: 1771.8575
1772.8
1773.8
1774.8
[M+Na]+
1795.8
1796.8
1775.8
1797.8
1776.8
1798.8
1777.8
100
%
0
1750
1760
1770
1780
1790
1800
1810
1820
1830
1840
1850
1860
m/z

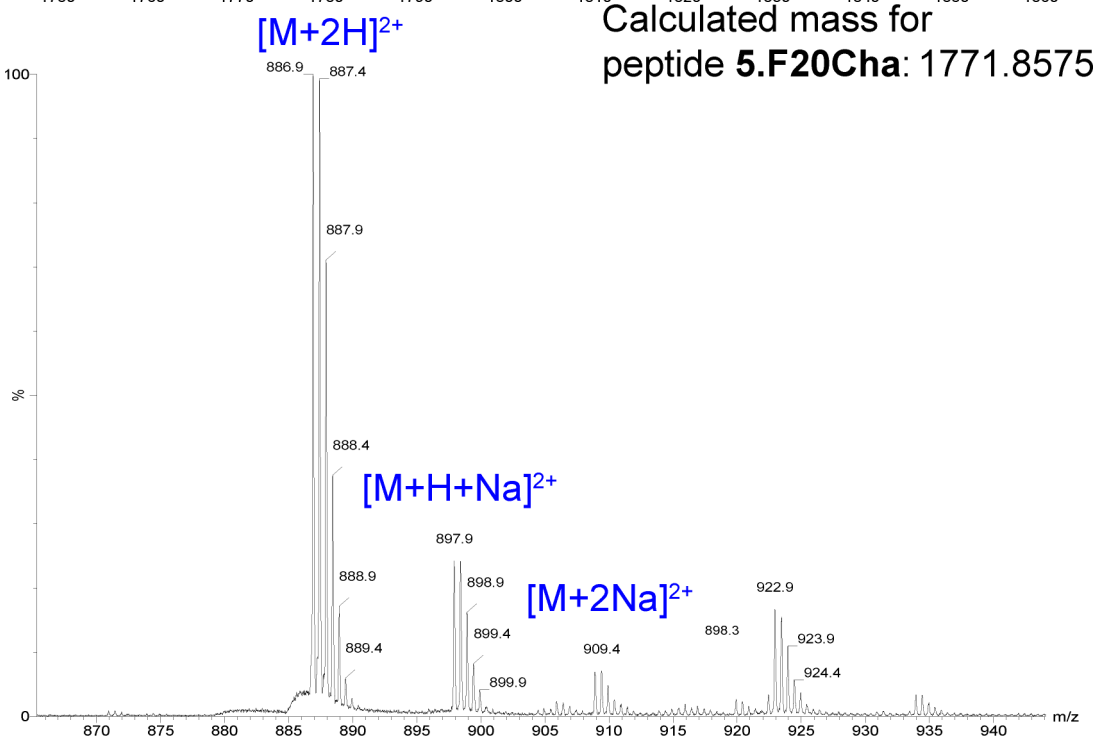
[M+2H]2+
Calculated mass for peptide **5.F20Cha**: 1771.8575
886.9
887.4
887.9
888.4
[M+H+Na]2+
897.9
888.9
898.9
[M+2Na]2+
922.9
899.4
898.3
889.4
909.4
923.9
899.9
924.4
100
%
0
870
875
880
885
890
895
900
905
910
915
920
925
930
935
940
m/z

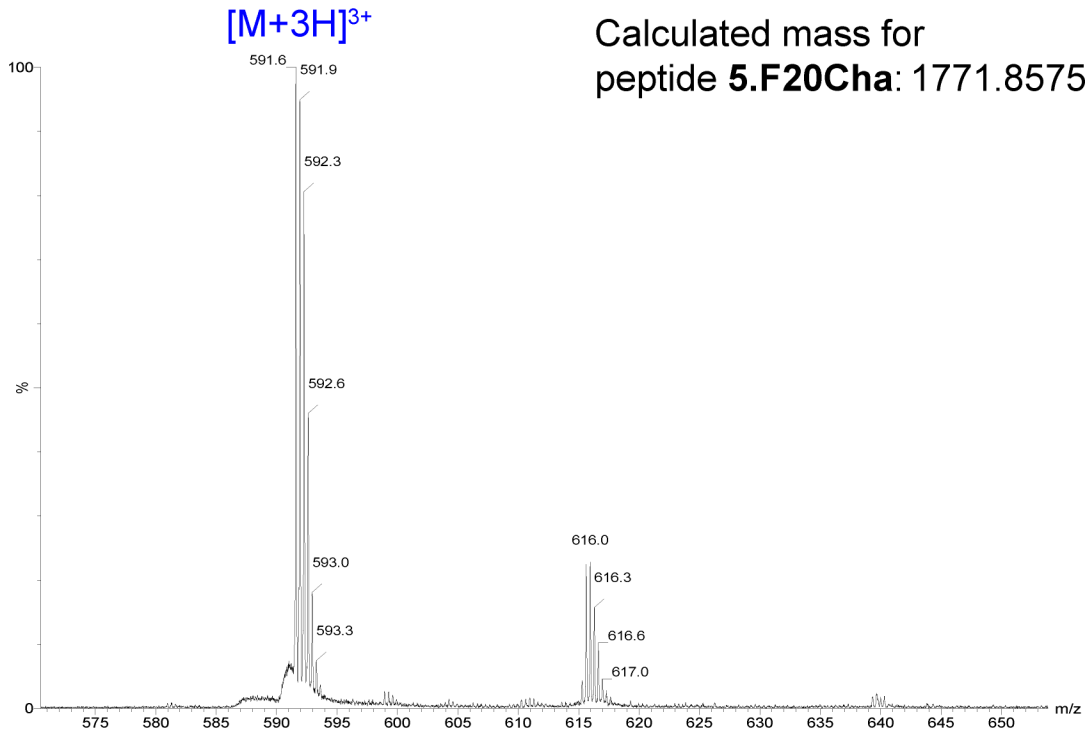
[M+3H]3+
Calculated mass for peptide 5.F20Cha: 1771.8575
100
%
0
591.6
591.9
592.3
592.6
593.0
593.3
616.0
616.3
616.6
617.0
575
580
585
590
595
600
605
610
615
620
625
630
635
640
645
650
m/z

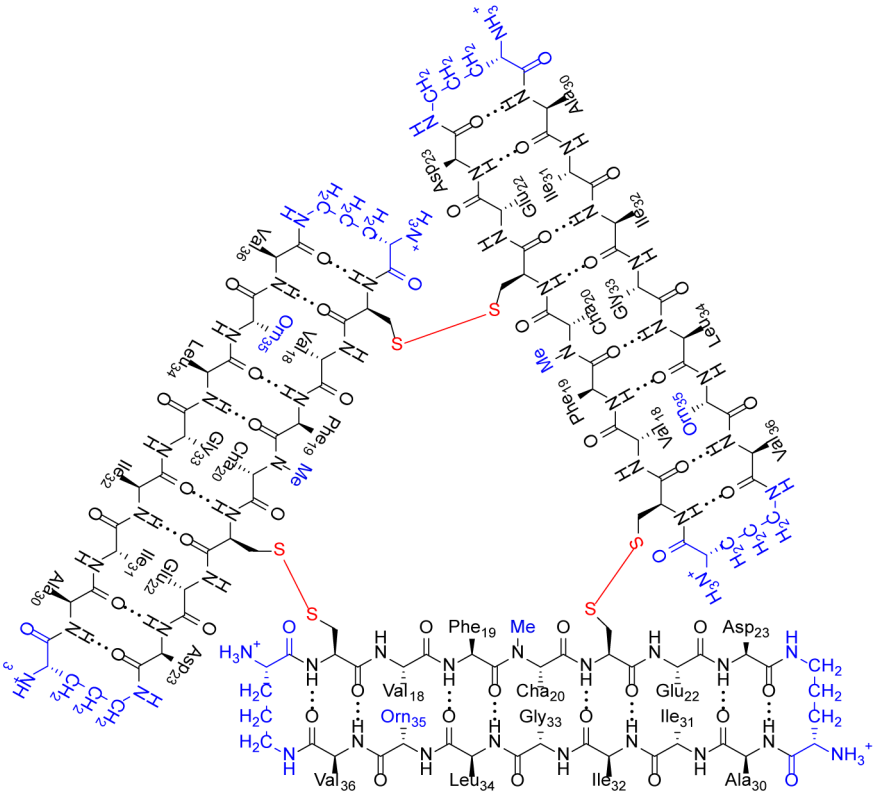

trimer **5.2**$_{\mathbf{F20Cha}}$

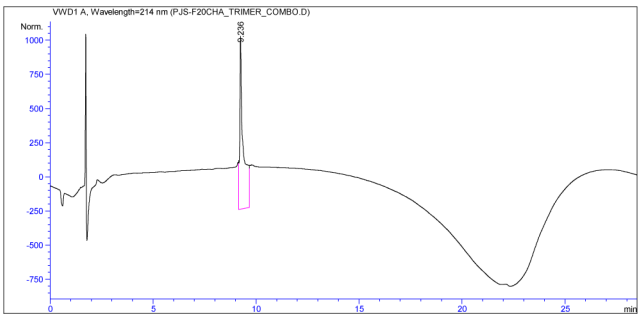

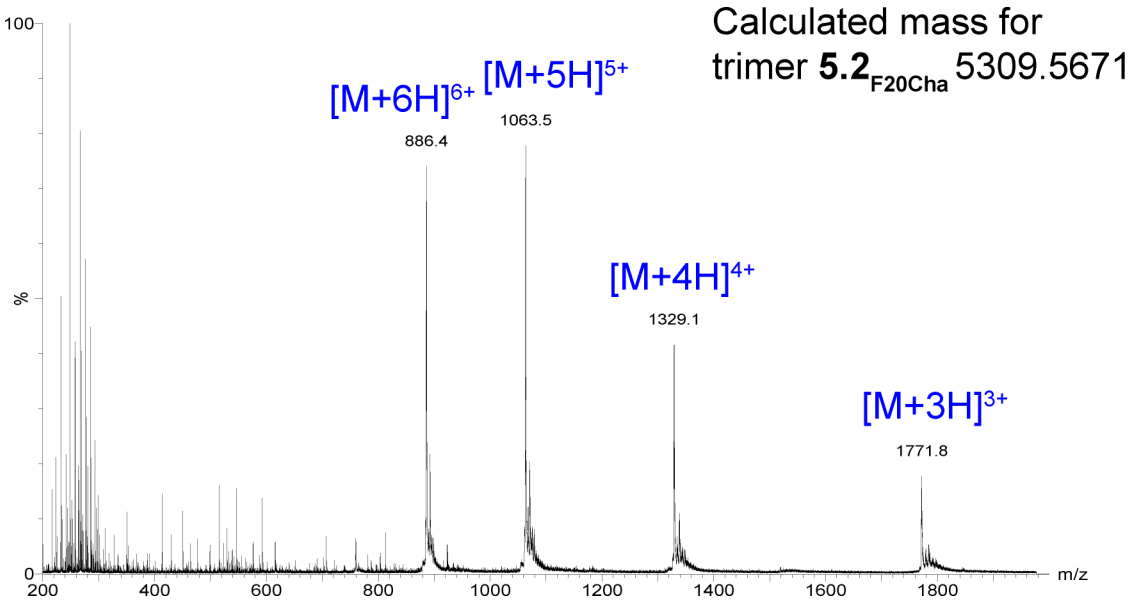
Calculated mass for
trimer **5.2**$_{F20Cha}$ 5309.5671
[M+6H]$^{6+}$
[M+5H]$^{5+}$
1063.5
886.4
[M+4H]$^{4+}$
1329.1
[M+3H]$^{3+}$
1771.8
100
%
0
200
400
600
800
1000
1200
1400
1600
1800
m/z

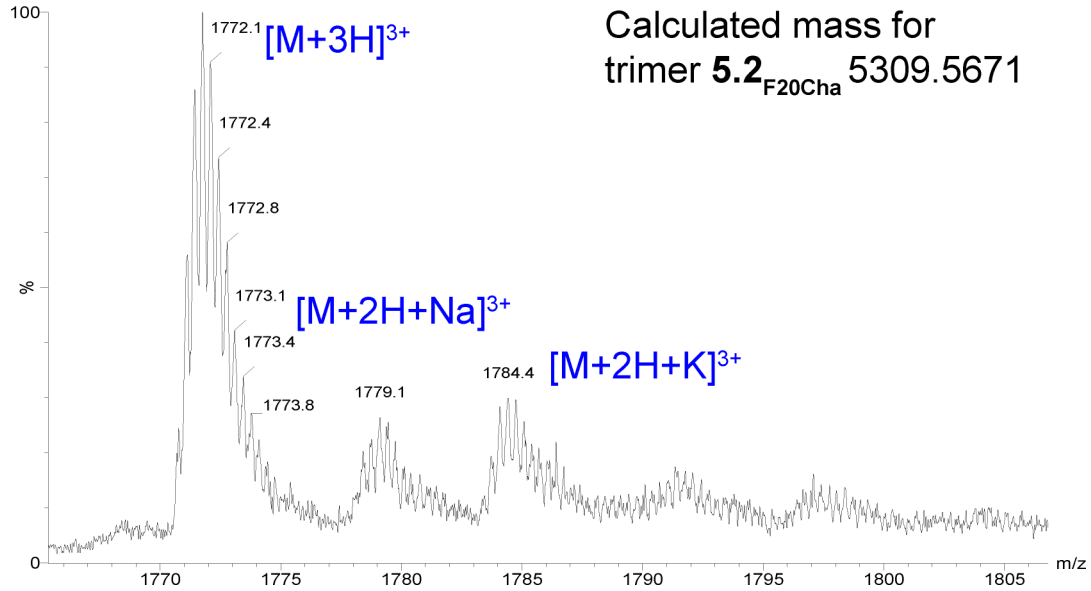
Calculated mass for
trimer **5.2**$_{F20Cha}$ 5309.5671
1772.1
[M+3H]$^{3+}$
1772.4
1772.8
1773.1
[M+2H+Na]$^{3+}$
1773.4
1773.8
1779.1
1784.4
[M+2H+K]$^{3+}$
100
%
0
1770
1775
1780
1785
1790
1795
1800
1805
m/z

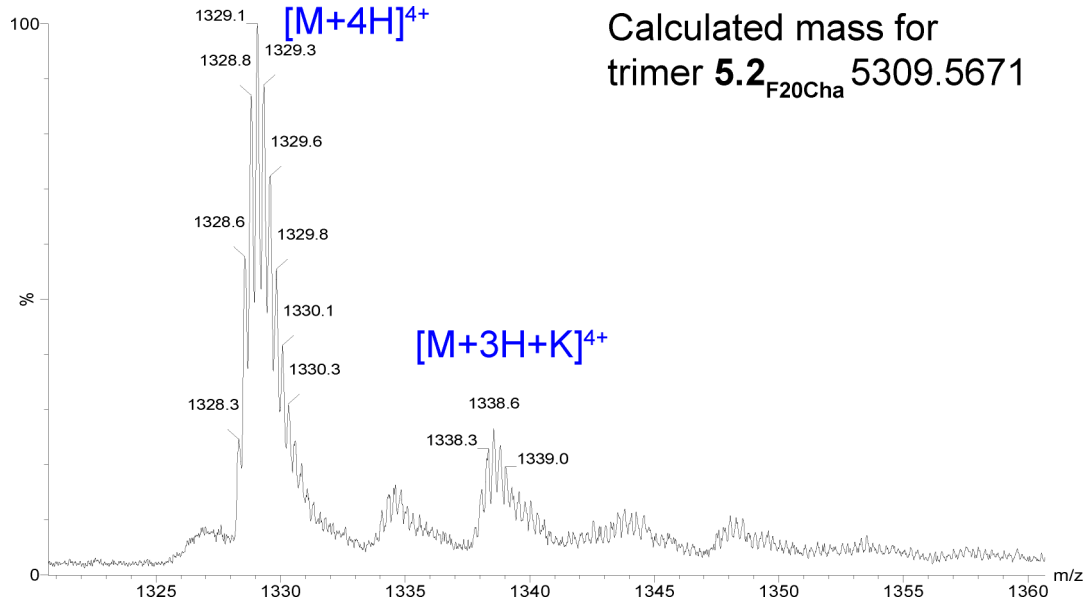
[M+4H]4+
Calculated mass for
trimer 5.2F20Cha 5309.5671
[M+3H+K]4+
1329.1
1329.3
1328.8
1329.6
1328.6
1329.8
1330.1
1330.3
1328.3
1338.6
1338.3
1339.0
100
%
0
1325
1330
1335
1340
1345
1350
1355
1360
m/z

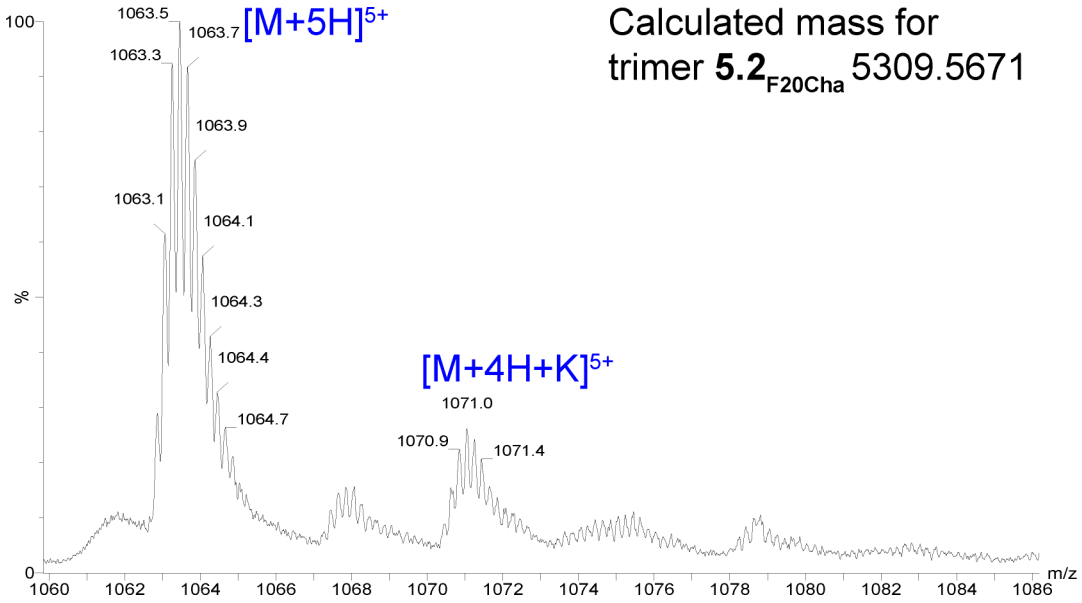
[M+5H]5+
Calculated mass for
trimer 5.2F20Cha 5309.5671
[M+4H+K]5+
1063.5
1063.7
1063.3
1063.9
1063.1
1064.1
1064.3
1064.4
1064.7
1071.0
1070.9
1071.4
100
%
0
1060
1062
1064
1066
1068
1070
1072
1074
1076
1078
1080
1082
1084
1086
m/z

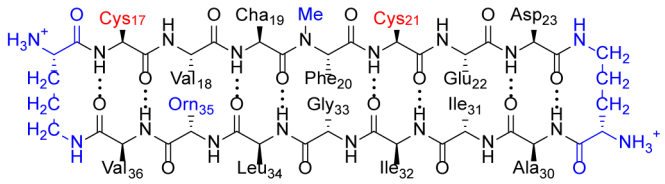

peptide **5.F19Cha**

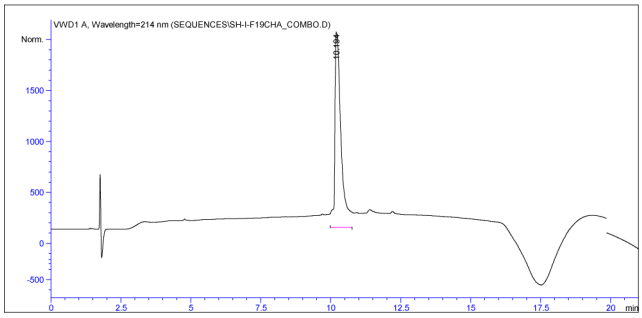

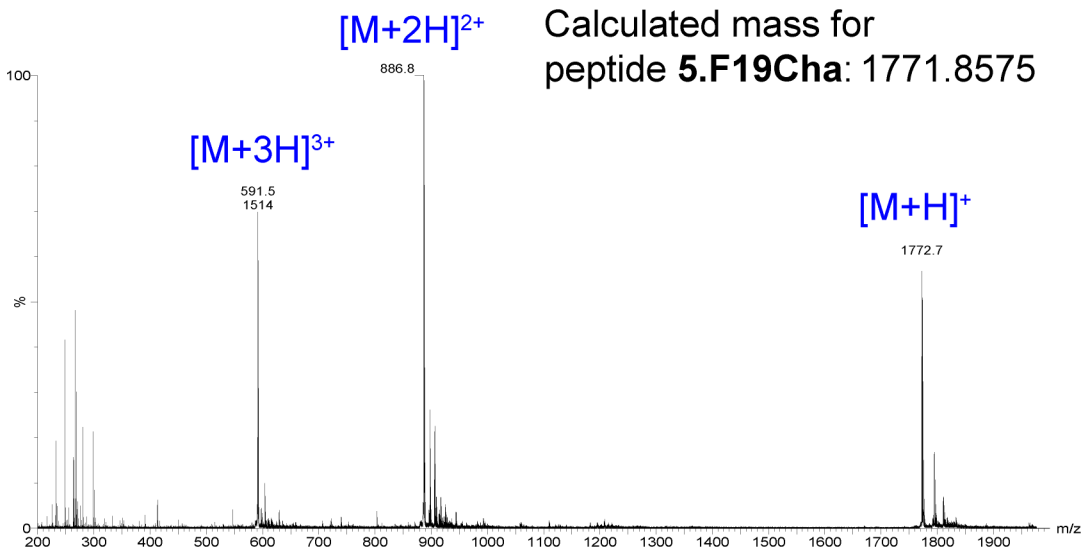

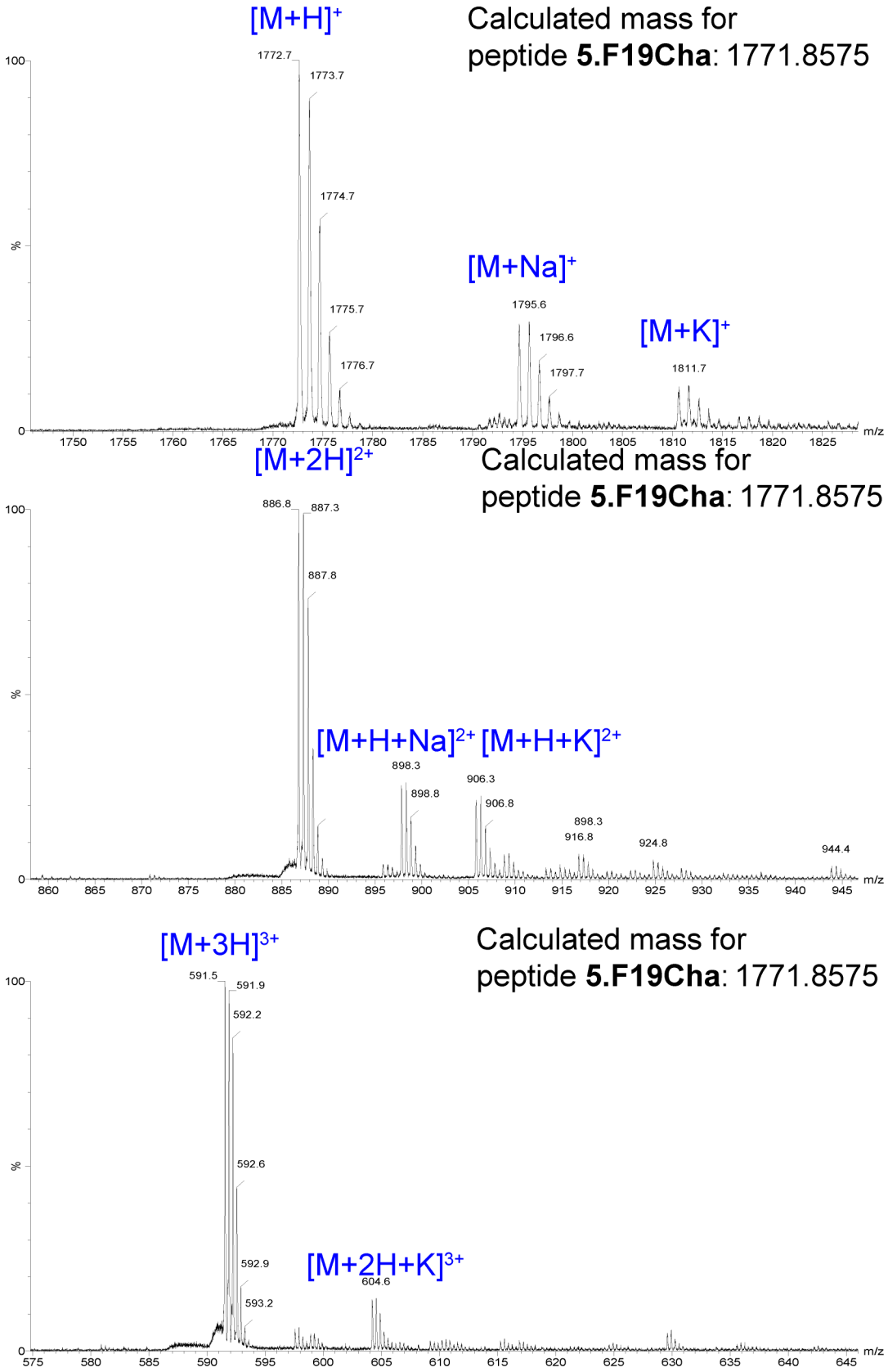
[M+H]+
Calculated mass for peptide 5.F19Cha: 1771.8575
1772.7
1773.7
1774.7
1775.7
1776.7
[M+Na]+
1795.6
1796.6
1797.7
[M+K]+
1811.7
[M+2H]2+
Calculated mass for peptide 5.F19Cha: 1771.8575
886.8
887.3
887.8
[M+H+Na]2+ [M+H+K]2+
898.3
898.8
906.3
906.8
898.3
916.8
924.8
944.4
[M+3H]3+
Calculated mass for peptide 5.F19Cha: 1771.8575
591.5
591.9
592.2
592.6
592.9
593.2
[M+2H+K]3+
604.6
m/z
%

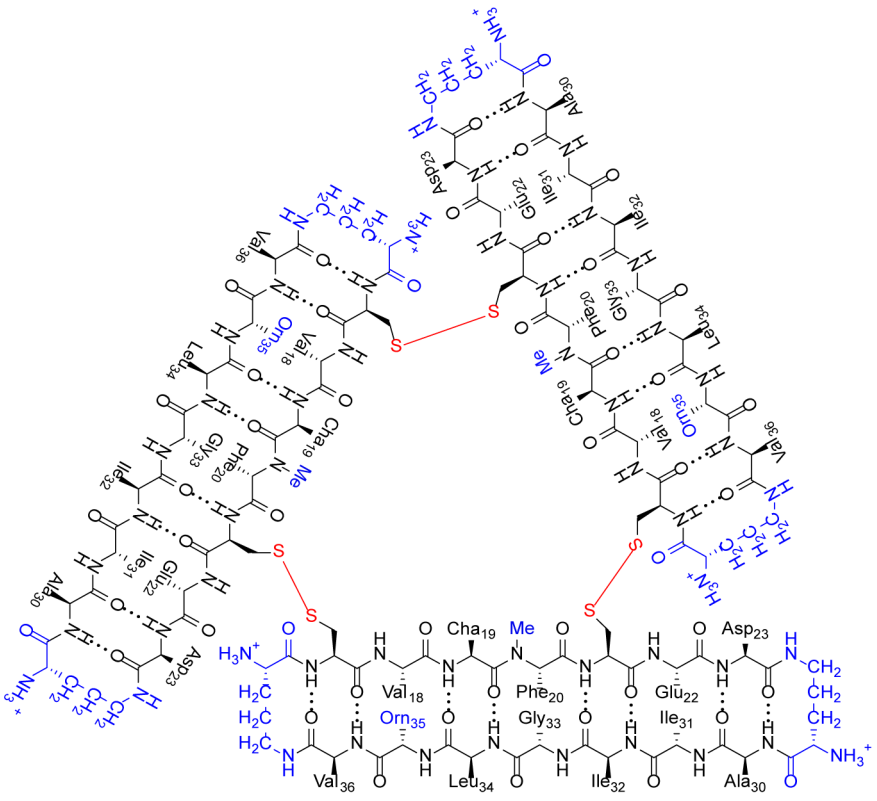

trimer **5.2**$_{\mathbf{F19Cha}}$

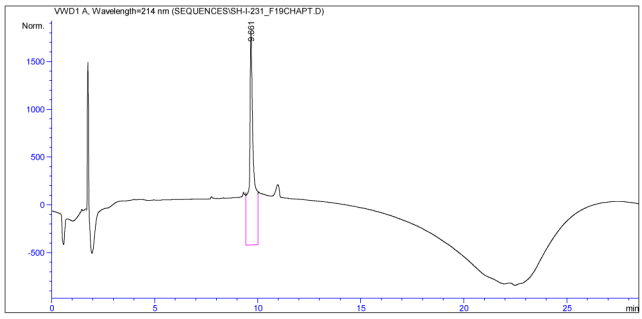

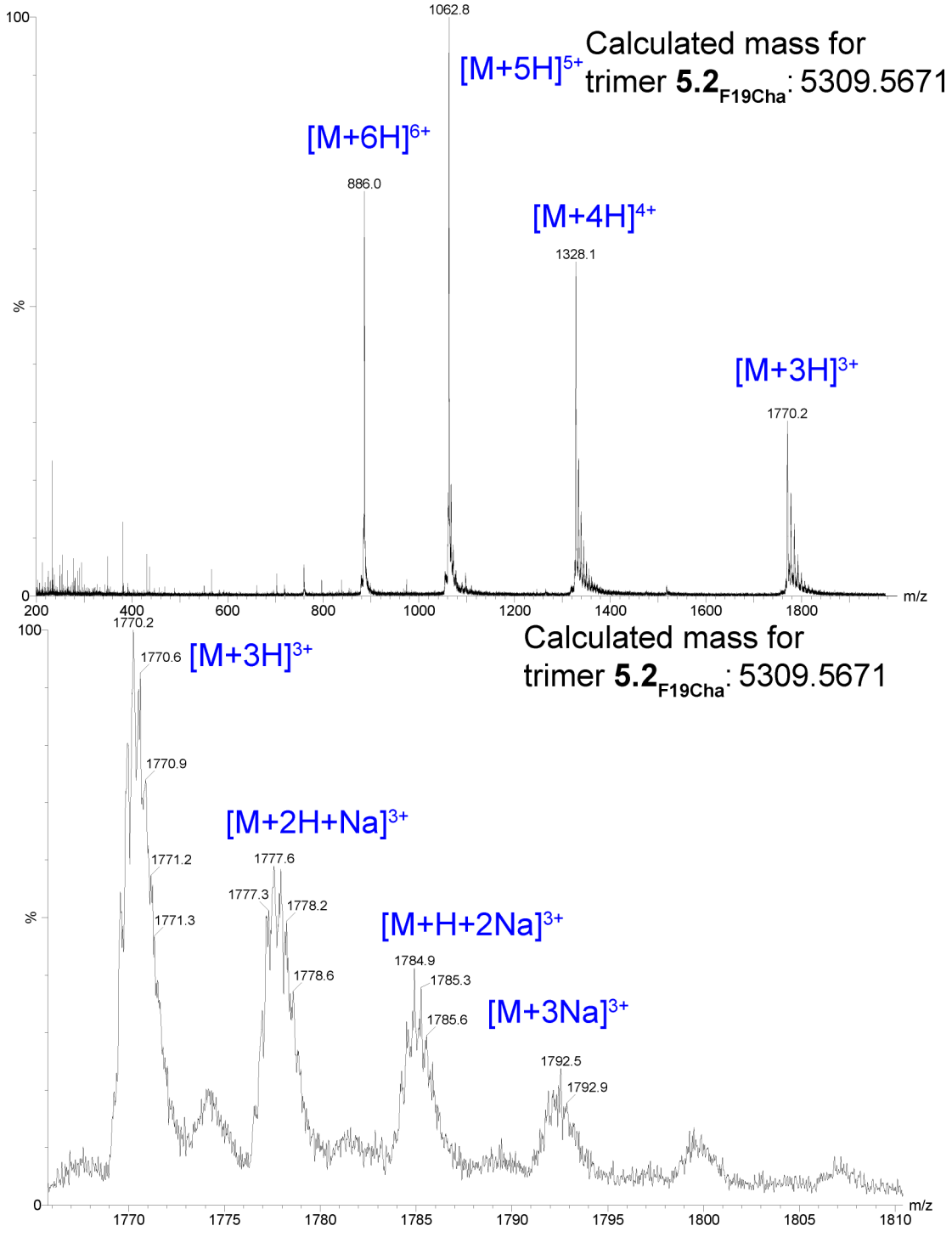
100
%
0
1062.8
[M+5H]5+
Calculated mass for
trimer 5.2F19Cha: 5309.5671
[M+6H]6+
886.0
[M+4H]4+
1328.1
[M+3H]3+
1770.2
200
400
600
800
1000
1200
1400
1600
1800
m/z
100
%
0
1770.2
1770.6
[M+3H]3+
Calculated mass for
trimer 5.2F19Cha: 5309.5671
1770.9
[M+2H+Na]3+
1771.2
1771.3
1777.6
1777.3
1778.2
[M+H+2Na]3+
1778.6
1784.9
1785.3
1785.6
[M+3Na]3+
1792.5
1792.9
1770
1775
1780
1785
1790
1795
1800
1805
1810
m/z

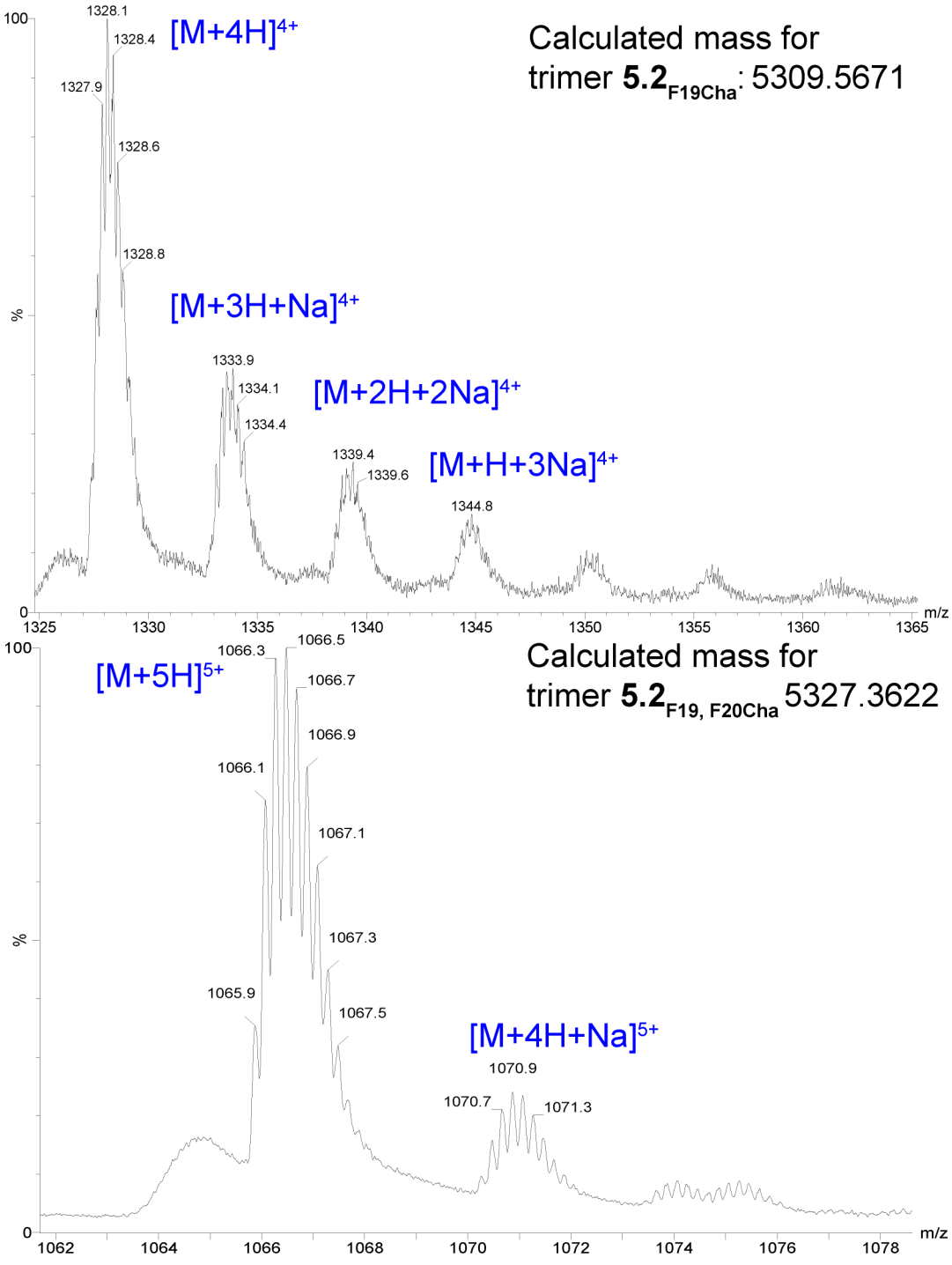
[M+4H]4+
Calculated mass for trimer 5.2F19Cha: 5309.5671
1328.1
1328.4
1327.9
1328.6
1328.8
[M+3H+Na]4+
1333.9
1334.1
[M+2H+2Na]4+
1334.4
1339.4
1339.6
[M+H+3Na]4+
1344.8
[M+5H]5+
Calculated mass for trimer 5.2F19, F20Cha 5327.3622
1066.5
1066.3
1066.7
1066.9
1066.1
1067.1
1067.3
1065.9
1067.5
[M+4H+Na]5+
1070.9
1070.7
1071.3
100
%
0
m/z
1325
1330
1335
1340
1345
1350
1355
1360
1365
1062
1064
1066
1068
1070
1072
1074
1076
1078

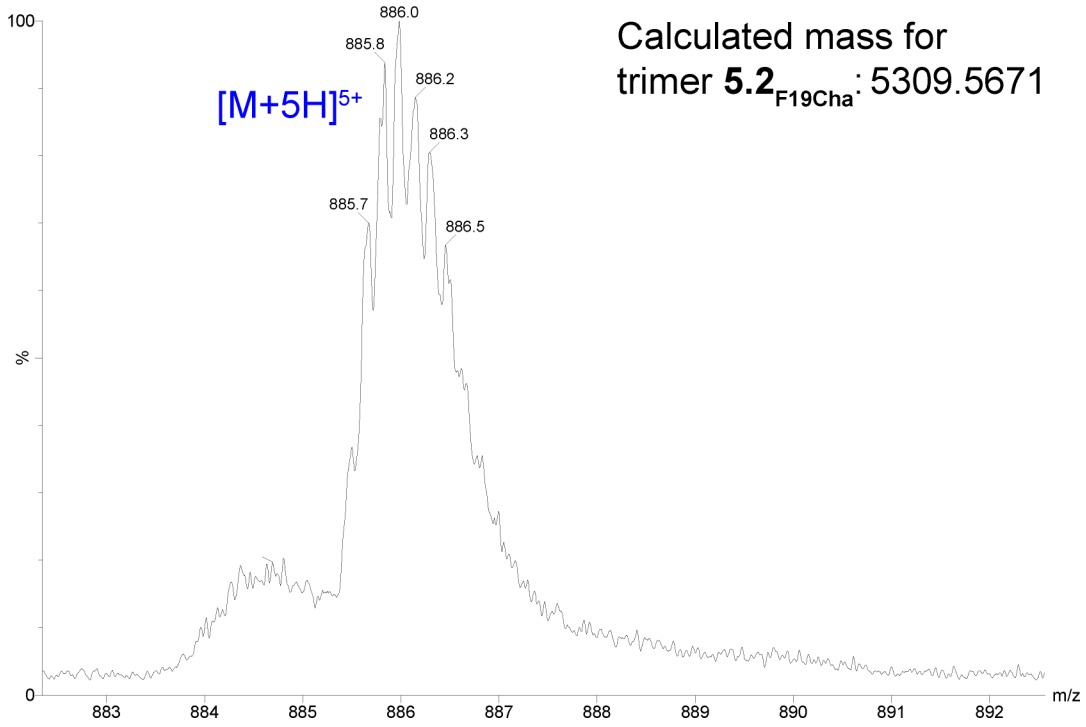
100
%
0
886.0
885.8
886.2
886.3
885.7
886.5
[M+5H]5+
Calculated mass for
trimer 5.2F19Cha: 5309.5671
883
884
885
886
887
888
889
890
891
892
m/z

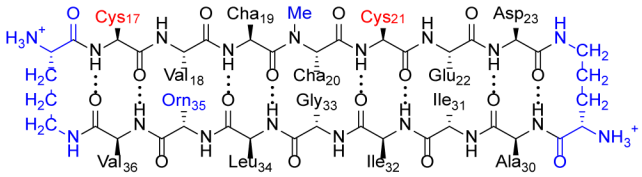

peptide **5.F19,F20Cha**

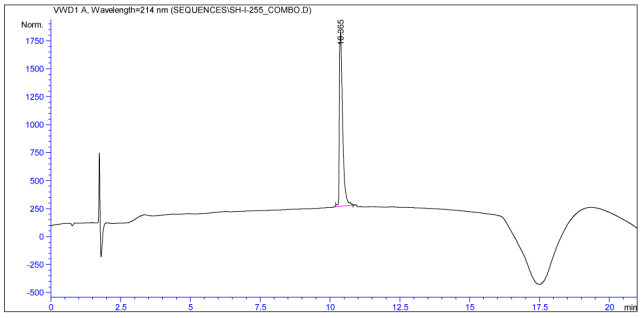

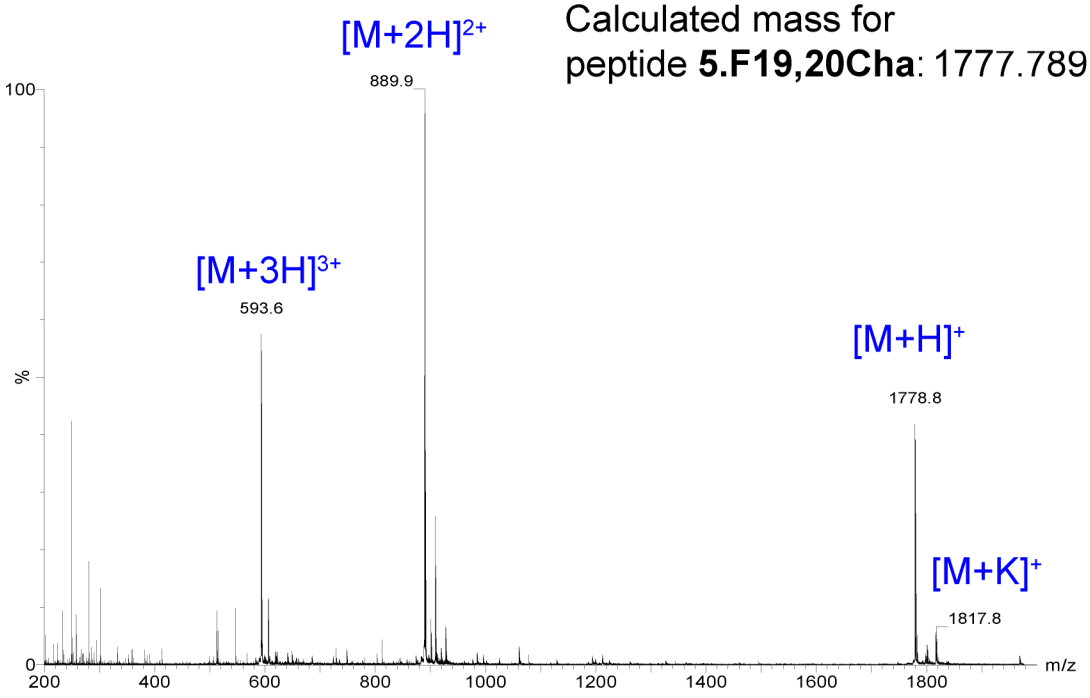

Calculated mass for peptide **5.F19,20Cha**: 1777.7891

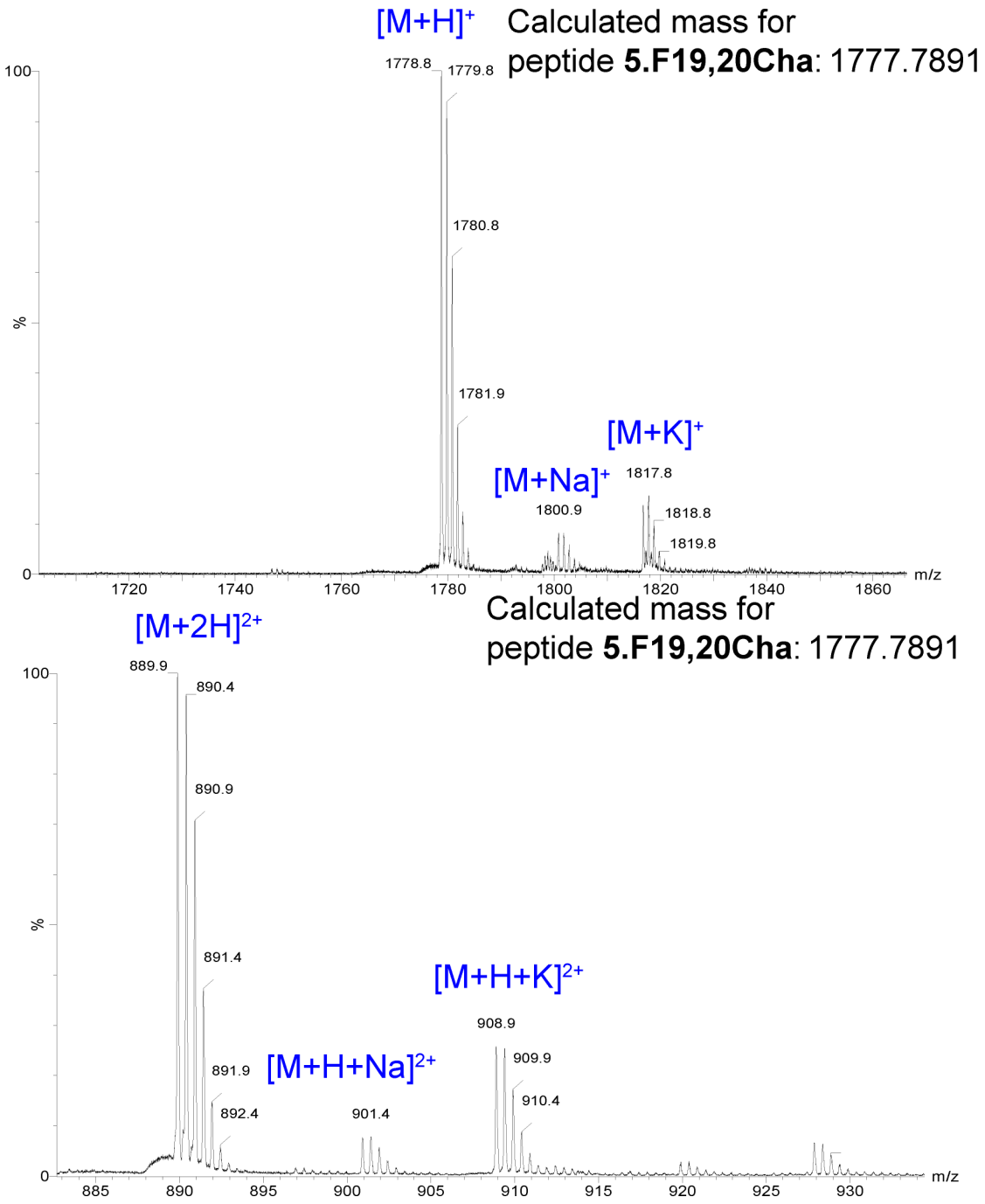
[M+H]+
Calculated mass for peptide 5.F19,20Cha: 1777.7891
1778.8
1779.8
1780.8
1781.9
[M+K]+
[M+Na]+
1817.8
1800.9
1818.8
1819.8
100
%
0
m/z
1720
1740
1760
1780
1800
1820
1840
1860
[M+2H]2+
Calculated mass for peptide 5.F19,20Cha: 1777.7891
889.9
890.4
890.9
891.4
891.9
892.4
[M+H+Na]2+
901.4
[M+H+K]2+
908.9
909.9
910.4
885
890
895
900
905
910
915
920
925
930

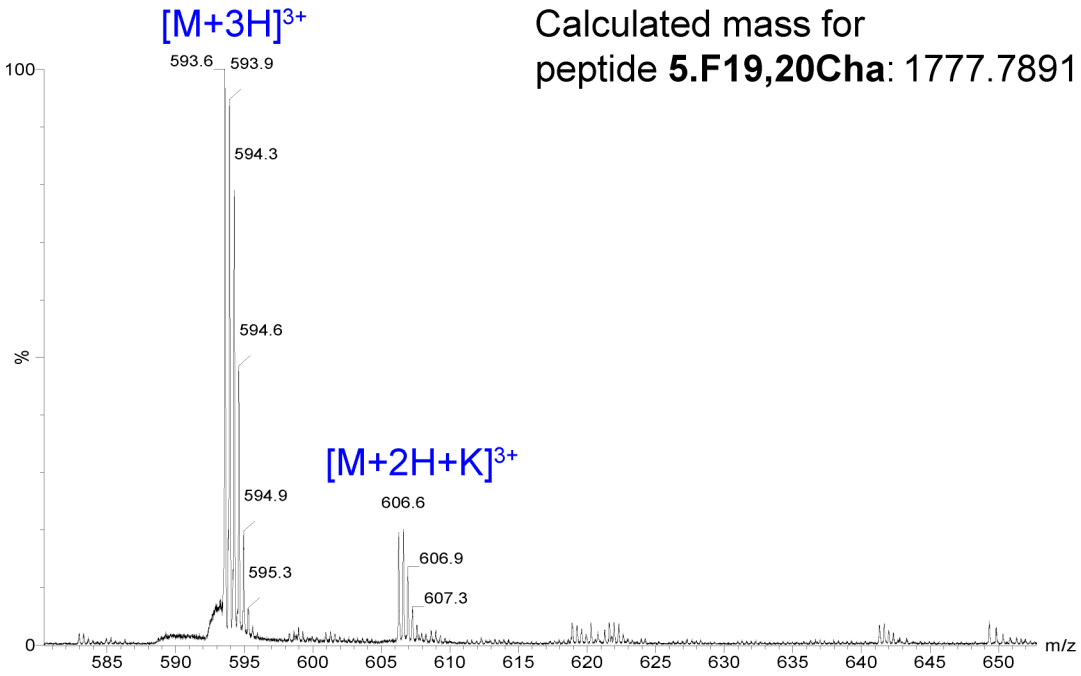
[M+3H]3+
Calculated mass for
peptide 5.F19,20Cha: 1777.7891
593.6
593.9
594.3
594.6
594.9
595.3
[M+2H+K]3+
606.6
606.9
607.3
100
%
0
585
590
595
600
605
610
615
620
625
630
635
640
645
650
m/z

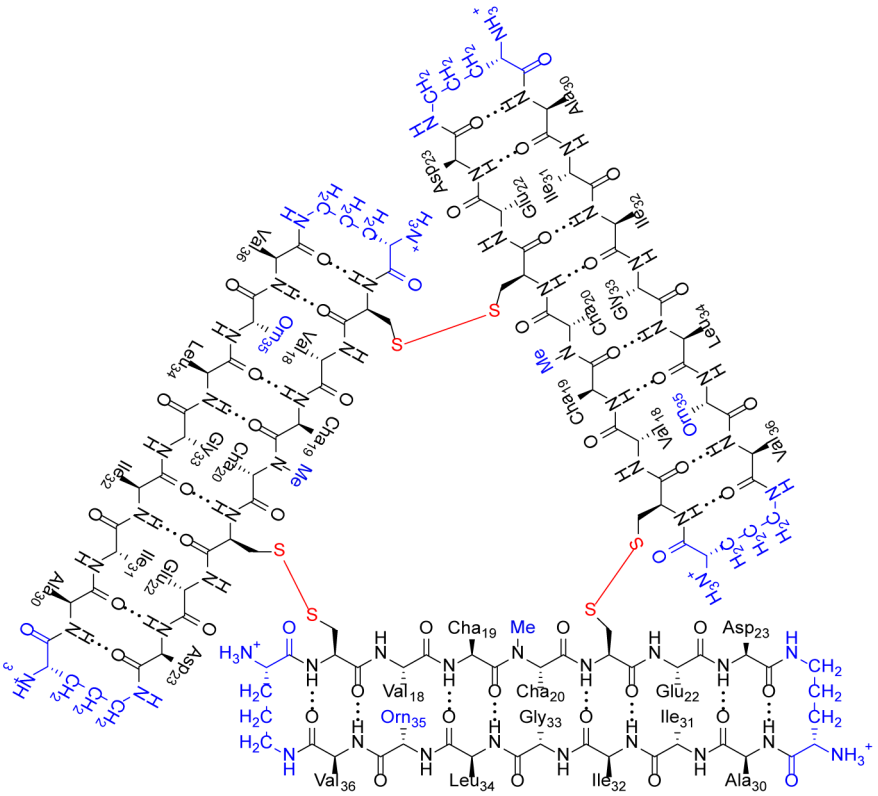

trimer **5.2**$_{\mathbf{F19,F20Cha}}$

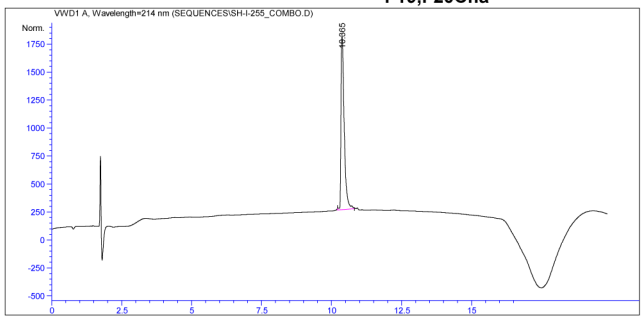

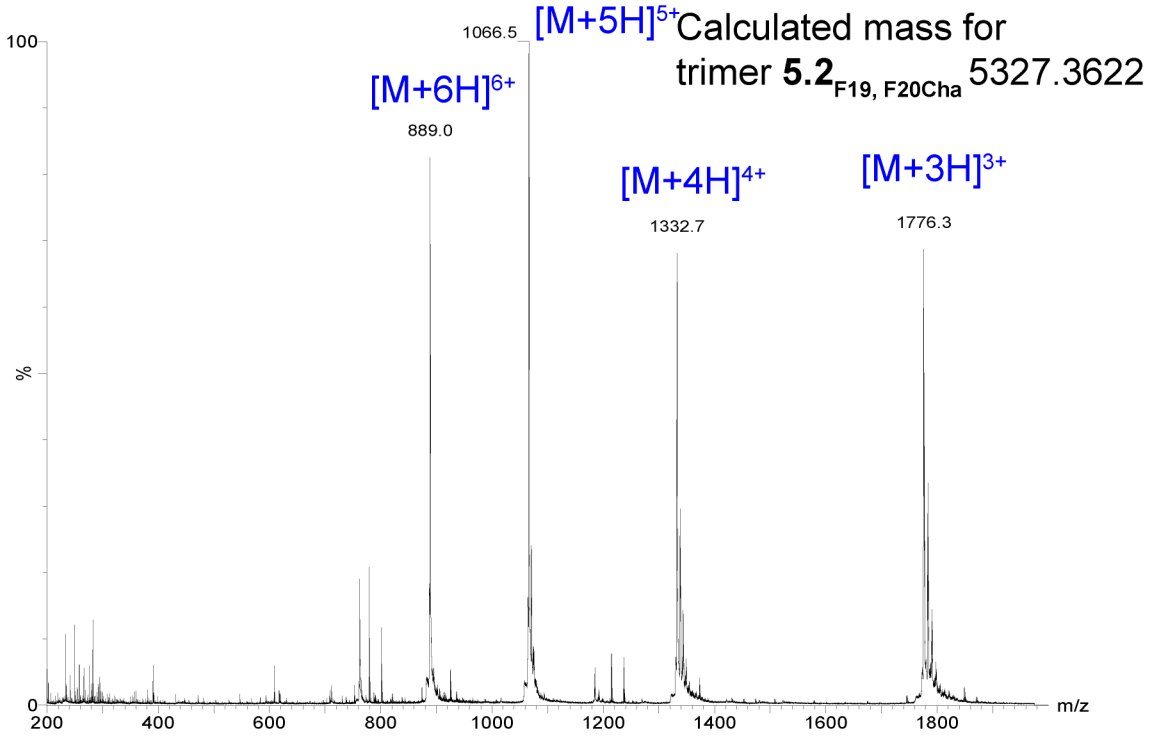
[M+5H]5+
1066.5
Calculated mass for
trimer 5.2F19, F20Cha 5327.3622
[M+6H]6+
889.0
[M+4H]4+
1332.7
[M+3H]3+
1776.3
100
%
0
200
400
600
800
1000
1200
1400
1600
1800
m/z

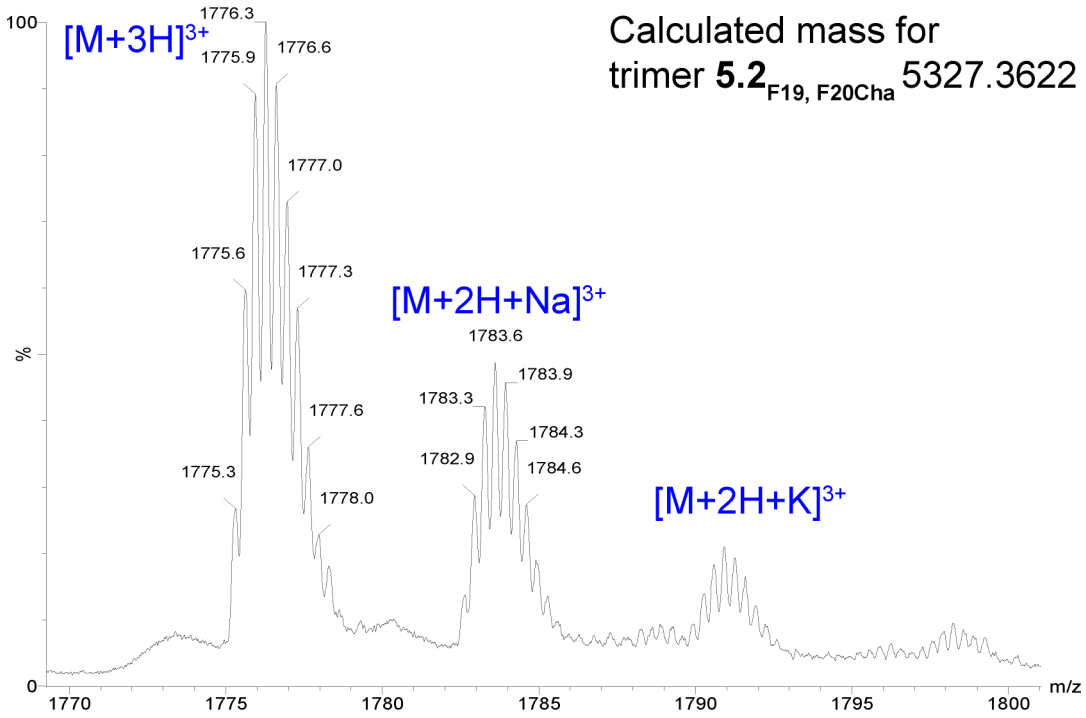
[M+3H]3+
1776.3
1775.9
1776.6
1777.0
1775.6
1777.3
[M+2H+Na]3+
1783.6
1783.9
1783.3
1777.6
1784.3
1782.9
1784.6
1775.3
1778.0
[M+2H+K]3+
Calculated mass for
trimer 5.2F19, F20Cha 5327.3622
100
%
0
1770
1775
1780
1785
1790
1795
1800
m/z

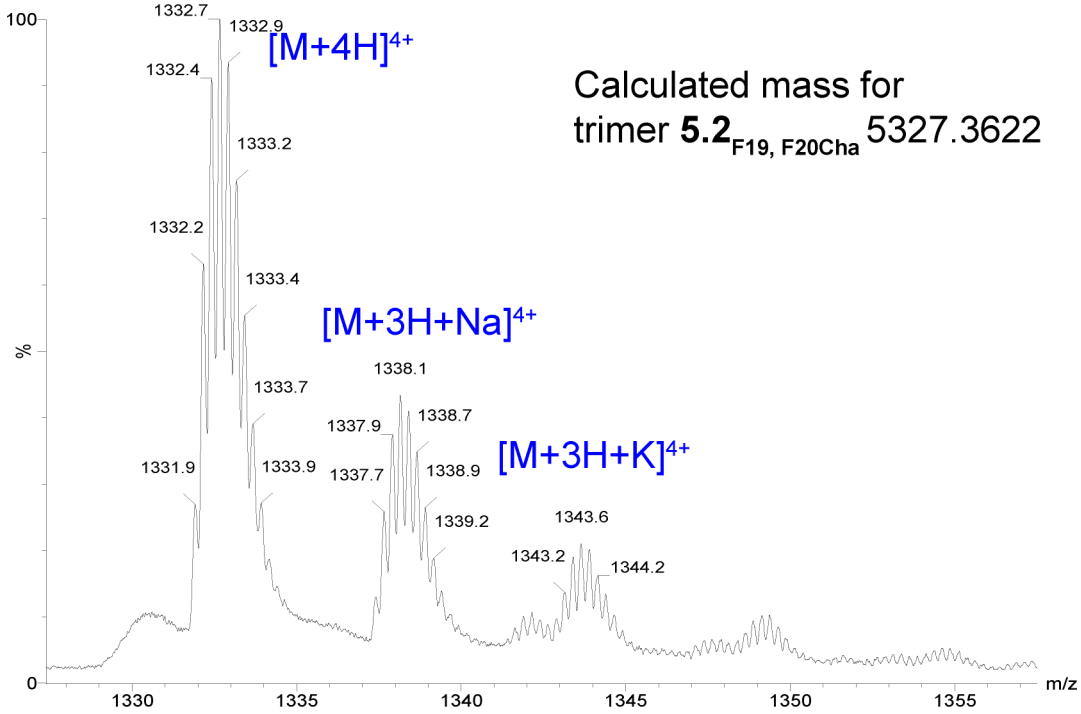

Calculated mass for trimer **5.2**$_{\text{F19, F20Cha}}$ 5327.3622

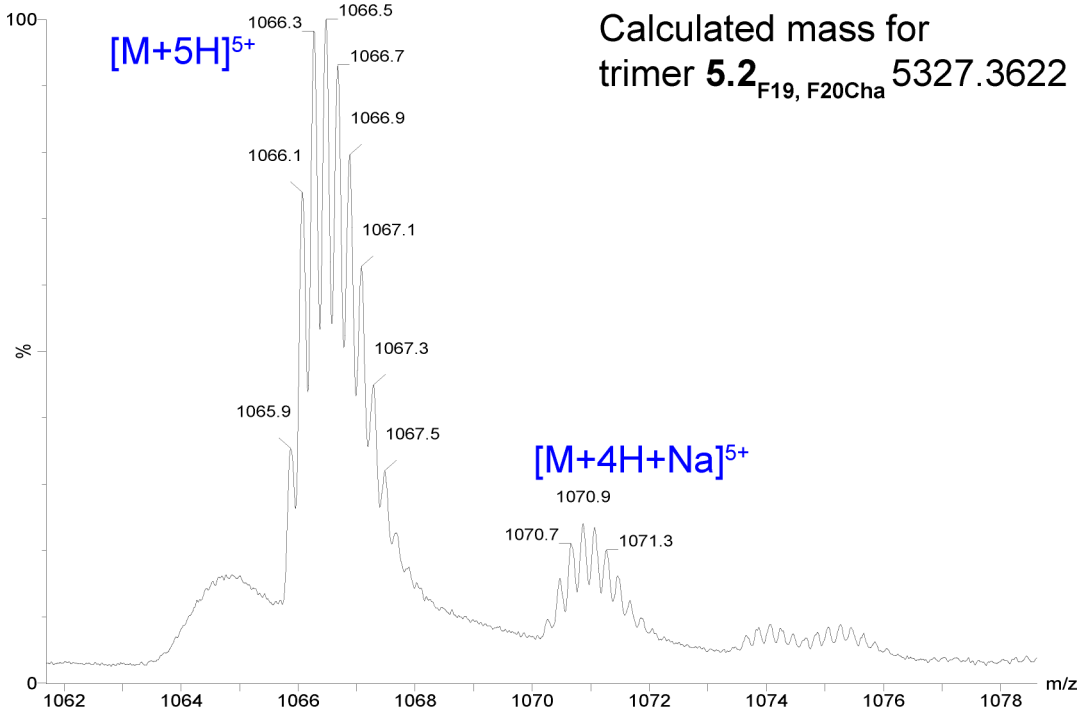

Calculated mass for trimer **5.2**$_{\text{F19, F20Cha}}$ 5327.3622

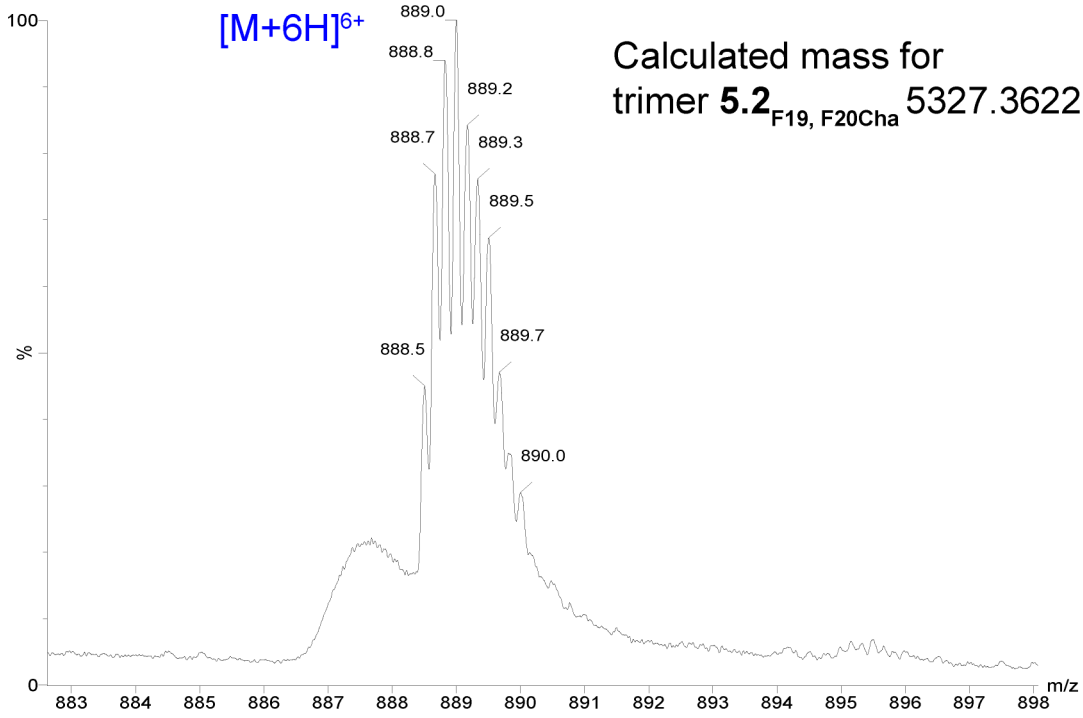
[M+6H]6+
Calculated mass for
trimer 5.2F19, F20Cha 5327.3622
889.0
888.8
889.2
888.7
889.3
889.5
889.7
888.5
890.0
100
%
0
883
884
885
886
887
888
889
890
891
892
893
894
895
896
897
898
m/z

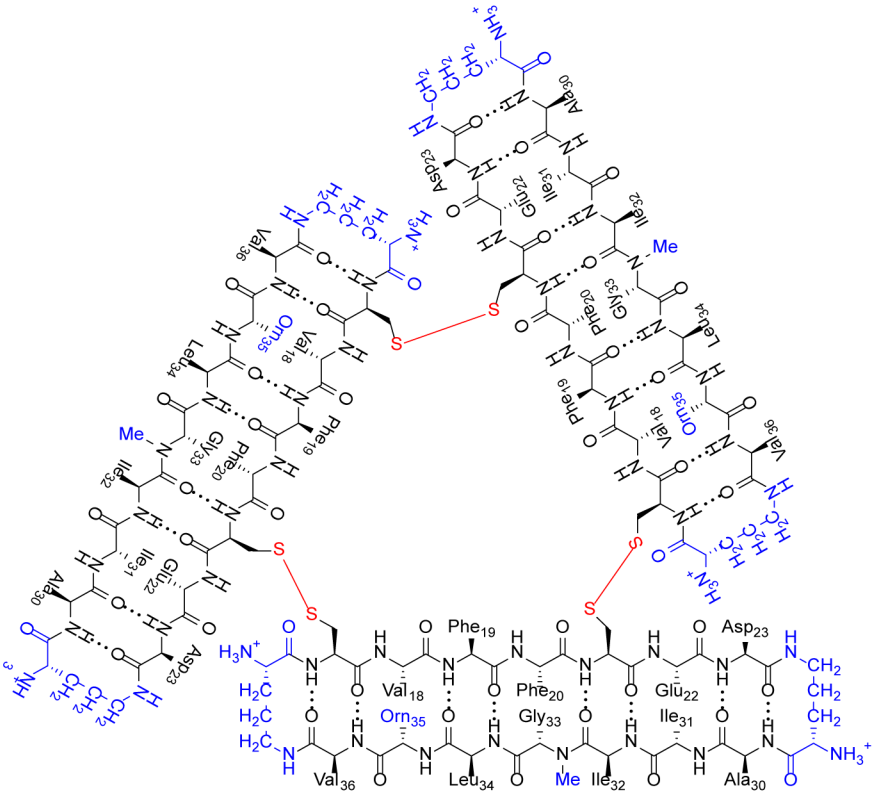

trimer **5.3**

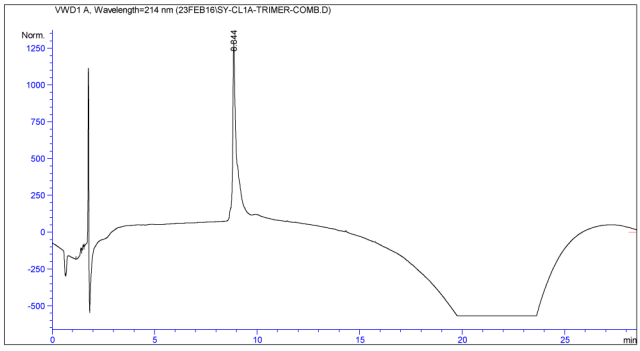
VWD1 A, Wavelength=214 nm (23FEB16\SY-CL1A-TRIMER-COMB.D)
Norm.
6.644
1250
1000
750
500
250
0
-250
-500
0
5
10
15
20
25
min

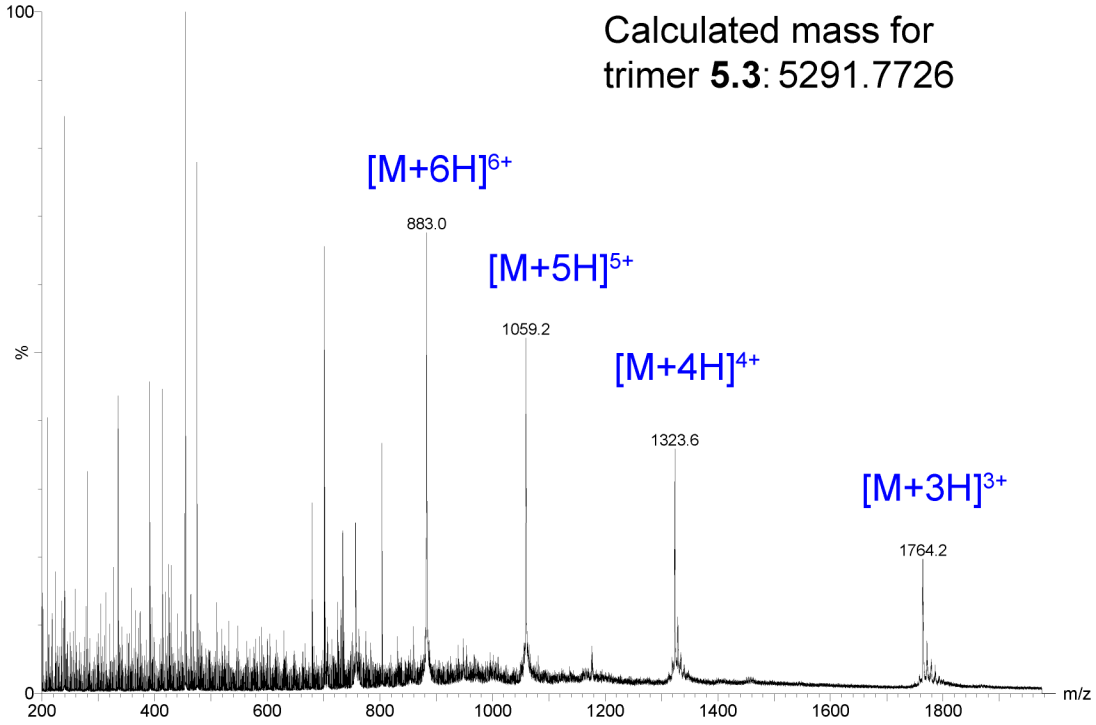
Calculated mass for
trimer **5.3**: 5291.7726
[M+6H]6+
883.0
[M+5H]5+
1059.2
[M+4H]4+
1323.6
[M+3H]3+
1764.2
100
%
0
200
400
600
800
1000
1200
1400
1600
1800
m/z

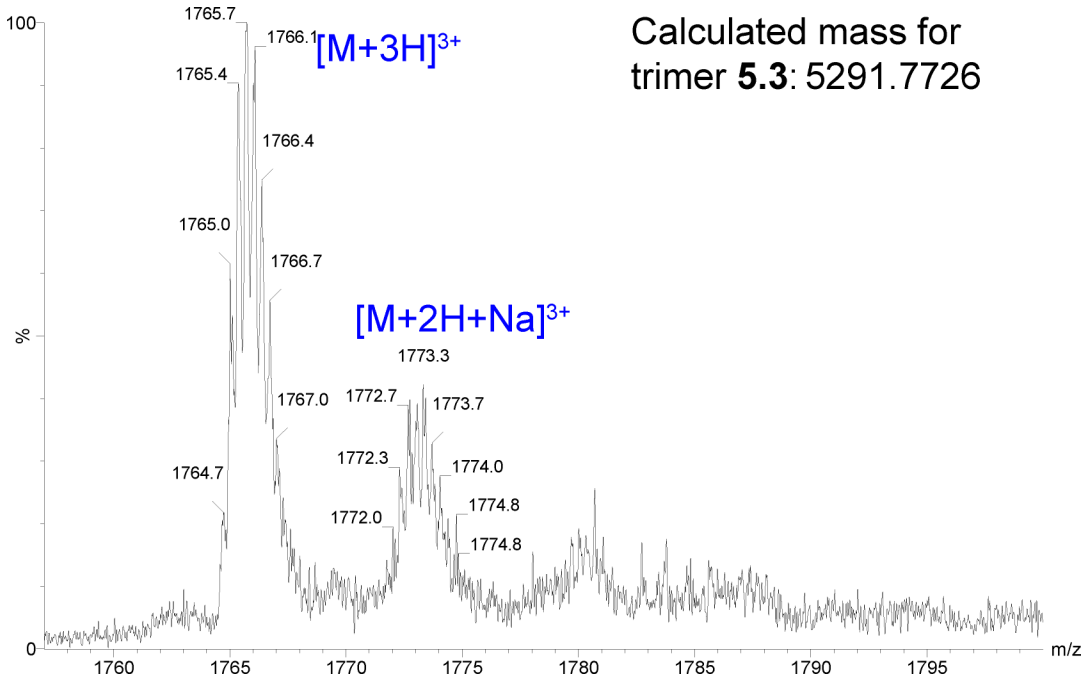
[M+3H]3+
Calculated mass for
trimer **5.3**: 5291.7726
1765.7
1766.1
1765.4
1766.4
1765.0
1766.7
[M+2H+Na]3+
1773.3
1767.0
1772.7
1773.7
1772.3
1774.0
1774.8
1764.7
1772.0
1774.8
100
%
0
1760
1765
1770
1775
1780
1785
1790
1795
m/z

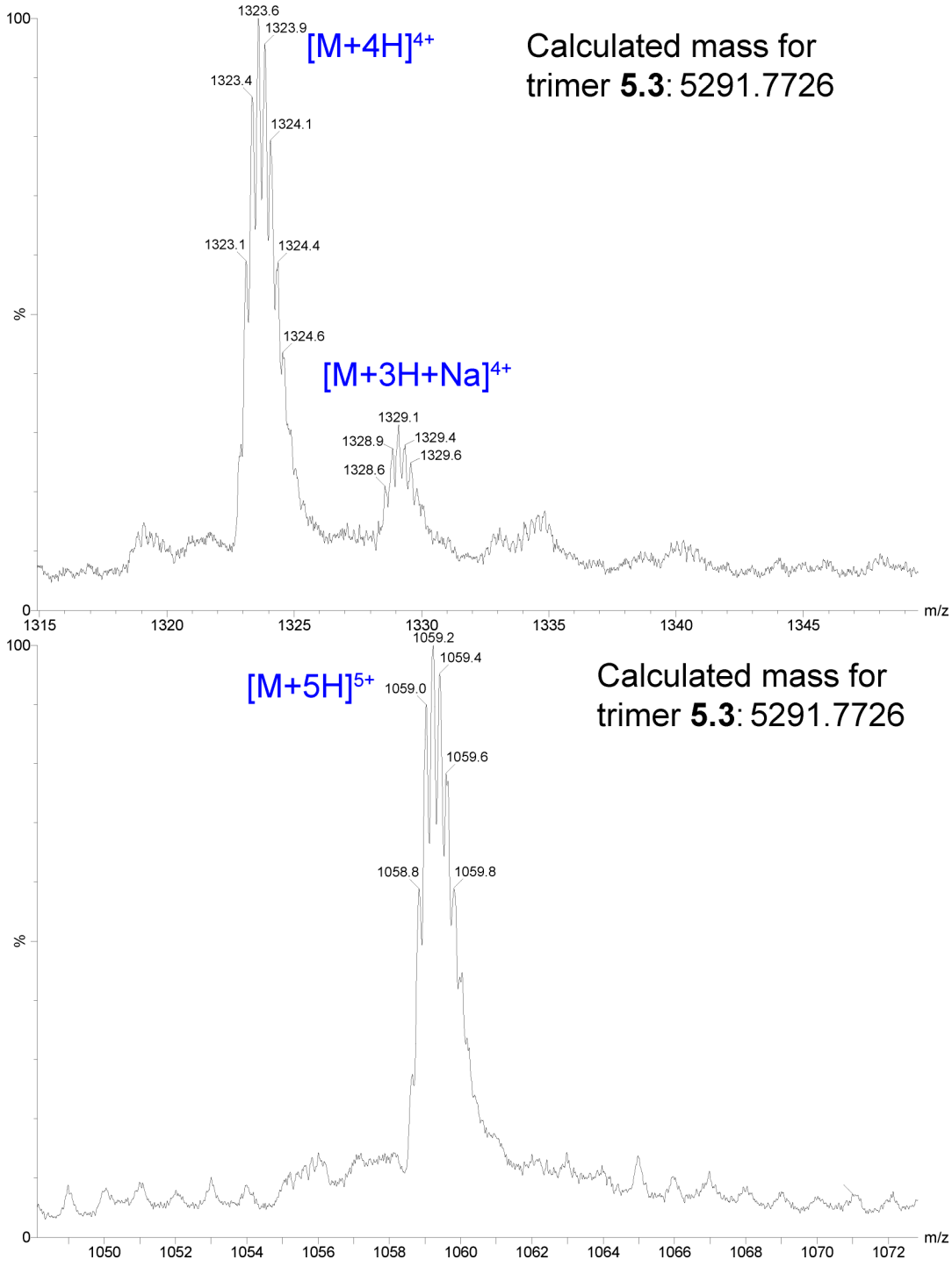
100
%
0
1323.6
1323.9
[M+4H]4+
1323.4
1324.1
1323.1
1324.4
1324.6
[M+3H+Na]4+
1329.1
1328.9
1329.4
1329.6
1328.6
1315
1320
1325
1330
1335
1340
1345
m/z
Calculated mass for
trimer 5.3: 5291.7726
100
%
0
1059.2
1059.4
[M+5H]5+
1059.0
1059.6
1058.8
1059.8
1050
1052
1054
1056
1058
1060
1062
1064
1066
1068
1070
1072
m/z
Calculated mass for
trimer 5.3: 5291.7726

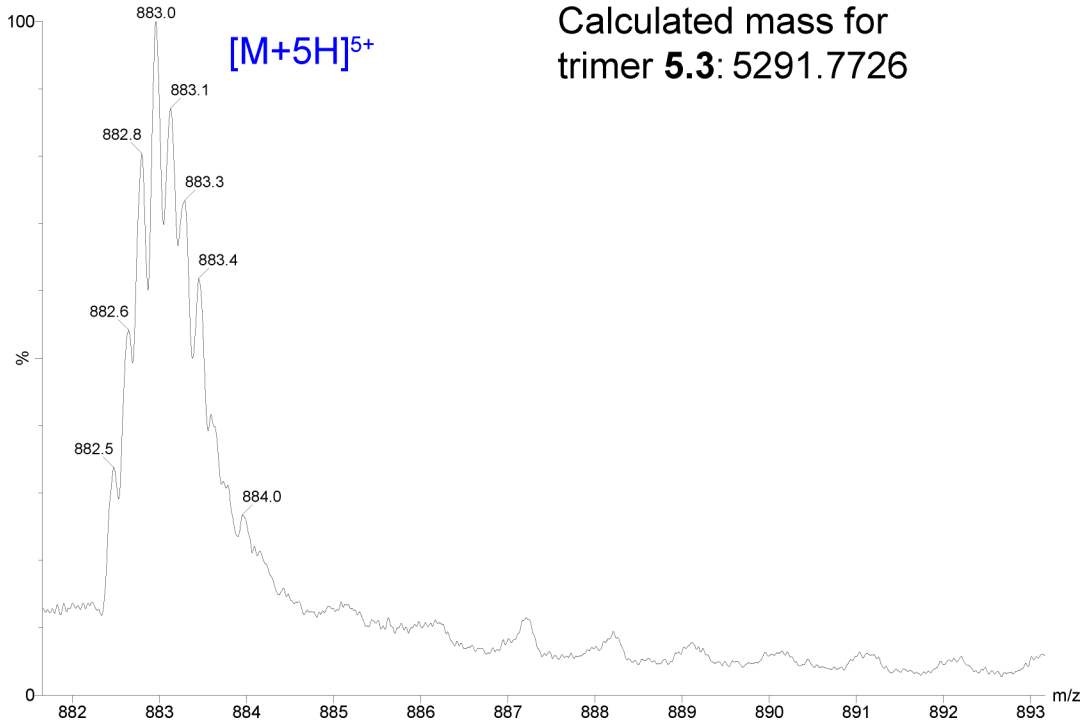
100
%
0
883.0
883.1
882.8
883.3
883.4
882.6
882.5
884.0
[M+5H]5+
Calculated mass for
trimer 5.3: 5291.7726
882
883
884
885
886
887
888
889
890
891
892
893
m/z

Bibliography

[1] alzheimer'sassociation.org, 2018 Alzheimer's disease facts and figures. *Alzheimers Dement.* **2018**, *14*, 367–429.

[2] Knowles, T. P. J.; Vendruscolo, M.; Dobson, C. M. The amyloid state and its association with protein misfolding diseases. *Nat. Rev. Mol. Cell Biol.* **2014**, *15*, 384–396.

[3] Chiti, F.; Dobson, C. M. Protein misfolding, amyloid formation, and human disease: A summary of the progress over the last decade. *Annu. Rev. Biochem.* **2017**, *86*, 27–68.

[4] Alzheimer, A. Über einen eigenartigen schweren Erkrankungsprozeß der Hirnrinde. *Neurologisches Centrablatt* **1906**, *23*, 1129–1136.

[5] Sipe, J. D.; Cohen, A. S. Review: History of the amyloid fibril. *J. Struct. Biol.* **2000**, *130*, 89–98.

[6] Masters, C. L.; Simms, G.; Winman, N. A.; Multhaup, G.; McDonald, B. L.; Beyreuther, K. Amyloid plaque core protein in Alzheimer's disease and down syndrome. *Proc. Natl. Acad. Sci. U.S.A.* **1985**, *82*, 4245–4249.

[7] Lippens, G.; Sillen, A.; Landrieu, I.; Amniai, L.; Sibille, N.; Barbier, P.; Leroy, A.; Hanoulle, X.; Wieruzeski, J.-M. Tau aggregation in Alzheimer's disease. *Prion* **2007**, *1*, 21–25.

[8] Eanes, E. D.; Glenner, G. G. X-ray diffraction studies on amyloid filaments. *J. Histochem. Cytochem.* **1958**, *16*, 673–677.

[9] Geddes, A. J.; Parker, K. D.; Atkins, E. D. T.; Beighton, E. "Cross-β" conformation in proteins. *J. Mol. Biol.* **1968**, *32*, 343–358.

[10] Petkova, A. T.; Yau, W. M.; Tycko, R. Experimental constraints on quaternary strucutre in Alzheimer's β-amyloid fibrils. *Biochemistry* **2006**, *45*, 489–512.

[11] Paravastu, A. K.; Leapman, R. D.; Yau, W. M.; Tycko, R. Molecular structural basis for polymorphism in Alzheimer's β-amyloid fibrils. *Proc. Natl. Acad. Sci. U.S.A.* **2008**, *105*, 18349–18354.

[12] Qiang, W.; Yau, W. M.; Luo, Y.; Mattson, M. P.; Tycko, R. Antiparallel β-sheet architecture in Iowa-mutant β-amyloid fibrils. *Proc. Natl. Acad. Sci. U.S.A.* **2012**, *109*, 4443–4448.

[13] Lu, J. X.; Qiang, W.; Yau, W. M.; Schwieters, C. D.; Meredith, S. C.; Tycko, R. Molecular structure of β-amyloid fibrils in Alzheimer's disease brain tissue. *Cell* **2013**, *14*, 1257–1268.

[14] Schütz, A. K.; Vagt, T.; Böckmann, A.; Glockschuber, R.; Meier, B. H. Atomic-resolution three-dimensional structure of amyloid β fibrils bearing the Osaka mutation. *Angew. Chem. Int. Ed.* **2015**, *54*, 331–335.

[15] Xiao, Y.; Ma, B.; McElheny, D.; Parthasarathy, S.; Long, F.; Hoshi, M.; Nussinov, R.; Ishii, Y. Aβ1–42 fibril structure illuminates self-recognition and replication of amyloid in Alzheimer's disease. *Nat. Struct. Mol. Biol.* **2015**, *22*, 499–505.

[16] Schmidt, M.; Rohou, A.; LAsker, K.; Yadav, J. K.; Schiene-Fischer, C.; Fandrich, M.; Grigorie, N. Peptide dimer structure in an Aβ1-42 fibril visualized with cryo-EM. *Proc. Natl. Acad. Sci. U.S.A.* **2015**, *112*, 11858–11863.

[17] Wälti, M. A.; Ravotti, F.; Arai, H.; Glabe, C. G.; Wall, J. S.; Böckmann, A.; Güntert, R.; Meier, B. H.; Riek, R. Atomic-resolution structure of a disease-relevant Aβ1–42 amyloid fibril. *Proc. Natl. Acad. Sci. U.S.A.* **2016**, *113*, E4976–E4984.

[18] Colvin, M. T.; Silver, R.; Ni, Q. Z.; Can, T. V.; Sergeyev, I.; Rosay, M.; Donovan, K. J.; Michael, B.; Wall, J.; Linse, S.; Griffin, R. G. Atomic resolution structure of monomorphic Aβ42 amyloid fibrils. *J. Am. Chem. Soc.* **2016**, *138*, 9663–9674.

[19] Gremer, L.; Schölzel, D.; Schenk, C.; Reinartz, E.; Labahn, J.; Ravelli, R. B. G.; Tusche, M.; Lopez-Iglesias, C.; Hoyer, W.; Heise, H.; Willbold, D.; Schröder, G. F. Fibril structure of amyloid-β1–42 by cryoelectron microscopy. *Science* **2017**, *358*, 116–119.

[20] Tycko, R. Solid-state NMR studies of amyloid fibril structure. *Annu. Rev. Phys. Chem.* **2011**, *62*, 279–299.

[21] Cheng, P.-N.; Pham, J. D.; Nowick, J. S. The supramolecular chemistry of β-sheets. *J. Am. Chem. Soc.* **2013**, *135*, 5477–5492.

[22] Tuttle, M. D.; Comellas, G.; Nieuwkoop, A. J.; Covell, D. J.; Berthold, D. A.; Kloepper, K. D.; Courtney, J. M.; Kim, J. K.; Barclay, A. M.; Kendall, A.; Wan, W.; Stubbs, G.; Scheiters, C. D.; Lee, V. M.; George, J. M.; Rienstra, C. M. Solid-state NMR structure of a pathogenic fibril of full-length human α-synuclein. *Nat. Struct. Mol. Biol.* **2016**, *23*, 409–415.

[23] Fitzpatrick, A. W. P.; Falcon, B.; He, S.; Murzin, A. G.; Murshudov, G.; Garringer, H. J.; Crowther, R. A.; Ghetti, B.; Goedert, M.; Scheres, S. H. W. Cryo-EM structures of tau filaments from Alzheimer's disease. *Nature* **2017**, *547*, 185–190.

[24] Nelson, R.; Sawaya, M. R.; Balbirnie, M.; Madsen, A. Ø.; Riekel, C.; Grothe, R.; Eisenberg, D. Structure of the cross-β spine of amyloid-like fibrils. *Nature* **2005**, *435*, 773–778.

[25] Sawaya, M. R.; Sambashivan, S.; Nelson, R.; Ivanova, M. I.; Sievers, S. A.; Apostol, M. I.; Thompson, M. J.; Balbirnie, M.; Wiltzius, J. J. W.; McFarlane, H. T.; Madsen, A. Ø.; Riekel, C.; Eisenberg, D. Atomic structures of amyloid cross-β spines reveal varied steric zippers. *Nature* **2007**, *447*, 453–457.

[26] Wiltzius, J. J.; Sievers, S. A.; Sawaya, M. R.; Cascio, D.; Popov, D.; Riekel, C.; Eisenberg, D. Atomic structure of the cross-β spine of islet amyloid polypeptide (amylin). *Protein Sci.* **2008**, *17*, 1467–1474.

[27] Wiltzius, J. J.; Landau, M.; Nelson, R.; Sawaya, M. R.; Apostol, M. I.; Goldschmidt, L.; Soriaga, A. B.; Cascio, D.; Rajashankar, K.; Eisenberg, D. Molecular mechanisms for protein-encoded inheritance. *Nat. Struct. Mol. Biol.* **2009**, *16*, 973–978.

[28] Colletier, J. P.; Laganowsky, A.; Landau, M.; Zhao, M.; Soriaga, A. B.; Goldschmidt, L.; Flot, D.; Cascio, D.; Sawaya, M. R.; Eisenberg, D. Molecular basis for amyloid-β polymorphism. *Proc. Natl. Acad. Sci. U.S.A.* **2011**, *108*, 16938–16943.

[29] Liu, C.; Sawaya, M. R.; Eisenberg, D. β2-microglobulin forms three-dimensional domain-swapped amyloid fibrils with disulfide linkages. *Nat. Struct. Mol. Biol.* **2011**, *18*, 49–55.

[30] Rodriguez, J. A.; Ivanova, M. I.; Sawaya, M. R.; Cascio, D.; Reyes, F. E.; Shi, D.; Sangwan, S.; Guenther, E. L.; Johnson, L. M.; Zheng, M.; Jiang, L.; Arbing, M. A.; Nannenga, B. L.; Hattne, J.; Whitelegge, J.; Brewster, A. S.; Messerschmidt, M.; Boutet, S.; Sauter, N. K.; Gonen, T.; Eisenberg, D. S. Structure of the toxic core of α-synuclein from invisible crystals. *Nature* **2015**, *525*, 486–490.

[31] Saelices, L.; Johnson, L. M.; Liang, W. Y.; Sawaya, M. R.; Cascio, D.; Ruchala, P.; Whitelegge, J.; Jiang, L.; Reik, R.; Eisenberg, D. S. Uncovering the mechanism of aggregation of human transthyretin. *J. Biol. Chem.* **2015**, *290*, 28932–28943.

[32] Soriaga, A. B.; Sangwan, S.; Macdonald, R.; Sawaya, M. R.; Eisenberg, D. Structures of IAPP amyloidogenic segments reveal a novel packing motif of out-of-register β-sheets. *J. Phys. Chem. B.* **2016**, *120*, 5810–5816.

[33] de la Cruz, M. J.; Hattne, J.; Shi, D.; Seidler, P.; Rodriguez, J.; Reyes, F. E.; Sawaya, M. R.; Cascio, D.; Weiss, S. C.; Kim, S. K.; Hinck, A. P.; Calero, G.; Eisenberg, D.; Gonen, T. Atomic-resolution structures from fragmented protein crystals with the cryoEM method microED. *Nat. Methods* **2017**, *14*, 399–402.

[34] Krotee, P.; Rodriguez, J. A.; Sawaya, M. R.; Cascio, D.; Reyes, F. E.; Shi, D.; Hattne, J.; Nannenga, B. L.; Oskarsson, M. E.; Philipp, S.; Griner, S.; Jiang, L.; Glabe, C. G.; Westermark, G. T.; Gonen, T.; Eisenberg, D. S. Atomic structures of fibrillar segments of hIAPP suggest tightly mated β-sheets are important for cytotoxicity. *ELife* **2017**, *6*, e19273.

[35] Riek, R.; Eisenberg, D. S. The activities of amyloids from a structural perspective. *Nature* **2016**, *539*, 227–235.

[36] Eisenberg, D. S.; Sawaya, M. R. Structural studies of amyloid proteins at the molecular level. *Annu. Rev. Biochem.* **2017**, *86*, 69–95.

[37] Tayeb-Fligelman, E.; Tabachnikov, O.; Moshe, A.; Goldshmidt-Tran, O.; Sawaya, M. R.; Coquelle, N.; Colletier, J. P.; Landau, M. The cytotoxic Staphylococcus aureus PSMα3 reveals a cross-α amyloid-like fibril. *Science* **2017**, *355*, 831–833.

[38] Cherny, I.; Gazit, E. Amyloids: not only pathological agents but also ordered nanomaterials. *Angew. Chem. Int. Ed.* **2008**, *47*, 4062–4069.

[39] Li, D.; Jones, E. M.; Sawaya, M. R.; Furukawa, H.; Luo, F.; Ivanova, M.; Sievers, S. A.; Wang, W.; Yaghi, O. M.; Liu, C.; Eisenberg, D. S. Structure-based design of functional amyloid materials. *J. Am. Chem. Soc.* **2014**, *136*, 18044–18051.

[40] Schneider, J. P.; Pochan, D. J.; Ozbas, B.; Rajagopal, K.; Pakstis, L.; Kertsinger, J. Responsive hydrogels from the intramolecular folding and self-assembly of a designed peptide. *J. Am. Chem. Soc.* **2002**, *124*, 15030–15037.

[41] Smith, D. J.; Brat, G. A.; Medina, S. H.; Tong, D.; Huang, Y.; Grahammer, J.; Furtmüller, G. J.; Oh, B. C.; Nagy-Smith, K. J.; Walczak, P.; Brandacher, G.; Schneider, J. P. A multiphase transitioning peptide hydrogel for suturing ultrasmall vessels. *Nat. Nanotechnol.* **2016**, *11*, 95–102.

[42] Nagy-Smith, K.; Moore, E.; Schneider, J. P.; Tycko, R. Molecular structure of monomorphic peptide fibrils within a kinetically trapped hydrogel network. *Proc. Natl. Acad. Sci. U.S.A.* **2015**, *112*, 9816–9821.

[43] Rufo, C. M.; Moroz, Y. S.; Moroz, O. V.; Stör, J.; Smith, T. A.; Hu, X.; DeGrado, W. F.; Korendovych, I. V. Short peptides self-assemble to produce catalytic amyloids. *Nat. Chem.* **2014**, *6*, 303–309.

[44] Makhlynets, O. V.; Gosavi, P. M.; Korendovych, I. V. Short self-assembling peptides are able to bind to copper and activate oxygen. *Angew. Chem. Int. Ed.* **2016**, *31*, 9017–9020.

[45] Lee, M.; Wang, T.; Makhlynets, O. V.; Wu, Y.; Polizzi, N. F.; Wu, H.; Gosavi, P. M.; Stör, J.; Korendovych, I. V.; DeGrado, W. F.; Hong, M. Zinc-binding structure of a catalytic amyloid from solid-state NMR.

[46] Lengyel, Z.; Rufo, C. M.; Moroz, Y. S.; Makhlynets, O. V.; Korendovych, I. V. Copper-containing catalytic amyloids promote phosphoester hydrolysis and tandem reactions. *ACS Catal.* **2018**, *8*, 59–62.

[47] Zozulia, O.; Dolan, M. A.; Korendovych, I. V. Catalytic peptide assemblies. *Chem. Soc. Rev.* **2018**, *Advanced Article*.

[48] Hardy, J. A.; Higgins, G. A. Alzheimer's disease: the amyloid cascade hypothesis. *Science* **1992**, *256*, 184–185.

[49] Hardy, J. A.; Selkoe, D. J. The amyloid hypothesis of Alzheimer's disease: progress and problems on the road to therapeutics. *Science* **2002**, *297*, 353–356.

[50] Selkoe, D. J.; Hardy, J. A. The amyloid hypothesis of Alzheimer's disease at 25 years. *EMBO Mol. Med.* **2016**, *8*, 595–608.

[51] Lee, S. J. C.; Nam, E.; Lee, H. J.; Savelieff, M. G.; Lim, M. H. Towards an understanding of amyloid-β oligomers: characterization, toxicity mechanisms, and inhibitors. *Chem. Soc. Rev.* **2017**, *46*, 310–323.

[52] Laganowsky, A.; Liu, C.; Sawaya, M. R.; Whitelegge, J. P.; Park, J.; Zhao, M.; Pensalfini, A.; Soriaga, A. B.; Landau, M.; Teng, P. K.; Cascio, D.; Glabe, C.; Eisenberg, D. Atomic view of a toxic amyloid small oligomer. *Science* **2012**, *335*, 1228–1231.

[53] Do, T. D.; LaPointe, N. E.; Nelson, R.; Krotee, P.; Hayden, E. Y.; Ulrich, B.; Quan, S.; Feinstein, S. C.; Teplow, D. B.; Eisenberg, D.; Shea, J.-E.; Bowers, M. T. Amyloid β-protein C-terminal fragments: Formation of cylindrins and β-barrels. *J. Am. Chem. Soc.* **2016**, *138*, 549–557.

[54] Apostol, M. I.; Perry, K.; Surewicz, W. K. Crystal structure of a human prion protein fragment reveals a motif for oligomer formation. *J. Am. Chem. Soc.* **2013**, *135*, 10202–10205.

[55] Kreutzer, A. G.; Nowick, J. S. Elucidating the structures of amyloid oligomers with macrocyclic β-hairpin peptides: insights into Alzheimer's disease and other amyloid diseases. *Acc. Chem. Res.* **2018**, *51*, 706–718.

[56] Spencer, R. K.; Chen, K. H.; Manuel, G.; Nowick, J. S. Recipe for β-Sheets: foldamers containing amyloidogenic peptide sequences. *Eur. J. Org. Chem.* **2013**, 3523–3528.

[57] Spencer, R. K.; Li, H.; Nowick, J. S. X-ray crystallographic structures of trimers and higher-order oligomeric assemblies of a peptide derived from $A\beta_{17–36}$. *J. Am. Chem. Soc.* **2014**, *136*, 5595–5598.

[58] Spencer, R. K.; Kreutzer, A. G.; Salveson, P. J.; Li, H.; Nowick, J. S. X-ray crystallographic structures of oligomers of peptides derived from β2-microclobulin. *J. Am. Chem. Soc.* **2015**, *137*, 6304–6311.

[59] Hoyer, W.; Grönwall, C.; Jonsson, A.; Ståhl, S.; Härd, T. Stabilaztion of a β-hairpin in monomeric Alzheimer's amyloid-β peptide inhibits amyloid formation. *Proc. Natl. Acad. Sci. U.S.A.* **2008**, *105*, 5099–5104.

[60] Kreutzer, A. G.; Hamza, I. L.; Spencer, R. K.; Nowick, J. S. X-ray crystallographic structures of a trimer, dodecamer and annular pore formed by a $A\beta_{17–36}$ β-hairpin. *J. Am. Chem. Soc.* **2016**, *138*, 4634–4642.

[61] Kreutzer, A. G.; Yoo, S.; Spencer, R. K.; Nowick, J. S. Stabilization, assembly, and toxicity of trimers derived from Aβ. *J. Am. Chem. Soc.* **2017**, *139*, 966–975.

[62] Kreutzer, A. G.; Spencer, R. K.; McKnelly, K. J.; Yoo, S.; Hamza, I. L.; Salveson, P. J.; Nowick, J. S. A hexamer of a peptide derived from Aβ16-36. *Biochemistry* **2017**, *56*, 6061–6071.

[63] Salveson, P. J.; Spencer, R. K.; Nowick, J. S. X-ray crystallographic structure of oligomers formed by a toxic β-hairpin derived from α-syniclein: trimers and higher-oligomers. *J. Am. Chem. Soc.* **2016**, *138*, 4458–4467.

[64] Salveson, P. J.; Spencer, R. K.; Kreutzer, A. G.; Nowick, J. S. X-ray crystallographic structure of a compact dodecamer from a peptide derived from $A\beta_{16-36}$. *Org. Lett.* **2017**, *19*, 3462–3465.

[65] Salveson, P. J.; Haerianardakani, S.; Thuy-Boun, A.; Kreutzer, A. G.; Nowick, J. S. Controlling the oligomerization state of Aβ-derived peptides with light. *J. Am. Chem. Soc.* **2018**, *140*, 5842–5852.

[66] Breydo, L.; Wu, J. W.; Uversky, V. N. α-Synuclein misfolding and Parkinson's disease. *Biochim. Biophys. Acta* **2012**, *1822*, 261–285.

[67] Lashuel, H. A.; Overk, C. R.; Oueslati, A.; Masliah, E. The many faces of α-synuclein: from structure and toxicity to therapeutic target. *Nature Rev. Neurosci.* **2013**, *14*, 38–48.

[68] Bendor, J. T.; Logan, T. P.; Edwards, R. H. The function of α-synuclein. *Neuron* **2013**, *79*, 1044–1066.

[69] Winner, B.; Jappelli, R.; Maji, S. K.; Desplats, P. A.; Boyer, L.; Aigner, S.; Hetzer, C.; Loher, T.; Vilar, M.; Campioni, S.; Tzitzilonis, C.; Soragni, A.; Jessberger, S.; Mira, H.; Consiglio, A.; Pham, E.; Masliah, E.; Gage, F. H.; Riek, R. In vivo demonstration that α-synuclein oligomers are toxic. *Proc. Natl. Acad. Sci. U.S.A.* **2011**, *108*, 4194–4199.

[70] Chen, S. W.; Drakulic, S.; Deas, E.; Ouberai, M.; Aprile, F. A.; Arranz, R.; Ness, S.; Roodveldt, C.; Guilliams, T.; De-Genst, E. J.; Klenerman, D.; Wood, N. W.; Knowles, T. P. J.; Alfonso, C.; Rivas, G.; Abramov, A. Y.; Valpuesta, J. M.; Dobson, C. M.; Cremades, N. Structural characterization of toxic oligomers that are kinetically trapped during α-synuclein fibril formation. *Proc. Natl. Acad. Sci. U.S.A.* **2015**, *112*, E1994–E2003.

[71] Pham, J. D.; Chim, N.; Goulding, C. W.; Nowick, J. S. Structures of oligomers of a peptide from β-amyloid. *J. Am. Chem. Soc.* **2013**, *135*, 12460–12467.

[72] Pham, J. D.; Demeler, B.; Nowick, J. S. Polymorphism of oligomers of a peptide from β-amyloid. *J. Am. Chem. Soc.* **2014**, *136*, 5432–5442.

[73] Pham, J. D.; Spencer, R. K.; Chen, K. H.; Nowick, J. S. A fibril-like assembly of oligomers of a peptide derived from β-amyloid. *J. Am. Chem. Soc.* **2014**, *136*, 12682–12690.

[74] Celej, M. S.; Sarroukh, R.; Goormaghtigh, E.; Fidelio, G. D.; Ruysschaert, J.-M.; Raussens, V. Toxic prefibrillar α-synuclein amyloid oligomers adopt a distinctive antiparallel β-sheet structure. *Biochem. J.* **2012**, *443*, 719–726.

[75] Gallea, J. I.; Celej, M. S. Structural insights into amyloid oligomers of the Parkinson disease-related protein α-synuclein. *J. Biol. Chem.* **2014**, *289*, 26733–26742.

[76] Paslawski, W.; Mysling, S.; Thomsen, K.; Jørgensen, T. J. D.; Otzen, D. E. Co-existence of two diffrent α-synuclein oligomers with different core structures determined by hydrogen/deuterium exchange mass spectrometry. *Angew. Chem. Int. Ed.* **2014**, *53*, 7560–7563.

[77] Mirecka, E. A.; Shaykhalishahi, H.; Gauhar, A.; Akgül, S.; Lecher, J.; Willbold, D.; Stoldt, M.; Hoyer, W. Sequestration of a β-hairpin for control of α-synuclein aggregation. *Angew. Chem. Int. Ed.* **2014**, *53*, 4227–4230.

[78] Dedmon, M. M.; Lindorff-Larsen, K.; Christodoulou, J.; Vendruscolo, M.; Dobson, C. M. Mapping long-range interactions in α-synuclein using spin-label NMR and ensemble molecular dynamics simulations. *J. Am. Chem. Soc.* **2005**, *127*, 476–477.

[79] Esteban-Martín, S.; Silvestre-Ryan, J.; Bertoncini, C. W.; Salvatella, X. Identification of fibril-like tertiary contacts in soluble monomeric α-synuclein. *Biophys. J.* **2013**, *105*, 1192–1198.

[80] Polymeropoulos, M. H.; Lavedan, C.; Leroy, E.; Ide, S. E.; Dehejia, A.; Dutra, A.; Pike, B.; Root, H.; Rubenstein, J.; Boyer, R.; Stenroos, E. S.; Chandrasekharappa, S.; Athanassiadou, A.; Papapetropoulos, T.; Johnson, W. G.; Lazzarini, A. M.; Duvoisin, R. C.; Di Iorio, G.; Globe, L. I.; Nussbaum, R. L. Mutation in the α-synuclein gene identified in families with Parkinson's disease. *Science* **1997**, *276*, 2045–2047.

[81] Krüger, R.; Kuhn, W.; Müller, T.; Woitalla, D.; Graeber, M.; Kösel, S.; Przuntek, H.; Epplen, J. T.; Schols, L.; Riess, O. Ala30Pro mutation in the gene encoding α-synuclein in Parkinson's disease. *Nat. Genet.* **1998**, *18*, 106–108.

[82] Zarranz, J. J.; Alegre, J.; Gómez-Esteban, J. C.; Lezcano, E.; Ros, R.; Ampuero, I.; Vidal, L.; Hoenicka, J.; Rodriguez, O.; Atarés, B.; Llorens, V.; Tortosa, E. G.; del Ser, T.; Muñoz, D. G.; de Yebenes, J. G. The new mutation, E46K, of α-synuclein causes Parkinson and Lewy Body Dementia. *Ann. Neurol.* **2003**, *55*, 164–173.

[83] Appel-Cresswell, S.; Vilarino-Guell, C.; Encarnacion, M.; Sherman, H.; Yu, I.; Shah, B.; Weir, D.; Thompson, C.; Szu-tu, C.; Trinh, J.; Aasly, J. O.; Rajput, A.; Rajput, A. H.; Stoessl, A. J.; Farrer, M. J. α-Synuclein p.H50Q, a novel pathogenic mutation for Parkinson's Disease. *Mov. Disord.* **2013**, *28*, 811–813.

[84] Lesage, S.; Anheim, M.; Letournel, F.; Bousset, L.; Honoré, A.; Rozas, N.; Pieri, L.; Madiona, K.; Dürr, A.; Melki, R.; Verny, C.; Brice, A. G51D α-synuclein mutation causes a novel Parkinsonian-Pyramidal syndrome. *Ann. Neurol.* **2013**, *73*, 459–471.

[85] Ghosh, D.; Sahay, S.; Ranjan, P.; Salot, S.; Mohite, G. M.; Singh, P. K.; Dwivedi, S.; Carvalho, E.; Banerjee, R.; Kumar, A.; Maji, S. K. The newly discovered Parkinson's disease associated Finnish mutation (A53E) attenuates α-synuclein aggregation and membrane binding. *Biochemistry* **2014**, *53*, 6419–6421.

[86] Yu, H.; Han, W.; Ma, W.; Schulten, K. Transient β-hairpin formation in α-synuclein monomer revealed by coarse-grained moleular dynamics simuations. *J. Chem. Phys.* **2015**, *143*, 243142.

[87] Nowick, J. S.; Brower, J. O. A new turn structure for the formation of β-hairpins in peptides. *J. Am. Chem. Soc.* **2003**, *125*, 876–877.

[88] Spencer, R. K.; Nowick, J. S. A newcomer's guide to peptide crystallography. *Isr. J. Chem.* **2015**, *55*, 689–710.

[89] Kabsch, W. Xds. *Acta Crystallogr., Sect. D: Biol. Crystallogr.* **2010**, *66*, 125–132.

[90] Adams, P. D.; Afonine, P. V.; Bunkóczi, G.; Chen, V. B.; Davis, I. W.; Echols, N.; Headd, J. J.; Hung, L.-W.; Kapral, G. J.; Grosse-Kunstleve, R. W.; McCoy, A. J.; Moriarty, N. W.; Oeffner, R.; Read, R. J.; Richardson, D. C.; Richardson, J. S.; Terwilliger, T. C.; Zwart, P. H. PHENIX: a comprehensive Python-based system for macromolecular structure solution. *Acta Crystallogr., Sect. D: Biol. Crystallogr.* **2010**, *66*, 213–221.

[91] Milton, R. C.; Milton, S. C.; Kent, S. B. Total chemical synthesis of a D-enzyme: the enantiomers of HIV-1 protease show reciprocal chiral substrate specificity. *Science* **1992**, *256*, 1445–1448.

[92] Yeates, T. O.; Kent, S. B. Racemic protein crystallography. *Annu. Rev. Biophys.* **2012**, *41*, 41–61.

[93] For examples of racemic peptide crystallography, see: (a) Mortenson, D. E.; Satyshur, K. A.; Guzei, I. A.; Forest, K. T.; Gellman, S. H. *J. Am. Chem. Soc.* **2012**, *134*, 2473–2476 (b) Wang, C. K.; King, G. J.; Northfield, S. E.; Ojeda, P. G.; Craik, D. J. *Angew. Chem. Int. Ed.* **2014**, *53*, 11236–11241 (c) Hayouka, Z.; Thomas, N. C.; Mortenson, D. E.; Satyshur, K. A.; Weisblum, B.; Forest, K. T.; Gellman, S. H. *J. Am. Chem. Soc.* **2015**, *137*, 11884–11887 (d) Mortenson, D. E.; Steinkruger, J. D.; Kreitler, D. F.; Perroni, D. V.; Sorenson, G. P.; Huang, L.; Mittal, R.; Yun, H. G.; Travis, B. R.; Mahanthappa, M. K.; Forest, K. T.; Gellman, S. H. *Proc. Natl. Acad. Sci. U.S.A.* **2015**, *112*, 13144–13149.

[94] For an excellent review using simulation-based approaches to understand the structures of oligomers formed by the β-amyloid peptide, see: Nasica-Labouze, J.; Nguyen, P. H.; Sterpone, F.; Berthoumieu, O.; Buchete, N.-V.; Cote, S.; De Simone, A.; Doig, A. J.; Faller, P.; Garcia, A.; Laio, A.; Li, M. S.; Melchionna, S.; Mousseau, N.; Mu, Y.; Paravastu, A.; Pasquali, S.; Rosenman, D. J.; Strodel, B.; Tarus, B.; Viles, J. H.; Zhang, T.; Wang, C.; Derreumaux, P. *Chem. Rev.* **2015**, *115*, 3518–3563.

[95] Sugita, Y.; Okamoto, Y. Replica-exchange molecular dynamics method for protein folding. *Chem. Phys. Lett.* **1999**, *314*, 141–151.

[96] Phillips, J. C.; Braun, R.; Wang, W.; Gumbart, J.; Tajkhorshid, E.; Villa, E.; Chipot, C.; Skeel, R. D.; Kalé, L.; Schulten, K. Scalable molecular dynamics with NAMD. *J. Comput. Chem.* **2005**, *26*, 1781–1802.

[97] Galvagnion, C.; Buell, A. K.; Meisl, G.; Michaels, T. C. T.; Vendruscolo, M.; Knowles, T. P. J.; Dobson, C. M. Lipid vesicles trigger α-synuclein aggregation by stimulating primary nucleation. *Nat. Chem. Biol.* **2015**, *11*, 229–234.

[98] Kelly, S. M.; Jess, T. J.; Price, N. C. How to study proteins by circular dichroiusm. *Biochim. Biophys. Acta* **2005**, *1751*, 119–139.

[99] Greenfield, N. J. Using circular dichroism spectra to estimate protein secondary structure. *Nat. Protoc.* **2007**, *1*, 2876–2890.

[100] Sinthuvanich, C.; Veiga, A. S.; Gupta, K.; Gaspar, D.; Blumenthal, R.; Schneider, J. P. Anticancer β-hairpin peptides: membrane-induced folding triggers activity. *J. Am. Chem. Soc.* **2012**, *134*, 6210–6217.

[101] The CD spectra of short peptides folded into well-defined β-hairpins often do not display canonical β-sheet signatures — a negative band at *ca.* 220 nm and a positive band below 200 nm. To the best of our knowledge, there is no singular CD signature for a β-hairpin, even in cases where a β-hairpin conformation is evident in NMR spectra. For examples of CD spectra of well-defined β-hairpins, see: (a) Blanco, F. J.; Rivas, G.; Serrano, L. *Nat. Struct. Biol.* **2.1994**, *1*, 584–590 (b) Stanger, H. E.; Gellman, S. H. *J. Am. Chem. Soc.* **2.1998**, *120*, 4236–4237 (c) Andersen, N. H.; Olsen, K. A.; Fesinmeyer, R. M.; Tan, X.; Hudson, F. M.; Eidenschink, L. A.; Farazi, S. R. *J. Am. Chem. Soc.* **2006**, *128*, 6101–6110 (d) Cline, L. L.; Waters, M. L. *J. Pept. Sci.* **2009**, *92*, 502–507 (e) Kier, B. L.; Shu, I.; Eidenschink, L. A.; Andersen, N. H. *Proc. Natl. Acad. Sci. U.S.A.* **2010**, *107*, 10466–10471.

[102] Auluck, P. K.; Careveo, G.; Lindquist, S. α-Synuclein: membrane interactions and toxicity in Parkinson's disease. *Annu. Rev. Cell Dev. Biol.* **2010**, *26*, 211–233.

[103] Korzeniewski, C.; Callewaert, D. M. An enzyme-release assay for natural cytotoxicity. *J. Immunol. Methods* **1983**, *64*, 313–320.

[104] Mosmann, T. Rapid colorimetric assay for cellular growth and survival: application to proliferation and cytotoxicity assays. *J. Immunol. Methods* **1983**, *65*, 55–63.

[105] Der-Sarkissian, A.; Jao, C. C.; Chen, J.; Langen, R. Structural organization of α-synuclin fibrils studied by site-directed spin labeling. *J. Biol. Chem.* **2003**, *278*, 37530–37535.

[106] Vilar, M.; Chou, H.-T.; Lührs, T.; Maji, S. K.; Riek-Loher, D.; Verel, R.; Manning, G.; Stahlberg, H.; Riek, R. The fold of α-synuclein fibrils. *Proc. Natl. Acad. Sci. U.S.A.* **2008**, *105*, 8637–8642.

[107] Commellas, G.; Lemkau, L. R.; Nieuwkoop, A. J.; Kloepper, K. D.; Ladror, D. T.; Ebisu, R.; Woods, W. S.; Lipton, A. S.; George, J. M.; Rienstra, C. M. Structured regions of α-synuclein fibrils include the early-onset Parkinson's disease mutation sites. *J. Mol. Biol.* **2011**, *411*, 881–895.

[108] Gath, J.; Bousset, L.; Habenstein, B.; Melki, R.; Meier, B. H.; Böckmann, A. Yet another polymorph of α-synuclein: solid-state sequential assignments. *Biomol. NMR. Assign.* **2014**, *8*, 395–404.

[109] The term NAC stands for non-β-amyloid component of β-amyloid plaques. The NAC was first identified as a 35-residue peptide that co-aggregated with β-amyloid in the brains of Alzheimer's disease patients: Uéda, K.; Fukushima, H.; Masliah, E.; Xia, Y.; Iwai, A.; Yoshimoto.; Otero, D. A.; Kondo, J.; Ihara, Y.; Saitoh, T. *Proc. Natl, Acad. Sci. U.S.A.* **2.1993**, *90*, 11282–11286.

[110] Giasson, B. I.; Murray, I. V. J.; Trojanowski, J. Q.; Lee, V. M.-Y. A hydrophobic stretch of 12 amino acid residues in the middle of α-synuclein is essential for filament assembly. *J. Biol. Chem.* **2001**, *276*, 2380–2386.

[111] Du, H.-N.; Tang, L.; Luo, X.-Y.; Li, H.-T.; Hu, J.; Zhou, J.-W.; Hu, H.-Y. A peptide motif consisting of glycine, alanine, and valine is required for the fibrillization and cytotoxicity of human α-synuclein. *Biochemistry* **2003**, *42*, 8870–8878.

[112] Periquet, M.; Fulga, T.; Myllykangas, L.; Schlossmacher, M. G.; Feany, M. B. Aggregated α-synuclein mediates dopaminergic neurotoxicity in vivo. *J. Neurosci.* **2007**, *27*, 3338–3346.

[113] Atsmon-Raz, Y.; Miller, Y. A proposed atomic structure of the self-assembly of the non-amyloid-β component of human alpha-synuclein as derived by computational tools. *J. Phys, Chem. B.* **2015**, *119*, 10005–10015.

[114] Dettmer, U.; Newman, A. J.; Soldner, F.; Luth, E. S.; Kim, N. C.; Von Saucken, V. E.; Sanderson, J. B.; Jaenisch, R.; Bartels, T.; Selkoe, D. Parkinson-causing α-synuclein missense mutations shift native tetramers to monomers as a mechanism for disease initiation. *Nat. Commun.* **2015**, *6*, 7314.

[115] Dettmer, U.; Newman, A. J.; Von Saucken, V. E.; Bartels, T.; Selkoe, D. KTKEGV repeat motifs are key mediators of normal α-synuclein tetramerization: Their mutation causes excess monomers and neurotoxicity. *Proc. Natl. Acad. Sci. U.S.A.* **2015**, *112*, 9596–9601.

[116] Cleary, J. P.; Walsh, D. M.; Hofmeister, J. J.; Shankar, G. M.; Kuskowski, M. A.; Selkoe, D. J.; Ashe, K. H. Natural oligomers of the amyloid-β protein specifically disrupt cognitive function. *Nat. Neurosci.* **2005**, *8*, 79–84.

[117] Our own attempts to study the assembly of peptide **2.1a** by NMR spectroscopy in buffered aqueous solution have proven unsuccessful, because peptide **2.1a** precipitates upon mixing with aqueous buffer at low millimolar concentrations.

[118] Evans, P. R.; Murshudov, G. N. How good are my data and what is the resolution? *Acta Crystallogr., Sect. D: Biol. Crystallogr.* **2013**, *69*, 1204–1214.

[119] McCoy, A. J.; Grosse-Kunstleve, R. W.; Adams, P. D.; Winn, M. D.; Stoironi, L. C.; Read, R. J. Phaser crystallographic software. *J. Appl. Cryst.* **2007**, *40*, 658–674.

[120] Emsley, P.; Lohkamp, B.; Scott, W. G.; Cowtan, K. Features and development of Coot. *Acta Crystallogr., Sect. D: Biol. Crystallogr.* **2010**, *66*, 486–501.

[121] Krissinel, E.; Henrick, K. Protein interfaces, surfaces and assemblies' service PISA at the European Bioinformatics Institute. *J. Mol. Biol.* **2007**, *372*, 774–797.

[122] Janin, J.; Bahadur, R. P.; Chakrabarti, P. Protein-protein interaction and quaternary structure. *Q. Rev. Biophys.* **2008**, *41*, 133–180.

[123] Yu, L.; Edalji, R.; Harlan, J. E.; Holzman, T. F.; Lopez, A. P.; Labkovsky, B.; Hillen, H.; Barghorn, S.; Ebert, U.; Richardson, P. L.; Miesbauer, L.; Solomon, L.; Bartley, D.; Walter, K.; Johnson, R. W.; Hajduk, P. J.; Olejniczak, E. T. Structural characterization of a soluble amyloid β-peptide oligomer. *Biochemistry* **2009**, *48*, 1870–1877.

[124] Dupuis, N. F.; Wu, C.; Shea, J.-E.; Bowers, M. T. Hunam islet amyloid polypeptide monomers form ordered β-hairpins: A possible direct amyloid precursor. *J. Am. Chem. Soc.* **2009**, *131*, 18283–18292.

[125] Larini, L.; Shea, J.-E. Role of beta-hairpin fomration in aggregation: The self-assembly of the amyloid-β(25-35) peptide. *Biophys. J.* **2012**, *103*, 576–586.

[126] Gu, L.; Liu, C.; Guo, Z. Structural insights into Aβ42 oligomers using site-directed spin labeling. *J. Biol. Chem.* **2013**, *288*, 18673–18683.

[127] Gu, L.; Liu, C.; Stroud, J. C.; Ngo, S.; Jiang, L.; Guo, Z. Antiparallel triple-strand architecture for prefibrillar Aβ42. *J. Biol. Chem.* **2014**, *289*, 27300–27313.

[128] Mirecka, E. A.; Feuerstein, S.; Gremer, L.; Schröder, G. F.; Stoldt, M.; Willbold, D.; Hoyer, W. β-Hairpin of islet amyloid polypeptide bound to an aggregation inhibitor. *Sci. Rep.* **2016**, *6*, 33474.

[129] Lendel, C.; Bjerring, M.; Dubnovitsky, A.; Kelly, R. T.; Filippov, A.; Antzutkin, O. N.; Nielsen, N. C.; Härd, T. A hexameric peptide barrel as building block of amyloid-β protofibrils. *Angew. Chem. Int. Ed.* **2014**, *53*, 12756–12760.

[130] We discovered that sonication permits the dissolution of Met_{35}-containing peptide **3.2**, which is substantially less soluble then Orn_{35}-containing peptide **1**.

[131] Townsend, M.; Shankar, G. M.; Mehta, T.; Walsh, D. M.; Selkoe, D. J. Effects of secreted oliogmers of amyloid-βpotein on hippocampal synaptic plasticity: a potent role for trimers. *J. Physiol.* **2006**, *572*, 477–492.

[132] Lesné, S.; Koh, M. T.; Kotilinek, L.; Kayed, R.; Glabe, C. G.; Yang, A.; Gallagher, M.; Ashe, K. H. A specific amyloid-β protein assembly in the brain impairs memory. *Nature* **2006**, *440*, 352–357.

[133] Young, D. D.; Deiters, A. Photochemical control of biological processes. *Org. Biomol. Chem.* **2007**, *5*, 999–1005.

[134] Yu, H.; Li, J.; Wu, D.; Qiu, Z.; Zhang, Y. Chemistry and biological applications of photo-labile organic molecules. *Chem. Soc. Rev.* **2010**, *39*, 464–473.

[135] Klán, R.; Šolomek, T.; Bochet, C. G.; Blanc, A.; Givens, R.; Rubina, M.; Popik, V.; Kostikov, A.; Wirz, J. Photoremovable protecting groups in chemistry and biology: reaction mechanisms and efficacy. *Chem. Rev.* **2013**, *113*, 119–191.

[136] Ankenbruck, N.; Courtney, T.; Naro, Y.; Deiters, A. Optochemical control of biological processes in cells and animals. *Angew. Chem. Int. Ed.* **2018**, *57*, 2768–2798.

[137] Callaway, E. M.; Yuste, R. Stimulating neurons with light. *Curr. Opin. Neurobiol.* **2002**, *12*, 587–592.

[138] Kramer, R. H.; Chambers, J. J.; Trauner, D. Photochemical tools for remote control of ion channels in excitable cells. *Nat. Chem. Biol.* **2005**, *1*, 360–365.

[139] Ellis-Davies, G. C. R. Neurobiology with caged calcium. *Chem. Rev.* **2008**, *108*, 1603–1613.

[140] Haines, L. A.; Rajagopal, K.; Ozbas, B.; Salick, D. A.; Pochan, D. J.; Schneider, J. P. Light-activated hydrogel formation via the triggered folding and self-assembly of a designed peptide. *J. Am. Chem. Soc.* **2005**, *127*, 17025–17029.

[141] Karginov, A. V.; Zou, Y.; Shirvanyants, D.; Kota, P.; Dokholyan, N. V.; Young, D. D.; Hahn, K. M.; Deiters, A. Light regulation of protein dimerization and kinase activity in living cells using photocaged rapamycin and engineered FKBP. *J. Am. Chem. Soc.* **2011**, *133*, 420–423.

[142] Umeda, N.; Ueno, T.; Pohlmeyer, C.; Nagano, T.; Inoue, T. A photocleavable rapamycin conjugate for spatiotemporal control of small GTPase activity. *J. Am. Chem. Soc.* **2011**, *133*, 12–14.

[143] Deiters, A. Light activation as a method of regulating and studying gene expression. *Curr. Opin. Chem. Biol.* **2009**, *13*, 678–686.

[144] Govan, J. M.; Lively, M. O.; Deiters, A. Photochemical control of DNA decoy function enables precise regulation of nuclear factor ϰB activity. *J. Am. Chem. Soc.* **2011**, *133*, 13176–13182.

[145] Ryu, K. A.; Stutts, L.; Tom, J. K.; Mancini, R. J.; Esser-Kahn, A. P. Stimulation of innate immune cells by light-activated TLR7/8 agonists. *J. Am. Chem. Soc.* **2014**, *136*, 10823–10825.

[146] Mancini, R. J.; Stutts, L.; Moore, T.; Esser-Kahn, A. P. Controlling the origins of inflammation with a photoactive lipopeptide immunopotentiator. *Angew. Chem. Int. Ed.* **2015**, *54*, 5962–5965.

[147] Stutts, L.; Esser-Kahn, A. P. A light-controlled TLR4 agonist and selectable activation of cell subpopulations. *ChemBioChem* **2015**, *16*, 1744–1748.

[148] Schelkle, K. M.; Griesbaum, T.; Ollech, D.; Becht, S.; Buckup, T.; Hamburger, M.; Wombacher, R. Light-induced protein dimerization by one- and two-photon activation of gibberellic acid derivatives in living cells. *Angew. Chem. Int. Ed.* **2015**, *54*, 2825–2829.

[149] Brown, K. A.; Zou, Y.; Shirvanyants, D.; Zhang, J.; Samanta, S.; Mantravadi, P. K.; Dokholyan, N. V.; Deiters, A. Light-cleavable rapamycin dimer as an optical trigger for protein dimerization. *Chem. Commun.* **2015**, *51*, 5702–5705.

[150] Ryu, K. A.; McGonnigal, B.; Moore, T.; Kargupta, T.; Mancini, R. J.; Esser-Kahn, A. P. Light guided in-vivo activation of innate immune cells with photocaged TLR 2/6 agonist. *Sci. Rep.* **2017**, *7*, 8074.

[151] Larson, M. E.; Lesné, S. E. Soluble Aβ olgiomer production and toxicity. *J. Neurochem.* **2012**, *120*, 125–139.

[152] Williams, T. L.; Serpell, L. C. Membrane and surface interactions of Alzheimer's Aβ peptide – insights into the mechanism of cytotoxicity. *FEBS J.* **2011**, *278*, 3905–3917.

[153] Benilova, I.; Karran, E.; De Stooper, B. The toxic Aβ oligomer and Alzheimer's disease: an emperor in need of clothes. *Nat. Neurosci.* **2012**, *15*, 349–357.

[154] Measey, T. J.; Gai, F. Light-triggered disassembly of amyloid fibrils. *Langmuir* **2012**, *28*, 12588–12592.

[155] Furutani, M.; Uemura, A.; Shigenaga, A.; Komiya, C.; Otaka, A.; Matsuura, K. A photoinduced growth system of peptide nanofibres addressed by DNA hybridization. *Chem. Commun.* **2015**, *51*, 8020–8022.

[156] Awad, L.; Jejelava, N.; Burai, R.; Lashuel, H. A. A new caged-glutamine derivative as a tool to control the assembly of glutamine-containing amyloidogenic peptides. *ChemBioChem* **2016**, *17*, 2353–2360.

[157] Johnson, E. G. B.; Lanning, J. D.; Meredith, S. C. Peptide backbone modification in the bend region of amyloid-β inhibits fibrillogenesis but not oligomer formation. *J. Pept. Sci.* **2016**, *22*, 368–373.

[158] Sangwan, S.; Zhao, A.; Adams, K. L.; Jayson, C. K.; Sawaya, M. R.; Guenther, E. L.; Pan, A. C.; Ngo, J.; Moore, D. M.; Soriaga, A. B.; Do, T. D.; Goldschmidt, L.; Nelson, R.; Bowers, M. T.; Koehler, C. M.; Shaw, D. E.; Novitch, B. G.; Eisenberg, D. S. Atomic strucutre of a toxic, oligomeric segment of SOD1 linked to amyotrophic lateral sclerosis (ALS). *Proc. Natl. Acad. Sci. U.S.A.* **2017**, *114*, 8770–8775.

[159] Sandberg, A.; Luheshi, L. M.; Söllvander, S.; Pereira de Barros, T.; Macao, B.; Knowles, T. P. J.; Biverstål, H.; Lendel, C.; Ekholm-Petterson, F.; Dubnovitsky, A.; Lannfelt, L.; Dobson, C. M.; Härd, T. Stabilization of neurotoxic Alzhemier amyloid-β oligomers by protein engineering. *Proc. Natl. Acad. Sci. U.S.A.* **2010**, *107*, 15595–15600.

[160] Scheidt, H. A.; Morgado, I.; Huster, D. Solid-state NMR reveals a close structural relationship between amyloid-β protofibrils and oligomers. *J. Biol. Chem.* **2012**, *287*, 22822–22826.

[161] Huang, D.; Zimmerman, M. I.; Martin, P. K.; Nix, A. J.; Rosenberry, T. L.; Paravastu, A. K. Antiparallel β-sheet structure within the C-terminal region of 42-residue of Alzheimers β-amyloid peptides when they form 150 kDa oligomers. *J. Mol. Biol.* **2015**, *427*, 2319–2328.

[162] Zuckermann, R. N.; Kerr, J. M.; Kent, S. B. H.; Moos, W. H. Efficient method for the preparation of peptoids [oligo(N-substituted glycines)] by submonomer solid-phase synthesis. *J. Am. Chem. Soc.* **1992**, *114*, 10646–10647.

[163] Johnson, E. C. B.; Kent, S. B. H. Synthesis, stability, and optimized photolytic cleavage of 4-methoxy-2-nitrobenzyl backbone-protected peptides. *Chem. Commun.* **2006**, 1557–1559.

[164] Tam, J. P.; Wu, C. R.; Liu, W.; Zhang, J. W. Disulfide bond formation in peptides by dimethyl sulfoxide. Scope and applications. *J. Am. Chem. Soc.* **1991**, *113*, 6657–6662.

[165] Khakshoor, O.; Nowick, J. S. Use of disulfide "staples" to stabilize β-sheet quaternary strucutre. *Org. Lett.* **2009**, *11*, 3000–3003.

[166] Foadi, J.; Aller, P.; Alguel, Y.; Cameron, A.; Axford, D.; Owen, R. L.; Armour, W.; Waterman, D. G.; Iwata, S.; Evans, G. Clustering procedures for the optimal selection of data sets from multiple crystals in macromolecular crystallography. *Acta Crystallogr., Sect. D: Biol. Crystallogr.* **2013**, *69*, 1617–1632.

[167] Schägger, H. Tricine-SDS-Page. *Nat. Protoc.* **2009**, *1*, 16–22.

[168] Simpson, R. J. *Proteins and Proteomics*; Cold Spring Harbor Laboratory Press: Cold Spring Harbor, NY, USA, 2003.

[169] Arias, M.; Vogel, H. J. Fluorescence and absorbance spectroscopy methods to study membrane perturbations by antimicrobial host defense peptides. *Methods Mol. Biol.* **2017**, *1584*, 141–157.

[170] Vassar, P. S.; Culling, C. F. Fluorescent stains, with special reference to amyloid and connective tissue. *Arch. Pathol.* **1959**, *68*, 487–498.

[171] Naiki, H.; Higuchi, K.; Hosokawa, M.; Takeda, T. Fluorometric determination of amyloid fibrils in vitro using the fluorescent dye, thioflavine T. *Anal. Biochem.* **1989**, *177*, 244–249.

[172] Westermark, G. T.; Johnson, K. H.; Westermark, P. Staining methods for identification of amyloid in tissue. *Methods Enzymol.* **1999**, *309*, 3–25.

[173] Frid, P.; Anisimov, S. V.; Popovic, N. Congo red and protein aggregation in neurodegenerative diseases. *Brain Res. Rev.* **2007**, *53*, 135–160.

[174] Hawe, A.; Sutter, M.; Jiskoot, W. Extrinsic fluorescent dyes as tools for protein characterization. *Pharm. Res.* **2008,**, *25*, 1487–1499.

[175] Gestwicki, J. E.; Crabtree, G. R.; Graef, I. A. Harnessing chaperones to generate small-molecule inhibitors of amyloid-β aggregation. *Science* **2004**, *306*, 865–869.

[176] Klunk, W. E.; Engler, H.; Nordberg, A.; Wang, Y.; Blomqvist, G.; Holt, D. P.; Bergström, M.; Savitcheva, I.; Huang, G. F.; Estrada, S.; Ausén, B.; Debnath, M. L.; Barletta, J.; Price, J. C.; Sandell, J.; Lopresti, B. J.; Wall, A.; Koivisto, R.; Antoni, G.; Mathis, C. A.; Långström, B. Imaging brain amyloid in Alzheimer's disease with Pittsburgh Compound-B. *Ann. Neurol.* **2004**, *55*, 306–319.

[177] Yang, L.; Rieves, D.; Ganley, C. Brain amyloid imaging–FDA approval of florbetapir F18 injection. *N. Engl. J. Med.* **2012**, *367*, 885–887.

[178] Hatai, J.; Motiei, L.; Margulies, D. Analyzing amyloid β aggregates with a combinatorial fluorescent molecular sensor. *J. Am. Chem. Soc.* **2017**, *139*, 2136–2139.

[179] Scherzer-Attali, R.; Pellarin, R.; Convertino, M.; Frydman-Marom, A.; Egoz-Matia, N.; Peled, S.; Levy-Sakin, M.; Shalev, D. E.; Caflisch, A.; Gazit, E.; Segal, D. Complete phenotypic recovery of an Alzheimer's disease model by a quinone-tryptophan hybrid aggregation inhibitor. *PLOS one.* **2010**, *5*, e11101.

[180] Landau, M.; Sawaya, M. R.; Faull, K. F.; Laganowsky, A.; Jiang, L.; Sievers, S. A.; Liu, J.; Barrio, J. R.; Eisenberg, D. Toward a pharmacophore for amyloid. *PLOS Biol.* **2011**, *9*, e1001080.

[181] Wu, C.; Scott, J.; Shea, J.-E. Binding of Congo red to amyloid protofibrils of the Alzheimer Aβ9-40 peptide probed by molecular dynamics simulations. *Biophys. J.* **2012**, *103*, 550–557.

[182] Skeby, K. K.; Sørensen, J.; Schiøtt, B. Identification of a common binding mode for imaging agents to amyloid fibrils from molecular dynamics simulations. *J. Am. Chem. Soc.* **2013**, *135*, 15114–15128.

[183] Scherzer-Attali, R.; Convertino, M.; Pellarin, R.; Gazit, E.; Segal, D.; Caflisch, A. Methylations of tryptophan-modified naphthoquinone affect its inhibitory potnetial toward Aβ aggregation. *J. Phys. Chem. B* **2013**, *117*, 1780–1789.

[184] Lemkul, J. A.; Bevan, D. R. The role of molecular simulations in the development of inhibitors of amyloid-β peptide aggregation for the treatment of Alzheimer's disease. *ACS Chem. Neurosci.* **2102**, *3*, 845–856.

[185] Parikh, N. D.; Klimov, D. K. Molecular mechanisms of Alzheimer's biomaker FDDNP binding to Aβ amyloid fibril. *J. Phys. Chem. B* **2015**, *119*, 11568–11580.

[186] Young, L. M.; Ashcroft, A. E.; Radford, S. E. Small molecule probes of protein aggregation. *Curr. Opin. Chem. Biol.* **2017**, *39*, 90–99.

[187] He, H.; Xu, J.; Cheng, D.-Y.; Fu, L.; Ge, Y.-S.; Jiang, F.-L.; Liu, Y. Identification of binding modes for amino naphthalene 2-cyanoacrylate (ANCA) probes to amyloid fibrils from molecular dynamics simulations. *J. Phys. Chem. B* **2017**, *121*, 1211–1221.

[188] Sangwan, S.; Sawaya, M. R.; Murray, K. A.; Hughes, M. P.; Eisenberg, D. S. Atomic structures of corkscrew-forming segments of SOD1 reveal varied oligomer conformations. *Protein Sci.* **2018**, *Early View*.

[189] Jiang, L.; Liu, C.; Leibly, D.; Landau, M.; Zhao, M.; Hughes, M. P.; Eisenberg, D. S. Structure-based discovery of fiber-binding compounds that reduce the cytotoxicity of amyloid-β. *ELife* **2013**, *2*, e00857.

[190] Maezawa, I.; Hong, H.-S.; Liu, R.; Wu, C.-Y.; Cheng, R. H.; Kung, M.-P.; Kung, H. F.; Lam, K. S.; Oddo, S.; LeFerla, F. M.; Jin, L.-W. Congo red and thioflavin-T analogs detect Aβ oligomers. *J. Neurochem.* **2008**, *104*, 457–468.

[191] Teoh, C. L.; Su, D.; Sahu, S.; Yun, S.-W.; Drummond, E.; Prelli, F.; Lim, S.; Cho, S.; Ham, S.; Wisniewski, T.; Chang, Y.-T. Chemical fluorescent probe for detection of Aβ oligomers. *J. Am. Chem. Soc.* **2015**, *137*, 13503–13509.

[192] Lv, G.; Sun, A.; Wei, P.; Zhang, N.; Haichuang, L.; Yi, T. A spiropyran-based fluorescent probe for the specific detection of β-amyloid peptide oligomers in Alzheimer's disease. *Chem. Commun.* **2016**, *52*, 8865–8868.

[193] Li, Y.; Xu, D.; Sun, A.; Ho, S.-L.; Poon, C.-Y.; Chan, H.-N.; Ng, O. T. W.; Yung, K. K. L.; Yan, H.; Li, H.-W.; Wong, M. S. Fluoro-substituted cyanine for reliable in vivo labelling of amyloid-β oligomers and neuroprotection against amyloid-β induced toxicity. *Chem. Sci.* **2017**, *8*, 8279–8284.

[194] Yates, E. V.; Meisl, G.; Knowles, T. P. J.; Dobson, C. M. An environmentally sensitive fluorescent dye as a multidimensional probe of amyloid formation. *J. Phys. Chem. B* **2016**, *120*, 2087–2094.

[195] Kumar, M.; Hong, Y.; Thorn, D. C.; Ecroyd, H.; Carver, J. A. Monitoring early-stage protein aggregation by an aggregation-induced emission fluorogen. *Anal. Chem.* **2017**, *89*, 9322–9329.

[196] Brahmachari, S.; Paul, A.; Segal, D.; Gazit, E. Inhibition of amyloid oligomerization into different supramolecular architectures by small molecules: mechanistic insights and design rules. *Future Med. Chem.* **2017**, *9*, 797–810.

[197] Reinke, A. A.; Gestwicki, J. E. Insight into amyloid structure using chemical probes. *Chem. Biol. Drug Des.* **2011**, *77*, 399–411.

[198] LeVine, H.; Walker, L. C. What amyloid ligands can tell us about molecular polymorphism and disease. *Neurobiol. Aging* **2016**, *42*, 205–212.

[199] Polyclonal and monoclonal antibodies have been developed as biochemical probes for amyloid oligomers. The structures of the oligomers that these antibodies recognize are also unknown: De Genst, E.; Messer, A.; Dobson, C. M. *Biochim. Biophys. Acta* **5.2014**, *1844*, 1907–1919.

[200] Kayed, R.; Head, E.; Thompson, J. L.; McIntire, T. M.; Milton, S. C.; Cotman, C. W.; Glabe, C. G. Common structure of soluble amyloid oligomers implies common mechanism of pathogenesis. *Science* **2003**, *300*, 486–489.

[201] Sievers, S. A.; Karanicolas, J.; Chang, H. W.; Zhao, A.; Jiang, L.; Zirafi, O.; Stevens, J. T.; Münch, J.; Baker, D.; Eisenberg, D. Structure-based design of non-natural amino-acid inhibitors of amyloid fibril formation. *Nature* **2011**, *475*, 96–100.

[202] Seidler, P. M.; Boyer, D. R.; Rodriguez, J. A.; Sawaya, M. R.; Cascio, D.; Murray, K.; Gonen, T.; Eisenberg, D. Structure-based inhibitors of tau aggregation. *Nat. Chem.* **2018**, *10*, 170–176.

[203] Duxbury, D. F. The photochemistry and photophysics of triphenylmethane dyes in solid and liquid media. *Chem. Rev.* **1993**, *93*, 381–433.

[204] Baptista, M. S.; Indig, G. L. Effect of BSA on photophysical and photochemical properties of triarylmethane dyes. *J. Phys. Chem. B* **1998**, *102*, 4678–4688.

[205] Bartlett, J. A.; Indig, G. L. Spectroscopic and photochemical properties of malachite green noncovalently bound to bovine serum albumin. *Dyes Pigm.* **1999**, *43*, 219–226.

[206] Qin, M.; Yin, T.; Shen, W. The interaction between crystal violet and bovine serum albumin: spectroscopic and molecular docking investigations. *J. Dispersion Sci. Technol.* **2015**, *37*, 1623–1629.

[207] Hong, Y.; Lam, J. W. Y.; Tang, B. Z. Aggregation-induced emission. *Chem. Soc. Rev.* **2011**, *40*, 5361–5388.

[208] Mei, J.; Leung, N. L. C.; Kwok, R. T. K.; Lam, J. W. Y.; Tang, B. Z. Aggregation-induced emission: Together we shine, united we soar! *Chem. Rev.* **2015**, *115*, 11718–11940.

[209] Job, P. Formation and stability of inorganic complexes in solution. *Ann. Chim.* **1928**, *9*, 113–203.

[210] Bruneau, E.; Lavabre, D.; Levy, G.; Micheau, J. C. Quantitative analysis of continuous-variation plots with a comparison of several methods. *J. Chem. Educ.* **1992**, *69*, 833–837.

[211] Olson, E. J.; Bühlmann, P. Getting more out of a Job Plot: determination of reactant to product stoichiometry in cases of displacement reactions and n:n complex formation. *J. Org. Chem.* **2011**, *76*, 8406–8412.

[212] Truex, N. L.; Nowick, J. S. Coassembly of peptides derived from β-sheet regions of β-amyloid. *J. Am. Chem. Soc.* **2016**, *138*, 13891–13900.

[213] Brookes, E.; Cao, W.; Demeler, B. A two-dimensional spectrum analysis for sedimentation velocity experiments of mictures with heterogeneity in molecular weight and shape. *Eur. Biophys. J.* **2010**, *39*, 405–415.

[214] Ulatowski, F.; Dąbrowa, K.; Bałakier, T.; Jurczak, J. Recognizing the limited applicability of job plots in studying host-guest interactions in supramolecular chemistry. *J. Org. Chem.* **2016**, *81*, 1746–1756.

[215] Lurtz, M. M.; Pedersen, S. E. Aminotriarylmethane dyes are high-affinity noncompetitive antagonists of the nicotinic acetylcholine receptor. *Mol. Pharmacol.* **1999**, *55*, 159–167.

[216] Schumacher, M. A.; Miller, M. C.; Grkovic, S.; Brown, M. H.; Skurray, R. A.; Brennan, R. G. Structural mechanisms of QacR induction and multidrug recognition. *Science* **2001**, *294*, 2158–2163.

[217] Arias, H. R.; Bhumireddy, P.; Spitzmaul, G.; Trudell, J. R.; Bouzat, C. Molecular mechanisms and binding site location for the noncompetitive antagonist crystal violet on nicotinic acetylcholine receptors. *Biochemistry* **2006**, *45*, 2014–2026.

[218] Yamasaki, S.; Nikaido, E.; Nakashima, R.; Sakurai, K.; Fujiwara, D.; Fujii, I.; Nishino, K. The crystal structure of multidrug-resistance regulator RamR with multiple drugs. *Nat. Commun.* **2013**, *4*, 2078.

[219] Allgardson, A.; Andersson, C. D.; Akfur, C.; Worek, F.; Linusson, A.; Ekström, F. An unusual dimeric inhibitor of acetylcholinesterase: Cooperative binding of crystal violet. *Molecules* **2017**, *22*, E1433.

[220] Morris, G. M.; Huey, R.; Lindstrom, W.; Sanner, M. F.; Belew, R. K.; Goodsell, D. S.; Olson, A. J. Autodock4 and AutoDockTools4: automated docking with selective receptor flexibility. *J. Comput. Chem.* **2009**, *30*, 2785–2791.

[221] Korn, A.; Surendran, D.; Krueger, M.; Maiti, S.; Huster, D. Ring structure modifications of phenylalanine 19 increase fibrillation kinetics and reduce toxicity of amyloid β (1-40). *Chem. Commun.* **2018**, *54*, 5430–5433.

[222] Hendrickson, W. A.; Teeter, M. M. Structure of the hydrophobic protein crambin determined directly from the anomalous scattering of sulphur. *Nature* **1981**, *290*, 107–113.

[223] Sarma, G. N.; Karplus, P. A. In-house sulfur SAD phasing: a case study of the effects of data quality and resolution cutoffs. *Acta Crystallogr., Sect. D: Biol. Crystallogr.* **2006**, *62*, 707–716.

[224] Lie, Q.; Dahmane, T.; Zhang, Z.; Assur, Z.; Brasch, J.; Shapiro, L.; Mancia, F.; Hendrickson, W. A. Structures from anomalous diffraction of native biological macromolecules. *Science* **2012**, *336*, 1033–1037.

[225] Liu, Q.; Liu, Q.; Hendrickson, W. A. Robust structural analysis of native biological macromolecules from multi-crystal anomalous diffraction data. *Acta Crystallogr., Sect. D: Biol. Crystallogr.* **2013**, *69*, 1314–1332.

[226] Liu, Q.; Hendrickson, W. A. Crystallographic phasing from weak anomalous signals. *Curr. Opin. Struct. Biol.* **2015**, *34*, 99–107.

[227] Liu, Q.; Hendrickson, W. A. Contemporary use of anomalous diffraction in biomolecular structure analysis. *Methods Mol. Biol.* **2017**, *1607*, 377–399.

[228] We were unable to determine the X-ray crystallographic structure of trimer $\mathbf{5.2_{F19Cha}}$ using either S-SAD or molecular replacement.

[229] The backbone RMSD overlay of the trimer **5.2** homologues with trimer **5.2** ranges from 0.9–1.1Å.

[230] Mohanty, J.; Shinde, M. N.; Barooah, N.; Bhasikuttan, A. C. Reversible insulin hexamer assembly promoted by ethyl violet: pH-controlled uptake and release. *J. Phys. Chem. Lett.* **2016**, *7*, 3978–3983.

[231] Jana, M. K.; Cappai, R.; Ciccotosto, G. D. Oligomeric amyloid-β toxicity can be inhibited by blocking its cellular binding in cortical neuronal cultures with addition of the triphenylmethane dye brilliant blue G. *ACS Chem. Neurosci.* **2016**, *7*, 1141–1147.

[232] We have been unable to determine if crystal violet or its homologues can detoxify trimer **5.2**, as these triphenylmethane dyes are toxic to the neuroblastoma SH-SY5Y cell line at concentrations at which the dyes associate with trimer **5.2**.

[233] Wong, H. E.; Qi, W.; Choi, H.-M.; Fernandez, E. J.; Kwon, I. A safe, blood-brain barrier permeable triphenylmethane dye inhibits amyloid-β neurotoxicity by generating nontoxic aggregates. *ACS Chem. Neurosci.* **2011**, *2*, 645–657.

[234] Chen, X.; Hu, J.; Jiang, L.; Xu, S.; Zheng, B.; Wang, C.; Zhang, J.; Wei, X.; Chang, L.; Wang, Q. Brilliant blue G improves cognition in an animal model of Alzheimer's disease and inhibits amyloid-β-induced loss of filopodia and dendrite spines in hippocampal neurons. *Neuroscience* **2014**, *279*, 94–101.

[235] Irwin, J. A.; Erisir, A.; Kwon, I. Oral triphenymethane food dye analog, brilliant blue G, prevents neuronal loss in APPSwDI/NOS2-/- mouse model. *Curr. Alzheimer Res.* **2016**, *13*, 663–677.

[236] Bancroft, J. D. Methyl green as a differentiator and counterstain in the methyl violet technique for the demonstration of amyloid. *Stain Technol.* **1983**, *38*, 336–337.

[237] Dsouza, R. N.; Pischel, U.; Nau, W. M. Fluorescent dyes and their supramolecular host/guest complexes with macrocycles in aqueous solution. *Chem. Rev.* **2011**, *111*, 7941–7980.

[238] Wu, J.; Kwon, B.; Liu, W.; Anslyn, E. V.; Wang, P.; Kim, J. S. Chromogenic/fluorogenic ensemble chemosensing systems. *Chem. Rev.* **2015**, *115*, 7893–7943.

[239] Babendure, J. R.; Adams, S. R.; Tsien, R. Y. Aptamers switch on fluorescence of triphenylmethane dyes. *J. Am. Chem. Soc.* **2003**, *125*, 14716–14717.

[240] Bhasikuttan, A. C.; Mohanty, J.; Nau, W. M.; Pal, H. Efficient fluorescence enhancement and cooperative binding of an organic dye in a supra-biomolecular host-protein assembly. *Angew. Chem. Int. Ed.* **2007**, *46*, 4120–4122.

[241] Szent-Gyorgi, C.; Schmidt, B. F.; Creeger, Y.; Fisher, G. W.; Zakel, K. L.; Adler, S.; Fitzpatrick, J. A. J.; Woolford, C. A.; Yan, Q.; Vasilev, K. V.; Berget, P. B.; Bruchez, M. P.; Jarvik, J. W.; Waggoner, A. Fluorogen-activating single-chain antibodies for imaging cell surface proteins. *Nat. Biotechnol.* **2008**, *26*, 235–240.

[242] Gotrik, M.; Sekhon, G.; Saurabh, S.; Nakamoto, M.; Eisenstein, M.; Soh, H. T. Direct selection of fluorescence-enhancing RNA aptamers. *J. Am. Chem. Soc.* **2018**, *140*, 3583–3591.

[243] Demeler, B.; Gorbet, G. In *Analytical Ultracentrifugation: Instrumentation, Software, and Applications*; Uchiyama, S., Stafford, W. F., Laue, T., Eds.; Springer, 2016; Chapter 8. Analytical Ultracentrifugation Data Analysis with UltraScan-III, pp 119–143.

[244] Demeler, B. Methods for the design and analysis of sedimentation velocity and sedimentation equilibrium experiments with proteins. *Cur. Protoc. Prot. Sci.* **2010**, *60*, 7.13.1–7.13.24.

[245] Gorbet, G.; Devlin, T.; Hernandez Uribe, B. I.; Demeler, A. K.; Lindsey, Z. L.; Gani, S.; Breton, S.; Weise-Cross, L.; Lafer, E. M.; Brookes, E. H.; Demeler, B. A parametrically constrained optimization method for fitting sedimentation velocity experiments. *Biophys. J.* **2014**, *106*, 1741–1750.

[246] Demeler, B.; van Holde, K. E. Sedimentation velocity analysis of highly heterogeneous systems. *Anal. Biochem.* **2004**, *335*, 279–288.

[247] Demeler, B.; Brookes, E. Monte Carlo analysis of sedimentation experiments. *Colloid Polym. Sci.* **2008**, *286*, 129–137.

[248] https://math.vanderbilt.edu/schectex/courses/cubic/.